STRUCTURE AND MECHANISM OF A EUKARYOTIC FMN ADENYLYLTRANSFERASE

Approved by supervisory committee

_____
Hong Zhang, Ph.D. (Mentor)

_____
Diana Tomchick, Ph.D. (Committee Chair)

_____
Kevin Gardner, Ph.D.

_____
Betsy Goldsmith, Ph.D.

This thesis is dedicated to my family.

STRUCTURE AND MECHANISM OF A EUKARYOTIC FMN ADENYLYLTRANSFERASE

by

CARLOS HUERTA JR.

DISSERTATION

Presented to the Faculty of the Graduate School of Biomedical Sciences
The University of Texas Southwestern Medical Center at Dallas
In Partial Fulfillment of the Requirements
For the Degree of

DOCTOR OF PHILOSOPHY
The University of Texas Southwestern Medical Center at Dallas
Dallas, Texas
December, 2009

ACKNOWLEDGEMENTS

There are many individuals that contributed to my graduate education and I would like to thank a few of them. First, I would like to honor my mentor, Dr. Hong Zhang. Dr. Zhang's support and encouragement was essential to the completion of my graduate education. Dr. Zhang's compassion to X-ray crystallography and biological science was fundamental in transforming me into a structural biologist.

I would also like to thank all past and current members of the Zhang laboratory. In particular, I would like to thank Dr. Nian Huang and Dr. Darek Martynowski for discussions in structure refinement and modeling, and Marcelo Raines for teaching me protein purification and crystallization. A special acknowledgement goes to Dr. Dominika Borek for teaching me how to solve my first protein structure and her support through-out my graduate education.

My graduate thesis would not be possible without the guidance and understanding of my dissertation committee members Dr. Diana Tomchick, Dr. Kevin Gardner and Dr. Elizabeth Goldsmith. I owe them and Dr. Zhang my deepest gratitude.

Finally, I would like to thank my family for all their support and encouragement. Without my mom, Mary Huerta, and my aunt, Jaimi Salas, my path to a graduate education would not exist. I would also like to thank my brother and my sister for encouragement and interest in my research.

STRUCTURE AND MECHANISM OF A EUKARYOTIC FMN ADENYLYLTRANSFERASE

Carlos Huerta Jr., Ph.D.

The University of Texas Southwestern Medical Center at Dallas, 2009

Supervising Professor: Hong Zhang, Ph.D.

ABSTRACT

Flavin mononucleotide adenylyltransferase (FMNAT) catalyzes the formation of the essential flavocoenzyme FAD and plays an important role in flavocoenzyme homeostasis regulation. By sequence comparison, bacterial and eukaryotic FMNAT enzymes belong to two different protein superfamilies and apparently utilize different set of active site residues to accomplish the same chemistry. Extensive biochemical studies from endogenous bacterial and mammalian FMNATs using FMN analogs and various cations have suggested that the architectures of the substrate binding and catalytic sites are different. Sequence comparison reveals that eukaryotic FMNAT is related to the PAPS reductase-like family, which belongs to the adenine nucleotide α hydrolase-like superfamily. Despite the classification of eukaryotic FMNAT, the residues

involved in substrate binding and catalysis are not completely known, as eukaryotic FMNAT has no sequence similarity to other known flavin binding proteins. To determine the unique flavin binding site, and to investigate the residues involved in substrate binding and the mechanism of catalysis, we utilized X-ray crystallography and biochemical methods.

Here we report the first structural characterization of a eukaryotic FMNAT from a pathogenic yeast *Candida glabrata* (*Cg*FMNAT). Four crystal structures of *Cg*FMNAT in different complexed forms were determined at resolutions between 1.20-1.95 Å, capturing the enzyme active site states prior to and after catalysis. These structures reveal a novel flavin-binding mode and a unique enzyme-bound FAD conformation. Comparison of the bacterial and eukaryotic FMNAT provides a structural basis for understanding the convergent evolution of the same FMNAT activity from different protein ancestors. The different complexed forms of *Cg*FMNAT allowed a structure-based investigation into the kinetic properties of eukaryotic FMNAT, whereby two "supermutants" were identified from mutagenic analysis. The steady-state kinetics and product inhibition properties of the two "supermutants" provided a basis for understanding the regulatory mechanisms of FAD homeostasis by FMNAT in eukaryotic organisms.

TABLE OF CONTENTS

PRIOR PUBLICATIONS

1. Yang K, Strauss E, **Huerta C**, and Zhang H. (2008) "Structural Basis for Substrate Binding and the Catalytic Mechanism of Type III Pantothenate Kinase." *Biochemistry*. 47, 1369-1380.

2. **Huerta C**, Borek D, Machius M, Grishin NV, and Zhang H. (2009) "Structure and Mechanism of a Eukaryotic FMN Adenylyltransferase." *Journal of Molecular Biology*. 389, 388-400.

LIST OF FIGURES

LIST OF TABLES

LIST OF ABBREVIATIONS

Å	Angstrom
AIF	Apoptosis-inducing factor
AMPCPP	α,β-methyleneadenosine 5'-triphosphate
APBS	Adaptive Poisson-Boltzmann Solver
APS	Adenosine phosphosulfate
ATP	Adenosine 5'-triphosphate
ATPase	ATP hydrolyzing enzyme
C-terminus	Carboxyl-terminus
CoREST	REST corepressor
CCP4	Collaborative computational project 4
DAAO	D-amino acid oxidase
DNA	Deoxyribonucleic acid
dNTP	Deoxyribonucleotide triphosphate
DTT	Dithiolthreitol
EC	Enzyme commission
Ero1	Endoplasmic reticulum oxidoreductin 1
FAD	Flavin adenine dinucleotide
FADS	Flavin adenine dinucleotide synthetase
$\boldsymbol{F_c}$	Calculated structure factor amplitude
FFT	Fast Fourier transform
FMN	Flavin mononucleotide
FMNAT	Flavin mononucleotide adenylyltransferase
$\boldsymbol{F_o}$	Observed structure factor amplitude
$\boldsymbol{g}$	Gravity acceleration
GMP	Guanosine monophosphate

GTP	Guanosine triphosphate
HEPES	4-(2-hydroxyethyl)-1-piperazineethanesulfonic acid
His_6	Six histidines
IPTG	Isopropyl-1-thio-β-D-galactopyranoside
LB	Luria-Bertani
LSD1	Lysine-specific demethylase 1
k_{cat}	Enzyme turnover rate
K_i	Inhibitor equilibrium constant
K_m	Michaelis-Menten constant
MAD	Multiple-wavelength anomalous diffraction
MAO	Monoamine oxidase
MESG	2-amino-6-mercapto-7-methylpurine riboside
Mg^{2+}	magnesium ion
$MgCl_2$	Magnesium chloride
MICAL	Molecule interacting with CasL
MoCo	Molybdenum cofactor
MoeA	Product of moeA gene
MogA	Product of mogA gene
MTHFR	5,10-methylenetetrahydrofolate reductase
N-terminus	Amine-terminus
N-type	Ammonium-type
Na^{1+}	Sodium ion
NaCl	Sodium chloride
NAD	Nicotinamide adenine dinucleotide
NH^{3+}	Ammonium
NaMN	Nicotinic acid mononucleotide

NMN	Nicotinamide mononucleotide
NMNAT	Nicotinamide mononucleotide adenylyltransferase
PAPS	3’-phosphoadenosine 5’-phosphosulfate
PCR	Polymerase chain reaction
Pfam	Protein families
PEG	Polyethylene glycol
PEG MME	Polyethylene glycol monomethyl ether
PNP	Purine nucleoside phosphorylase
PPase	Inorganic pyrophosphatase
PP_i	Inorganic pyrophosphate
RFK	Riboflavin kinase
RT	Room temperature
SAD	Single anomalous diffraction
SCOP	Structural classification of proteins
SDS-PAGE	Sodium dodecyl-sulfate polyacrylamide gel electrophoresis
SeMet	Selenomethionyl
TEV	Tobacco etch virus
T_m	Melting temperature
Tris	Tris(hydroxymethyl) aminomethane
tRNA	Transfer ribonucleic acid
V_{max}	Maximum velocity
w/v	Weight per volume
XMP	Xanthosine 5’-monophosphate

CHAPTER 1

General Introduction

Biological Function of Flavin Cofactors

The riboflavin derivatives flavin mononucleotide (FMN) and flavin adenine dinucleotide (FAD) are essential cofactors involved in many oxidation/reduction (redox) reactions in the cell[1]. The functional and chemical versatility of these cofactors, in association with various flavoproteins (proteins that bind flavins), allows them to be involved in a large variety of reaction types and to participate in many cellular processes ranging from energy production, metabolism, light emission, DNA repair, chromatin remodeling, and protein folding to detoxification, neural development, and apoptosis[2-4]. Due to the involvement of flavocofactors in wide-ranging cellular processes, riboflavin deficiency in human leads to a multitude of physiological aberrations, such as abnormal fetal development, inadequate ion absorption, cardiovascular disease and corneal defects[5].

The flavocofactors, FMN and FAD, have many biological functions. Primarily, they act as redox agents that can undergo one- and two-electron transfer processes. The flavocofactors can also act as nucleophiles and

electrophiles that form a flavin-adduct intermediate[1,6-9]. The electron transfer occurs at the N1 and N5 atom positions of the isoalloxazine ring (**Fig. 1.1**), whereas flavin-adduct intermediates occur on the C4a and N5 atom positions. Flavoproteins, which are flavin-dependent for catalysis, have the flavin non-covalently or covalently bound (either permanently or reversibly) as a cofactor[8,10,11]. The covalent bond can occur as a single linkage between the isoalloxazine ring of the flavin and a Cys, His or Tyr residue of the flavoprotein[8,10], or as a dual linkage involving Cys and His[11] (**Fig. 1.2**).

The type of flavoprotein the flavins associate with dictates the chemical reaction type that the flavin will perform[1]. Oxidases and monooxygenases are two flavin-dependent flavoproteins that require molecular oxygen for the catalytic process, in which hydrogen peroxide is an end product for oxidases and water for monooxygenases[12]. An example of an oxidase is the FAD-dependent D-amino acid oxidase (DAAO) that deaminates neutral and hydrophobic amino acids with the production of hydrogen peroxide, ammonia and an α-keto acid[13] (**Fig. 1.3**). In the case of monooxygenases, NADH or NAD(P)H is the electron donor rather than the substrate as in DAAO[1,13]. During the catalytic process a flavin-adduct intermediate (peroxide or hydroperoxide) on the C4a atom of the isoalloxazine ring occurs (**Fig. 1.4**), with the subsequent transfer of an oxygen or hydroxyl to the substrate.

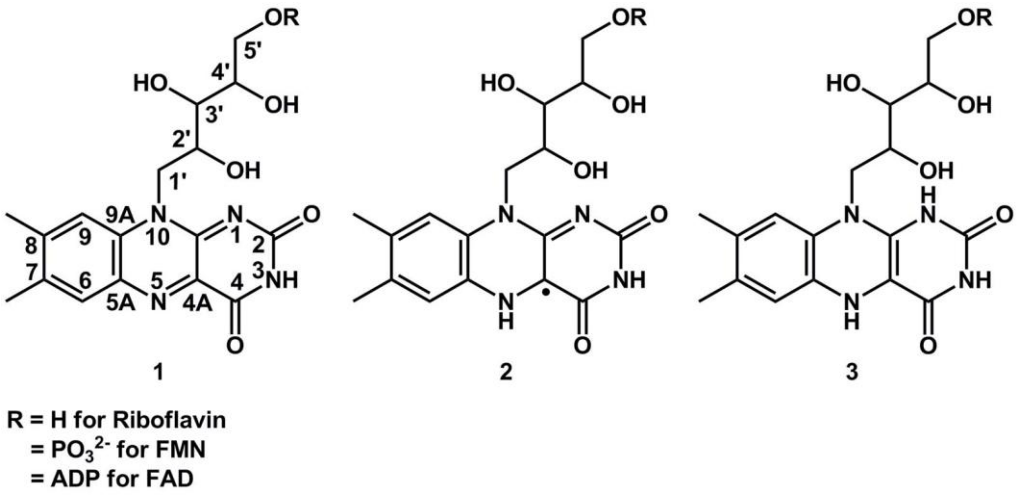

Figure 1.1 Structures of flavocofactors. The oxidation-reduction states of the flavocofactors are shown with **1** being the oxidized state, **2** the one-electron reduced (neutral semiquinone) state and **3** the two-electron reduced (hydroquinone) state. The substitution of R stands for "H", "PO_3^{2-}" or "ADP" for riboflavin, FMN and FAD, respectively.

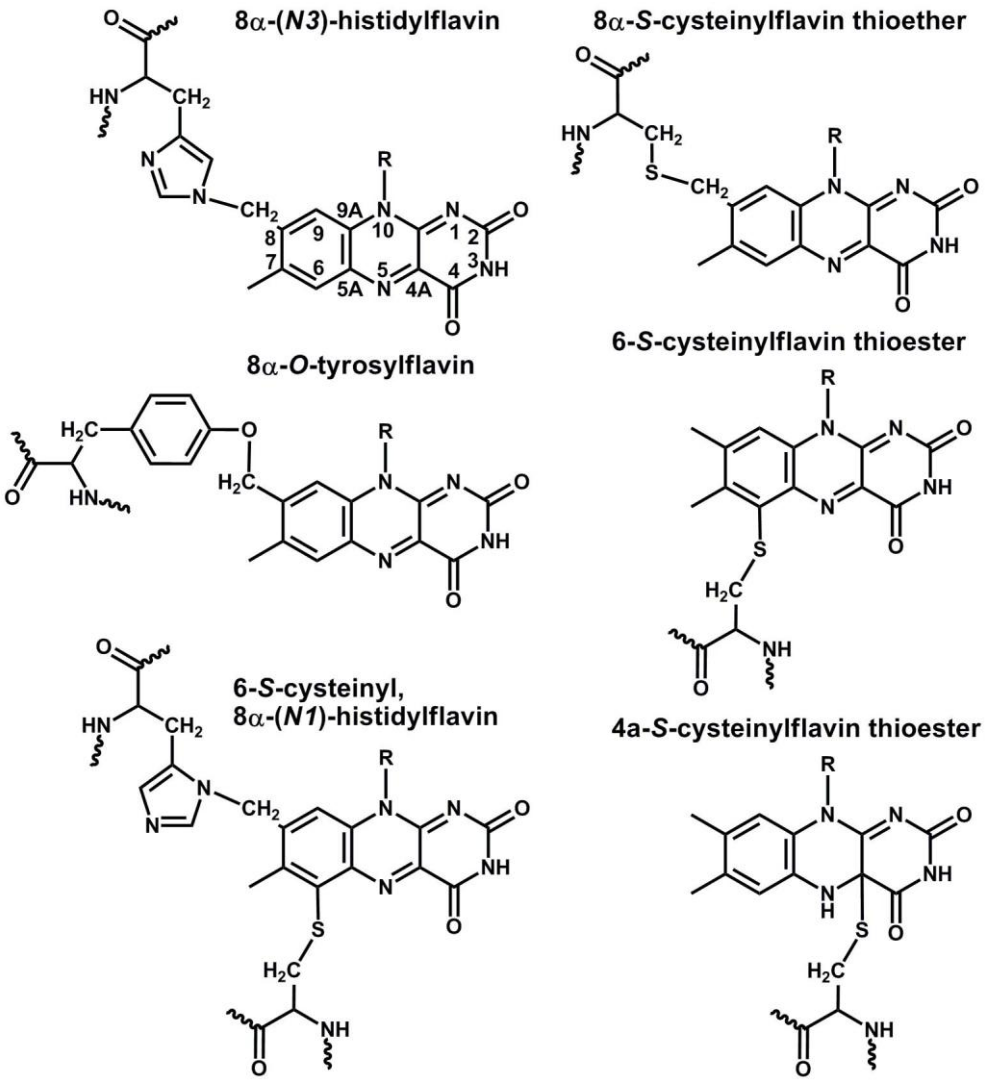

Figure 1.2 Structures of six covalent linkages between the flavin cofactor and flavoenzyme.

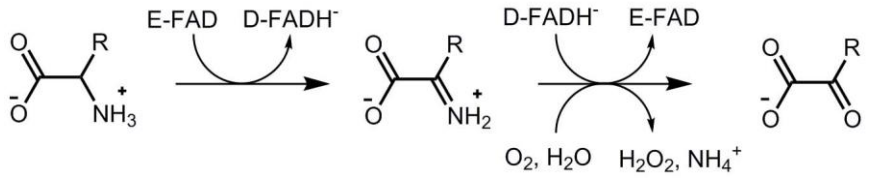

Figure 1.3 D-amino acid oxidase (DAAO) reaction scheme. DAAO catalyzes the deamination of neutral and hydrophobic amino acids with the first half reaction involving the reduction of FAD and formation of an imino acid intermediate. In the second half reaction, in the presence of molecular oxygen (O_2) and water, the imino acid is converted to an α-keto acid with the formation of hydrogen peroxide (H_2O_2) and ammonia (NH_4^+).

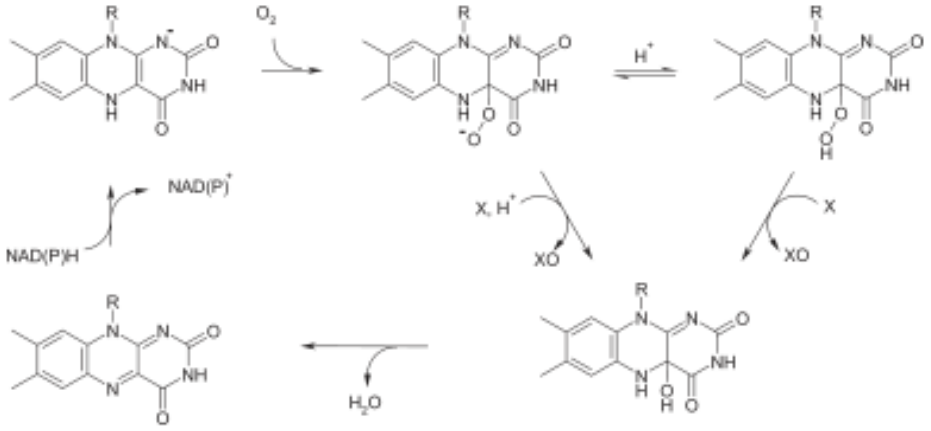

Figure 1.4 General mechanism of flavin-dependent monooxygenases. FAD is reduced by NAD(P)H with the transfer of two electrons that is followed by a flavin-adduct formation of peroxide or hydroperoxide. The "X" represents the substrate to be oxygenated or hydoxylated ("XO"). Figure adapted from van Berkel WJK, Chemistry of Flavoenzymes 2008[14].

Recently, flavoproteins are emerging to be involved in biological processes other than metabolism[2,4]. In addition to its fundamental role in basic metabolism such as respiration, amino acids and fatty acid metabolism, flavoproteins are also involved in other cellular processes, such as transcription regulation, tumorigenesis and apoptosis. For example, lysine-specific demethylase (LSD1) is a flavin-dependent amine oxidase that demethylates mono- and di-methylated histone H3 at lysine 4 (K4) of the nucleosomes[15]. The mechanism of demethylation is similar to that of the DAAO catalytic process, where the FAD is reduced by the fourth Lys residue (substrate) of the histone, with the subsequent release of hydrogen peroxide and formaldehyde[16] (**Fig. 1.5**). The methylation of H3K4 serves as a gene activation marker, with transcription repressed by demethylation by LSD1 and the associated co-repressor CoREST and histone deacetylase[15,17]. The activity of LSD1 on H3K4 has been shown to regulate hematopoietic differentiation, which is involved in generating neutrophils and maintaining the lymphoid development[18]. In addition, LSD1 can be a gene activator by demethylating H3K9 through the association with the androgen receptor[19]. The association is linked to the androgen-receptor-dependent gene activation, with overexpression correlated to prostate cancer and tumor recurrence during therapy[19,20]. Other demethylases have been implicated in cancer, as well as neurological disorders, with the latter being associated with a dysfunctional

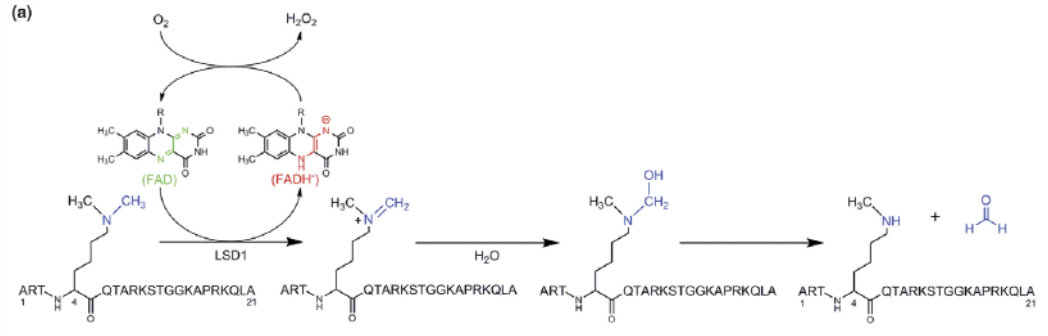

Figure 1.5 Lysine specific demethylase (LSD1) catalyzed reaction. A methyl-group from Lys4 of histone 3 is oxidized to form an iminium ion following a two electron transfer to FAD. The iminium ion is hydrolyzed to produce formaldehyde and demethylated lysine. The reduced flavin is then oxidized to form FAD by molecular oxygen that produces hydrogen peroxide. Figure adapted from Culhane JC, Curr Opin Chem Biol, 2007[21].

demethylase[22]. Another example is the apoptosis inducing factor (AIF) which is a FAD/NAD(P)H binding protein[23,24] residing in the mitochondrial intermembrane space[25]. In response to poly(ADP ribose) polymerase-1 (PARP-1) activation by DNA damage, AIF translocates to the nucleus and binds to the DNA to induce apoptosis through chromatin condensation and fragmentation independent of FAD binding[25-27]. The binding of AIF to DNA is required to induce apoptosis[23]. Aside from apoptosis, the primary physiological role of AIF is inside the mitochondria where it is involved in the assembly/maintenance of the respiratory complex I, which is part of the oxidative phosphorylation process[28]. Alteration of AIF is shown to cause mouse skeletal muscle atrophy and cardiomyopathy, which is correlative with oxidative phosphorylation defects[29]. Additionally, these pathologies may be in response to increase oxidative stress, as it is proposed that AIF may be a free radical scavenger[29], which was previously proposed in mouse with a defective AIF that lead to neurodegeneration[30].

Other flavoproteins that are known to be involved in neuronal development and signaling include MICAL (molecule interacting with CasL) and DAAO. MICAL is a multidomain, cytosolic protein with a functionally essential N-terminal domain that is a flavin-dependent monooxygenase that utilizes NAD(P)H[31-33]. The functional property of the N-terminal domain is shown to be required for the signaling events that guide axonal growth in the developing

nervous systems[31,34]. However, the catalytic mechanism to which MICAL relays the signaling process is not known. DAAO is shown to have a significant role in modulating D-serine (D-Ser) levels in the brain by converting D-amino acids to α-keto acids and ammonia[35]. As D-Ser functions as an agonist at the glycine binding site of N-methyl-D-aspartate (NMDA) receptors and a co-agonist for glutamate activation of the NMDA receptors[36,37], the lack of degradation leads to neuronal disorders such as schizophrenia, ischemia, epilepsy and neurodegeneration[35,38,39]. Following a stroke, neuronal damage occurs as a consequence of the release of D-Ser, with the neuronal damage inhibited by DAAO[35,39]. Aside from neurons, in the presence of supplemental D-amino acids, DAAO is shown to inhibit tumor growth and has a detoxifying role[35,40,41]. Other flavoproteins involved in regulating neuronal signaling are monoamine oxidases (MAO) A and B. Both oxidases catalyze the degradation of amine-containing neurotransmitters, such as serotonin that is a specific substrate for MAOA and dopamine that is a substrate for both[6]. Inappropriate metabolism of the neurotransmitters lead to aggressive behavior, stress, panic attacks and depression, and it has been shown that elevated expression of MAOB is linked to Parkinson's disease [42,43].

Biosynthetic Pathway of Flavocofactors

Riboflavin, also known as vitamin B_2, is the universal precursor for the biosynthesis of FMN and FAD, the primary forms of flavins in cells[3,44]. In plants, yeast and many prokaryotes, riboflavin is either synthesized *de novo*, or obtained from the environment and transported into the cells[44]. Higher eukaryotes, such as humans, lack the *de novo* riboflavin biosynthesis machinery, and the only means of obtaining riboflavin is through the diet[3,44]. As such, the biosynthesis of riboflavin and the flavocofactors FMN and FAD can be divided into two categories, the biosynthesis of riboflavin and flavocofactors.

Biosynthesis of riboflavin

The *de novo* biosynthesis of riboflavin requires one molecule of guanosine triphosphate (GTP) and two molecules of ribulose 5-phosphate from the purine and pentose phosphate biosynthetic pathways[45]. In the first step of pathway, which is the committed step, GTP (**1**) (**Fig. 1.6**) is converted to 2,5-diamino-6-ribosylamino-4(3*H*)-pyrimidinone 5'-phosphate (**2**) by GTP cyclohydrolase II (**I**) with the release of PP_i and formate, and the opening of the imidazole ring[46-49]. In the case of archaebacteria, this reaction may be catalyzed by two separate enzymes, with the second substrate intermediate unique to archaebacteria[50]. The substrate intermediate (**2**) (or the third substrate intermediate from archaea) is converted to 5-amino-6-ribitylamino-2,4(1*H*,3*H*)-pyrimidinedione 5'-phosphate

(**5**) by two reaction steps that involve a deamination of the heterocyclic ring and reduction of the ribosyl side chain. In bacteria and plants, the deamination is catalyzed first by 2,5-diamino-6-ribosylamino-4(3*H*)-pyrimidinone 5'-phosphate deaminase (**II**) to yield 5-amino-6-ribosylamino-2,4(1*H*,3*H*)-pyrimidinedione 5'-phosphate (**3**), which is then reduced by 5-amino-6-ribosylamino-2,4(1*H*,3*H*)-pyrimidinedione 5'-phosphate reductase (**III**) to yield substrate intermediate (**5**)[51-55]. In yeast and archaebacteria, the reduction precedes the deamination[56-60]. It is known that the next step is dephosphorylation (**VI**) to generate 5-amino-6-ribitylamino-2,4(1*H*,3*H*)-pyrimidinedione (**6**), since the phosphorylated intermediate (**5**) cannot serve as a substrate for the proceeding 6,7-dimethyl-8-ribityllumazine synthase (**VIII**) step[61,62]. However, nothing is known about the reaction step. Following dephosphorylation, the lumazine synthase (**VIII**) catalyzes the condensation of the substrate intermediate (**6**) with 3,4-dihydroxy-2-butanone 4-phosphate (3,4-DHBP) (**8**) forming 6,7-dimethyl-8-ribityllumazine (**9**)[62,63]. The four carbon substrate intermediate (**8**) is formed from ribulose 5-phosphate (**7**) by a rearrangement/elimination process catalyzed by 3,4-dihydroxy-2-butanone 4-phosphate synthase (**VII**)[64,65]. In the final reaction step, a dismutation reaction is catalyzed by riboflavin synthase (**IX**) that involves two molecules of 6,7-dimethyl-8-ribityllumazine (**9**)[66-68]. During the reaction, a four carbon unit, which was derived from ribulose 5-phosphate (**7**), is transferred from

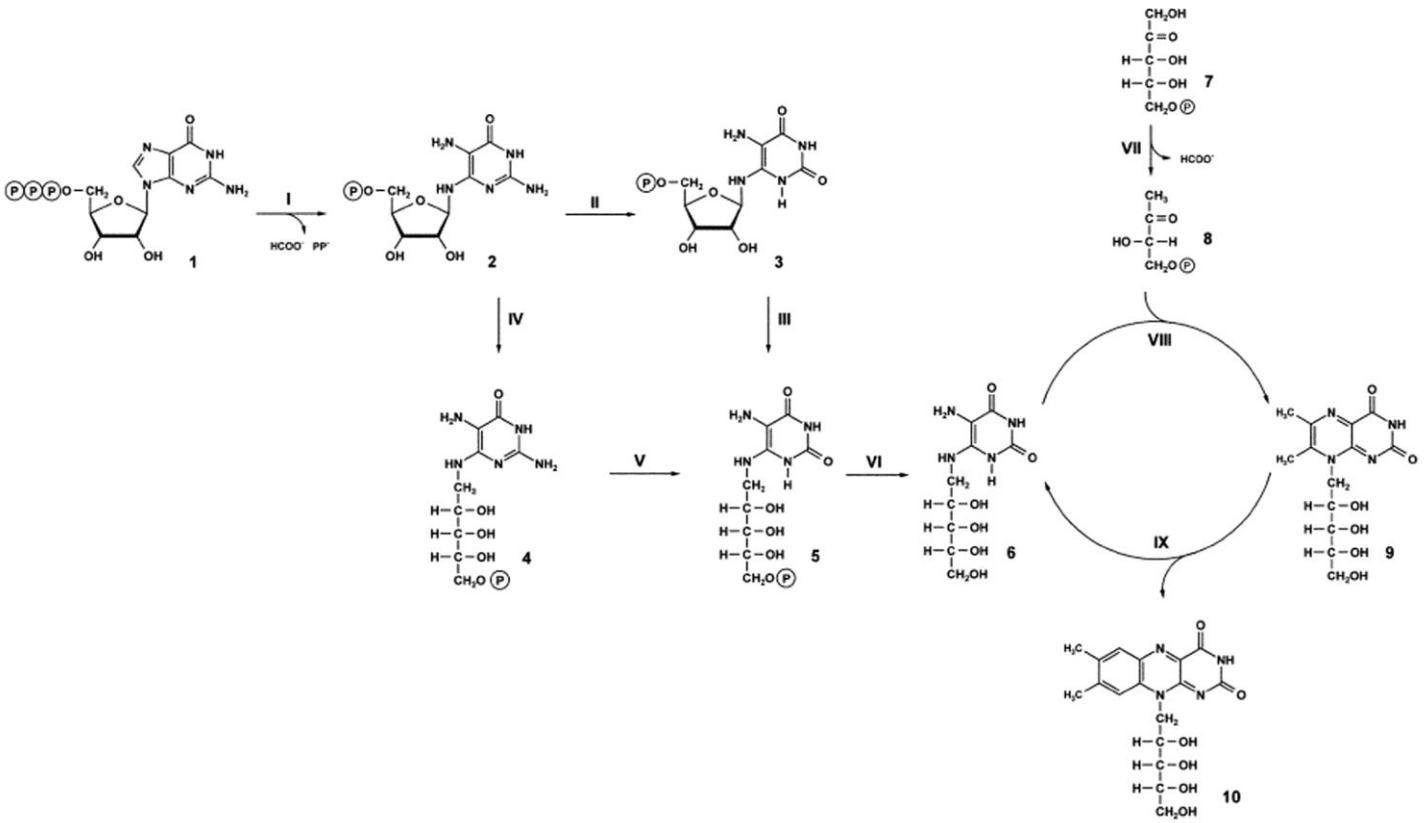
1
2
3
4
5
6
7
8
9
10
I
II
III
IV
V
VI
VII
VIII
IX
HCOO⁻
PP
HCOO⁻

Figure 1.6 Scheme for *de novo* biosynthesis of riboflavin. Catalytic steps are GTP cyclohydrolase II (**I**), 2,5-diamino-6-ribosylamino-4(3*H*)-pyrimidinone 5'-phosphate deaminase (**II**), 5-amino-6-ribosylamino-2,4(1*H*,3*H*)-pyrimidinedione 5'-phosphate reductase (**III**), 2,5-diamino-6-ribosylamino-4(3*H*)-pyrimidinone 5'-phosphate reductase (**IV**), 2,5-diamino-6-ribosylamino-4(3*H*)-pyrimidinone 5'-phosphate deaminase (**V**), hypothetical phosphatase (**VI**), 3,4-dihydroxy-2-butanone 4-phosphate synthase (**VII**), lumazine synthase (**VIII**) and riboflavin synthase (**IX**). Substrates formed during the process are GTP (**1**), 2,5-diamino-6-ribosylamino-4(3*H*)-pyrimidinone 5'-phosphate (**2**), 5-amino-6-ribosylamino-2,4(1*H*,3*H*)-pyrimidinedione 5'-phosphate (**3**), 2,5-diamino-6-ribosylamino-4(3*H*)-pyrimidinone 5'-phosphate (**4**), 5-amino-6-ribitylamino-2,4(1*H*,3*H*)-pyrimidinedione 5'-phosphate (**5**), 5-amino-6-ribitylamino-2,4(1*H*,3*H*)-pyrimidinedione (**6**), ribulose 5-phosphate (**7**), 3,4-dihydroxy-2-butanone 4-phosphate (3,4-DHBP) (**8**), 6,7-dimethyl-8-ribityllumazine (**9**) and riboflavin (**10**). Figure adapted from Fischer M, Nat Prod Rep, 2005[44].

one molecule to the other to generate riboflavin (**10**) and 5-amino-6-ribitylamino-2,4(1*H*,3*H*)-pyrmidinedione (**6**), which can be reused as substrate for lumazine synthase (**VIII**)[69]. Thus, the utilization of a second ribulose 5-phosphate for riboflavin biosynthesis is derived from a previous catalytic reaction by lumazine synthase (**VIII**).

Biosynthesis of flavocofactors

Converting riboflavin to FMN and FAD involves two universally conserved enzymes: riboflavin kinase (RFK) and flavin mononucleotide adenylyltransferase (FMNAT-historically also referred to as FAD synthetase). In bacteria and eukaryotes, RFK (ATP:riboflavin 5'-phosphotransferase; EC 2.7.1.26) phosphorylates riboflavin to FMN, while FMNAT (ATP:FMN adenylyltransferase; EC 2.7.7.2) adenylates FMN to form FAD[70-73] (**Fig. 1.7**). Recently, archaeal RFK was identified and it utilizes cytidine triphosphate (CTP) instead of ATP[74,75]. Whether FMNAT from archaebacteria utilizes CTP as in archaebacteria RFK is unknown, as the protein is currently not identified.

Genes of riboflavin biosynthesis

The genes that encode the enzymes of the riboflavin biosynthetic pathway are evolutionarily conserved and have been experimentally identified for bacterial, yeast and plant species. Of the bacterial species investigated, the most extensively investigated are *Bacillus subtilis* (*B. subtilis*) and *Escherichia coli*

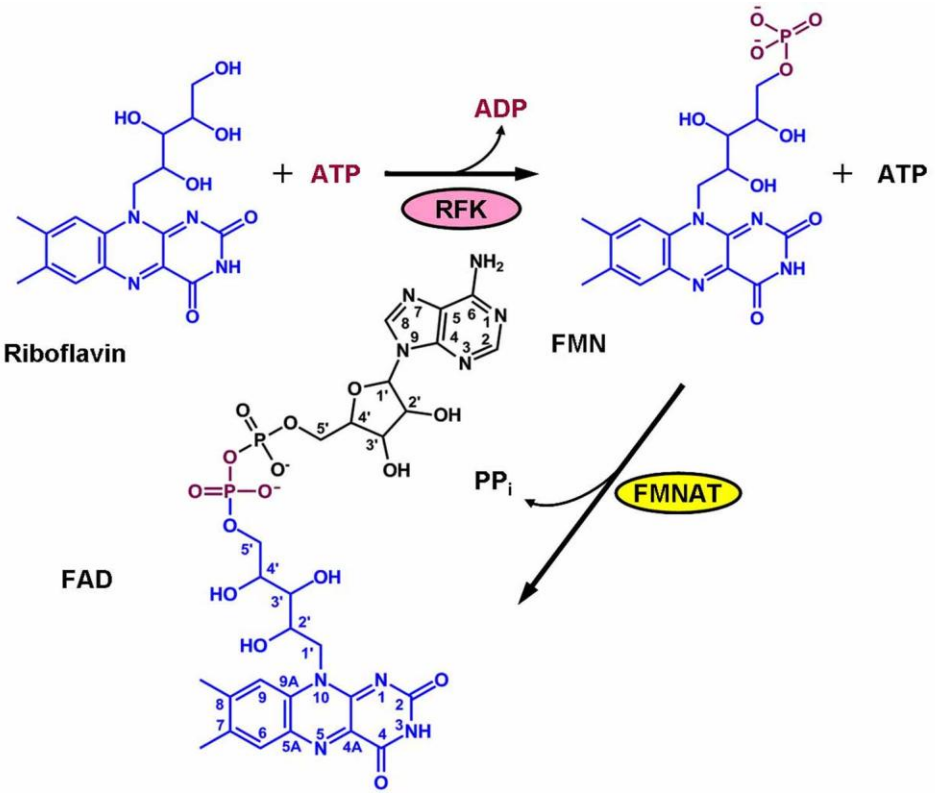

Figure 1.7 Reaction catalyzed by riboflavin kinase (RFK) and FMN adenylyltransferase (FMNAT).

(*E. coli*)[76-81]. In *E. coli*, GTP cyclohydrolase II and 3,4-DHBP synthase are encoded by *ribA* and *ribB* respectively, whereas in *B. subtilis* the enzymes are encoded by one gene *ribA* (**Fig. 1.8**). The deaminase and reductase is a bifunctional enzyme encoded by *ribD* and *ribG* in *E. coli* and *B subtilis*, respectively. In *E. coli* and *B. subtilis*, the lumazine synthase (also referred to as riboflavin synthase β-subunit) is encoded by *ribH*. The riboflavin synthase (also referred to as riboflavin synthase α-subunit) is encoded by *ribE* in *E. coli* or *ribB* in *B. subtilis*.

Organization of the *rib* genes varies among bacteria species. In *E. coli*, the *rib* genes are scattered on the chromosome, whereas in *B. subtilis* the *rib* genes are part of a single operon known as the *rib* operon[77,78]. The arrangement of the genes on the *rib* operon is *rib*GBAHT (or *rib*GBAH), with the function of *ribT* unknown[45]. For consistency, the *E. coli* genes are typically used and are presented as *rib*DE(B/A)HT, where *rib*(B/A) represents the bi-functional *rib*A in *B. subtilis*, or *rib*DEAHT. The *rib* genes of *E. coli* are not regulated in a coordinated manner, as in *B. subtilis*, in which the genes of the *rib* operon are co-regulated[77,78].

Several studies from yeast *Saccharomyces cerevisiae* (*S. cerevisiae*) and *Candida guilliermondii* have identified the genes involved in riboflavin biosynthesis[82-85]. The genes, along with the functional activity in parenthesis, are *rib1* (GTP cyclohydrolase II), *rib2* (deaminase), *rib3* (3,4-DHBP synthase), *rib4*

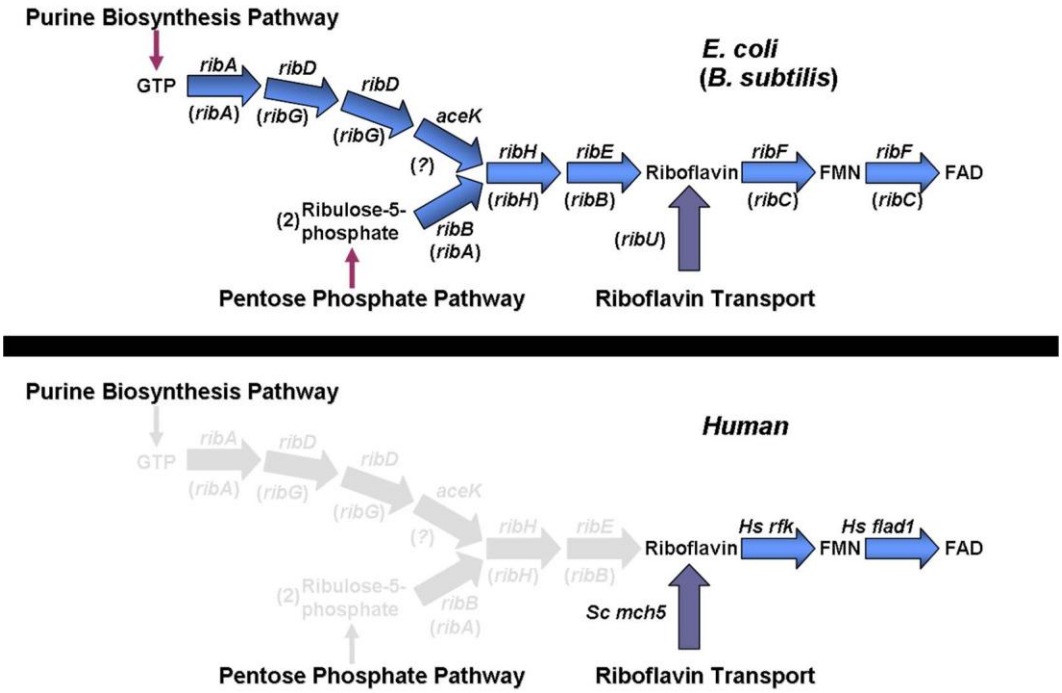

Figure 1.8 Genes involved in flavin biosynthesis. Top panel shows bacterial genes, with *B. subtilis* genes in parenthesis. The gene *aceK* is proposed to encode the hypothetical protein phosphatase in *E. coli*, as annotated in Kyoto Encyclopedia of Genes and Genomes (KEGG)[86]. Bottom panel shows human genes involved in flavocofactor biosynthesis.

(lumazine synthase), *rib5* (riboflavin synthase) and *rib7* (reductase). Majority of the riboflavin biosynthetic genes have been identified in plants, which include the bifunctional enzyme GTP cyclohydrolase II/3,4-DHBP synthase, deaminase, lumazine synthase and riboflavin synthase[44,52,87,88]. For yeasts and plants, the deaminase is not associated with the reductase as in prokaryotes[52,83].

Aside from there being no homologous GTP cyclohydrolase II in archae-bacteria, and the different organization of GTP cyclohydrolase II and 3,4-DHBP synthase in bacteria and eukaryotes, as well as the different organization and reaction order of the deaminase and reductase, there are also additional variations in the pathways. In yeasts and a bacterium *Brucella abortus*, lumazine synthase has a homopentamer quaternary structure[89-93], whereas in prokaryotes and spinach plant a 60 subunit circular capsid described as a dodecamers of pentamers is formed[93-100]. Furthermore, several archaebacteria riboflavin synthase share no sequence similarity to riboflavin synthase in bacteria and eukaryotes, but show significant sequence similarity to lumazine synthase[101,102]. The structure is a homopentamer[102,103], as in lumazine synthase, which is different from that of the homotrimer in bacteria and eukaryotes[84,90,104,105]. These observations suggest that a class of archaeal riboflavin synthase is evolutionarily related to lumazine synthase and may have evolved from a common ancestor.

In *E. coli* and many pathogenic bacteria, riboflavin is only obtained by the endogenous biosynthetic pathway[44]. The enzymes involved in riboflavin biosynthesis are fundamental as the bacteria apparently lack a riboflavin transport system[45,106]. In fact, a riboflavin auxotroph *E. coli* requires an excessively higher concentration of riboflavin in the growth media than an auxotroph bacterium *Lactococcus lactis*, which has a gene that encodes for a riboflavin transporter[107]. Therefore, enzymes of the riboflavin biosynthesis have been emphasized as suitable targets for discovering anti-microbial therapeutics against pathogenic species[44,108].

Genes of flavocofactor biosynthesis

The genes involved in the universally conserved last two steps of flavocofactor FMN and FAD biosynthesis have been experimentally identified in prokaryotic and eukaryotic species. In bacteria, RFK and FMNAT are encoded in the same gene *ribF* (for *E. coli*) or *ribC* (for *B. subtilis*), with the FMNAT domain located at the N-terminus and with the RFK domain located at the C-terminus of the bifunctional enzyme[71,109] (**Fig. 1.9**). In archaebacterium *Methanocaldococcus jannaschii*, the RFK gene is referred to as *ribK*[74]. For eukaryotes, RFK and FMNAT are encoded in separate genes. Plant species also have a bifunctional RFK enzyme as determined from *A. thaliana*. However, the gene encodes for a bifunctional RFK/FMN hydrolase enzyme, where the FMN hydrolase is located at

the N-terminus and the RFK domain located at the C-terminus[110]. Moreover, two genes have been identified to encode FMNAT[111]. For yeast *S. cerevisiae*, RFK and FMNAT are encoded by *fmn1* and *fad1*, whereas in humans the genes are referred to as *rfk1* and *flad1*[72,73,112,113] (**Fig. 1.9**). Two isoforms of *flad1* have been experimentally characterized[112,113]. In higher eukaryotes, the gene encoding FMNAT also contains a second domain with sequence similarity to proteins involved in molybdenum cofactor (MoCo) biosynthesis such as MogA and MoeA[114,115] (**Fig. 1.9**). The potential function of this MoCo-binding protein-like domain is unknown.

The reduced form of FMN is shown to be the substrate for *ribC* of *B. subtilis*, as well as the identified monofunctional RFK encoded by *ribR*[116,117]. Another monofunctional RFK is experimentally determined to be encoded in *Streptococcus agalactiae* by the gene *mreA*, which is shown to be involved in macrolide resistance[118]. The mechanism of macrolide resistance is proposed to be by efflux[118].

Eventhough riboflavin kinase of eukaryotes and bacteria are more similar to each other than to archaeal RFK[75], they belong to the same protein family[74,119]. In contrast, eukaryotic and bacterial FMNATs share little sequence similarity and belong to different protein families. An exception is in the plant *A. thaliana*, encodes two FMNATs with one homologous to eukaryotic FMNAT and the other

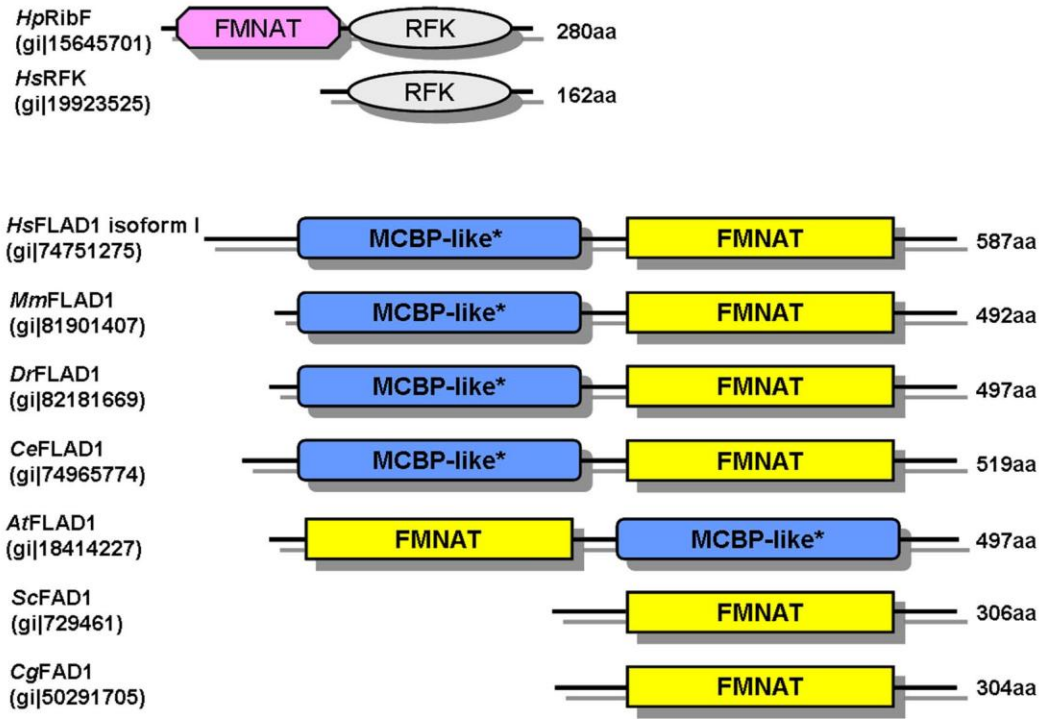

Figure 1.9 Comparison of the organization of bacterial and eukaryotic RFKs and FMNATs. For each species the gi number, in parenthesis, and the protein identification is shown. Abbreviation for the molybdenum cofactor biosynthesis protein-like sequence is indicated by the asterisk (*). *Hp*, *Helicobacter pylori*; *Hs*, *Homo sapiens*; *Mm*, *Mus musculus*; *Dr* , *Danio rerio*; *Ce*, *Caenorhabditis elegans*; *Af*, *Aspergillus fumigates*; *Sc*, *Saccharomyces cerevisiae* and *Cg*, *Candida glabrata*.

to bacterial FMNAT[110]. The *A. thaliana* FMNAT homologous to bacterial FMNAT was experimentally determined to have FMNAT activity[111].

Riboflavin transporter

The importance of extracellular riboflavin uptake by a membrane riboflavin transporter has been investigated for several mammalian cell types, bacteria and yeast[107,120-126]. Despite being able to synthesize riboflavin, yeast are also able to transport riboflavin from the environment[124,125]. A riboflavin transporter has been identified in *S. cerevisiae* and is encoded by the gene *mch5*[127] (**Fig. 1.8**). Riboflavin is transported by a facilitated diffusion mechanism, allowing a flux of riboflavin down a concentration gradient. Bacterial riboflavin transporters, for which several have been experimentally identified, are not related to the yeast transporter[81,107,128]. The riboflavin transporter YpaA from *B. subtilis* (**Fig. 1.8**) and RibU from *Lactobacillus lactis* (*L. lactis*) are homologous membrane proteins that belong to the same superfamily, therefore it is proposed to refer YpaA as RibU[107,128]. However, *B. subtilis* YpaA requires energy to transport riboflavin from the extracellular side, whereas *L. lactis* acts as a facilitator. The riboflavin transporter PnuX from *Corynebacterium glutamicum* is also a facilitator transporter, but has sequence similarity to the riboflavin transporter RibM from *Streptomyces davawensis*[81,128]. The transporters YpaA/RibU and PnuX/RibM represent two different classes of riboflavin

transporters in bacterial species. Even with the evidence for a riboflavin transporter and the identification of the transporters from various species, a mammalian riboflavin transporter gene has not been identified.

For some bacteria, the presence of riboflavin in the growth media is essential for growth[128]. The bacteria investigated are pathogens[44,128] that are devoid of the genes involved in riboflavin biosynthesis, as assessed through comparative gene analysis[106]. As an alternative, the bacteria were shown to have a gene encoding a riboflavin transporter[106].

FMNAT Protein Family

Prokaryotic and eukaryotic RFKs are similar in sequence and structure, and they belong to a unique protein family containing only riboflavin kinases[74,75,119,129]. In contrast, the evolutionary link between bacterial and eukaryotic FMNATs is less clear as they show little sequence similarity and are classified in different protein superfamilies in SCOP[130] or different clans in Pfam[131] databases. The bacterial FMNAT domain of the bifunctional RFK/FMNAT belongs to the (H/T)xGH motif containing nucleotidylyl transferase superfamily. In contrast, eukaryotic FMNAT is currently classified as a member of the 3'-phosphoadenosine 5'-phosphosulfate (PAPS) reductase-like

family, which has conserved motifs different from those of nucleotidylyl transferases.

Well known and characterized proteins in the nucleotidylyl transferases superfamily include class I tRNA synthetases, NMN or NaMN (nicotinamide or nicotinic acid mononucleotide) adenylyltransferases, cytidylyltransferases and a few other nucleotidyl transferases[132-137]. In addition to the signature nucleotidylyl transferase (H/T)xGH motif, a second sequence motif (ISSTxxR) is also observed in the nucleotidyl transferase superfamily, which is known to interact with the β- and γ-phosphates of the nucleotide ATP. Within the adenine nucleotide α hydrolase-like superfamily, members of PAPS reductase-like family share sequence and structural similarity to N-type ATP pyrophosphatases and PP-loop ATPase families[138-141]. The families share a conserved motif referred to as the PP-loop. For N-type ATP pyrophosphatases and PP-loop ATPase families the PP-loop consensus sequence is SGGxD(S/T)[142,143], whereas for the PAPS reductase-like family it is a generally conserved sequence of SxG[138,140,142], with x representing any amino acid. The PP-loop interacts with the β- and γ-phosphates of the nucleotide ATP or derivatives.

Crystal structures for several members of the PAPS reductase-like family have been determined, in which a core fold is conserved[138-140]. The structures have a central twisted six-stranded β-sheet with five parallel β-strands and one

anti-parallel β-strand. The central β-sheet is interleaved with helices, with one or two α-helices, occurring N-terminal to the first β-strand. The core of the protein has a topology of β3α2β2α1β1|α3β4β6β5, where the crossover helix α3 connects β3 to β4 and places β4 parallel and adjacent to β1. The orientation and placement of strand β5, which connects β4 and β6, is anti-parallel to all other strands. This core fold is different from that of the (H/T)xGH nucleotidylyl transferase superfamily, which has a typical Rossmann-fold topology β3α2β2α1β1|α3β4α4β5[141,144]. Therefore, the different sequence conservation, and structural arrangement and elaboration separate the two superfamilies[141].

Enzymatic Properties of Bacteria and Eukaryotic FMNATs

Despite substantial differences in sequence and structure, the mammalian and bacterial FMNAT enzymes have similar kinetic properties[70,145]. Both enzymes catalyze the formation of FAD through an ordered bi-bi mechanism and have the same substrate binding and product release order where ATP binds first to the enzyme followed by FMN, and product inorganic pyrophosphate (PP_i) is released first followed by the release of FAD. Dependence and specificity for divalent cations differs for eukaryotic and bacterial FMNATs. Studies on the effect of different divalent cations, indicates rat liver FMNAT requires Mg^{2+},

whereas bacterial FMNAT can utilize different divalent cations[71,146]. In regards to rat liver FMNAT, addition of 1 mM Zn^{2+} in the reaction mixture inhibited the activity by 60%, with Ca^{2+} and Mn^{2+} showing 30% and 15% of the activity, respectively[146]. Other divalent cations (Ba^{2+}, Co^{2+}, Cu^{2+}, Cd^{2+}, Fe^{2+}, Ni^{2+}, Sn^{2+} and Sr^{2+}) show no activity[146]. In addition to cation selectivity, extensive studies were performed on bacterial and eukaryotic FMNAT using FMN analogs[147-150]. Eukaryotic rat liver FMNAT is able to better tolerate substitutions in the 7- and 8-methyl position of the FMN isoalloxazine benzenoid ring compared to the bacterial *Brevibacterium ammoniagenes* FMNAT domain of FADS (*Ba*FADS). Eukaryotic FMNAT and *Ba*FADS are able to utilize 8-chloro- and 7,8-dichloro-FMN as substrates. However, as determined for the eukaryotic enzyme, these substitutions result in an increase in K_m and a decrease in V_{max}, with the greatest change occurring with 7,8-dichloro[149,150]. In contrast, 7-chloro-FMN results in similar K_m and V_{max} as the substrate FMN for eukaryotic FMNAT[150]. Alternatively, substitution of the 7- and 8-methyl with a less electronegative halide of 7,8-dibromo-FMN results in an ~2-fold decrease of K_m and V_{max}, whereas 8-chloro results in an ~2-fold increase of K_m and decrease of V_{max} in eukaryotic FMNAT[150]. *Ba*FADS is able to use 7-bromo-FMN as a substrate[149], however the kinetic parameters and whether 7,8-dibromo-FMN can be used as a substrate are not known. Inhibition by FMN analogs 1-deaza-FMN (K_i = 283 μM)

and 1,5-dideaza-FMN (K_i = 29 μM) are observed for eukaryotic FMNAT, while 1-deaza-FMN and 5-dideaza-FMN appear to have no effect on the catalytic activity in *Ba*FADS[147-149]. These results suggest that the architecture of the substrate binding site is different between eukaryotic and bacterial FMNATs.

Regulation of FAD Biosynthesis

The regulation of FAD homeostasis is important as several studies of cellular processes in eukaryotes, such as oxidative protein folding and homocysteine metabolism, are sensitive to FAD levels[151,152]. In yeast, the activity of FAD-dependent Ero1 protein, which mediates oxidative protein folding in the endoplasmic reticulum through protein disulfide isomerase, is dependent on the FAD concentration[152]. Similarly, in a riboflavin deficient study involving HepG2 hepatocarcinoma cells, oxidative protein folding was decreased[122]. The reduction of available flavins also resulted in cell growth arrest by the increased expression of GADD153 gene, which is mediated in response to endoplasmic reticulum stress elements[122,153,154]. Additionally, clinical studies of a mutation, C677T polymorphism, in 5,10-methylenetetrahydrofolate reductase (MTHFR) results in an increase of plasma total homocyteine, which is a risk factor for coronary, cerebral, and peripheral arteries disease, as well as for venous thrombosis[151]. The mutant shows a decrease in the flavin concentration in the plasma, except for

FAD, when compared to the control (non-mutant MTHFR)[151]. A possible reason for the unchanged plasma FAD concentration is that FAD is under strict metabolic control, as indicated by riboflavin deficiency studies in men and rats[151].

In addition to these studies, a pronounced product feedback inhibition was observed for rat liver FMNAT, and it was suggested that such a property would enable FMNAT to play a role in regulating cellular FAD homeostasis as the K_i values of FAD against FMN (0.75 μM) and Mg^{2+}-ATP (1.3 μM) are close to the concentration of free FAD (0.4 μM)[145]. In this respect, how the concentration of FAD is controlled based on cellular needs is not known.

In *B. subtilis*, the *rib* operon contains a regulatory element called the RFN element that is present within the 5'-untranslated region (5'-UTR)[155,156]. Mutations leading to riboflavin overproduction were mapped to various regions within the RFN element, as well as *ribC* (bifunctional FADS) and *ribR* (monofunctional RFK)[109,157,158]. The RFN element folds into a secondary structure that binds FMN with high affinity[159,160] and prevents the expression of the downstream genes by transcription termination or a translation mechanism that sequesters a ribosome-binding site[106,159]. RNA from the RFN element acts as a metabolic-sensor (riboswitch) that regulates riboflavin biosynthesis by binding FMN, in the absence of proteins[106,159]. RFN elements are found upstream of many bacteria riboflavin biosynthesis operons, including riboflavin transporters[106,155].

Objective of Research

Both RFK and FMNAT are essential enzymes needed for generating the indispensable flavocofactors FMN and FAD[44]. The essentiality of the two enzymes has been established experimentally in bacterial[161] and yeast species[72,73,152], and has been inferred to all other organisms. In conjunction to the essentiality in bacteria, an *in vivo* study of *Salmonella enterica* infection in mice indicated *ribF* is expressed during the virulence states, which is one of the few genes that are not currently targeted by antimicrobial agents[162,163]. The significant differences between eukaryotic and bacterial FMNATs make them a particularly attractive target for developing selective anti-infectious drugs[161]. Structural analyses of both eukaryotic and bacterial FMNATs will reveal the different configurations of the substrate binding and catalytic sites, which may benefit a structure-based inhibitor development effort. Such analyses will also address two fundamental questions: a) how eukaryotic and bacterial FMNAT accomplish the same chemistry with different active site architectures, and b) what mechanistic controls are embedded in eukaryotic FMNAT to influence FAD homeostasis. Here we report the first structural characterization of a eukaryotic FMNAT from *Candida glabrata*, an opportunistic yeast pathogen causing candidemia and invasive candidiasis[164-167]. We have determined the crystal structures of *C. glabrata* FMNAT (*Cg*FMNAT) in the apo-form and in three different complexed

forms [with ATP, with substrate FMN and the ATP analog α,β-methyleneadenosine 5'-triphosphate (AMPCPP), and with products FAD and PP_i, respectively]. These structures reveal a novel flavin-binding mode and the detailed catalytic site configuration that are likely shared among all eukaryotic FMNATs. Combined with the results from steady-state kinetic analysis, a mechanism for eukaryotic FMNAT catalyzed adenylyl transfer reaction is proposed.

CHAPTER 2

Structure Determination of apo-*Cg*FMNAT

(Parts of this chapter are adapted from Huerta *et al*., 2009)

INTRODUCTION

Riboflavin is the precursor to the biosynthesis of the flavocofactors[3,44], FMN and FAD, and is shown to be essential for the function of cellular processes[122,128]. In plants, yeast and many bacteria, riboflavin is synthesized *de novo* through the riboflavin biosynthetic machinery[44,128], whereas higher eukaryotes, such as humans, obtain riboflavin from the diet[3,44]. Biosynthesis of the flavocofactors involves two universally conserved enzymes RFK and FMNAT. The structure of bacterial FADS was solved from a bacteria thermophile *Thermotoga maritima* (*Tm*FADS)[168,169]. From sequence and structure analysis, the FMNAT domain of *Tm*FADS belongs to the (H/T)xGH motif-containing nucleotidyl- transferase superfamily. Based on sequence similarity, eukaryotic FMNAT is currently classified as a member of the PAPS reductase-like family belonging to the adenine nucleotide α hydrolase-like superfamily in SCOP[130], which has conserved motifs different from those of nucleotidylyl transferase.

Members of the PAPS reductase-like family include PAPS reductase, adenosine 5'-phosphosulfate (APS) reductase and ATP sulfurylase. All members

are from bacterial species[138-140], with the exception of yeast PAPS reductase (unpublished; PDB ID: 2oq2), which are involved in the sulfate assimilation pathway. The pathway is important for generating sulfur metabolites[170-173], such as cysteine and methionine, as well as sulfated metabolites[174-176]. PAPS reductase-like family also shares sequence and structural similarity with the N-type ATP pyrophosphatases and PP-loop ATPase family[138-141], which belong to the same superfamily[130,142].

A sequence alignment of eukaryotic FMNATs with members of the PAPS reductase-like family shows eukaryotic FMNAT has a low percent sequence identity to other members within the family. Selecting human and yeast *Candida glabrata* FMNAT (*Cg*FMNAT) the sequence identities to *E. coli* PAPS reductase is 12% and 10%, respectively, whereas it is 13% and 7% to *Pseudomonas aeruginosa* APS reductase, and 10% and 12% to *Pseudomonas syringae* ATP sulfurylase. Despite the low sequence identity, eukaryotic FMNAT maintains sequence identity for several motif regions identified in APS sulfurylase, which are highly conserved within the family[138] (**Fig. 2.1**), that include the PP-loop, LDTG and Arg-loop. However, the PP-loop motif region in eukaryotic FMNAT is different from that of the PAPS reductase-like family. Instead, it displays similarity to the consensus sequence of SGGxD(S/T) from the N-type ATP pyrophosphatases and PP-loop ATPase families[142,143].

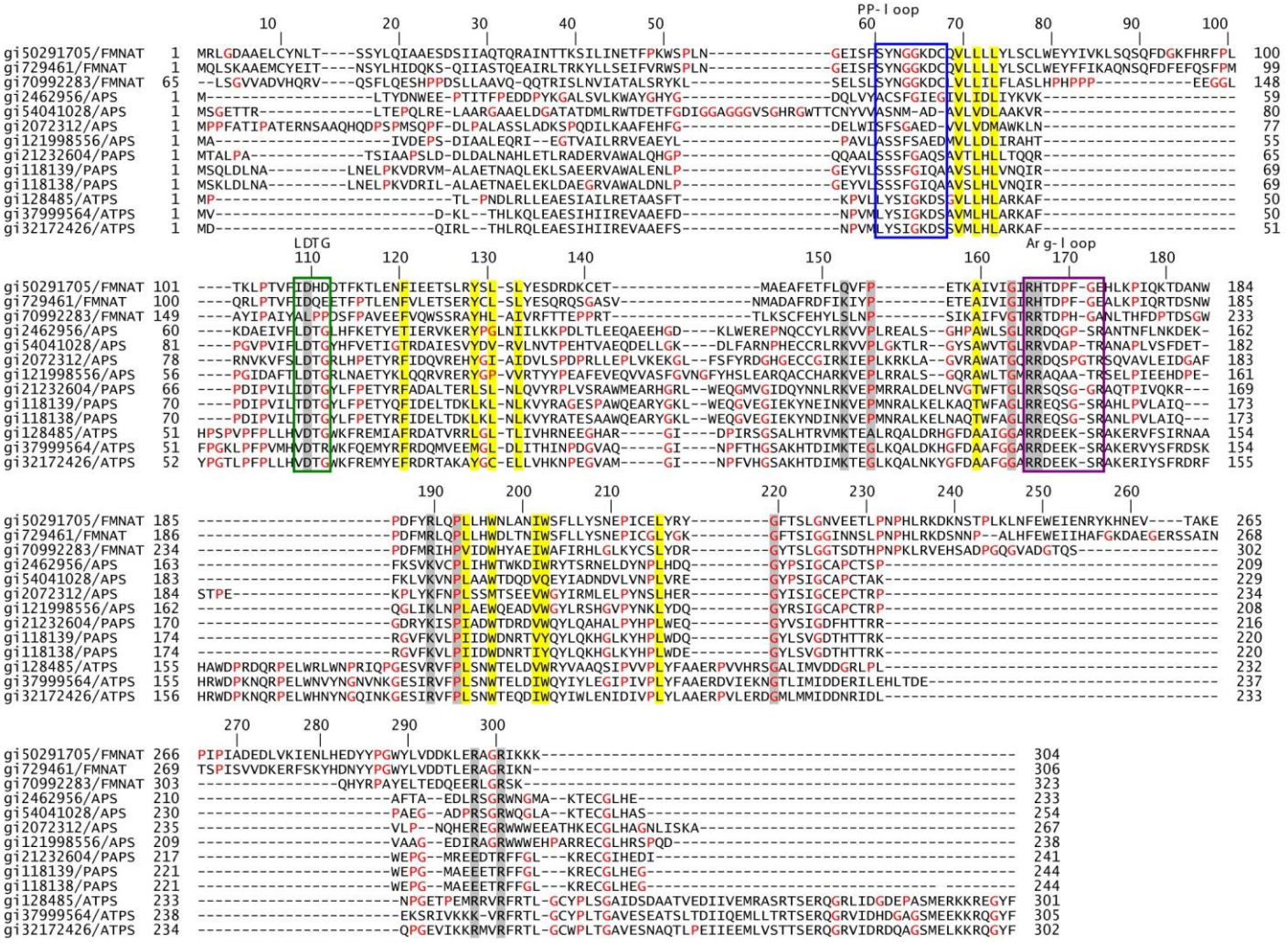
PP-1 loop
LDTG
Arg-1 loop
gi50291705/FMNAT
gi729461/FMNAT
gi70992283/FMNAT
gi2462956/APS
gi54041028/APS
gi2072312/APS
gi121998556/APS
gi21232604/PAPS
gi118139/PAPS
gi118138/PAPS
gi128485/ATPS
gi37999564/ATPS
gi32172426/ATPS

Figure 2.1 Multiple sequence alignment of PAPS reductase-like family members and eukaryotic FMNATs. The residue numbers of *Candida glabrata* FMNAT are marked at the top of the alignment. Each sequence is labeled by the gi number and protein name. The first and last residues of each sequence are numbered at the beginning and end. Structural motifs of APS reductase are boxed and extended to cover other sequences. Glycine and proline residues are in red; conserved glycine, proline and charged/polar residues are highlighted in gray and conserved hydrophobic/aromatic residues in yellow. Species in the alignment are: gi50291705, *Candida glabrata*; gi729461, *Saccharomyces cerevisiae*; gi70992283, *Aspergillus fumigates*; gi2462956, *Bacillus subtilis*; gi54041028, *Mycobacterium tuberculosis*; gi2072312, *Pseudomonas aeruginosa*; gi121998556, *Halorhodospira halophila*; gi21232604, *Xanthomonas campestris*; gi118139, *Salmonella enterica*; gi118138, *Escherichia coli*; gi128485, *Azospirillum brasilense*; gi37999564, *Pseudomonas syringae* and gi32172426, *Escherichia coli*. Sequence alignment was constructed by PROMALS[177] and manually modified.

The protein crystal structures for several members of the PAPS reductase-like family have been solved, which has a core fold considerably similar to the N-type ATP pyrophosphatases and PP-loop ATPase (**Fig. 2.2**). Three structural motifs conserved in the PAPS reductase-like family that interact with the nucleotide are identified that include the PP-loop, LDTG and Arg-loop[138]. The N-type ATP pyrophosphatases and PP-loop ATPase families maintain similar structural motifs PP-loop and LDTG but lack structural similarity to the Arg-loop. Due to the relatively high sequence conservation between eukaryotic FMNAT and the PAPS reductase-like family, the ATP binding mode is expected to be similar. However, the flavin binding represents a new function for the superfamily with the binding mode completely unknown. The flavin binding mode cannot be inferred from *Tm*FADS FMNAT domain, as eukaryotic and bacterial FMNAT belong to different superfamilies that share little sequence similarity. Since eukaryotic FMNAT represents a new member of the superfamily with low sequence similarity to the PAPS reductase-like family. A structure of eukaryotic FMNAT is necessary in order to understand its function and mechanism. In addition, based on the sequence alignment, *C. glabrata* and *S. cerevisiae* FMNATs possess a C-terminal insertion domain (~ 60 residues) that is not shared among the family, including other higher eukaryotic FMNATs (**Fig. 2.1**). Therefore, structural analysis is required to elucidate the structural variations.

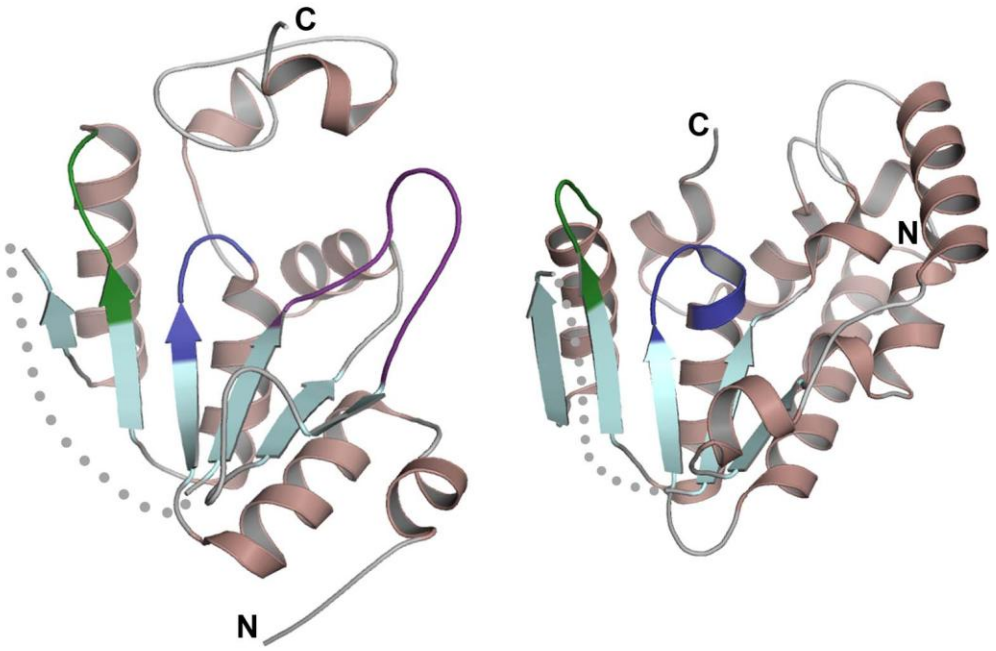

Figure 2.2 Fold comparisons for members of the adenine nucleotide α hydrolase-like superfamily. Structural motifs are colored dark blue for PP-loop, dark green for adenine-loop and purple for Arg-loop motifs. The dots represent a portion of the structures omitted in the figure for clarity purpose. The PDB identifications are in parentheses.

To begin investigating, *C. glabrata* and *S. cerevisiae* FMNATs were cloned, expressed and purified. In light of the increased protein solubility, *Cg*FMNAT was selected for X-ray structure determination. We present the first structure of eukaryotic FMNAT from *C. glabrata* in the apo-form. A complete description of the overall fold is given and a region for ATP interaction is proposed.

MATERIALS

Amino acids and other reagents were purchased from Sigma-Aldrich Inc. (St Louis, MO), unless stated otherwise. (L)-+-selenomethionine was purchased from Acros Organics (Geel, Belgium). For PCR, True Fidelity DNA polymerase was purchased from Continental Lab Products (San Diego, CA), and *Nco*I and *Sal*I restriction enzymes were purchased from New England Biolabs (Ipswich, MA). The dNTP's (dATP, dGTP, dTTP and dCTP) were purchased from Roche (Indianapolis, IN). High-throughput (HT) crystal screens, PEG/Ion screen, additive screen, 96-well round bottom sitting-drop plates, 24-well crystallization plates, silicon and paraffin oil, sodium acetate buffer and hydrochloric acid solution for the crystallization experiments were purchased from Hampton Research (Aliso Viejo, CA). Wizard III crystallization screen was purchased from Emerald BioSystems (Bainbridge Island, WA). Nickel-sepharose high

performance resin, Resource Q media, and pre-packed phenyl sepharose HR 10/10 column and Superdex 75 HiLoad 16/60 column were purchased from GE Healthcare (Piscataway, NJ). The nickel-nitrilotriacetic acid (Ni-NTA) resin was purchased from Qiagen (Valencia, CA) and the micro bio-spin chromatography columns purchased from Bio-Rad (Hercules, CA). The ÄKTA FPLC (fast protein liquid chromatography) system was used for performing protein purification (GE Healthcare). Primers were ordered from Integrated DNA Technologies (Coralville, IA). Genomic DNA from *C. glabrata* (strain NCYC 388, ATCC 36909D) and *S. cerevisiae* (strain NRRL Y-53, ATCC 2601D) was purchased from ATCC (Manassas, VA).

METHODS

Cloning, expression and purification of *S. cerevisiae* and apo-*Cg*FMNAT

The predicted gene *fad1* encoding *Sc*FMNAT (gi:6320159, encoding 306 amino acids) and *Cg*FMNAT protein (gi:50291750, encoding 304 amino acids) were amplified from *S. cerevisiae* and *C. glabrata* genomic DNA, respectively, by PCR and cloned into the *Nco*I and *Sal*I restriction sites of the pHIS parallel expression vector containing a T7 promoter, N-terminal His_6-tag and tobacco etch virus (TEV) protease cleavage site[178]. The primers used to amplify *fad1* from *S. cerevisiae* genomic DNA are as follow: 5'-

GGG**CCATGG**TGATGCAGTTGAGCAAGGCTGCTG-3', encoding a *Nco*I restriction site (bold) prior to the start codon (underlined); and the reverse primer 5'-GGG**GTCGAC**TTAATTCTTGATCCTGCCTGCTCTCTC-3', encoding a *Sal*I restriction site (bold). For *C. glabrata*, the forward primer, 5'-GGG**CCATGG**TGATGCGTTTGGGTGACGCTGC-3', and the reverse primer, 5'-GGG**GTCGAC**TCATTTCTTTTTAATTCTTCCTGCTCTTTC-3', utilized the same restriction sites, respectively. Two nucleotides were added after the *Nco*I site for in-frame translation of *fad1*. Including the two amino acids after the TEV cleavage site, a total of four residues (Gly-Ala-Met-Val) prior to the *fad1* start methionine residue were added in the construct. The correct sequences of the inserts were confirmed by DNA sequencing from McDermott Center at the University of Texas Southwestern Medical Center.

For small scale protein expression, pHIS-*Cg*FMNAT and pHIS-*Sc*FMNAT plasmids were transformed into *E. coli* BL21(DE3) (Novagen; Madison, WI) and cells were grown in 50 ml Luria-Bertani (LB) broth, containing 100 μg/ml ampicillin, at 37 ºC until absorption at 600 nm reached 0.6–0.7. His_6-*Cg*FMNAT and His_6-*Sc*FMNAT protein expression was induced with 0.8 mM isopropyl-1-thio-β-D-galactopyranoside (IPTG) and continued incubation at 20 ºC for approximately 16 hours. Cells were harvested by centrifugation at 4,000 rpm for 20 minutes at 4 ºC and the resulting pellet resuspended in 3 ml lysis buffer [20

mM HEPES, pH 8.0, 100 mM NaCl, 10 % glycerol, 0.03% Brij-35, 1 mM dithiolthreitol (DTT) and 2 mM phenylmethylsulfonyl fluoride (PMSF)]. Cell suspension was frozen with liquid nitrogen, thawed and completely lysed by sonication (550 Sonic Dismembrator, Fisher Scientific; Pittsburgh, PA) for 2 minutes with 5 seconds pulse on and off periods. Lysate was centrifuged at 16,000 *g* for 20 minutes at 4 ºC and resultant supernatant was decanted and stored on ice. Purification of *Cg*FMNAT and *Sc*FMNAT protein from the supernatant consisted of a single purification step. The clarified cell lysate was passed through a 200 µl nickel-nitrilotriacetic acid resin volume, packed in a Bio-Rad chromatography column, equilibrated with Buffer A (50 mM Tris, pH 8.0, 200 mM NaCl, 0.03% Brij-35 and 2 mM β-mercaptoethanol). The resin was washed with 1 ml Salt Wash Buffer (8 ml Buffer At + 2 ml 5 M NaCl + 100 µl 30% Brij-35), followed by two elution steps of His_6-*Cg*FMNAT and His_6-*Sc*FMNAT with 200 µl Elution Buffer (7.5 ml Buffer At + 2.5 ml 1 M imidazole). The flow-through of the supernatant, wash and elution were collected (**Fig. 2.3a and b**).

Because the yield of *Cg*FMNAT was much higher than *Sc*FMNAT, as observed from the SDS-PAGE protein profile in figure 2.3a and b, we selected *Cg*FMNAT for large scale protein expression and subsequent structure analysis. The pHIS-*Cg*FMNAT plasmid was transformed into *E. coli* BL21(DE3) and cells were grown in 4−1 L Luria-Bertani (LB) broth, containing 100 µg/ml ampicillin,

with protein expression performed identically as for the small scale protein purification. Cells were harvested by centrifugation at 4,000 rpm for 30 minutes at 4 ºC and the resulting pellet resuspended in 30 ml lysis buffer per 1 L culture. Cell suspension was frozen with liquid nitrogen, thawed and completely lysed by sonication for 5 minutes with 5 seconds pulse on and off periods. Lysate was centrifuged at 25,000 *g* for 30 minutes at 4 ºC and resultant supernatant was decanted and stored on ice.

Purification of *Cg*FMNAT protein from supernatant consisted of four steps resulting in homogeneous apo-*Cg*FMNAT protein. The clarified cell lysate was passed through a nickel-sepharose affinity column equilibrated with Buffer A (20 mM HEPES, pH 8.0, 300 mM NaCl, 20 mM imidazole, 5% glycerol and 1 mM DTT) and His_6-*Cg*FMNAT was eluted with a 20–500 mM imidazole gradient with Buffer B (Buffer A plus 500 mM imidazole). Incubation with TEV protease cleaved the His_6-tag during overnight dialysis in 2 L dialysis buffer (20 mM HEPES, pH 7.5, 50 mM NaCl, 5% glycerol and 1 mM DTT) at 4 ºC and the His_6-tag was removed from *Cg*FMNAT by passing through the nickel-sepharose column a second time. The column was equilibrated with 20 mM HEPES, pH 7.5, 5% glycerol and 1 mM DTT. As a second purification step, protein was loaded onto a Resource Q anion exchange column equilibrated with Buffer C (20 mM HEPES, pH 7.5, 5% glycerol and 1 mM DTT) and eluted with a 0−350 mM NaCl

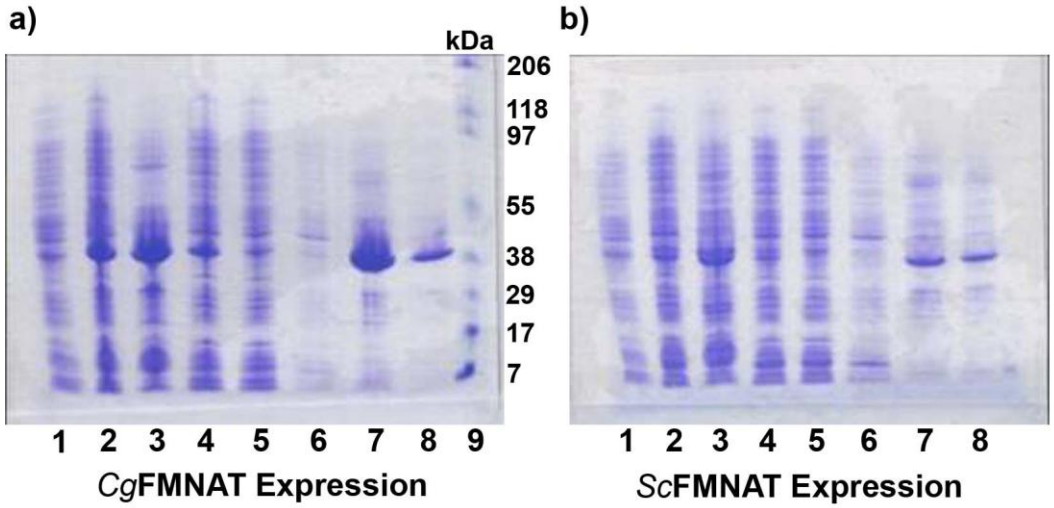

Figure 2.3 SDS-PAGE showing yeast FMNAT protein expression levels. a.) *Candida glabrata* FMNAT protein expression level. b.) *Saccharomyces cerevisiae* protein expression level. Lane numbers are as follow: 1.) Total lysate of non-induced culture, 2.) Total lysate of induced culture, 3.) Pellet, 4.) Supernatant, 5.) Flow-through from nickel column, 6.) Wash, 7.) First elution fraction, 8.) Second elution fraction and 9.) Pre-stained SDS-PAGE protein standard broad range (Bio-Rad), with molecular weight shown in kilo-Daltons (kDa).

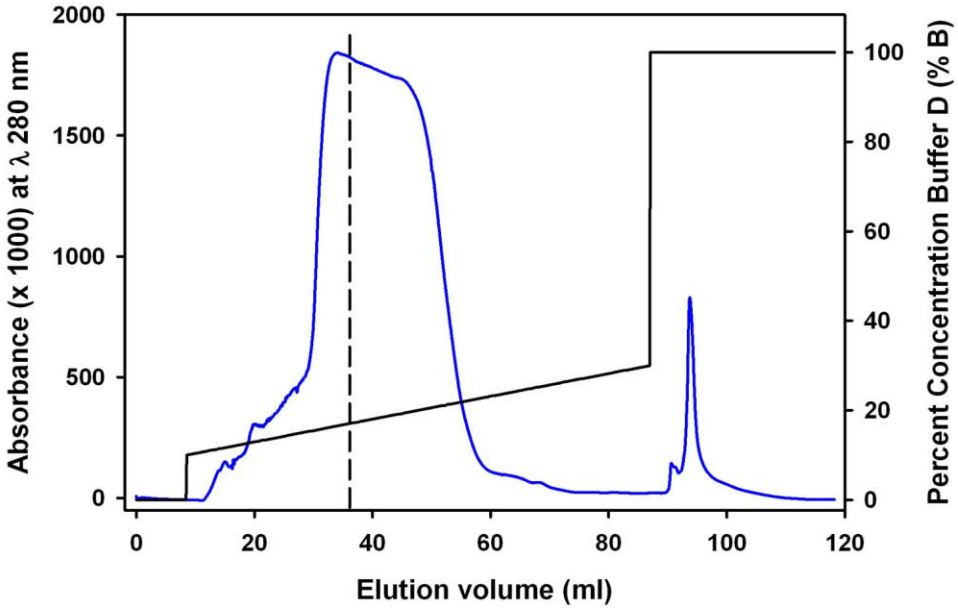

Figure 2.4 Elution profile of *Cg*FMNAT from a Resource Q anion exchange column. Protein was eluted with a 0−350 mM NaCl gradient (solid black line) and monitored by absorption at 280 nm (solid blue line). Two pools were collected as indicated by the vertical dash line. The first pool, elution volume 33 to 36 ml, had a bright yellow color and was later shown to contain the *Cg*FMNAT-FAD complex. The second pool, from 37 to 56 ml, had a light yellow color, indicating the presence of flavin with partial occupancy.

gradient with Buffer D (20 mM HEPES, pH 7.5, 1 M NaCl, 5% glycerol and 1 mM DTT), which yielded two pools (**Fig. 2.4**). The first pool had a bright yellow color and was later shown to contain the *Cg*FMNAT-FAD complex. The second pool had a light yellow color, indicating the presence of flavin with partial occupancy. To remove the flavin and obtain homogeneous apo-*Cg*FMNAT, the second pool was concentrated between 10–12 mg/ml and incubated with 1.5 M ammonium sulfate on ice and loaded onto a phenyl-sepharose hydrophobic-interaction chromatography column equilibrated with Buffer E (20 mM HEPES, pH 7.5 and 1.5 M ammonium sulfate). The protein was eluted with a 1.5 M–0 ammonium sulfate gradient with Buffer F (20 mM HEPES, pH 7.5). Residual ammonium sulfate in the protein sample was removed with overnight dialysis in 4 liters dialysis buffer (20 mM HEPES, pH 7.5, 50 mM NaCl and 1 mM DTT) at 4 ºC. The final purification step for apo-*Cg*FMNAT was gel filtration using a Superdex 75 16/60 gel filtration column equilibrated with gel filtration buffer (20 mM HEPES, pH 7.5, 150 mM NaCl and 1 mM DTT). Detection of flavin was measured by a UV/visible wavelength scan using a Beckman Coulter DU 640 spectrophotometer (Fullerton, CA).

The selenomethionyl (SeMet) apo-*Cg*FMNAT was expressed in *E. coli* BL21(DE3) grown in minimal media supplemented with selenomethionine and other nutrients[179] and purified using the same procedure as for apo-*Cg*FMNAT.

The protein purity was monitored by PhastGel SDS-PAGE (GE Healthcare) and the protein concentration was determined using Bio-Rad (Hercules, CA) protein assay. Amicon ultra 10,000 molecular weight cut-off centrifuge filter tubes (Millipore; Billerica, MA) were used to concentrate the protein.

Crystallization of apo-*Cg*FMNAT

Hampton HT screens (Salt, Index and Crystal Screen), PEG/Ion screen and Wizard III screen were used to identify initial protein crystallization conditions in 96-well sitting-drop plates. The plates were set-up by mixing 1 μl protein (~24 mg/ml in gel filtration buffer) with equal volume of reservoir solution and equilibrated against the reservoir at 20 °C. Two hits were selected from Hampton Crystal Screen HT: (1) 0.1 M sodium acetate, pH 4.6 and 8% (w/v) polyethylene glycol (PEG) 4000 and (2) 0.1 M sodium acetate, pH 4.6, 0.2 M ammonium sulfate and 30% (w/v) polyethylene glycol monomethyl ether (PEG MME) 2000 (**Fig. 2.5a and b**). The initial step for optimization of the crystallization conditions for better crystal growth was to vary the reagents in 24-well plates using the hanging-drop and sitting-drop vapor diffusion method, with 1.5 μl protein mixed with equal volume of reservoir solution and equilibrated against the reservoir at 20 °C. The following conditions were tested: (1) 0.1 M sodium acetate, pH 4.4−5.4 and 6−12% (w/v) PEG 4000 and (2) 0.1 M sodium acetate, pH 4.4−5.4, 0.2 M ammonium sulfate and 24−30% (w/v) PEG MME

2000. In parallel, different protein concentrations at approximately 12 mg/ml and 24 mg/ml were examined, with better crystal growth occurring with ~24 mg/ml protein using the hanging-drop vapor diffusion method. Further optimization of crystallization conditions included varying the salt concentration of (2), varying the protein to reservoir mix ratio, adding different salts, an additive screen, streak-seeding, different buffers, exchange PEG and PEG MME with a lower and higher molecular weight PEG and PEG MME, incubation at different temperatures (4 °C, 12 °C and 16 °C) and varying the rate of vapor diffusion using silicon and paraffin oil. Crystal quality and selection of cryoprotectant was monitored by several diffraction images collected in-house with X-ray from a rotating anode generator (Rigaku FRE SuperBright) and recorded on a RAXIS IV++ (Rigaku) image plate detector. From the optimizations, the best reservoir conditions contained 0.1 M sodium acetate, pH 4.8−5.0 and 10−12% PEG 4000, and after incubation at 20 °C, produced prism-shaped crystals of size 0.15 x 0.05 x 0.05 mm^3 (**Fig. 2.5c and d**). To obtain crystals with better diffraction to higher resolution, the reagents and greased 24-well plates were chilled on ice before setting up crystallization drops. Thorough chilling of the plate was accomplished by surrounding the plate with ice. The apo-*Cg*FMNAT crystals were grown by mixing 1.5 μl of protein (~24 mg/ml) with 1.5 μl of reservoir solution composed of 0.1 M sodium acetate, pH 4.4–5.4 and 6–12% PEG 4000, and equilibrated

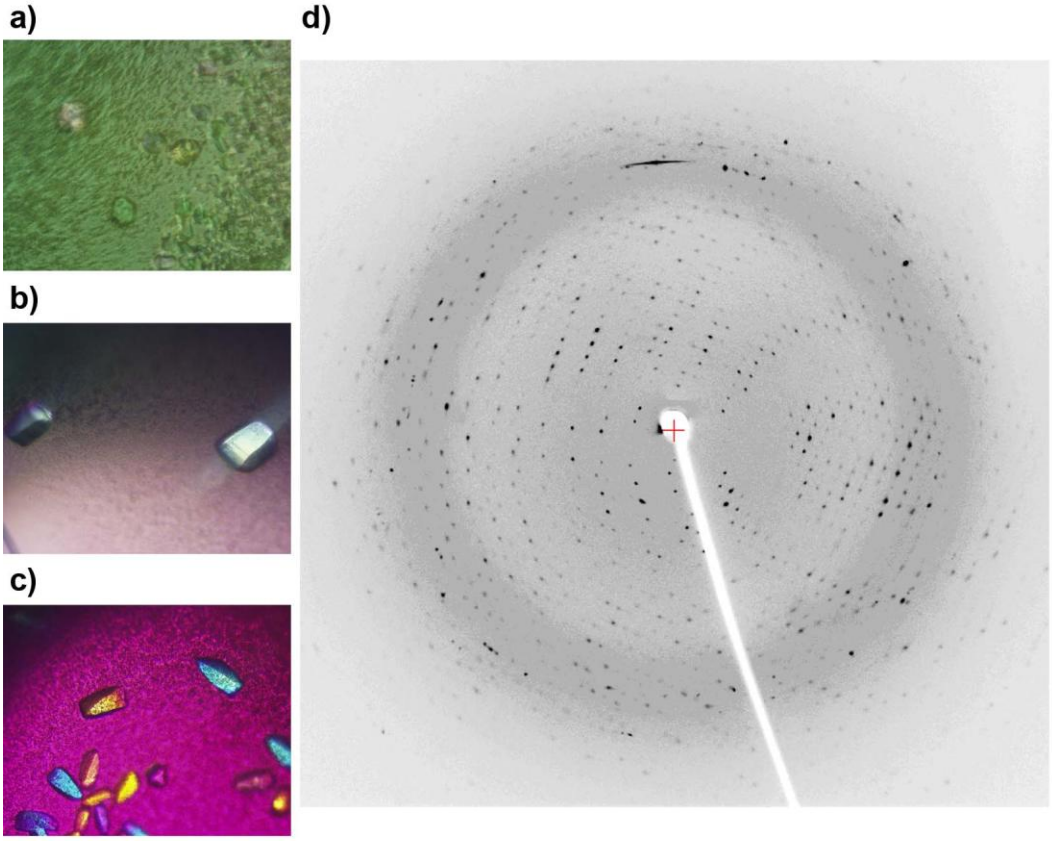

Figure 2.5 Initial and optimized crystallization conditions for apo-*Cg*FMNAT. a) From Hampton Research Crystal Screen HT solution D1 with 0.1 M sodium acetate, pH 4.6 and 8% (w/v) PEG 4000 and b) solution F1 with 0.1 M sodium acetate, pH 4.6, 0.2 M ammonium sulfate and 30% (w/v) PEG MME 2000. c) Optimization of a) condition yielded better crystal morphology in 0.1 M sodium acetate, pH 5.0 and 12% (w/v) PEG 4000 at 20 °C incubation. d) Crystal from c) diffracted to ~2.6 Å resolution. Images in Figure a-c were taken at 10x magnification.

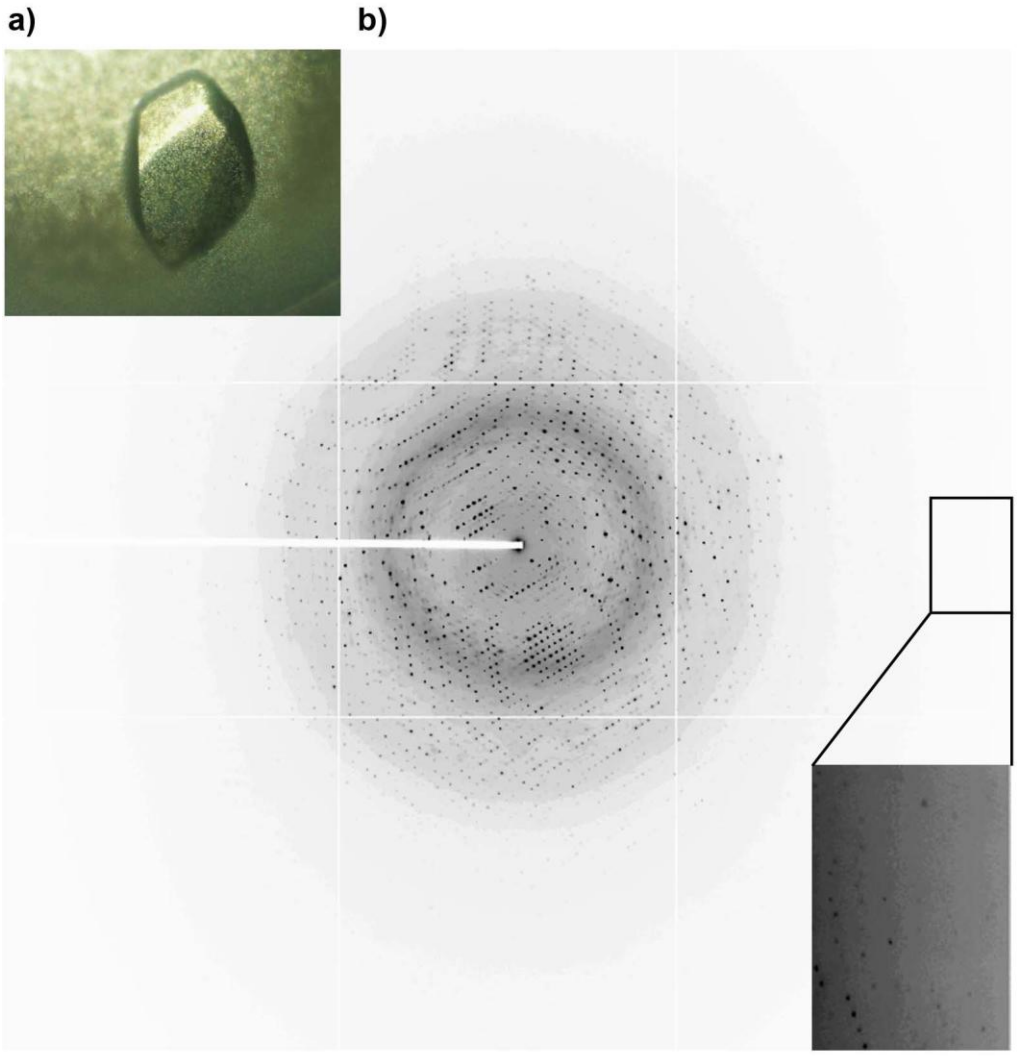

Figure 2.6 Improvement of crystal size and resolution. a) Prechilling the reagents and crystallization plate resulted in a crystal size of 0.55 x 0.35 x 0.35 mm^3 in 0.1 M sodium acetate, pH 5.0 and 6 % (w/v) PEG 4000 at 16 °C incubation. b) A diffraction image to 1.2 Å resolution is shown with an inset (enlarged from the small rectangle outlined in black lines on b)) showing diffraction spots at the edge.

against the reservoir at 16 ºC using the hanging-drop vapor diffusion method. Prism-shaped apo-*Cg*FMNAT crystals grew to a maximum size of 0.55 x 0.35 x 0.35 mm^3 within several days (**Fig. 2.6a**) in 0.1 M sodium acetate, pH 4.8–5.0 and 6% PEG 4000. The crystal diffracted to 1.48 Å at the in-house X-ray source. SeMet apo-*Cg*FMNAT crystals were grown under similar conditions as the native protein. Crystals of the same morphology grew to a maximum size of 0.25 x 0.15 x 0.15 mm^3 within several days in 0.1 M sodium acetate, pH 4.8–5.0 and 6–8% PEG 4000. Crystals were cryoprotected in a solution containing all the reservoir components and increments of glucose [10%, 20% and 30% (w/v)], flash-frozen in liquid propane and stored in liquid nitrogen.

Data collection, X-ray structure determination and refinement

Prior to the synchrotron data collection a 1.48 Å dataset was collected in-house from the same crystal used for the 1.2 Å data collection. Synchrotron X-ray beam-line 19-BM and 19-ID were used to collect diffraction data recorded on a SBC-3 CCD X-ray Detector and ADSC Quantum 315, respectively, at the Advance Photon Source (APS), Argonne National Laboratory. A 2.18 Å single-wavelength anomalous diffraction (SAD) dataset from a SeMet apo-*Cg*FMNAT crystal and a 1.5 Å dataset from a native apo-*Cg*FMNAT crystal was collected at beam-line 19-BM. Two data collection passes was performed on a single native crystal for the 1.2 Å dataset at beam-line 19-ID. For the first pass, data was

collected to 1.5 Å with the X-ray beam attenuated to reduce radiation damage to the protein crystal and to prevent individual spot intensity at low resolutions exceeding the CCD detector limit. Data at 1.2 Å were collected in the second pass with a higher X-ray flux (**Fig. 2.6b**). All datasets were indexed, integrated and scaled with the HKL3000 package[180]. Both passes for the 1.2 Å dataset was scaled together and used for structure refinement. The crystals belong to either $P3_121$ or $P3_221$ space group for the native and SeMet apo-*Cg*FMNAT datasets, with unit cell dimensions a=b=80.1 Å, c=78.1 Å, $\alpha=\beta=90°$ and $\gamma=120°$ for the 1.2 Å dataset. Data collection statistics for the 2.18 Å SAD and 1.2 Å native datasets are presented in **Table 2.1**. All scaled dataset intensities were converted to structure factor amplitude in the mtz file format using the CCP4 package[181].

The initial phases for apo-*Cg*FMNAT were obtained from the SAD data collected on the SeMet apo-*Cg*FMNAT crystal. To optimize the anomalous diffraction, an X-ray fluorescence scan of the SeMet apo-*Cg*FMNAT crystal was conducted near the absorption edge (K-edge) of selenium (Se) at beam-line 19-BM. The SAD dataset was collected at wavelength 0.97927 Å corresponding to the peak point. Aside from the N-terminal methionine, *Cg*FMNAT has only one non-terminal methionine. In general, one methionine per 100 residues is required for SAD and MAD (multiple-wavelength anomalous diffraction) phasing[182-184]. Therefore, it was not clear whether there would be sufficient signal for phase

Table 2.1. Data Collection and Refinement Statistics

Protein	Selenomethionyl apo-*Cg*FMNAT	apo-*Cg*FMNAT
Space Group/Monomer per Asymmetric Unit	$P3_221/1$	$P3_221/1$
Data	SAD	Native
Wavelength (Å)	0.97927	0.97931
Resolution (Å)	50.0-2.18	50.0-1.20
Unit cell dimensions		
a, b, c (Å)	80.31, 80.31, 78.27	80.09, 80.09, 78.09
α, β, γ (º)	90.0, 90.0, 120.0	90.0, 90.0, 120.0
Total no. of reflections	200196	1036966
No. of unique reflections	15582	90728
% Completeness	99.9 (100.0)[a]	99.9 (99.7)
R_{sym}[b]	0.091 (0.335)	0.070 (0.442)
I/σ	38.9 (8.5)	48.2 (2.3)
Mosaicity (º)	0.6	0.4
Model Refinement		Anisotropic[e]
Resolution range (Å)		50.0-1.20
R_{work}[c] (%)		16.2
R_{free}[d] (%)		17.8
No. of protein atoms		2502
No. of ligand atoms		13
No. of water molecules		390
Average B-factor (Å^2)		
Protein atoms		17.1
Ligand atoms		21.3
Water molecules		29.3
Rmsd bond length (Å)		0.015
Rmsd bond angle (º)		1.621
Ramachandran Plot		
% favored region		98.6
% allowed region		1.4
% outliers		0.0

[a]Values in parenthesis are for highest-resolution shell.
[b]$R_{sym} = \Sigma_{hkl} [(\Sigma_j (|I_j - \langle I \rangle|) / \Sigma_j I_j]$. $\langle I \rangle$ is the average for all *j* measurements of reflection *hkl*.
[c]$R_{work} = \Sigma_{hkl} |F_o - F_c| / \Sigma_{hkl} |F_o|$, where F_o and F_c are the observed and calculated structure factors, respectively.
[d]R_{free} calculated from randomly selected 1.5% reflections that are excluded from refinement for cross-validation.
[e]Six anisotropic displacement parameters are used for selected atoms, while isotropic B-factors were used for remaining atoms. Anisotropic displacement parameters were evaluated and assigned using ANISOANL and PARVATI.

determination. Heavy atom search and phasing were performed using SHELXC/D and E, as incorporated in the HKL3000 package, at 2.5 Å. Two Se sites were found and used for calculating phases. Refinement of heavy atom positions and phases was also performed with MLPHARE[185] followed by density modification using DM[186]. The figure-of-merit after MLPHARE was 0.15 and significantly improved to 0.70 after DM for the 2.18 Å SAD dataset collected. During phase determination, the space group was determined to be $P3_221$ with one *Cg*FMNAT molecule per asymmetric unit.

From the initial phases a model composed of 169 residues out of 308 was built using Resolve[187]. These phases were extended to 1.5 Å using the native dataset with DM in the CCP4 package, which resulted in a much improved electron density map. The R_{free} set was preserved and extended to 1.5 Å using the CCP4 package. A model of 272 residues out of 308 was built using ARP/wARP[188]. Refinement against the 1.2 Å native apo-*Cg*FMNAT dataset proceeded in two stages using REFMAC[189] with manual model building performed with Coot[190]. The first stage consisted of restrained refinements of isotropic B-factors with tight restraints. In the second stage, anisotropic B-factors were included in the refinements and stereochemical restraints were gradually loosened with each refinement step. Anisotropic displacement parameters were analyzed by ANISOANL in the CCP4 package and PARVATI server[191].

Anisotropic displacements parameters were assigned to atoms with B-factor approximately 21 or lower and well defined electron density. Water molecules were added by ARP/wARP and manually inspected. The final model has 291 residues out of 308, a glucose molecule and a chloride ion with R_{work} 16.2% and R_{free} 17.8%. The model was assessed by MolProbity[192] and complete model statistics is listed in **Table 2.1**.

An anomalous difference map was generated from a native apo-*Cg*FMNAT crystal anomalous dataset collected at 1.48 Å at UT Southwestern Medical in-house X-ray facility. The dataset was scaled with the anomalous flag on in HKL2000. Using the CCP4 package, the phases were transferred from the 1.2 Å data to the 1.48 Å data and the anomalous difference map was generated using FFT.

All images of structures, electron density and electrostatic surface potentials were generated using *i*PyMol (http://www.pymol.org). The pdb2pqr server[193] was used to generate a pqr file using PARSE atomic radii and charges[194]. Electrostatic surface potentials were calculated using APBS[195] plugin for PyMol using the default settings, with a monovalent cation and anion concentration of 0.15 M and the potential ramped between -5 kT/e (red) and +5 kT/e (blue). Structural alignment was performed using Secondary Structure Matching[196].

Adobe Creative Suite 2 (http://www.adobe.com) was used to label and format images.

RESULTS

Quality of apo-*Cg*FMNAT model

To obtain crystals that diffracted to 1.2 Å, the reagents and greased 24-well plates needed to be chilled on ice before setting up crystallization drops. The observation leading to such a procedure was the accumulation of condensed vapor during plate set-up at room temperature (RT) and incubation at 20 ºC. Plate set-up at RT, then incubation at lower temperatures, produced smaller crystals with poor diffraction or slightly larger fragile crystals. Incubation at 16 °C, after set-up on ice, produced large well-defined crystals diffracting to high resolution (**Fig. 2.6a and b**). The crystal structure of apo-*Cg*FMNAT was solved by the single-wavelength anomalous diffraction (SAD) phasing method using selenomethionine as the source of anomalous diffraction and was refined using data to a resolution of 1.2 Å collected from a native crystal (**Table 2.1**). There is one *Cg*FMNAT molecule in the asymmetric unit and six molecules in the space group $P3_221$. Crystal-packing analysis and quaternary analysis from PISA[197] suggests that the functional unit of *Cg*FMNAT is a monomer, which is consistent with the gel filtration result that showed *Cg*FMNAT is monomeric in solution (**Fig. 2.7**). The

refined model contains residues -3–304, except for residues 85–101, for which we found no associated electron density and are presumably disordered. Residues -3–0 (Gly-Ala-Met-Val) were introduced during cloning. For the model, the main chain dihedral angles (ϕ, ψ) for all residues are in the allowed Ramachandran area (**Table 2.1**) and has an average B-factor of 17.1 $Å^2$ (**Fig. 2.8**). A β-D-glucose molecule was modeled with an average B-factor of 25.5 $Å^2$ and is derived from the cryoprotectant. A chloride ion, with a B-factor of 17.1 $Å^2$ is modeled due to the presence of a large spherical density situated in a positively charged pocket, also referred to as an anion or oxy-anion pocket, formed by the amide-backbones of a loop (*PP-loop*) connecting β1 to helix α3 (**Fig. 2.9**). Modeling a water molecule resulted in an average B-factor of 9.2 $Å^2$, lower than the surrounding protein atoms, and with a presence of a strong positive F_o-F_c difference electron density peak. Additionally, there is a positive peak in the anomalous difference map at the same position from the dataset collected in-house at X-ray wavelength 1.5418 Å (**Fig. 2.9**). There are two known atom types in the crystal to contribute to anomalous diffraction at the given wavelength. Sulfur atom from methionine and cysteine residues, and chloride ion from the gel filtration buffer. The environment of the anomalous difference peak indicates that a chloride ion is the most likely candidate. Many side chain and main chain double conformations, and loop flexibility were clearly observable in the electron density at 1.2 Å.

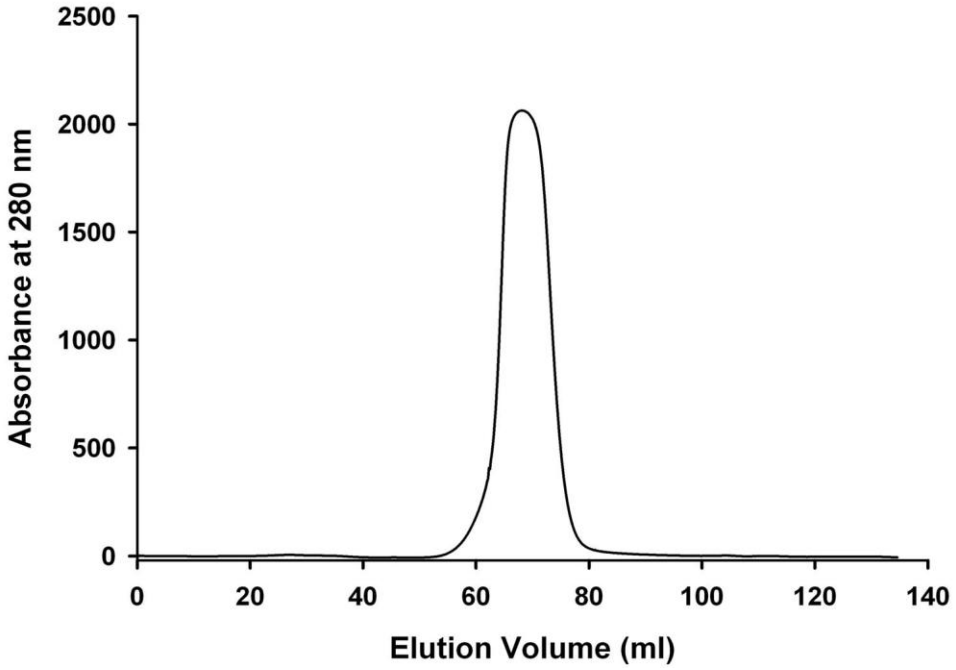

Figure 2.7 apo-*Cg*FMNAT elution profile from a Superdex 75 16/60 gel filtration column. The single peak maximum occurs at 68.0 ml, corresponding to a molecular weight of ~38 kDa. The theoretical molecular mass for *Cg*FMNAT is 35,568 Da.

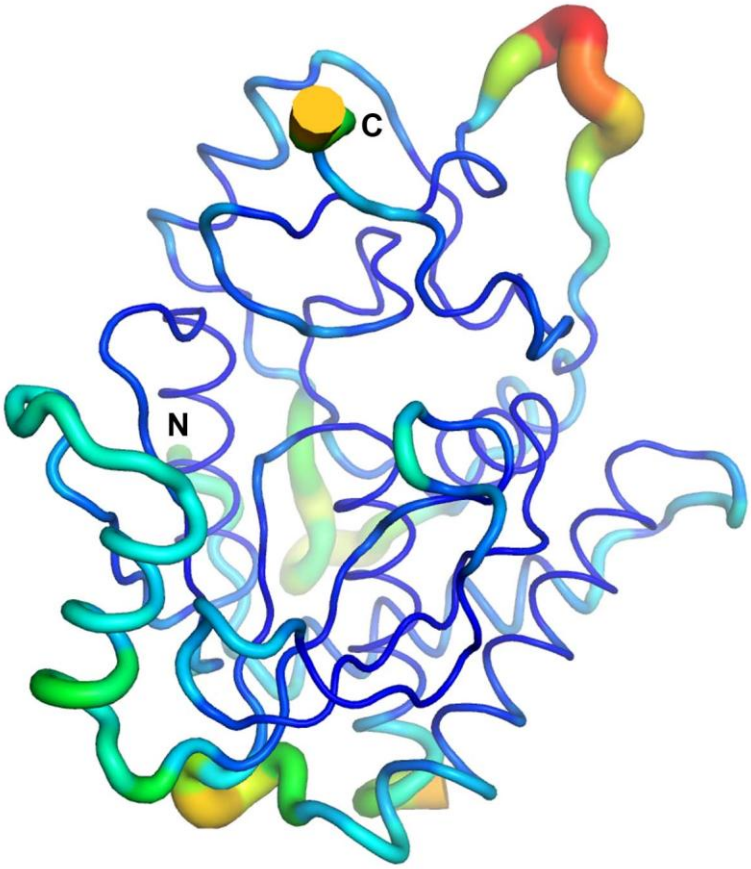

Figure 2.8 Cartoon putty of *Cg*FMNAT. The putty width becomes wider with an increase in B-factor. The color is ramped from blue to red, with blue being the lowest B-factor and red the highest B-factor. The lowest main chain B-factor for a residue is 10.5 $Å^2$ and the highest is 42.3 $Å^2$. Including the main chain and side chain for each residue the lowest B-factor is 10.9 $Å^2$ and the highest is 45.7 $Å^2$, and the average is 17.1 $Å^2$.

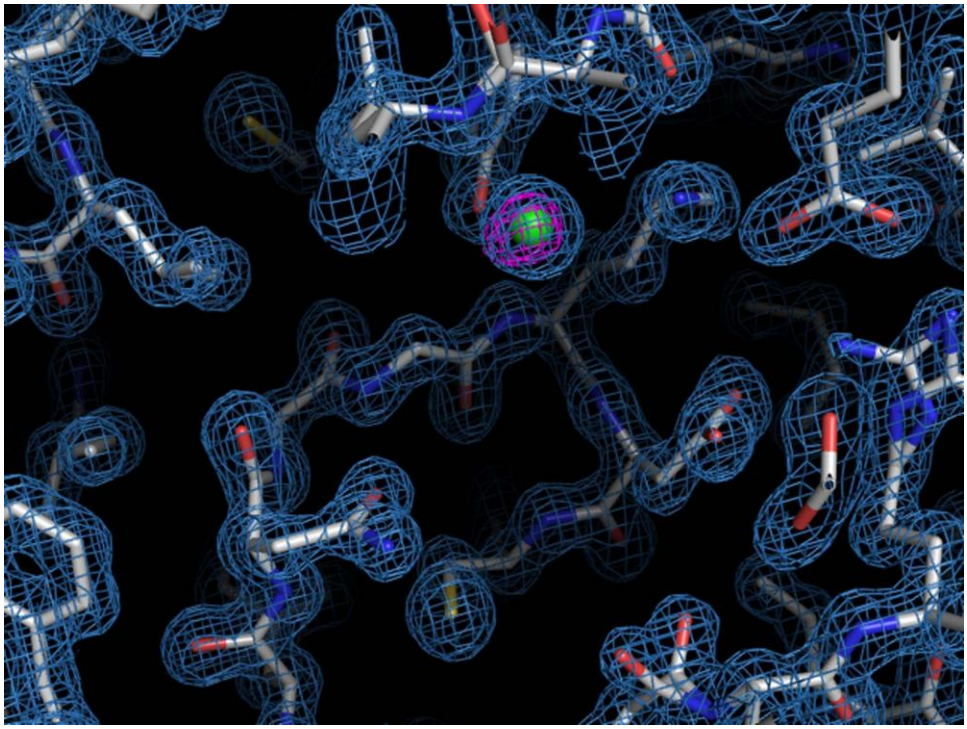

Figure 2.9 Electron density map of apo-*Cg*FMNAT at 1.2 Å resolution. A $2F_o$-F_c electron density map (sky blue) contoured at 1.5σ is shown for local residues of apo-*Cg*FMNAT surrounding an anion pocket. The protein is colored by atom type with carbon atoms colored white. A chloride ion (green sphere) was identified in the anion pocket by the presence of an anomalous difference peak contoured at 6σ (magenta).

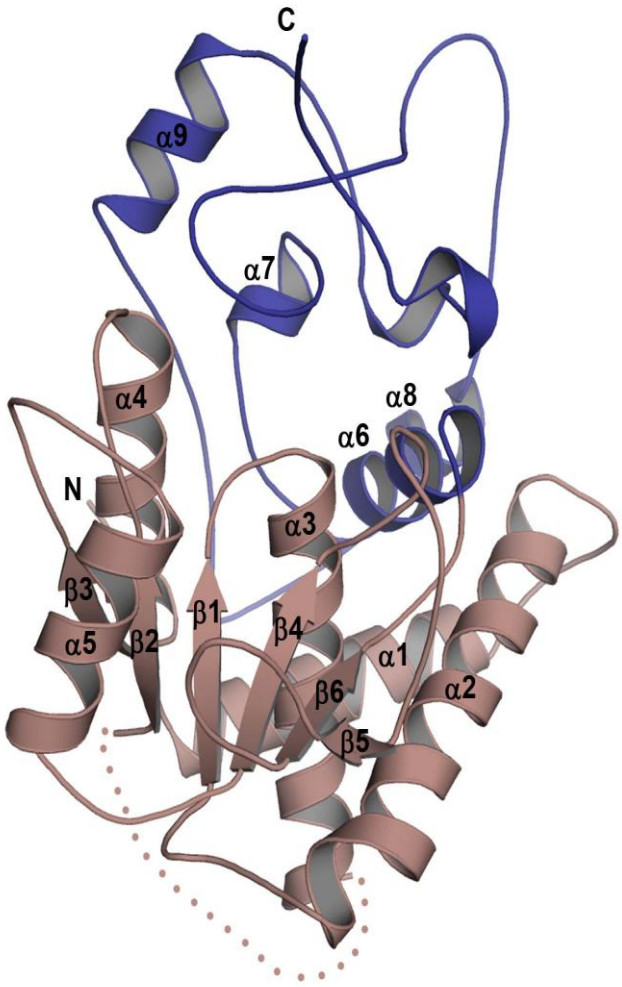

Figure 2.10 Ribbon representation of apo-*Cg*FMNAT. The N-terminal domain colored in raspberry is composed of residues 1–196 and the C-terminal domain colored in dark blue is composed of residues 197–304. The dots connecting α3 to β2 represent the residues not modeled (disordered).

Other regions with less well defined electron density and increased B-factors can be inferred as displaying conformational flexibility (**Fig. 2.8**).

Description of apo-*Cg*FMNAT structure

*Cg*FMNAT is composed of two domains (**Fig. 2.10**). The N-terminal domain, containing residues 1−196, has an α/β fold with a central, twisted six-stranded β-sheet sandwiched by α-helices. Five β-strands of the central β-sheet are parallel to each other and have a Rossmann-like fold topology. Starting at the N-terminus, *Cg*FMNAT has two long helices, α1 and α2, that are followed by the first β-strand (β1) of the Rossmann-like fold core. The core has a topology of β3α4β2α3β1|α5β4β6β5, where the crossover helix α5 connects β3 to β4 and places β4 parallel and adjacent to β1. Deviation from the typical Rossmann-fold[144] topology is in the orientation and placement of strand β5, which connects β4 and β6 and is anti-parallel to all other strands. In a typical Rossmann-fold protein, an α-helix would be in the place of β5 and connects β4 and the next adjacent and parallel strand β6. The carboxyl-termini of β1 and β4 transform into loops and extend in opposite directions from the β-sheet plane. Like most Rossmann-fold nucleotide-binding proteins, a crevice is formed between the two central strands β1 and β4, constituting the primary nucleotide-binding site[144]. The loop extending from β1 to α3 (*PP-loop*) has the sequence ^{62}NGGKDC$_{67}$, which is

slightly altered from the signature motif SGGxD(S/T)[142] of the "adenine nucleotide α hydrolase-like" protein superfamily at the first position (Asn62 instead of a Ser).

The C-terminal domain, residues 197−304 of *Cg*FMNAT, is composed largely of loops (64%) interlaced by α6–α9 and two short 3_{10}-helices (**Fig. 2.10**). Upon examination of the crystal packing there was minimal inter-lattice contact, therefore the C-terminal domain is intrinsically structural, as supported by the low B-factors (**Fig. 2.8**). From α6 a loop extends upwards placing α7 and the following hairpin loop above the crevice formed by β1 and β4. A long V-shaped loop then connects α8 to α9, placing α9 adjacent to α7. This loop follows a V-shaped outline formed by α1 and α4, and appears to be flexible at the vertex (**Fig. 2.8**). Following helix α9, a loop and a 3_{10}-helix extends towards the gap between α7 and α8 and places a 3_{10}-helix underneath the loop between α7 and α8. A roughly flat surface is formed by the C-terminal domain (**Fig. 2.11a**). From an electrostatic surface potential view, a negatively charged pocket exists on this face of the molecule, flanked by a positively charged patch on the left and a negatively charged patch on the right (**Fig. 2.11b**).

The crevice formed by β1 and β4 from the Rossmann-like N-terminal domain is the primary nucleotide binding site in the superfamily. The area above

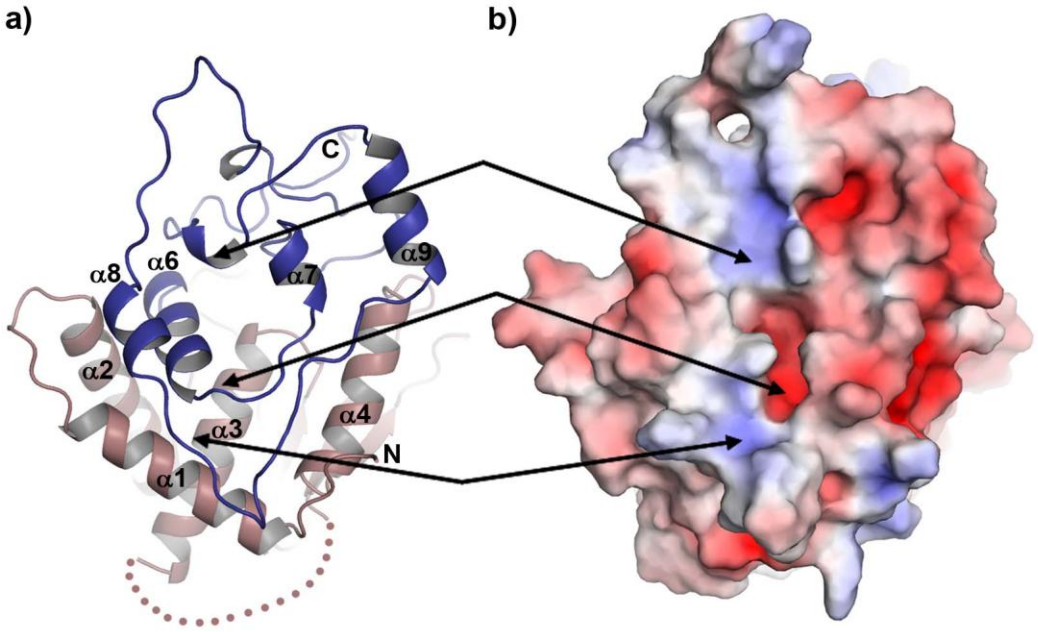

Figure 2.11 Ribbon diagram and electrostatic surface potential of apo-*Cg*FMNAT. a) The C-terminal domain (dark blue) is oriented in a manner that places the flat surface parallel to the page. b) An electrostatic surface potential of apo-*Cg*FMNAT in the same orientation as in a) reveals a negatively charged pocket formed by the C-terminal domain. Corresponding areas in a) and b) are indicated with arrows.

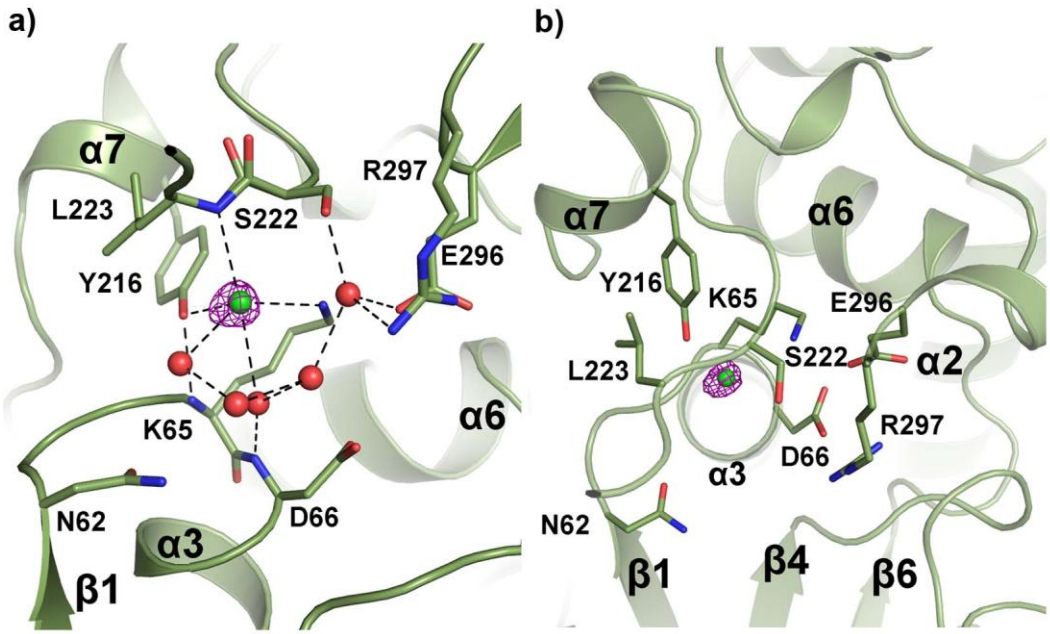

Figure 2.12 Binding site for a chloride ion. Water molecules are shown as red spheres and protein residues are colored by atom type with carbon atoms colored forest green. Hydrogen bonds are indicated by black dash lines. a) A chloride ion (green sphere) identified by the presence of an anomalous difference peak contoured at 6σ (magenta) forms hydrogen bonds with the surrounding protein and water atoms with distances of 2.9–3.3 Å, typical for a chloride ion. b) The chloride ion is positioned above α3, and in-line with the helix dipole.

helix α3 is an anion pocket generated by the positive dipole of α3, as the peptide amides are oriented upward towards the pocket and the carbonyls oriented downward. The βγ-phosphate of ATP from N-type ATP pyrophosphatases and PP-loop ATPase families is known to bind in this anion pocket. In apo-*Cg*FMNAT a chloride ion is located in the anion pocket and centered above α3 (**Fig. 2.12a and b**). The chloride ion forms five hydrogen bonds to the ammonium group of Lys65 of the *PP-loop* (3.3 Å), hydroxyl of Tyr216 (2.9 Å), the amide of Leu223 (3.2 Å) and two water molecules as depicted in **Fig. 2.12b**. A surface representation shows the chloride ion located deep inside a large pocket, presumably the nucleotide binding site, formed by β1 and β4 of the Rossmann-like fold, the *PP-loop*, α3 and surrounding residues (**Fig. 2.13**). An electrostatic surface potential shows the positive charge on the surface generated from residues interacting with and surrounding the chloride ion and contributing to the anion pocket (**Fig. 2.13**).

A modeled glucose molecule, as defined by the high resolution electron density, is stacked between the protein monomer in the asymmetric unit and a symmetry-related *Cg*FMNAT molecule. The glucose molecule interacts with several residues from both monomers and well defined water molecules (**Fig. 2.14a**). From the same asymmetric unit the glucose interacts with the main chain

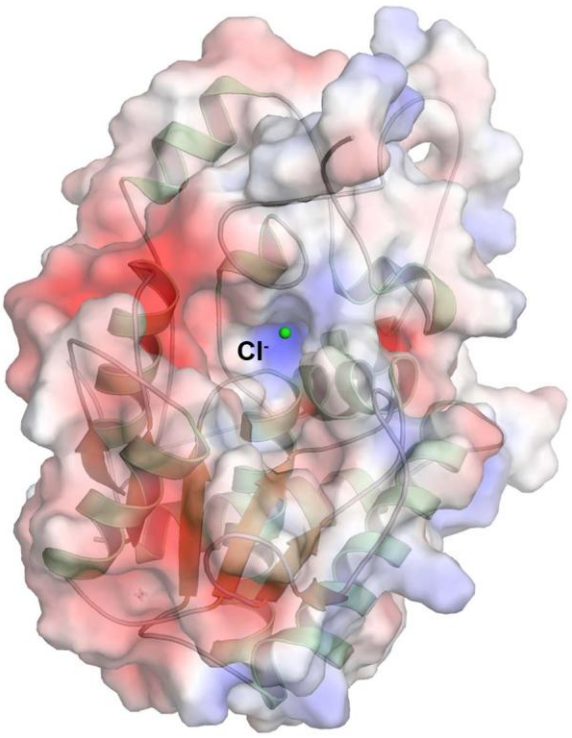

Figure 2.13 An electrostatic surface potential of apo-*Cg*FMNAT with the bound chloride ion localized in a positive charge area deep inside a large pocket.

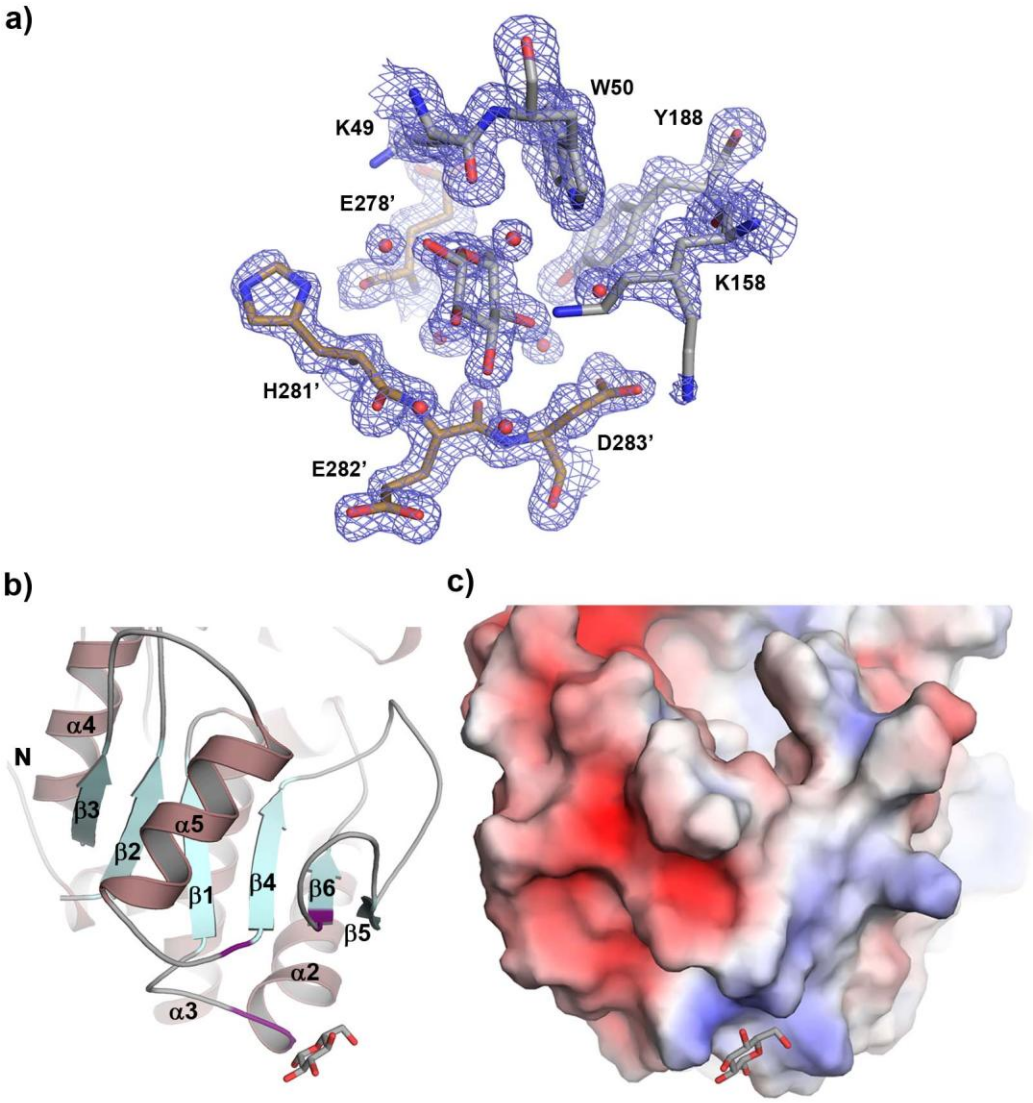

Figure 2.14 Glucose interaction site. a) A $2F_o$-F_c electron density map (blue) contoured at 1.0σ is shown for glucose, waters (red sphere) and residues interacting with the glucose. Atoms are colored by atom type with carbon atoms colored gray for apo-*Cg*FMNAT and brown for the symmetry-related apo-*Cg*FMNAT. b) Ribbon representation of apo-*Cg*FMNAT with residue K49, W50, K158 and Y188 sites colored purple. c) The glucose is located in a positive charge depression on apo-*Cg*FMNAT.

carbonyl of Lys49 and ammonium group of Lys158 through hydrogen bonds, and with Trp50 and Tyr188 through van der Waals interaction. Additional interactions occur with residues Glu278', His281', Glu282' and Asp283' from a symmetry-related *Cg*FMNAT molecule, primarily through van der Waals interaction, with a hydrogen bond to the main chain carbonyl of Asp283'. The arrangement of Lys49 and Trp50 following α2, Lys158 before β4 and Tyr188 on strand β6 may aide in localizing the glucose molecule, as these residues form a positive charge depression around the glucose (**Fig. 2.14b and c**). Capping the depression are residues from the symmetry-related protein. The water molecules at the two monomer interface may also contribute to the stability of the glucose.

There were a total of 27 residues for which double conformations are observed and all occur at the solvent accessible region of apo-*Cg*FMNAT (**Fig. 2.15**). Four residues adopt double conformations in the main chain regions (**Fig. 2.16a and c**), sixteen residues have double side chain conformations (**Fig. 2.14a** and **Fig. 2.16b and c**) and the double conformations of seven residues involve both main chain and side chain atoms (**Fig. 2.17**). The solvent exposed loop connecting α1 to α2, residues 21−24, displays conformational flexibility of the peptide bonds (**Fig. 2.17**). Double peptide bond conformations from Gly163 and Ser222 are shown in **Fig. 2.16a and c**, which take part in forming the substrate

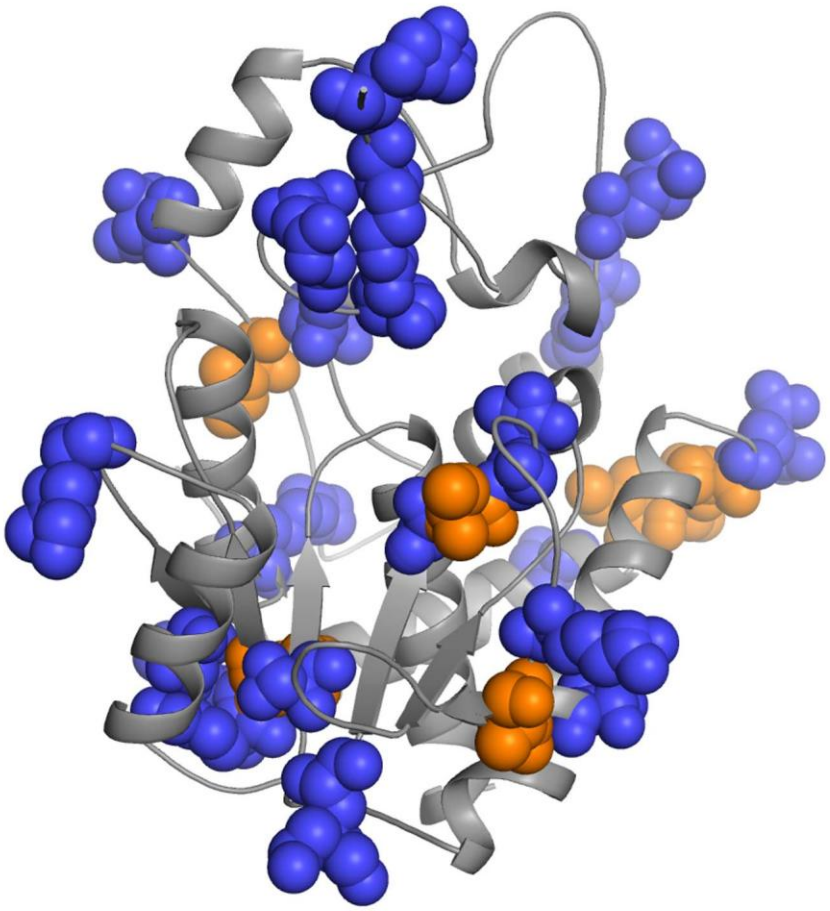

Figure 2.15 Residues with double conformations are shown on a ribbon representation of apo-*Cg*FMNAT. Residues with double conformations are shown as spheres, with hydrophilic residues in blue and hydrophobic residues in orange. All double conformations occur at the solvent accessible regions.

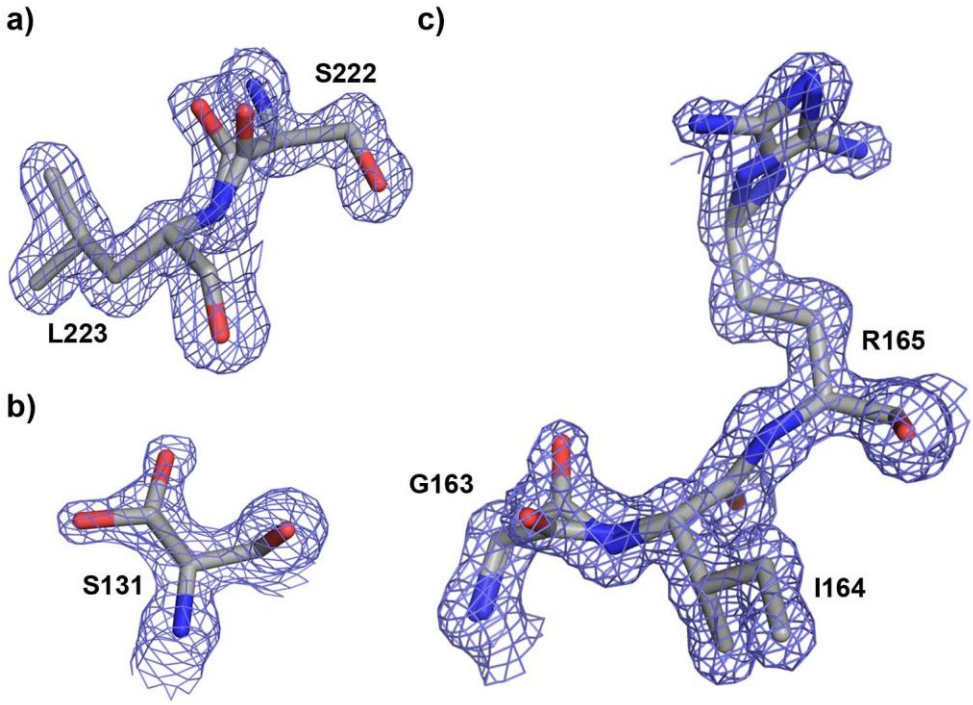

Figure 2.16 $2F_o$-F_c Electron density maps (blue) contoured at 1.0σ for representative residues modeled with double conformations. a) The carbonyl of the peptide bond of S222 is observed fluctuating between two positions. b) Side chain double conformations of S131. c) Two conformations for G163 main chain are observed and a rotation of the guandinium group of R165 is clearly evident.

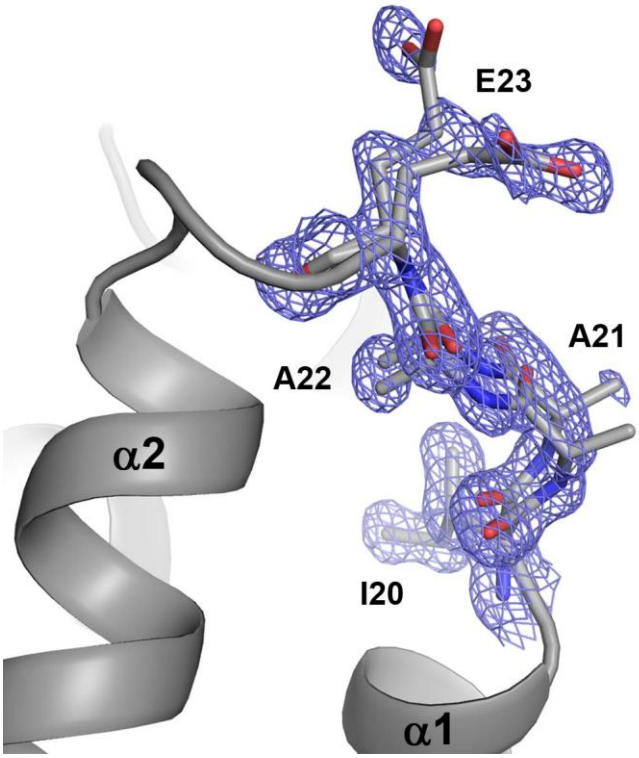

Figure 2.17 Flexible loop between two helices. Part of the loop connecting helix α1 and α2 is observed in double conformations. A $2F_o$-F_c electron density map (blue) is shown contoured at 1.0σ.

Table 2.2. apo-*Cg*FMNAT Residues with Double Conformations

Residue	Substrate Binding Site	MC/SC[1]	SS[2]
Ser16	No	SC	H (α1)
Ile20	No	MC	L
Ala21	No	MC/SC	L
Ala22	No	MC/SC	L
Glu23	No	MC/SC	L
Ser40	No	SC	H (α2)
Ser58	Yes	SC	S (β1)
Lys102	No	MC/SC	L
Leu103	No	MC/SC	S (β2)
Arg127	No	SC	H (α4)
Ser131	No	SC	S (β3)
Lys139	No	SC	L
Lys158	No	SC	L
Gly163	Yes	MC/SC	S (β4)
Ile164	Yes	MC	L
Arg165	Yes	SC	L
Lys175	No	SC	L
Ile177	No	SC	S (β5)
Glu214	No	SC	H (α7)
Ser222	Yes	MC	L
Glu228	No	SC	L
Lys245	No	SC	L
Glu249	No	SC	H (α8)
Ile267	No	SC	L
Asp271	No	MC/SC	L
Arg300	Yes	MC	L
Lys302	No	SC	L

[1]MC stands for main chain and SC stand for side chain.
[2]SS stands for secondary structure.

binding pocket. A summary of residues with double conformation is listed in **Table 2.2**.

Structural comparison to adenine nucleotide α hydrolase-like superfamily

Comparison of apo-*Cg*FMNAT with known protein structures using the Dali server[198] indicates that the core of *Cg*FMNAT is most similar to the members of the PAPS reductase-like family. These include bacterial adenosine 5'-phosphosulfate (APS) reductase[138] [Protein Data Bank (PDB) ID 2goy; Z-score of 15.4 and rmsd of 2.5 Å for 174 superimposed C_α atoms], PAPS reductase[140] (1sur, Z-score of 14.0 and rmsd of 2.4 Å for 159 superimposed C_α atoms), and ATP sulfurylase[139] (1zun, Z-score of 13.1 and rmsd of 2.9 Å for 160 superimposed C_α atoms). Similar to *Cg*FMNAT, these proteins also have a core domain of a modified Rossmann-fold topology where the 5th β-strand of the central six-stranded β-sheet is anti-parallel to the rest of the strands (**Fig. 2.18a**). This unique topological variation distinguishes them from other members of the adenine nucleotide α hydrolase-like protein superfamily, such as N-type ATP pyrophosphatases (e.g., GMP synthetase[143] and β-lactam synthetase[199]) and PP-loop ATPase (e.g., tRNA-Ile-lysidine synthetase[200]) (**Fig. 2.18b**). This unique topological variation replaces a helix with a β-strand, thereby altering the topology at the edge of the domain. Furthermore, in PAPS reductase-like family

the central twisted β-sheet is not enclosed by helices as in the N-type ATP pyrophosphatases and PP-loop ATPase families (**Fig. 2.18a and c**).

The nucleotide binding motifs conserved in the superfamily are also conserved in *Cg*FMNAT. The *PP-loop* and adenine-loop (or LDTG in APS reductase[138]) are nucleotide binding motifs featured in all proteins in the superfamily and are highlighted in three proteins in **Fig. 2.18a and b**. The *PP-loop* connects the carboxy-terminus of the first β-strand to the following helix. The adenine-loop connects the second β-stand and succeeding helix. Additional motifs in the PAPS reductase-like family include the arginine-loop (Arg-loop), which connects β4 to β5 in APS reductase and contains three conserved arginines[138]. This motif is also present in PAPS reductase and ATP sulfurylase with three conserved arginines. An equivalent topological feature is also present in *Cg*FMNAT and has one arginine. From a structure-based alignment, this arginine in *Cg*FMNAT is well conserved in members of the PAP reductase-like family (**Fig. 2.19**). For members of N-type ATP pyrophosphatases and PP-loop ATPase families there is no Arg-loop and the corresponding region usually contains one or more helices (**Fig. 2.18b**). The C-terminus of APS reductase that superimposes with the last 3_{10}-helix and the proceeding loop at the C-terminus of *Cg*FMNAT (**Fig. 2.18a**) is shown to have two arginines interacting with the substrate APS, which are conserved in *Cg*FMNAT (**Fig. 2.19**).

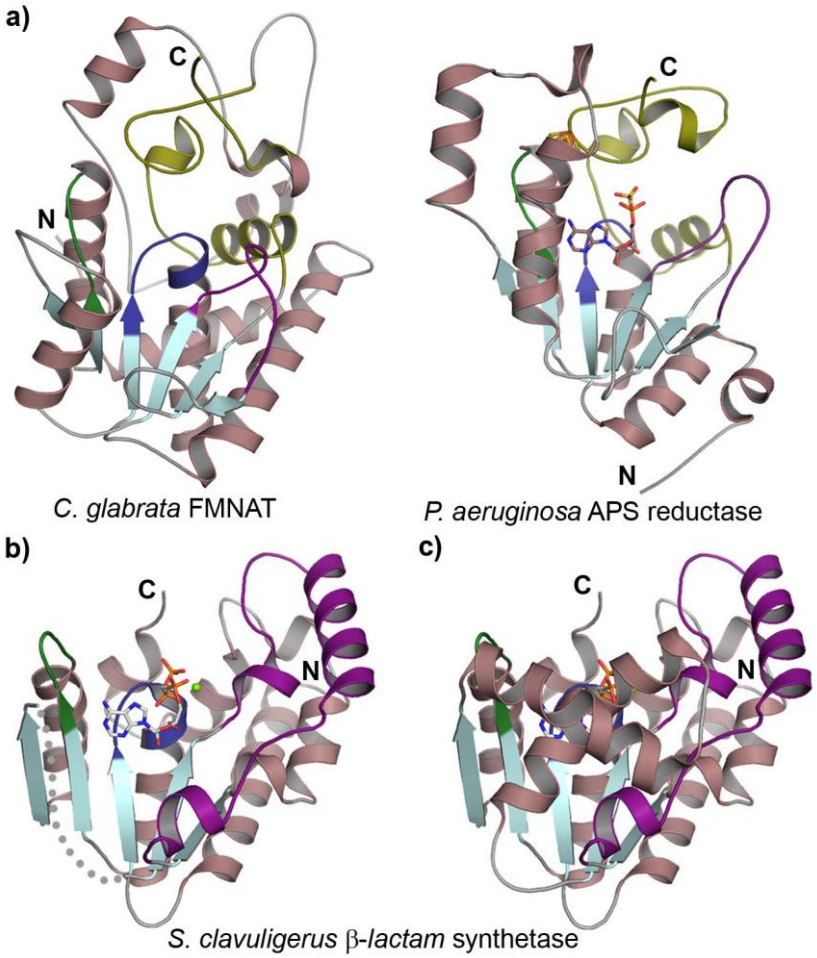

Figure 2.18 Comparison of apo-*Cg*FMNAT structure to members of the adenine nucleotide α hydrolase-like superfamily. Bound ligands are shown as sticks. Equivalent structural motifs involved in substrate binding are colored dark blue for PP-loop, dark green for adenine-loop and purple for Arg-loop motifs. a) C-terminal domain of apo-*Cg*FMNAT superimposible to APS reductase is colored dark yellow. The APS and [4Fe,4S] cluster are colored by atom type with carbon atoms colored raspberry. b) Region in β-lactam synthetase corresponding to Arg-loop is shown in magenta and removed region indicated by gray dots. c) β-lactam synthetase in the same orientation as in b) with removed helices shown. ATP in b) and c) is colored by atom type with carbon atoms colored gray and a green sphere for magnesium ion.

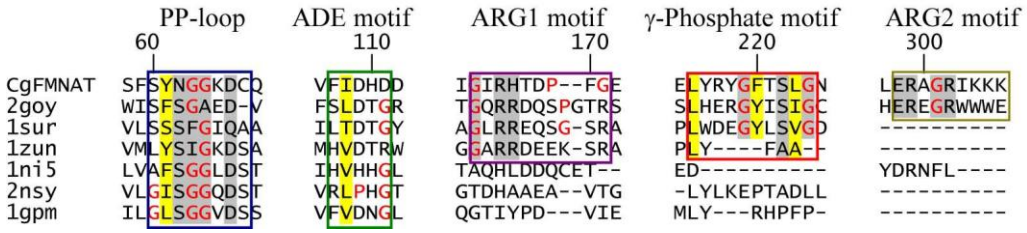

Figure 2.19 Structure-based multiple sequence alignment of protein representatives from "adenine nucleotide α hydrolase-like" superfamily. Each sequence is labeled by the PDB code, except *Cg*FMNAT. The residue numbers of *Cg*FMNAT are marked at the top of the alignment. Conserved structural motifs are boxed and conserved residues within the motifs highlighted. Glycine and proline residues are in red; conserved glycine and charged/polar residues are highlighted in gray and conserved hydrophobic/aromatic residues in yellow. Members of PAPS reductase-like family are 2goy (APS reductase), 1sur (PAPS reductase) and 1zun (ATP sulfurylase); member of PP-loop ATPase family is 1ni5 (tRNA-Ile-lysidine synthetase); and members of N-type ATP pyrophosphatases are 2nsy (NH^{3+}-dependent NAD synthetase) and 1gpm (GMP synthetase).

The C-terminal domain of *Cg*FMNAT is uniquely elaborated and expanded with long loops. Compared to other members of the PAPS reductase-like family, parts of the C-terminal domain structure are conserved, as shown for APS reductase and ATP sulfurylase (**Fig. 2.18a and Fig. 2.20**). These include regions from helix α6 to α7 of *Cg*FMNAT corresponding to that of APS reductase and ATP sulfurylase (**Fig. 2.18a and Fig. 2.20**), and the last 3_{10} helix and the proceeding loop of the C-terminus end corresponding to the C-terminus of APS reductase (**Fig. 2.18a**). The aforementioned regions of *Cg*FMNAT show significant structural similarity to the equivalent regions of APS reductase.

DISCUSSION

Our high-resolution structure of yeast FMNAT presents the first characterization of a eukaryotic version of this essential enzyme. Although the overall structure of *Cg*FMNAT shares significant similarity with PAPS reductase-like family of proteins, as reflected in several shared nucleotide binding motifs and the unique deviation from the typical Rossmann fold topology, the elaborated C-terminal domain and the long N-terminal helix α1 are unique to *Cg*FMNAT (**Fig. 2.18 and 2.20**). Replacing the first conserved Ser in the *PP-loop* signature motif SGGxD(S/T) with Asn (^{62}NGGKDC$_{67}$), unique only to eukaryotic FMNAT

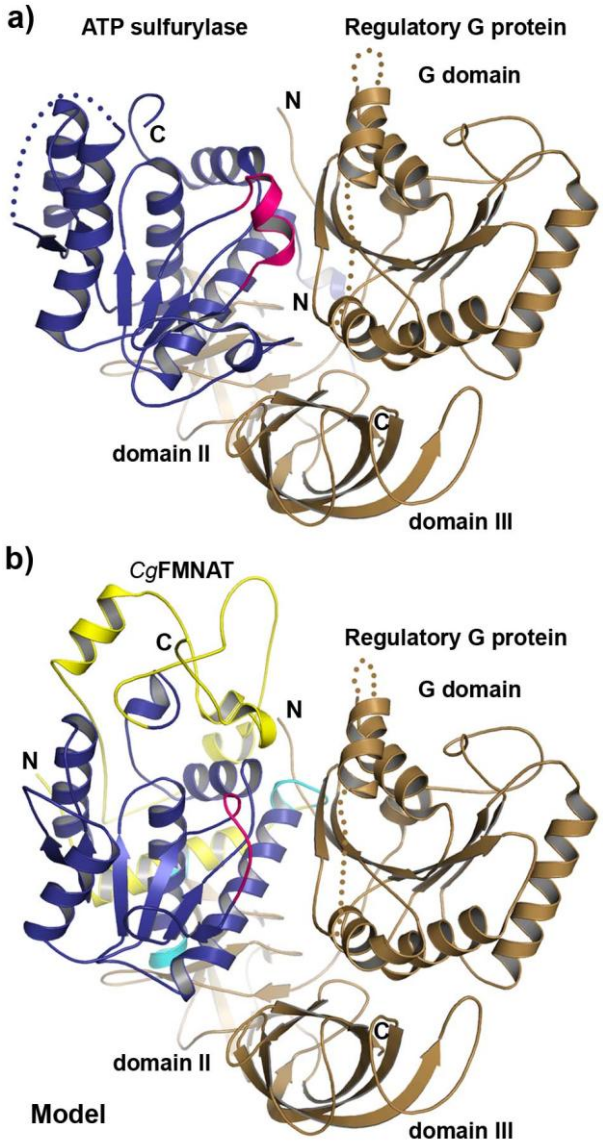

Figure 2.20 Superimposing *Cg*FMNAT to ATP sulfurylase-regulatory G protein. a) ATP sulfurylase-regulatory G protein complex. A portion of the Arg-loop in a) ATP sulfurylase and b) apo-*Cg*FMNAT is colored dark pink. b) Model of helix α1 and portion of the C-terminal domain specific to apo-*Cg*FMNAT are colored yellow and secondary structure clashes with the G domain and domain II are colored cyan. Residues missing in the ATP sulfurylase-regulatory G protein complex are shown with dots.

in the adenine nucleotide α hydrolase-like superfamily (**Fig. 2.19**), does not perturb the *PP-loop* motif conformation. Suggesting that N62 could be involved in binding to ATP in a similar manner as Ser in N-type ATP pyrophosphatases and PP-loop ATPase.

The function of the large C-terminal domain of yeast *Cg*FMNAT is currently unknown. A hypothesis is that it might be involved in interaction with other proteins. A negatively charged pocket surrounded by negatively and positively charged regions as shown in **Fig. 2.11b** could indicate a binding site for an unidentified ligand. The notion of potential protein-protein interaction could be partially inferred from the similarity of eukaryotic FMNAT to PAPS reductase-like family.

It is known that the activities for some members of the PAPS reductase-like family are modulated through protein-protein interactions[138,139]. For example, ATP sulfurylase is a monomer known to associate with a regulatory G protein (CysN), in which the G protein regulates ATP sulfurylase by energetically coupling hydrolysis of GTP to the extremely thermodynamically unfavorable formation of APS[139]. Superimposing apo-*Cg*FMNAT to ATP sulfurylase-regulatory G protein complex shows *Cg*FMNAT fits into the equivalent position as ATP sulfurylase with minimal secondary structure clashes with CysN (regulatory G protein) (**Fig. 2.20b**). ATP sulfurylase's N-terminal helix α1 forms

intermolecular contacts with CysN G domain and domain II (**Fig. 2.20a**). The structural element equivalent to ATP sulfurylase's α1 in *Cg*FMNAT is α2, for which similar intermolecular contacts could be formed, with secondary structure clashes only at the loop connecting α1 to α2 and the first three residues of α2 (**Fig. 2.20b**). Taking into consideration the sequence and structural similarity to the PAPS reductase-like family, and the comparative analysis to ATP sulfurylase-regulatory G protein complex, it is possible that *Cg*FMNAT could be a modulatory monofunctional enzyme.

In summary, we present here a high-resolution structure of a eukaryotic FMN adenylyltransferase revealing structural similarities and differences to proteins in the PAPS reductase-like family and other members of the superfamily. Details about the *PP-loop* configuration and a proposed region for βγ-phosphate binding was obtained through the observation of a chloride ion bound in an anion pocket conserved in the superfamily and known for interacting with the βγ-phosphate of ATP. Unlike any other members of the PAPS reductase-like family, currently, *Cg*FMNAT is the only member in the family that is not part of the sulfate assimilation pathway. It possesses a uniquely elaborated C-terminal domain, which might have additional functions.

CHAPTER 3

Structures of *Cg*FMNAT Complexes

(Parts of this chapter are adapted from Huerta *et al*., 2009)

INTRODUCTION

Structure determination of the apo-*Cg*FMNAT shows that the overall fold of the protein is very similar to PAPS reductase-like family, in which three nucleotide binding motifs, the *PP-loop*, Arg-loop and ADE motif (termed LDTG motif in ref. 136), are conserved. The structure also provided information about the uniqueness of the tertiary structure, such as the long N-terminal helix α1 and an elaborated organization of the C-terminal domain. Additionally, through structural comparison the eukaryotic FMNAT *PP-loop* consensus sequence is identified as NGGKDC, which contains residues Asn and Lys that are not conserved in the superfamily.

Members of the PAPS reductase-like family are involved in the sulfate assimilation pathway that binds to the nucleotide or a derivative of the nucleotide ATP[138-140]. APS and PAPS reductase bind to their respective substrates as stated from their enzyme function, whereas ATP sulfurylase is currently the only member that binds ATP[138-140]. Closely related families to the PAPS reductase-like family include the N-type ATP pyrophosphatases and PP-loop ATPase

families[138-141], which also belong the same adenine nucleotide α hydrolase-like superfamily[130,142]. The N-type ATP pyrophosphatases family is comprised of many protein members that bind ATP and synthesize different products, such enzymes include GMP synthetase, NH_3^+-dependent NAD synthetase and β-lactam synthetase[143,199,201]. All members share a similar nucleotide binding site that conserves the PP-loop and ADE structural motifs.

A proposed region for ATP binding can be inferred by structural superposition with homologous proteins, such as APS reductase and ATP sulfurylase. However, the degree by which the ATP binding is altered by the Asn and Lys of the eukaryotic FMNAT *PP-loop* is unknown. Additionally, *Cg*FMNAT has no structure and sequence similarity to other known flavoproteins. The fact that *Cg*FMNAT has no similarity to any other flavoproteins is an indication the FMN binding site is likely to be unique. Determining *Cg*FMNAT structures with substrates and product FAD is thus necessary for understanding substrate binding and catalytic mechanism of this essential enzyme. Additionally, the structures will allow a more discriminatory analysis between eukaryotic and bacterial FMNAT, as well as between FMNATs from different eukaryotic organisms. Such analysis will address the fundamental question of how eukaryotic and bacterial FMNAT accomplish the same chemistry with different active site architectures. It will also benefit a structure-based

inhibitor development effort targeting bacterial FMNAT. We have determined the crystal structures of *Cg*FMNAT in three different complexed forms (with ATP, with substrate FMN and the ATP analog AMPCPP, and with products FAD and PP_i, respectively). These structures reveal a novel flavin-binding mode and the detailed catalytic site configuration that are likely shared among all eukaryotic FMNATs.

MATERIALS

ATP, AMPCPP (α,β-methyleneadenosine 5'-triphosphate), FMN, FAD, sodium pyrophosphate and all other reagents were purchased from Sigma-Aldrich Inc. (St Louis, MO), unless stated otherwise. Seed bead kit, and other materials and reagents used for crystallization, as previously stated in Chapter 2, were purchased from Hampton Research (Aliso Viejo, CA). The 96-well U-bottom plate manufactured by Nunc (Rochester, NY) was purchased from Fisher Scientific (Pittsburgh, PA). Media and columns used for purification, as stated in Chapter 2, were purchased from GE Healthcare (Piscataway, NJ).

METHODS

Expression and purification

The expression of *Cg*FMNAT and purification of apo-*Cg*FMNAT is described in Chapter 2. Protein eluted from Resource Q anion exchange column yielded two pools (**Fig. 2.3**). The first pool had a bright yellow color and was later shown to contain the *Cg*FMNAT-FAD complex. The second pool had a light yellow color and was used to obtain homogeneous apo-*Cg*FMNAT, as stated in Chapter 2. The final purification step for *Cg*FMNAT-FAD was gel filtration using a Superdex 75 16/60 gel filtration column equilibrated with gel filtration buffer (20 mM HEPES, pH 7.5, 150 mM NaCl, 5% glycerol and 1 mM DTT).

Crystallization

Crystallization set-up for *Cg*FMNAT-ATP and *Cg*FMNAT substrate ternary complexes were performed using 24-well plates and the hanging drop vapor diffusion method. A 100 mM ATP stock and a 50 mM FMN stock was prepared by dissolving each molecule in 20 mM HEPES, pH 7.5. A 200 mM AMPCPP stock was prepared by dissolving AMPCPP in ddH_2O (distilled-deionized H_20). The FMN stock was stored at 4 ºC for one day, and the ATP and AMPCPP stocks were stored at -20 ºC. To obtain *Cg*FMNAT-ATP complex, ATP at 10 mM final concentration was incubated with ~22 mg/ml protein on ice and placed in a 4 ºC cold room for 6 hours. The *Cg*FMNAT-ATP complex crystals were grown under similar conditions as those for apo-*Cg*FMNAT. Prism-shaped crystals of 0.20 x 0.09 x 0.09 mm^3 appeared within 2 days in 0.1 M sodium

acetate, pH 4.4–4.6 and 6–8% (w/v) PEG 4000. The *Cg*FMNAT substrate ternary complex was obtained by incubating 0.2 mM FMN and 5 mM AMPCPP with ~20 mg/ml protein on ice and placed in a 4 ºC cold room for 3 hours. Plate setup was at RT and the co-crystals of *Cg*FMNAT substrate ternary complex were grown at 20 °C under similar conditions as those for apo-*Cg*FMNAT, though consecutive streak-seeding procedure was performed in order to obtain single crystals. For the first and second streak-seeding rounds, the protein concentration was reduced to ~10 mg/ml and incubated with 0.2 mM FMN and 5 mM AMPCPP. Plate crystals of 0.15 x 0.15 x 0.05 mm^3 appeared after several days in 0.1 M sodium acetate, pH 4.6 and 8–10% (w/v) PEG 4000. All crystals were cryoprotected in a solution containing all the reservoir components, appropriate concentration of substrate(s) and increments of glucose [10%, 20% and 30% (w/v)], flash-frozen in liquid propane and stored in liquid nitrogen. For cryoprotecting the substrate ternary complex crystals, magnesium sulfate at 5 mM final concentration was added along with glucose.

Hampton HT screens Salt, Index and Crystal Screen were used to identify protein crystallization conditions for *Cg*FMNAT-FAD complex. Three hits were selected from Hampton Index and Crystal Screens for optimization: (1) 0.1 M sodium acetate, pH 4.6, 0.2 M ammonium sulfate and 30% (w/v) PEG MME 2000, (2) 0.1 M sodium cacodylate, pH 6.5, 0.2 M magnesium acetate and 20%

(w/v) PEG 8000 and (3) 0.1 M Tris, pH 8.5, 0.2 M lithium sulfate and 25% (w/v) PEG 3350 (**Fig. 3.1a and b**). The initial step for optimization of the crystallization conditions was to vary the reagents in 24-well plates using the hanging-drop and sitting-drop vapor diffusion method. Each plate was set-up by mixing 1.5 μl protein with equal volume of reservoir solution and equilibrated against the following reservoir conditions at 20 °C: (1) 0.1 M sodium acetate, pH 4.4−5.4, 0.2 M ammonium sulfate and 24−30% (w/v) PEG MME 2000, (2) 0.1 M sodium cacodylate, pH 5.4−7.4, 0.2 M magnesium acetate and 16−22% (w/v) PEG 8000, and (3) 0.1 M Tris, pH 7.3−8.8, 0.2 M lithium sulfate and 21−27% (w/v) PEG 3350. In parallel, different protein concentrations were tested at approximately 10 mg/ml, 20 mg/ml and 50 mg/ml, with better crystal growth occurring with ~20 mg/ml protein using the hanging-drop vapor diffusion method. Further optimization of crystallization conditions were performed according to a similar procedure as that for apo-*Cg*FMNAT, as described in Chapter 2, including MicroBatch crystallization[202] using 96-well U-bottom plates and micro-seeding using the Seed Bead kit. Optimizations, crystal quality and selection of cryoprotection were checked by several diffraction images collected in-house with X-ray from a rotating anode generator (Rigaku FRE SuperBright) and recorded on an RAXIS IV++ (Rigaku) image plate detector (**Fig. 3.2a and b**). The best crystals came from replacing the ammonium sulfate salt from the

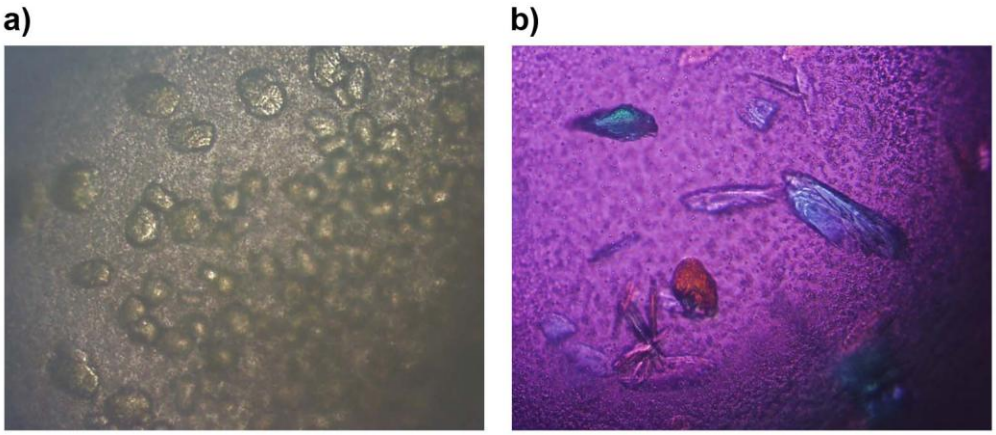

Figure 3.1 Initial crystallization conditions giving *Cg*FMNAT-FAD crystals. a) Rock-shaped crystals from 0.1 M sodium acetate, pH 4.6, 0.2 M ammonium sulfate and 30% (w/v) PEG MME 2000. b) Non-single crystals from 0.1 M sodium cacodylate, pH 6.5, 0.2 M magnesium acetate and 20% (w/v) PEG 8000 and viewed through a polarized lens. Images were taken at 10x magnification.

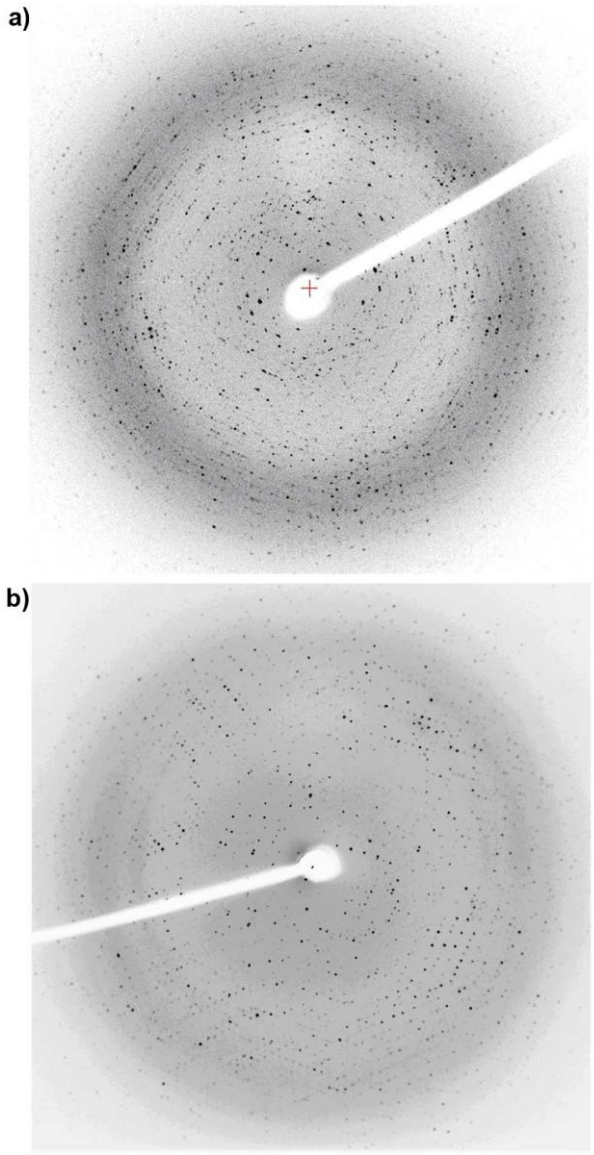

Figure 3.2 Diffraction images from two *Cg*FMNAT-FAD crystals. a) Diffraction image at 2.6 Å from a crystal obtained in 0.1 M sodium acetate, pH 4.8, 0.2 M magnesium sulfate and 26% (w/v) PEG MME 2000. b) Diffraction image at 2.6 Å from a crystal obtained in 0.1 M sodium acetate, pH 4.0, 0.2 M magnesium sulfate and 28% (w/v) PEG MME 2000 using the Microbatch method.

original condition [0.1 M sodium acetate, pH 4.6, 0.2 ammonium sulfate and 30% (w/v) PEG MME 2000] with 0.2 M magnesium sulfate. This condition produced non-single, hexagonal-shaped crystals of size 0.45 x 0.45 x 0.15 mm^3 (**Fig. 3.3a**) using the hang-drop or MicroBatch (100% paraffin oil) method. To obtain single uniformly packed crystals, 2 mM sodium pyrophosphate was incubated with ~20 mg/ml *Cg*FMNAT-FAD on ice and placed in a 4 ºC cold room overnight to yield *Cg*FMNAT product ternary complex prior to setting up crystallization trays. A 100 mM sodium pyrophosphate stock was prepared by dissolving sodium pyrophosphate in ddH_2O. The complex crystals were grown by mixing 1.5 µl *Cg*FMNAT-FAD-PP_i complex with 1.5 µl reservoir solution composed of 0.1 M sodium acetate, pH 4.4–5.4, 0.2 M magnesium sulfate and 20–26% (w/v) PEG MME 2000, and equilibrating against the reservoir at 20ºC. Thin plate crystal of 0.3 x 0.3 x 0.05 mm^3 appeared within 2 days in 0.1 M sodium acetate, pH 4.8, 0.2 M magnesium sulfate and 20–22% (w/v) PEG MME 2000 (**Fig. 3.3b**). Crystals were cryoprotected in a solution containing all the reservoir components, 2 mM sodium pyrophosphate and increments of glucose [10%, 20% and 30% (w/v)], flash-frozen in liquid propane and stored in liquid nitrogen.

Data collection, X-ray structure determination and refinement

The 1.35 Å *Cg*FMNAT product ternary complex data set was collected at beam-line 19-ID at the Advance Photon Source (APS), Argonne National

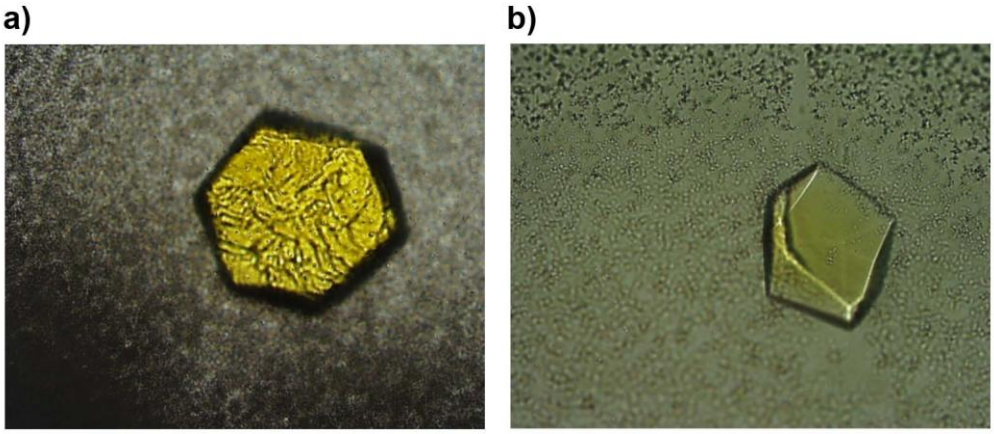

Figure 3.3 *Cg*FMNAT-FAD and ternary product complex crystals after optimization from the original hits. a) A non-single hexagonal crystal of size 0.45 x 0.45 x 0.15 mm^3 from 0.1 M sodium acetate pH 5.0, 0.2 M magnesium sulfate and 23% (w/v) PEG MME 2000. b) A single plate crystal of size 0.3 x 0.3 x 0.05 mm^3 from 0.1 M sodium acetate pH 4.8, 0.2 M magnesium sulfate and 20% (w/v) PEG MME 2000, obtained after incubating the protein with 2 mM pyrophosphate.

Laboratory, with two passes. The first pass was collected at low intensity using short exposure time to prevent individual spot overload on the detector at lower resolutions, and the second pass was collected with higher intensity and longer exposure time (**Fig. 3.4**). The frames collected from the two passes were scaled together and the resolution was cut-off at 1.35 Å during scaling, according to the criteria $I/\sigma \geq 2.0$ for the highest resolution shell. The *Cg*FMNAT-ATP complex data set at 1.87 Å and the 1.95 Å data set for the substrate ternary complex was collected in-house with X-ray from a rotating anode generator (Rigaku FRE SuperBright), recorded on an RAXIS IV++ (Rigaku) image plate detector. All data were processed with the HKL2000 package[203]. Data-collection statistics are presented in **Table 3.1**.

The initial phases of all complexes were determined by the molecular replacement method using the program MolRep[204] and the refined apo-*Cg*FMNAT as the search model. The refinements were performed using REFMAC[189] and manual model building was performed with Coot[190]. Refinement against the 1.35 Å product ternary complex data occurred in two stages in a similar manner as that for apo-*Cg*FMNAT described in Chapter 2. Anisotropic B-factors were analyzed by ANISOANL in the CCP4 package[181] and PARVATI server[191]. Water molecules were added by PHENIX[205] and manually inspected. The R_{work}/R_{free} for the final model of ATP binary complex, and substrate and

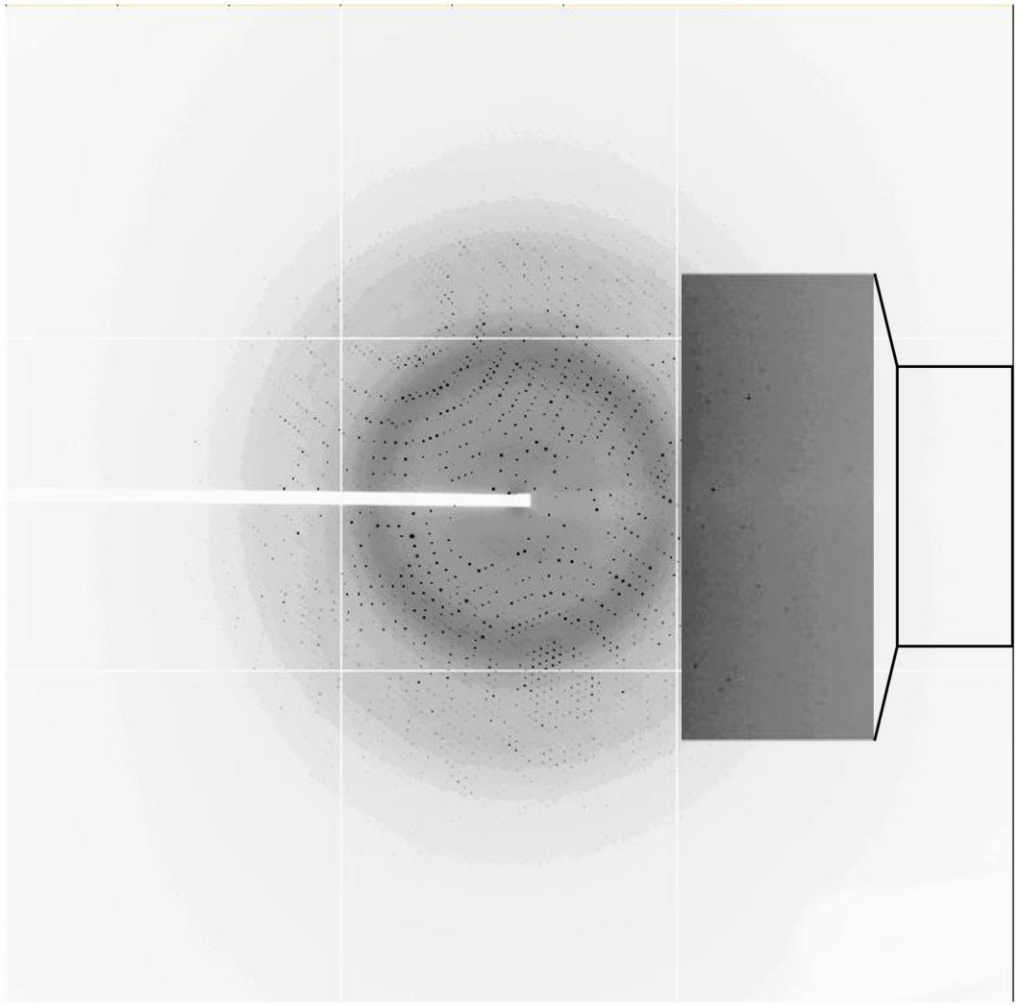

Figure 3.4 Diffraction image from product ternary complex crystal. Inset: An enlarged image from the small rectangle outlined in black lines shows diffraction spots near the 1.27 Å resolution edge.

product ternary complexes are 17.4%/22.2%, 17.5%/23.6% and 15.3%/18.7%, respectively. The models were assessed by MolProbity[192] and complete refinement statistics are listed in **Table 3.1**.

All images of structures, ligands, electron density and electrostatic surface potentials were generated using *i*PyMol (http://www.pymol.org). The pdb2pqr server[193] was used to generate a pqr file using PARSE atomic radii and charges[194]. Electrostatic surface potentials were calculated using APBS[195] plugin for PyMol using the default settings, with a monovalent cation and anion concentration of 0.15 M and the potential ramped between -5 kT/e (red) and +5 kT/e (blue). Structure-based alignment was performed using Secondary Structure Matching[196]. Adobe Creative Suite 2 (http://www.adobe.com) was used to label and format images.

Table 3.1. Data Collection and Refinement Statistics

Protein	**ATP complex**	**Ternary complex with substrates**	**Ternary complex with products**
Space Group/Monomer per Asymmetric Unit	$P3_221/1$	C2/6	C2/6
Data	Native	Native	Native
Wavelength (Å)	1.54178	1.54178	0.97874
Resolution (Å)	50.0-1.87	50.0-1.95	50.0-1.35
Unit cell dimensions			
a, b, c (Å)	79.79, 79.79, 77.94	207.83, 81.75, 136.70	206.58, 81.48, 136.60
α, β, γ (º)	90.0, 90.0, 120.0	90.0, 129.67, 90.0	90.0, 129.79, 90.0
Total no. of reflections	124769	312183	2800906
No. of unique reflections	24161	123738	380943
% Completeness	99.9 (99.6)[a]	96.4 (97.1)	100 (99.8)
R_{sym}[b]	0.078 (0.549)	0.088 (0.447)	0.077 (0.551)
I/σ	22.0 (2.5)	11.5 (2.1)	35.9 (2.4)
Mosaicity (º)	0.7	0.5	0.4
Model Refinement	Isotropic	Isotropic	Anisotropic[e]
Resolution range (Å)	50.0-1.87	35.1-1.95	32.2-1.35
R_{work}[c] (%)	17.4	17.5	15.3
R_{free}[d] (%)	22.2	23.6	18.7
No. of protein atoms	2397	14700	14968
No. of ligand atoms	44	397	417
No. of water molecules	303	1790	1870
Average B-factor ($Å^2$)			
Protein atoms	19.3	18.2	17.1
Ligand atoms	23.5	17.5	15.8
Water molecules	30.8	28.5	30.4
Rmsd bond length (Å)	0.015	0.014	0.014
Rmsd bond angle (º)	1.536	1.458	1.523
Ramachandran Plot			
% favored region	98.6	98.9	99.1
% allowed region	1.05	1.1	0.9
% outliers	0.35	0.0	0.0

[a]Values in parenthesis are for highest-resolution shell.
[b]$R_{sym} = \Sigma_{hkl} [(\Sigma_j (|I_j - \langle I \rangle|) / \Sigma_j I_j]$. $\langle I \rangle$ is the average for all *j* measurements of reflection *hkl*.
[c]$R_{work} = \Sigma_{hkl} |F_o - F_c| / \Sigma_{hkl} |F_o|$, where F_o and F_c are the observed and calculated structure factors, respectively.
[d]R_{free} calculated from randomly selected 5% reflections that is excluded from refinement for cross-validation.
[e]Six anisotropic displacement parameters are used for selected atoms, while isotropic B-factors were used for remaining atoms. Anisotropic displacement parameters were evaluated and assigned using PARVATI and ANISOANL.

RESULTS

Quality of *Cg*FMNAT complex structures

The *Cg*FMNAT-ATP complex crystal is isomorphous to the apo-*Cg*FMNAT in space group $P3_221$, with the model refined using data to a resolution of 1.87 Å. This model contains residues -3–83 and 103–304 with an average B-factor of 19.3 $Å^2$ (**Fig. 3.5**). The bound ATP molecule has well defined electron density (**Fig. 3.6a**). Crystals of the substrate and product ternary complexes are isomorphous to each other and exhibit the symmetry of space group C2. They were refined using data to resolutions of 1.95 Å and 1.35 Å, respectively, with six monomers in the asymmetric unit. For the substrate ternary complex, the densities for AMPCPP and Mg^{2+} ion are well defined and double conformations of the AMPCPP phosphate tail are observed (**Fig. 3.6b**). The density for the phosphoribityl tail of FMN, on the other hand, is discontinuous, indicating significant conformational flexibility (**Fig. 3.6b**). For the product ternary complex, the densities for both products FAD and pyrophosphate are well defined (**Fig. 3.6c**). In addition to the ordered water molecules, four sulfates and one glucose molecule were modeled. The monomers of the substrate and product ternary complex have an average B-factor range of 15.6–20.8 $Å^2$ (**Fig. 3.7**) and 15.1–20.4 $Å^2$ (**Fig. 3.8**), respectively. The flexible loop region (residues 84–100), referred to as SQFD-loop, disordered in the apo- and ATP-complexed

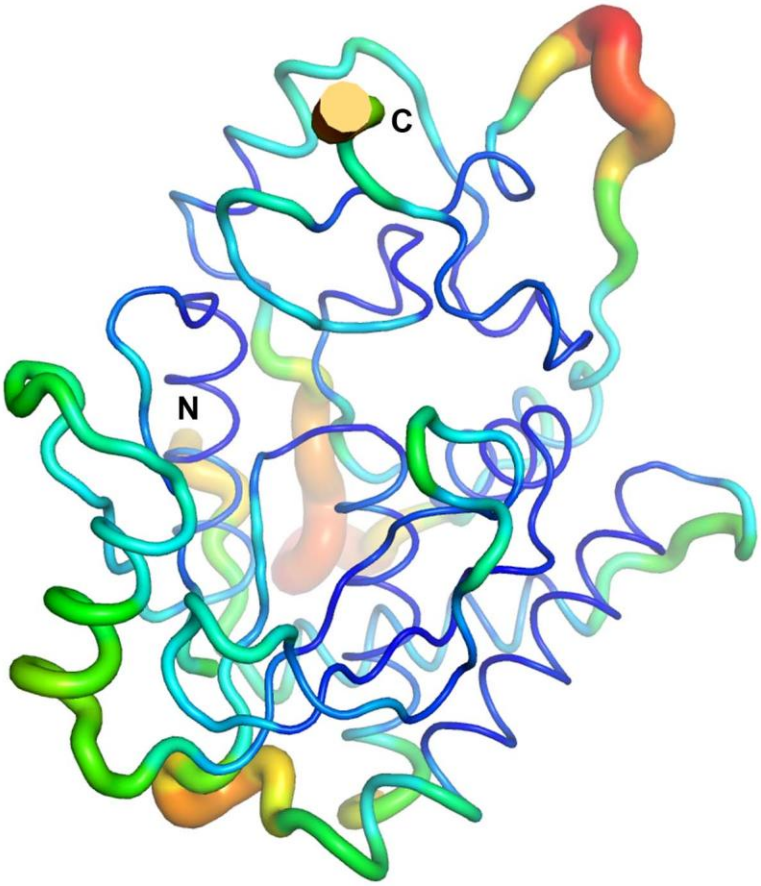

Figure 3.5 Cartoon putty of *Cg*FMNAT-ATP complex. The putty width becomes wider with an increase in B-factor. The color is ramped from blue to red, with blue being the lowest B-factor and red the highest B-factor. The lowest main chain B-factor for a residue is 11.2 $Å^2$ and the highest is 41.1 $Å^2$. Including the main chain and side chain for each residue the lowest B-factor is 11.5 $Å^2$ and the highest is 43.2 $Å^2$, and the average is 19.3 $Å^2$.

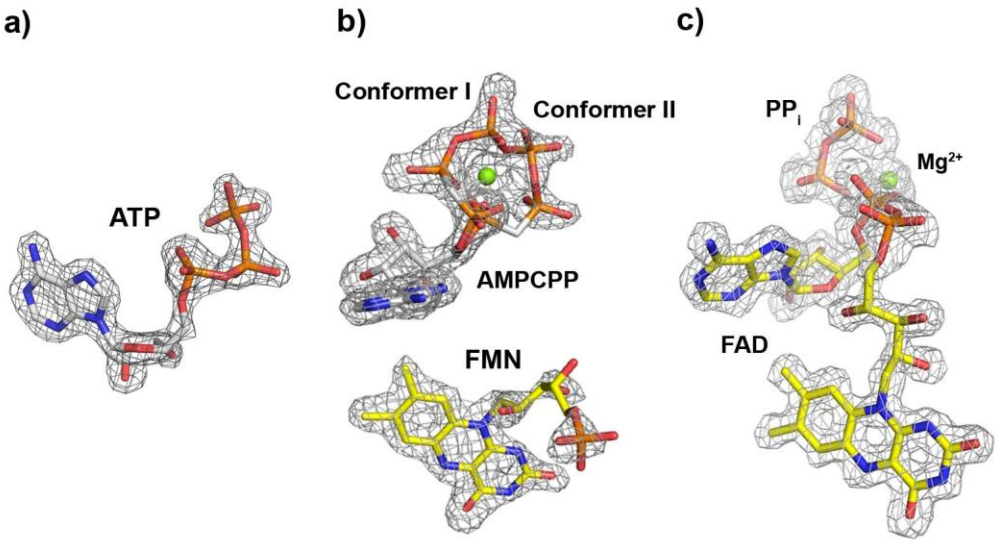

Figure 3.6 Electron densities of the bound ligands. Simulated-annealing F_o-F_c omit maps of a) ATP in the binary complex; b) AMPCPP and FMN from the substrate ternary complex, and c) FAD and PP_i from the product ternary complex. The maps are contoured at 3.0σ for a) and c), and 2.5σ for b). Atoms are colored by atom type, carbon atoms of ATP and AMPCPP are colored white, and FMN and FAD carbon atoms are colored yellow. Magnesium ion is shown as a green sphere.

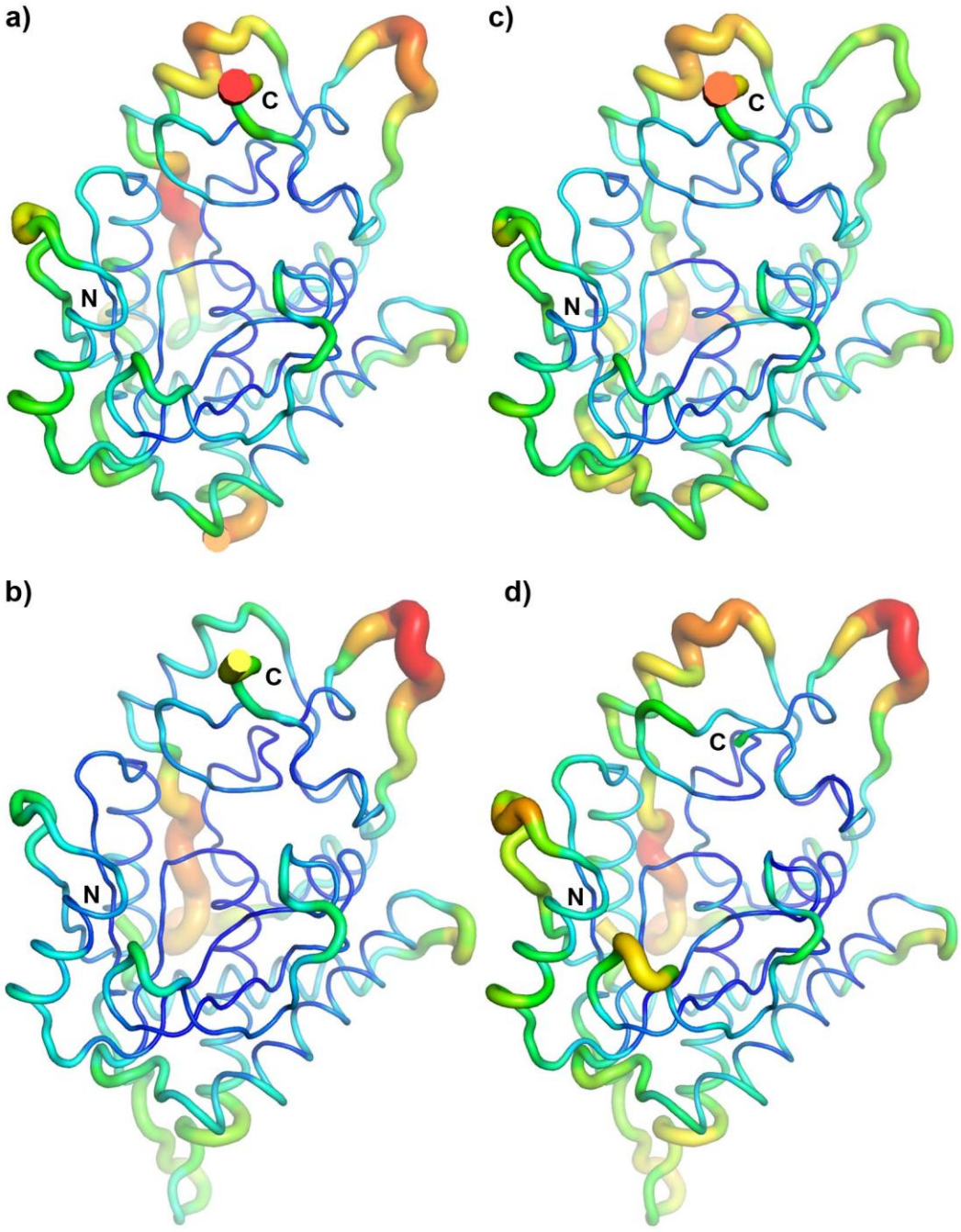

Figure 3.7 Cartoon putty representation of the six monomers of the substrate ternary complex colored and scaled by B-factor.

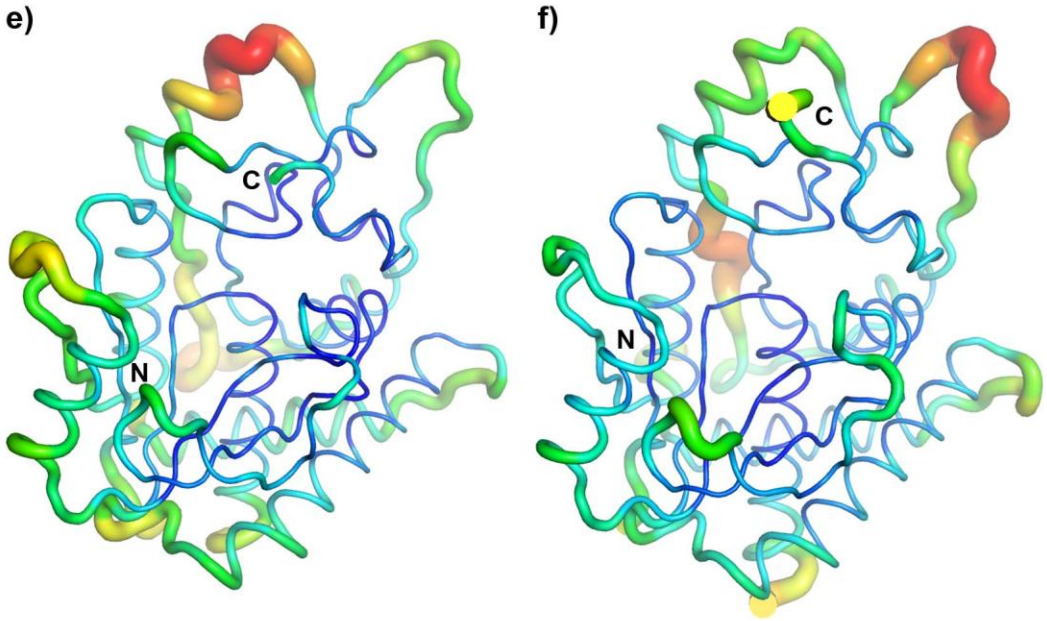

Figure 3.7 (continued) Cartoon putty representation of the six monomers of the substrate ternary complex colored and scaled by B-factor. The putty width becomes wider with an increase in B-factor, with blue being the lowest B-factor and red the highest B-factor. For each monomer the average B-factor is listed first followed by the lowest and highest B-factor for main chain only, then main chain and side chain combined. a) Monomer A 15.6 $Å^2$, 6.9/38.2 $Å^2$ and 6.5/39.8 $Å^2$. b) Monomer B 18.7 $Å^2$, 8.2/53.5 $Å^2$ and 8.5/54.0 $Å^2$. c) Monomer C 18.1 $Å^2$, 8.2/40.3 $Å^2$ and 8.3/41.8 $Å^2$. d) Monomer D 18.4 $Å^2$, 8.1/42.8 $Å^2$ and 7.9/43.2 $Å^2$. e) Monomer E 20.8 $Å^2$, 10.3/47.7 $Å^2$ and 10.3/49.0 $Å^2$. f) Monomer F 17.8 $Å^2$, 6.3/50.1 $Å^2$ and 6.4/50.5 $Å^2$.

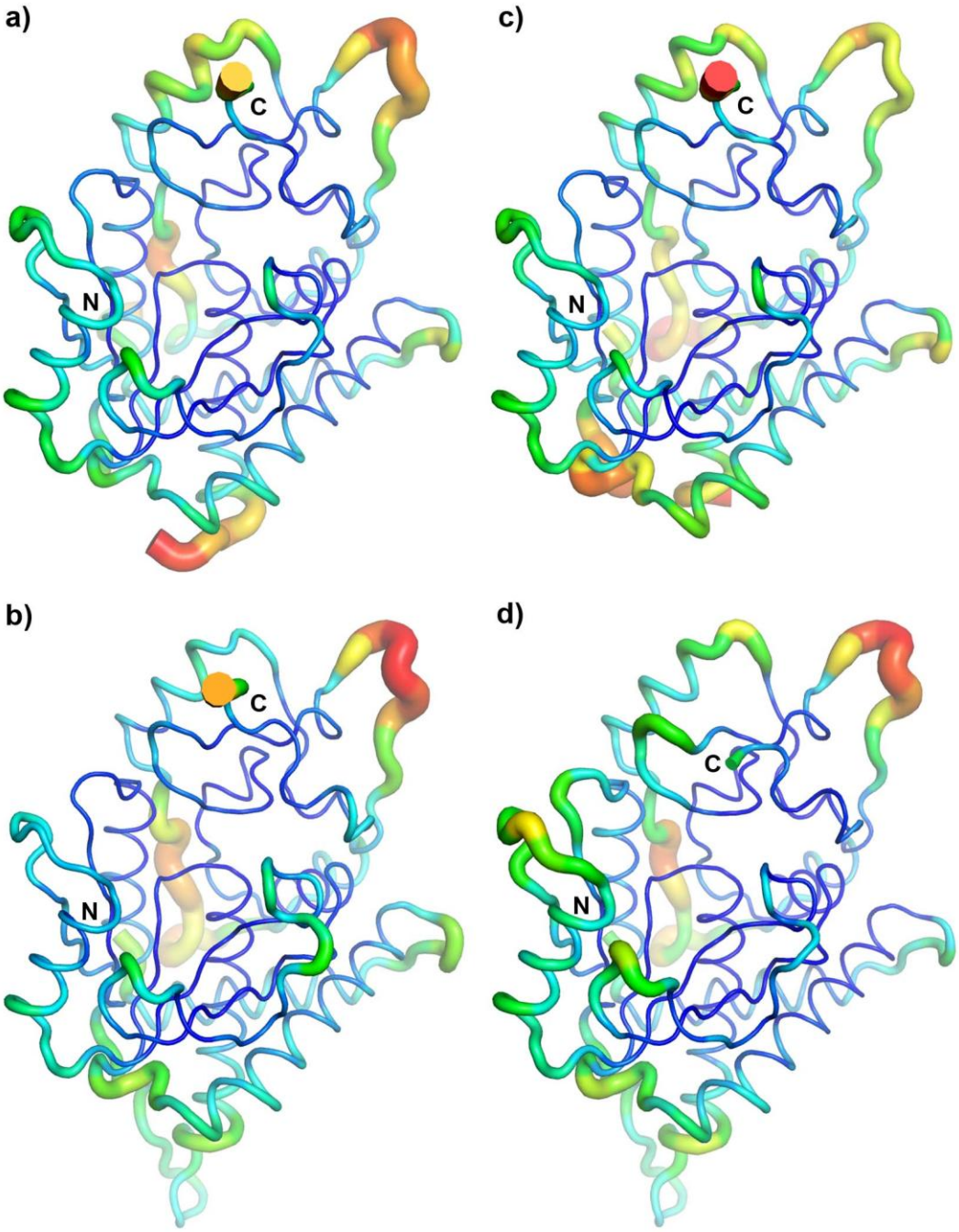

Figure 3.8 Cartoon putty representation of the six monomers of the product ternary complex colored and scaled by B-factor.

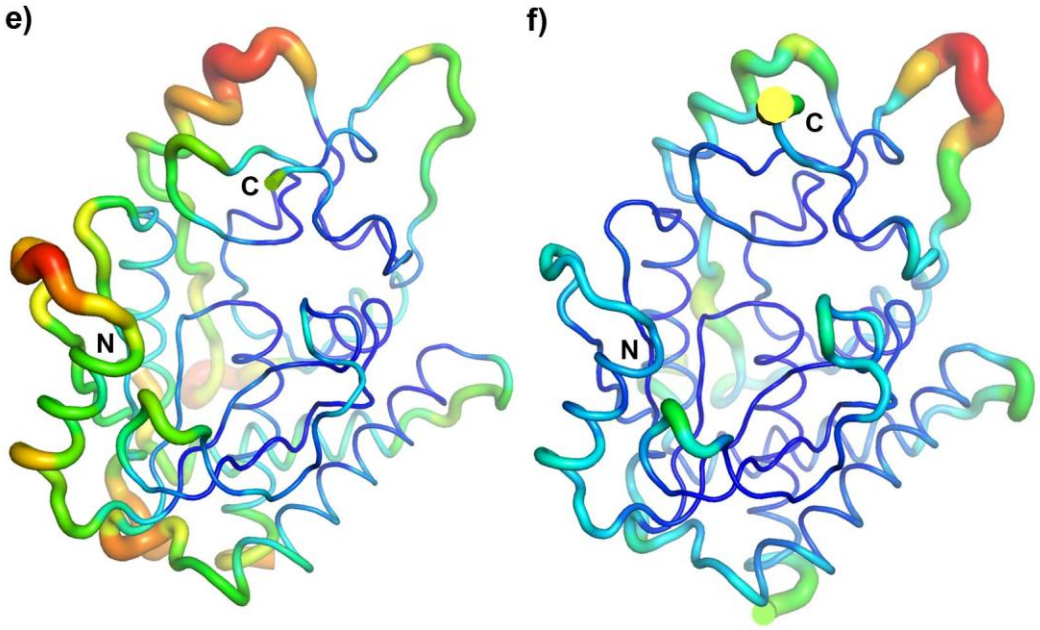

Figure 3.8 (continued) Cartoon putty representation of the six monomers of the product ternary complex colored and scaled by B-factor. The putty width becomes wider with an increase in B-factor, with blue being the lowest B-factor and red the highest B-factor. For each monomer the average B-factor is listed first followed by the lowest and highest B-factor for main chain only, then main chain and side chain combined. a) Monomer A 15.1 $Å^2$, 7.3/38.4 $Å^2$ and 7.3/38.3 $Å^2$. b) Monomer B 18.2 $Å^2$, 8.6/48.3 $Å^2$ and 8.6/49.3 $Å^2$. c) Monomer C 17.0 $Å^2$, 8.9/34.9 $Å^2$ and 9.1/37.6 $Å^2$. d) Monomer D 16.8 $Å^2$, 8.1/43.7 $Å^2$ and 8.4/45.3 $Å^2$. e) Monomer E 20.4 $Å^2$, 10.2/40.5 $Å^2$ and 10.3/42.3 $Å^2$. f) Monomer F 15.4 $Å^2$, 7.6/47.0 $Å^2$ and 7.6/47.9 $Å^2$.

*Cg*FMNAT structures, is ordered in two of the six crystallographically independent *Cg*FMNAT monomers in the ternary complexes, presumably due to crystal-packing interactions (**Fig. 3.9**). Residues modeled for the six crystallographically independent monomers of the substrate ternary complex are: monomer A from -3–87 and 100–304; monomer B from 0–304; monomer C from 0–83 and 98–304; monomer D from 0–300; monomer E from 1–83 and 98–300, and monomer F from -3–87 and 99–304. Similarly, product ternary complex modeled residues are: monomer A from -3–89 and 99–304; monomer B from 0–304; monomer C from 0–84 and 98–304; monomer D from 0–300; monomer E from 0–84 and 98–300, and monomer F from -3–87 and 99–304. For all models the main chain dihedral angles (ϕ, ψ) for all residues are in the allowed Ramachandran area. The exception is Gly224, as identified by Molprobity[206] in the ATP binary complex structure, which is associated with well defined electron density. A number of side chain and main chain double conformations were clearly observable in all structure complexes and are listed in **Table 3.2**. All the double conformations occur at the solvent accessible region of *Cg*FMNAT. Relevant residue double conformation will be further discussed in the following sections.

Additional small molecules were present in the ATP binary and substrate ternary complex. For the ATP binary complex a pyrophosphate (PP_i) molecule

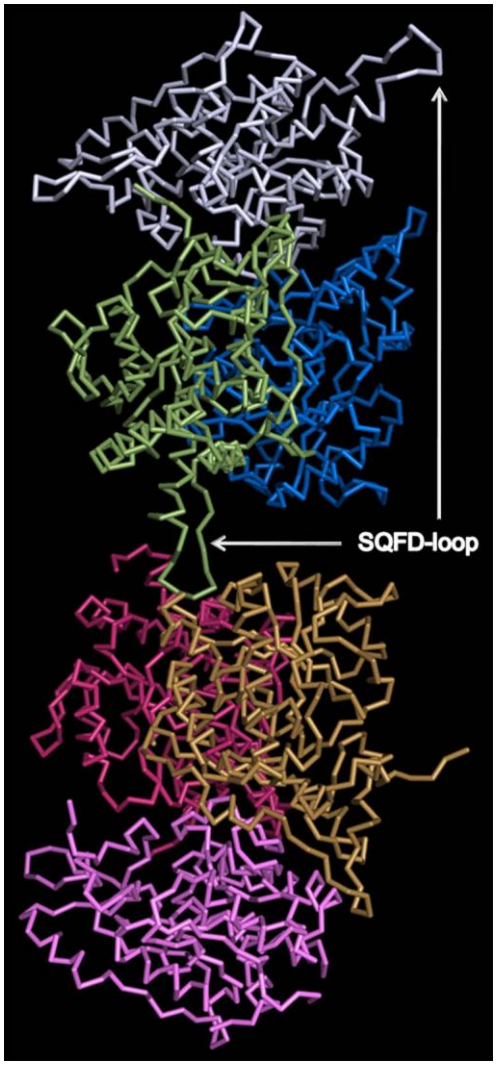

Figure 3.9 View of the six crystallographically independent *Cg*FMNAT product ternary complex monomers. Each monomer is colored differently. The SQFD-loop is ordered in monomer B and D and is indicated by white arrows.

Table 3.2. Double Conformations in *Cg*FMNAT Complexes							
Residue	**ATP complex**	**Substrate ternary complex[1]**	**Product ternary complex**	***apo*-form[2]**	**Binding Site**	**MC/SC[3]**	**SS[4]**
Ser15			D		No	SC	H (α1)
Ser16			A,B,C	✓	No	SC	H (α1)
Ser40	✓		C,F	✓	No	SC	H (α2)
Ser58		A,C,F	A,B,C,D,E,F	✓	Yes	SC	S (β1)
Ser60		A,B,C,D,F	A,B,C,D,E,F		Yes	SC	S (β1)
Cys67	✓				Yes	SC	H (α3)
Ser76			D		No	SC	H (α3)
Leu78			B,D		No	SC	H (α3)
Leu103			E	✓	No	SC	S (β2)
Glu118			D		No	SC	H (α4)
Ser125		C,E	A,B,C,E,F		No	SC	H (α4)
Leu126			A,F		No	SC	H (α4)
Arg137			B,C,D,F		No	SC	L
Asp138			F		No	MC	L
Lys139			F	✓	No	MC	L
Cys140		A,B,F	A,B,C,F		No	SC	L
Lys158	✓			✓	No	SC	L
Glu172			F		No	MC	L
His173			D,E,F		No	MC/SC	L
Lys175			A,B	✓	No	SC	L
Asp181			D,E,		Yes	SC	L
Asn197		A,E	A,D,E		No	SC	L
Glu214			A,B,C,F	✓	No	SC	H (α7)
Ser222	✓			✓	Yes	MC/SC	L
Leu223	✓				Yes	MC	L
Gly224	✓				Yes	MC	L
Val226			A,B,E,F		No	SC	L
Glu227			B		No	SC	L
Asp238			A		No	SC	L
Glu249			A,D	✓	No	SC	H (α8)
Arg255			A,C		No	SC	L
His258			B,C		No	SC	L
Asp271	✓			✓	No	SC	H (α9)
Glu272			A,B,E,F		No	SC	H (α9)
Leu280			A,E		No	MC/SC	H (α9)
His281			A,E		No	MC/SC	L
Glu282			E		No	MC	L
Arg297			A,B,C,D,F		Yes	SC	L
Ala298			B		No	MC	L
Gly299			B		No	MC	L
Arg300			B	✓	No	MC	L

[1]Monomers are listed for substrate and product ternary complexes.
[2]Double conformations presented in Chapter 2.
[3]MC stands for main chain and SC stands for side chain.
[4]SS stands for secondary structure.

molecule and an acetate molecule were modeled. For the substrate ternary complex a sulfate molecule was modeled. The presence of PP_i in the ATP binary complex is possibly derived from hydrolysis of ATP. Determination of the identities of the small molecules was based on known components from the crystallization solution fitting to the electron density and neighboring interactions.

Comparison of *Cg*FMNAT complex structures

Superposition of the equivalent C_α backbones of monomers B through F to monomer A of the substrate ternary complex gives a pair-wise root mean square deviation (rmsd) of 0.40 Å, 0.39 Å, 0.50 Å, 0.46 Å and 0.30 Å; and monomers B through F to monomer A of the product ternary complex gives 0.51 Å, 0.40 Å, 0.49 Å, 0.46 Å and 0.27 Å (**Fig. 3.10**), indicating the monomers in the asymmetric unit are identical to each other. A closer examination of these superpositions reveals conformational flexibility in loop regions, such as the SQFD-loop and near the C-terminus. The last five residues in monomer D and E of both ternary complexes are disordered and not modeled. Superposition of the equivalent C_α backbones of apo-protein, ATP binary complex and substrate ternary complex (monomer C) to product ternary complex (monomer B) gives a pair-wise rmsd of 0.42 Å, 0.41 Å, and 0.27 Å, respectively, also indicating no substantial global conformational changes among different structural states of *Cg*FMNAT (**Fig. 3.11**).

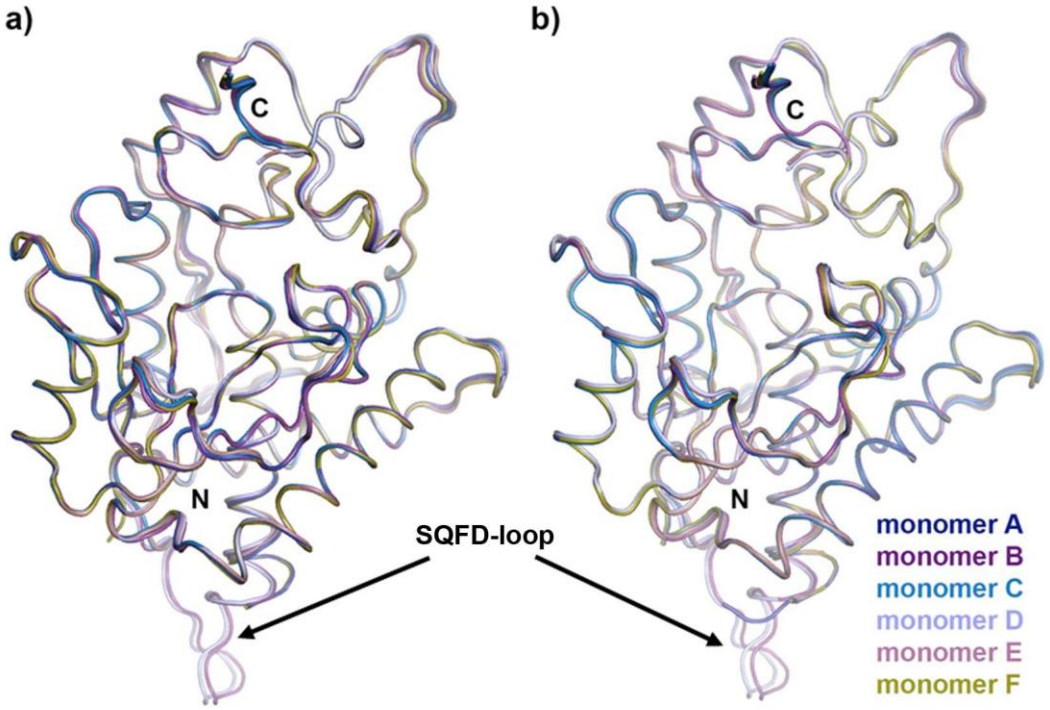

Figure 3.10 Comparison of monomers from *Cg*FMNAT ternary complexes. The six monomers in the asymmetric unit are colored differently. a) Substrate ternary complex monomers with pair-wise root mean square deviations (rmsd) of 0.40 Å, 0.39 Å, 0.50 Å, 0.46 Å and 0.30 Å, respectively. b) Product ternary complex monomers with pair-wise rmsd of 0.51 Å, 0.40 Å, 0.49 Å, 0.46 Å and 0.27 Å, respectively.

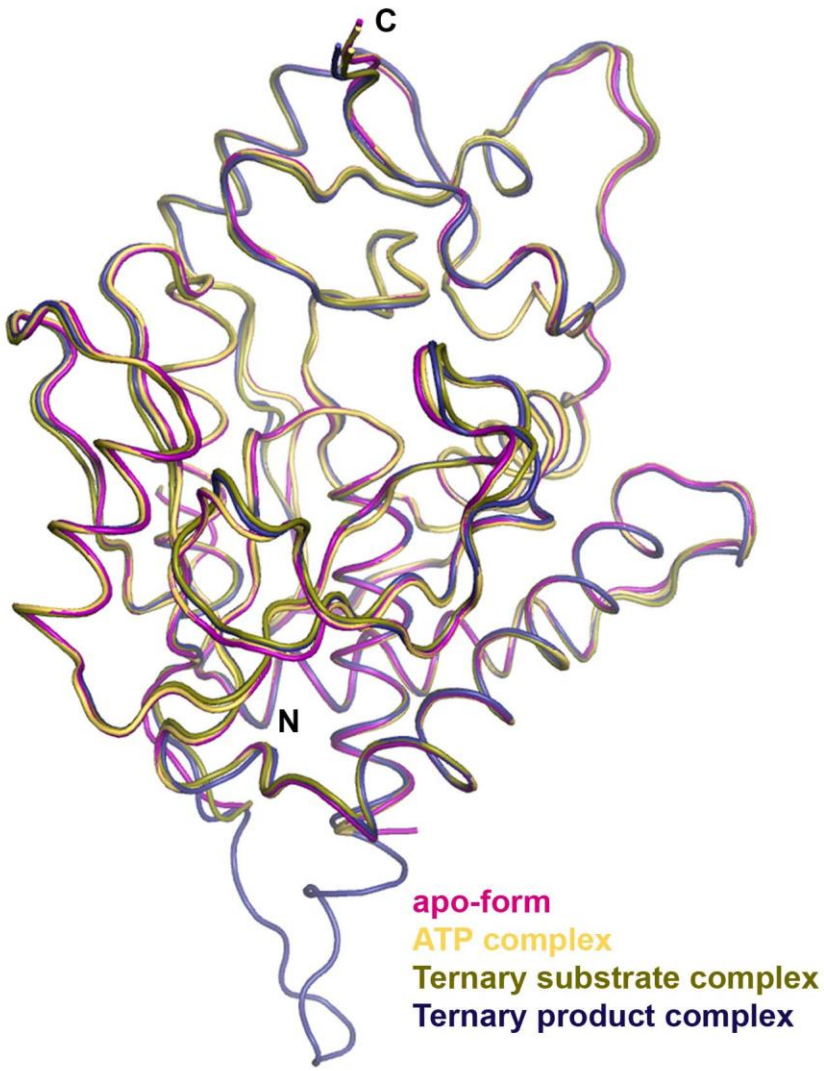

Figure 3.11 Comparison of *Cg*FMNAT structures. Superposition of apo-form (magenta), ATP complex (tan) and substrate ternary complex monomer C (dark yellow) to product ternary complex monomer B (dark blue) gives a pair-wise rmsd of 0.42 Å, 0.41 Å, and 0.27 Å, respectively.

A majority of the loop regions that display conformational changes in the superposition, tend to have higher B-factors, as shown with the B-factor putty (**Fig. 2.7, 3.5, 3.7, and 3.8**). Examples include the loop connecting α1 to α2, part of the SQFP-loop and the loops of the C-terminal domain. Additional regions that have higher B-factors, but do not show conformational changes from the superposition, are helix α5 and α9. Most of these observations are consistent across the different space groups, as well as between monomers of the same and different ternary complexes. Given the resolution for each structural state of *Cg*FMNAT, the B-factors may correlate to conformational flexibility, thus providing more information on the structure of *Cg*FMNAT.

The loop connecting helix α3 to strand β2 is referred to as the SQFD-loop due to the conserved sequence SQFD in *Saccharomycetaceae* family of yeasts including *C. glabrata* and *S. cerevisiae*[207,208]. This loop is disordered in the apo- and ATP-*Cg*FMNAT binary complex structures (**Fig. 3.11**), but becomes ordered in two of the six crystallographically independent monomers in the ternary complexes (**Fig. 3.10**). The tip of each loop containing the SQFD sequence packs inside a cavity that is formed in part by helix α3 and portions of the SQFD-loop of an adjacent monomer (**Fig. 3.12a**). The nature of the packing leads to the burying of the SQFD hydrophobic residue Phe91 from the solvent, and formation of intramolecular and intermolecular hydrogen bonds within the ordered loop and

with the adjacent monomer, respectively (**Fig. 3.12a and b**). In retrospect, the cavity is present in all *Cg*FMNAT structures with a disordered SQFD-loop, therefore the formation of the interactions leading to an ordered SQFD-loop are presumably due to crystal-packing.

Although the superposition of the equivalent C_α backbones of apo-form, ATP binary complex and ternary complexes reveal no significant conformational changes beyond loop flexibility, inspection of the molecular surfaces and electrostatic potentials provides additional details. Orienting the C-terminal domain as in Chapter 2 for the apo-form (**Fig. 2.10**) reveals variations of the negatively charged pocket, with the exception of the ATP binary complex **(Fig. 3.13),** which is the same as the apo-*Cg*FMNAT. In particular, the pocket opening increases for five of the independently modeled six monomers of the substrate and product ternary complexes (**Fig. 3.14 and 3.15**). Additionally, in the product ternary complex the area of the positive surface potential reduces and a negative surface potential develops, with the two charged surfaces separated by the formation of a neutral surface potential (**Fig. 3.15**). Evaluation of the superposition indicates side chain conformational change and loop flexibility alters the width and surface potentials of the pocket (**Fig. 3.16**). It is notable that these changes are specific for different states of *Cg*FMNAT (apo-form and ternary complexes) and are not artifacts of crystallization. Therefore, these

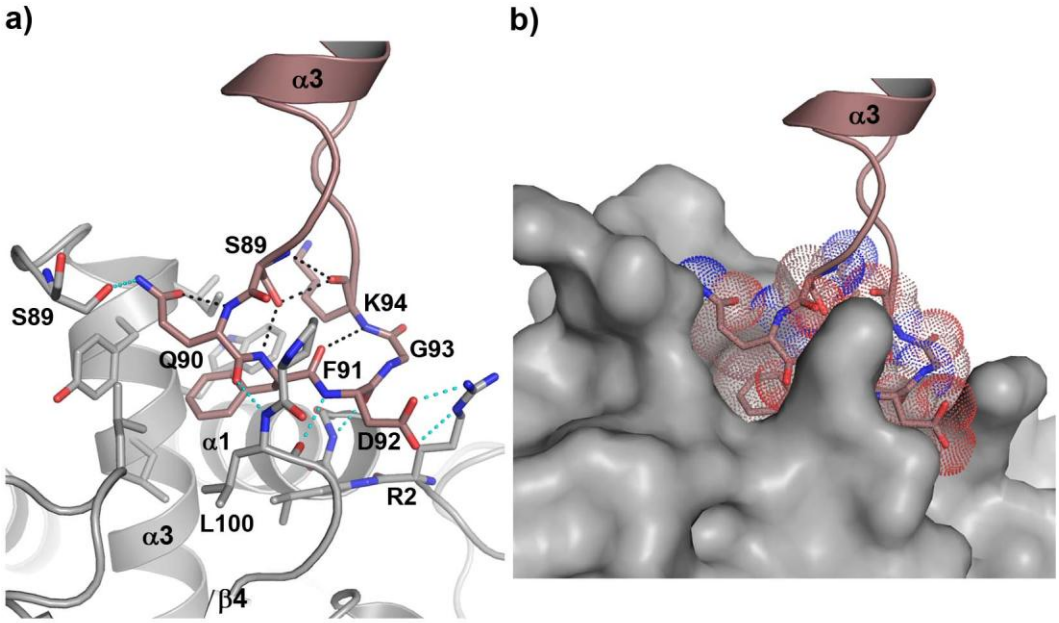

Figure 3.12 SQFD-loop interacting with another monomer. a) Residues of the SQFD-loop from monomer B interacting with residues of monomer A are shown as sticks and colored by atom type, with carbon atoms colored raspberry in monomer B and gray in monomer A. Monomer B SQFD-loop intramolecular and intermolecular hydrogen bonds are shown as black dash lines and cyan dash lines, respectively. Select residues are numbered for reference. b) Residues of the SQFD-loop from monomer B are shown as sticks with dotted spheres and monomer A is shown as a gray molecular surface.

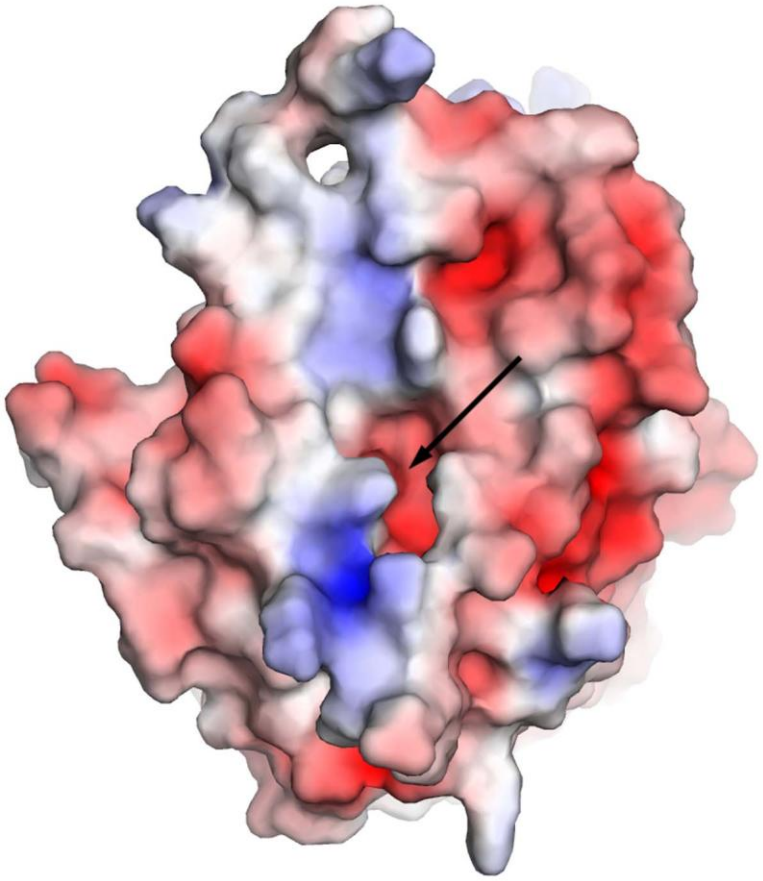

Figure 3.13 Electrostatic surface potential of *Cg*FMNAT ATP binary complex. The C-terminal domain is oriented in a manner to place the flat surface parallel to the page and reveals a positively charged channel disrupted by a negatively charged pocket, indicated by a black arrow, formed by the C-terminal domain.

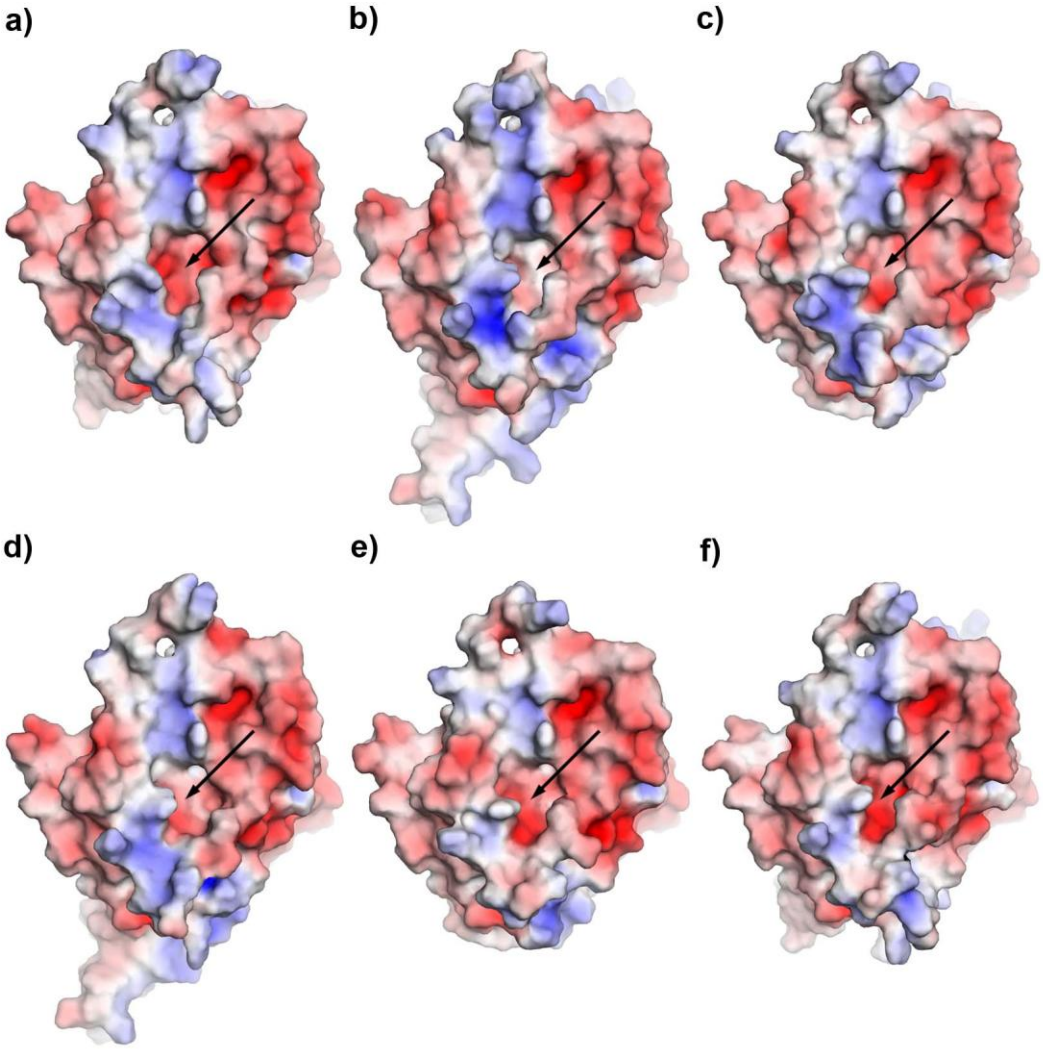

Figure 3.14 Electrostatic surface potential of the six monomers of *Cg*FMNAT substrate ternary complex. The C-terminal domain is in the same orientation as in Fig. 3.13. The opening of the pocket, as indicated by an arrow for each independently modeled monomer, is wider than the apo-form and ATP binary complex.

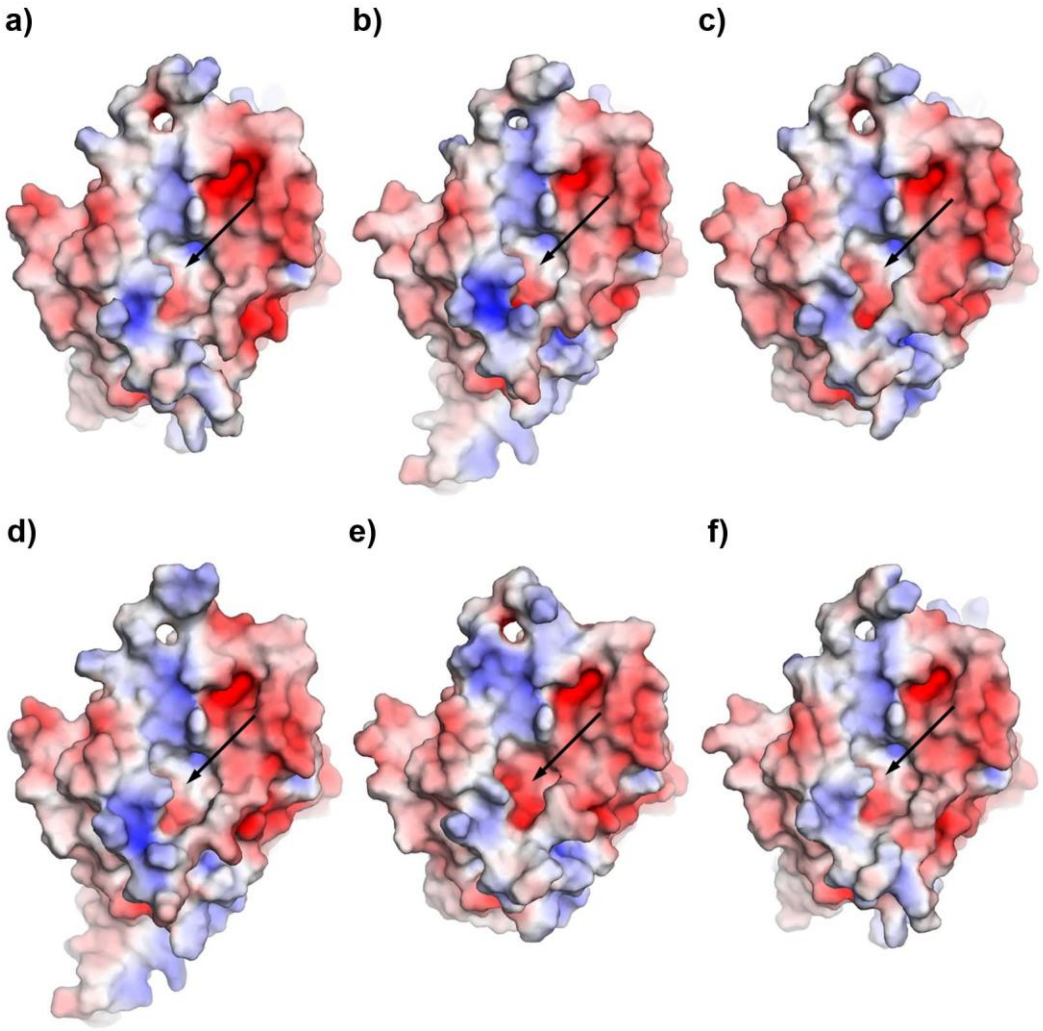

Figure 3.15 Electrostatic surface potential of the six monomers of *Cg*FMNAT product ternary complex. The C-terminal domain is in the same orientation as in Fig. 3.13. The opening of the pocket, as indicated by an arrow for each independently modeled monomer, is similar to the substrate ternary complex.

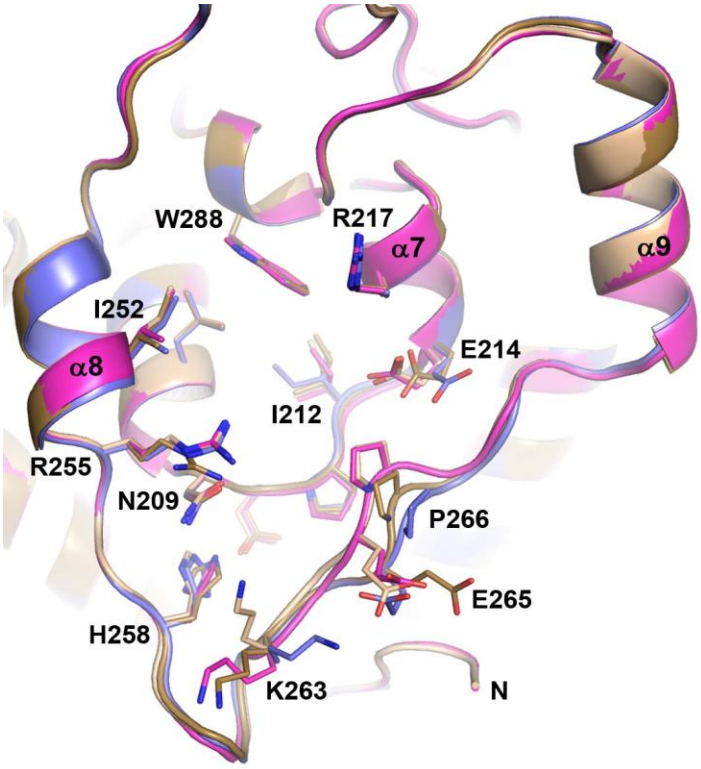

Figure 3.16 Comparison of *Cg*FMNAT C-terminal domains. Superposition of apo-form (magenta), ATP complex (tan) and substrate ternary complex monomer C (dark yellow) to product ternary complex monomer B (dark blue) provides insight into the variation of the pocket size and charge. The pocket size and charge are affected by loop flexibility and side chain conformation.

changes could potentially be relevant to the biological function of *Cg*FMNAT as the pocket is on the opposite side of the substrate binding site.

Substrate binary and ternary complexes - ATP binding site

The structures of the *Cg*FMNAT-ATP binary complex and the substrate ternary complex reveal details about the interactions between the enzyme and the substrates. Five structural motifs are identified to be involved in ATP and Mg^{2+} binding (**Fig. 3.17**). As discussed in the previous chapter, the *PP-loop* motif, extending from β1 to the N-terminus of α3, has the sequence of $^{60}SYNGGKDC_{67}$ and is generally conserved in the superfamily[142]. The *ADE motif*, named for ADEnine binding, corresponds to the LDTG motif in APS reductase[138] and consists of a short stretch of four residues, $^{107}FIDH_{110}$, following strand β2. The first arginine-containing *ARG1 motif* (named Arg-loop in ref. 136) is located in the loop connecting β4 to β5 and consists of residues $^{163}GIRHTD_{168}$. The complexes further highlighted two additional nucleotide binding motifs. The *γ-phosphate motif* encompasses part of α7 and the following hairpin loop from the C-terminal domain situated above the nucleotide binding site. Near the C-terminus of the protein, another arginine-rich motif, *ARG2*, of sequence $^{296}ERAGR_{300}$ is also involved in nucleotide binding.

With the substrate ternary complex obtained in the presence of Mg^{2+} providing more information about the nucleotide binding site than the Mg^{2+}-free

ATP binary complex, the binding site will be discussed mostly in the context of the ternary complex and compared to ATP binary complex (**Fig. 3.18a**). For simplicity, the AMPCPP phosphoryl groups will be referred to as α-, β- and γ-phosphates. The AMPCPP nucleotide adopts an anti-conformation with a 3'-endo ribose pucker, and lies in the crevice formed by β1 and β4, with its βγ-phosphate tail positioned in the anion-binding pocket near the N-terminus of α3 (**Fig. 3.18b and Fig. 3.19a and b**). A different configuration of the βγ-phosphate tail is observed in the ATP binary complex, which remains positioned in the same anion pocket (**Fig. 3.18a**). In the apo-*Cg*FMNAT structure a chloride ion, presumably recruited from the crystallization medium, occupies this pocket (**Fig. 3.18c**). A hydrogen-bond network is formed between AMPCPP and residues from four of the six motifs (**Fig. 3.18b**), that include the PP-loop, ADE, ARG1, and γ-phosphate motifs. The adenine N1 nitrogen and N6 amino groups are hydrogen bonded to the main chain amide and carbonyl of Ile108 (part of the ADE motif), respectively. The N3 of adenine forms a hydrogen bond to the side chain of Ser60 of the PP-loop motif, while the O2' hydroxyl of AMPCPP ribose interacts with the main chain carbonyl and an alternate side chain conformation of Ser60. The O2' hydroxyl forms another hydrogen bond with the main chain amide of Gly163 of the ARG1 motif, which no longer has double conformations upon nucleotide binding. The phosphates of AMPCPP interact extensively with the PP-loop motif.

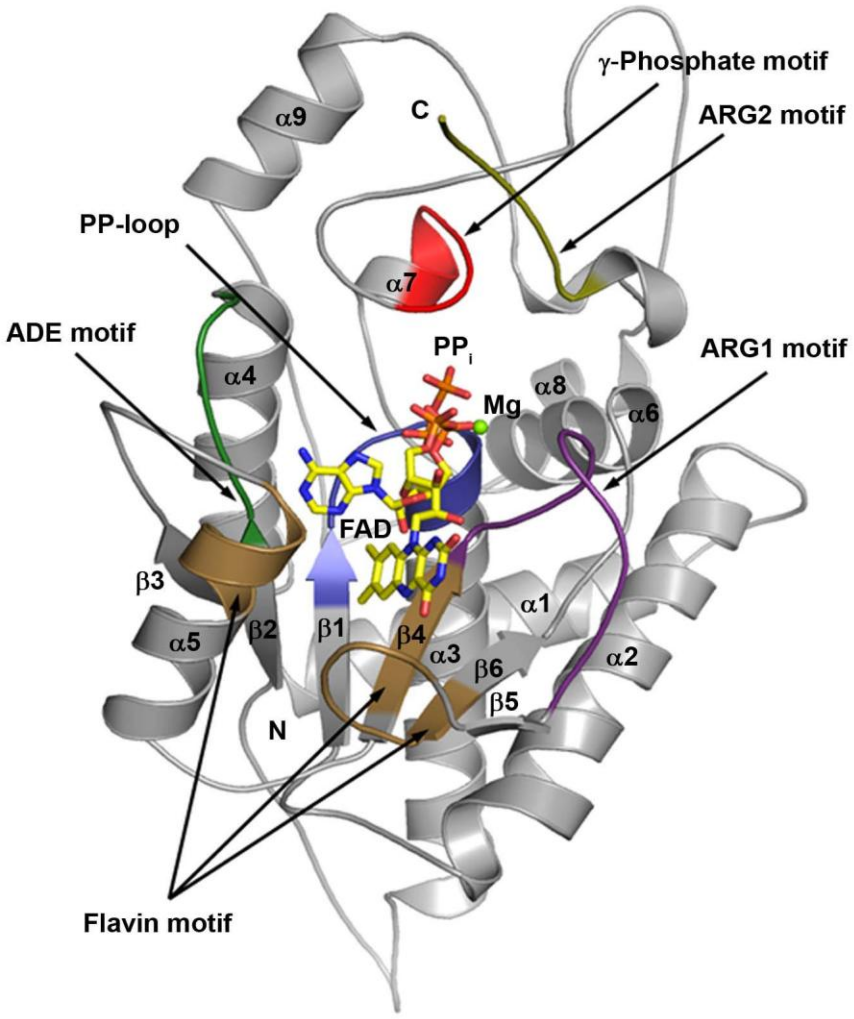

Figure 3.17 Ribbon diagram of *Cg*FMNAT in complex with the products FAD, PP_i, and Mg^{2+}. Secondary structure elements are labeled. Structure motifs involved in substrate binding and catalysis are labeled and highlighted with different colors. In dark blue is PP-loop, forest green is ADE motif, magenta is ARG1 motif, red is γ-phosphate motif and brown is the flavin motif. The magnesium ion is shown as a green sphere.

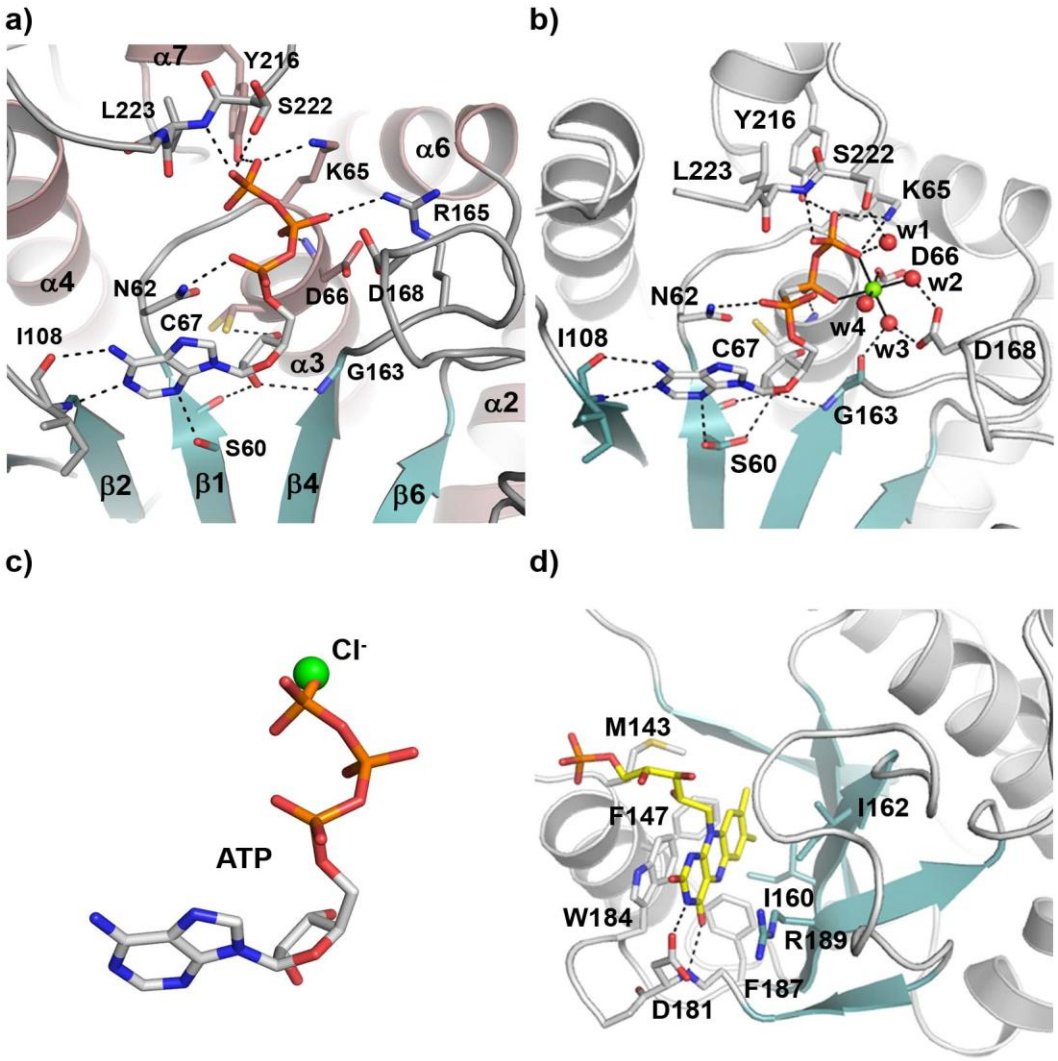

Figure 3.18 Substrate binding site in ATP binary and substrate ternary complexes. a) Details of the ATP-binding site. b) The catalytically competent Mg^{2+}-AMPCPP conformer I shown. c) Superposition of the bound chloride ion (dark green sphere) in apo-*Cg*FMNAT to ATP. d) Details of FMN binding site. The Mg^{2+} ion is shown as a green sphere and water ligands are shown as red spheres. Hydrogen bonds are shown as dash lines and metal ligand interactions are shown as solid lines.

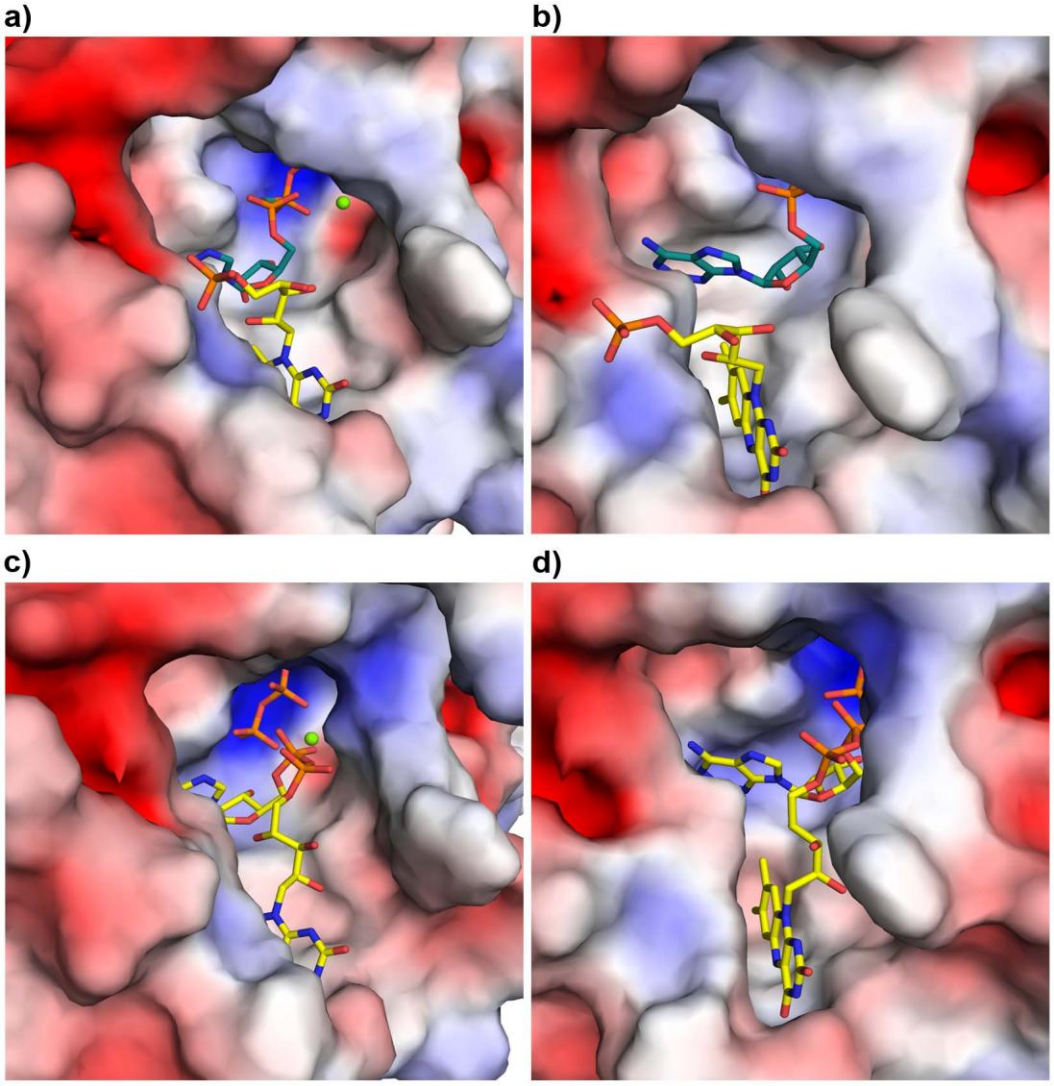

Figure 3.19 Electrostatic surface potential of the substrate binding site. Two views of the binding site electrostatic potential are presented for substrate ternary complex in a) and b), and for product ternary complex in c) and d). Substrates and products are shown as sticks. For a) and b), FMN and AMPCPP are colored by atom type with carbon atoms colored cyan for AMPCPP and yellow for FMN. For c) and d), FAD and PP_i are colored by atom type with carbon atoms colored yellow for FAD. The Mg^{2+} ion is shown as a green sphere.

through both main chain and side chain moieties. The α-phosphate interacts with the side chain of Asn62, the β-phosphate interacts with the main chain amide of Cys67 and the γ-phosphate forms two hydrogen bonds to the side chain of Lys65. Despite the different configuration of the triphosphate tail in the ATP binary complex, interactions with Asn62 and Lys65 are maintained (**Fig. 3.18a**). Additionally, the γ-phosphate forms additional hydrogen bonds with the hydroxyl of Tyr216 and Leu223 main chain amide. Both residues are from the γ-phosphate motif (**Fig. 3.18b**).

In the presence of magnesium ions, as in the case of the substrate ternary complex, the AMPCPP phosphate tail adopts two distinct conformations (conformer I and II, **Fig. 3.6b and Fig. 3.20a and b**), both of which differ from that observed in the Mg^{2+}-free ATP binary complex structure (**Fig. 3.21**). Among the six *Cg*FMNAT substrate ternary complexes in the asymmetric unit, three contain the bound AMPCPP in conformer I (chain C, D, E), two in conformer II (chain B and F), and one (chain A) in double conformations. In the first conformer, the Mg^{2+} is liganded to the β- and γ-phosphate oxygens, the Asp66 side chain carboxyl and three conserved water molecules, w2, w3, and w4 (**Fig. 3.18b**). W2 and w3 are further coordinated to the carboxylate group of Asp168 of the ARG1 motif. In the second conformer, all three AMPCPP phosphoryl

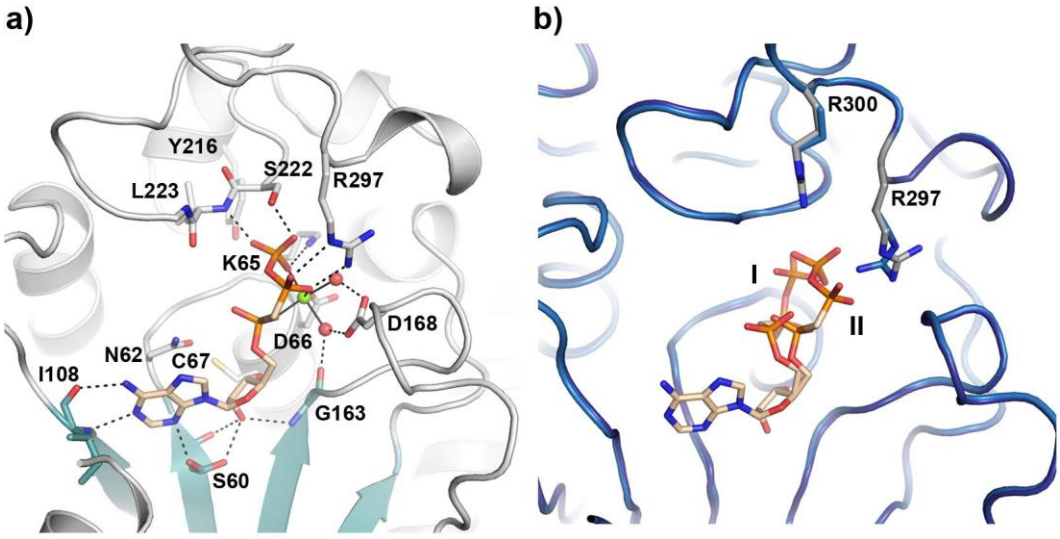

Figure 3.20 Alternate conformation of AMPCPP in substrate binding site. a) Details of the Mg^{2+}-ATP binding site shown with the AMPCPP conformer II. The Mg^{2+} ion is shown as a green sphere and water ligands are shown as red spheres. Hydrogen bonds are shown as dash lines and metal ligation are shown as solid lines. b) Superposition of monomer C (sky blue) to monomer A (dark blue) shows the conformational change of Arg297 with each AMPCPP conformer. AMPCPP, Arg297 and Arg300 are shown as sticks with atoms colored by atom type, and carbon atoms colored tan for AMPCPP, sky blue for monomer C and gray for monomer A.

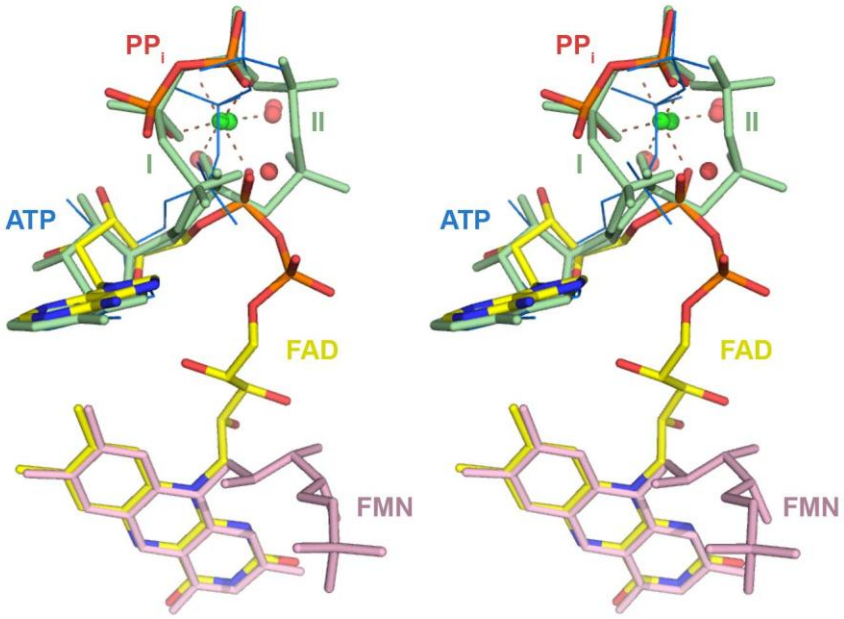

Figure 3.21 Stereo view of the superposition of bound ATP, Mg^{2+}, FMN and FAD. The dual conformations of ATP (light green) in the substrate ternary complex are marked as I and II. The ATP molecule in the Mg^{2+}-free binary complex structure is shown as blue thin lines. The substrate FMN is colored pink, while the product FAD is colored by atom types with carbon atoms in yellow. The Mg^{2+} ion (green sphere) and corresponding water ligands to FAD (red spheres) are also shown.

moieties are coordinated to the Mg^{2+} ion, with the β-phosphate oxygen substituting the w4 water ligand. The β-phosphate in this conformation also interacts with Arg279 of the ARG2 motif through two hydrogen bonds (**Fig. 3.20a**), which doesn't occur for conformer I. The largest difference between these AMPCPP conformations is in the position of the β-phosphate, which moves 5.1 Å between conformer I and II, while the α- and γ-phosphates move 1.6 Å and 2.2 Å, respectively. In both conformers, the bound Mg^{2+} ion remains in the same position and maintains a six-ligand octahedral configuration (**Fig. 3.21**). In the Mg^{2+}-free ATP binary complex structure, the position of the β-phosphate largely overlaps with the Mg^{2+} binding site (**Fig. 3.21**). Since AMPCPP is an analog of ATP, it is reasonable to consider AMPCPP conformer I and II as representatives of ATP conformations, and therefore the substrate ternary complex defines the Mg^{2+}ATP binding site. From the two conformers, the Mg^{2+}ATP conformer I is more relevant as discussed below.

Substrate ternary complex - Flavin binding site

Unexpectedly, the flavin-binding site, as revealed in the ternary substrate complex, is located on the same side of the central β-sheet as the adenosine moiety of AMPCPP, where a deep trough is formed between the face of the β-sheet, helix α5, and the loop connecting the anti-parallel β5 to β6 (**Fig. 3.18d and**

3.19b). This pocket forms a unique binding site for the flavin isoalloxazine ring different from that observed in any other FMN- or FAD-binding protein[209]. Residues from a broad range of structural elements are involved in the interaction with the isoalloxazine ring (**Fig. 3.17 and 3.18d**). These include Met143 and Phe147 from helix α5, Ile160 to Ile162 from strand β4; Asp181, Trp184 and Phe187 from the loop connecting β5 to β6, and Arg189 from strand β6. These residues are highly conserved among eukaryotic FMNATs (**Fig. 3.22**) and are collectively referred to as the *Flavin motif*. The isoalloxazine ring is sandwiched between the indole ring of Trp184 and the planar guanidinium group of Arg189 (**Fig. 3.18d**). Deeply buried in the flavin-binding pocket is the hydrophobic dimethylbenzene moiety of the isoalloxazine ring, forming van der Waals contacts with hydrophobic side chains of Met143, Phe147, Ile160, Ile162, and Phe187 (**Fig. 3.18d**). The hydrophilic lumazine side of the ring forms two specific hydrogen bonds with the enzyme, between its C4 carbonyl and the main chain amide of Asp181, and between its N3 amide and the side chain of Asp 181, respectively. The isoalloxazine group is also in van der Waals contact with the adenosine moiety of AMPCPP (**Fig. 3.21**).

In contrast to the extensive interactions with the isoalloxazine ring, there are few contacts between the enzyme and the FMN phosphoribityl tail (**Fig. 3.18d**). As a result, the conformation of this part of the substrate is not well

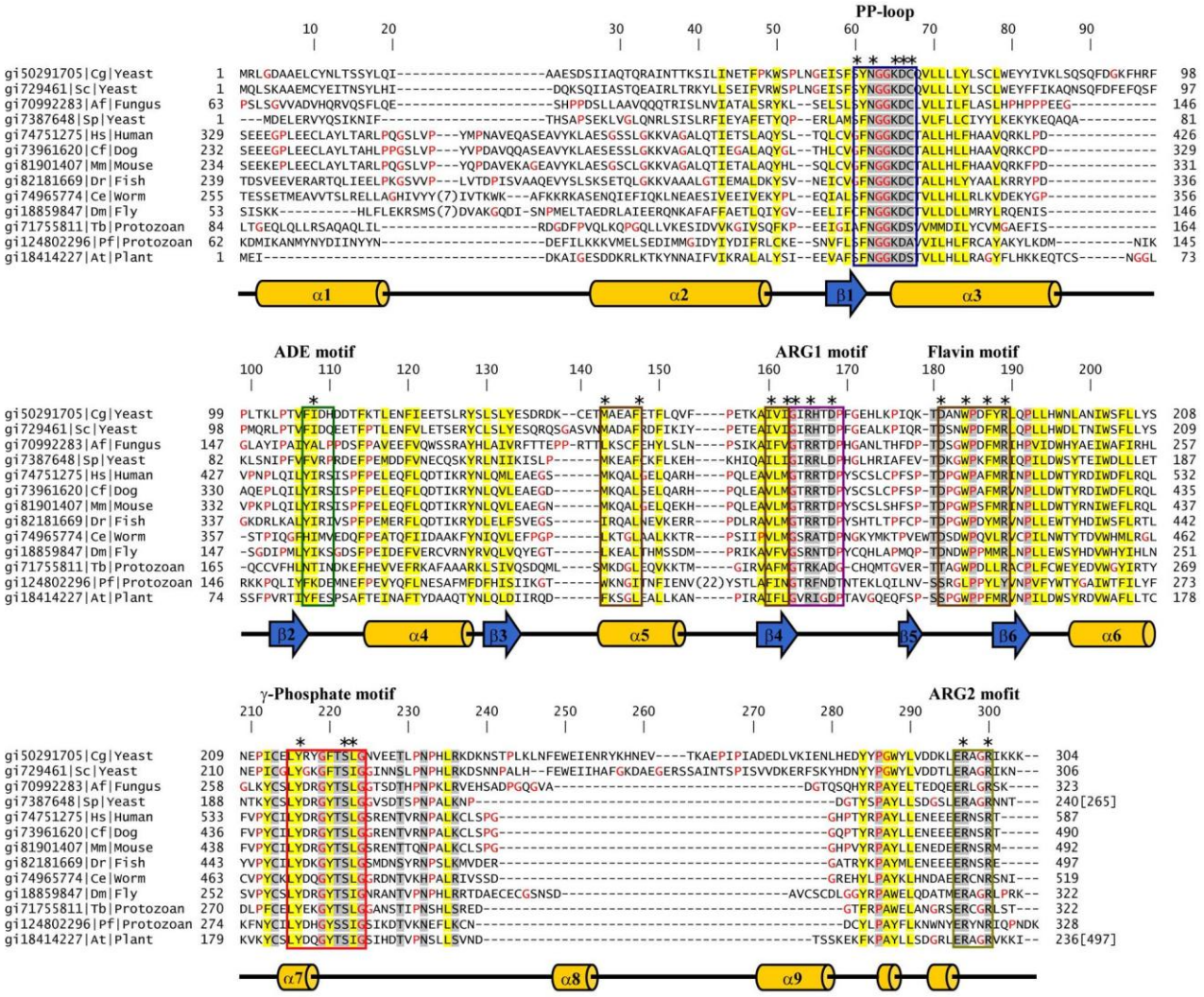
PP-loop
ADE motif
ARG1 motif
Flavin motif
γ-Phosphate motif
ARG2 mofit
α1
α2
β1
α3
β2
α4
β3
α5
β4
β5
β6
α6
α7
α8
α9

Figure 3.22 Multiple sequence alignment of eukaryotic FMNATs. The residue numbers and secondary structure elements of *Cg*FMNAT are marked at the top and bottom of the alignment, respectively. Each sequence is labeled by the gi number, species name abbreviation, and common species name. The first and last residues of each sequence are numbered at the beginning and end, with numbers in parentheses indicating residues not shown and total number of residues in brackets. Structural motifs of *Cg*FMNAT are boxed. Residues involved in substrate/product interaction are indicated by asterisks (∗). Glycine and proline residues are in red; conserved glycine, proline and charged/polar residues are highlighted in gray and conserved hydrophobic/aromatic residues in yellow. Abbreviation of species name is as follow: Cg, *Candida glabrata*; Sc, *Saccharomyces cerevisiae*; Af, *Aspergillus fumigates*; Sp, *Schizosaccharomyces pombe*; Hs, *Homo sapiens*; Cf, *Canis familiaris*; Mm, *Mus musculus*; Dr, *Danio rerio*; Ce, *Caenorhabditis elegans*; Dm, *Drosophila melanogaster*; Tb, *Trypanosoma brucei*; Pf, *Plasmodium falciparum* and At, *Arabidopsis thaliana*. Sequence alignment was constructed by PROMALS[177] and manually modified.

defined as indicated by the high B-factors, partial occupancy, and discontinuous density (**Fig. 3.6b**). In five of the six monomers in the asymmetric unit, FMN phosphoribityl tail is seen pointing toward the solvent, away from the bound AMPCPP, probably due to electrostatic repulsion, and is positioned over the N-terminal end of helix α5 **(Fig. 3.18b and 3.19a and b**). This observed conformation of FMN is apparently not in the catalytically ready state, as the phosphate is too far from the bound AMPCPP. Clearly the flexibility of FMN phosphoribityl tail would allow it to adopt multiple conformations and to move close to the ATP so that the adenylyltransferase reaction could occur. An alternative position of the FMN phosphoribityl tail is observed and modeled based on the observed density in monomer E and is within hydrogen bond distance to Arg297 (**Fig. 3.23**). The position of the FMN phosphoribityl tail seems to be energetically unfavorable as only one monomer adopts this conformation and the density is not as well defined as the previously described FMN conformation. These observations illustrate the considerable conformational flexibility of the phosphoribityl tail of FMN in the binding site that allows it to move close to the ATP.

Product ternary complex

The product ternary complex is formed between *Cg*FMNAT and FAD plus PP_i (**Fig. 3.24**). Comparing the substrate and product ternary complexes,

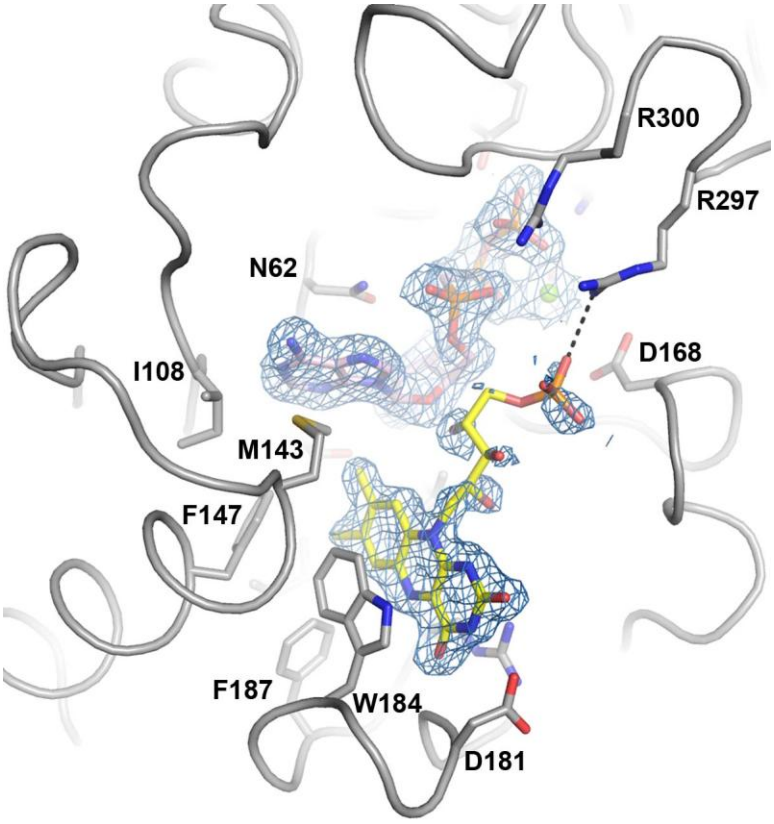

Figure 3.23 Alternate conformation of FMN. A $2F_o$-F_c electron density map (blue) contoured at 1.0σ is shown for the substrates in monomer E. The alternate FMN conformation allows the phosphoryl group of FMN to hydrogen bond with Arg297. The Mg^{2+} ion is shown as a green sphere and water ligands are shown as red spheres. Hydrogen bonds are shown as dash lines and ionic interactions are shown as solid lines.

the positions of the isoalloxazine ring of the flavin and the adenosine moieties of the nucleotides remain essentially unchanged (**Fig. 3.21**). The isoalloxazine group is in van der Waals contact with the adenosine moiety of either AMPCPP or FAD, suggesting that the adenosine group is part of the isoalloxazine-binding pocket (**Fig. 3.21**). The phosphoribityl of the product FAD becomes well ordered when covalently linked to the adenylyl group of ATP (**Fig. 3.6c**). The position of the PP_i product is also well defined in the crystal structure and is identical to that of the βγ-phosphates of AMPCPP in conformer I (**Fig. 3.21**). The Mg^{2+} ion in the product ternary complex is coordinated to the PP_i, the adenylyl phosphate of FAD, Asp66 and two water molecules in a configuration with features of both AMPCPP conformers in the substrate ternary complex (**Fig. 3.21 and 3.24**). Arg297 from the C-terminal ARG2 motif is found to interact with the diphosphate moiety of FAD (**Fig. 3.24**) supporting its potential involvement in binding the phosphate groups of both ATP and FMN substrates, and positioning them for the adenylyl transfer reaction.

Superposition of the equivalent C_α backbones of monomers from the substrate and product ternary complexes shows alternate conformations of the ARG2 motif located at the C-terminus in two of the six monomers (**Fig. 3.10a and b**). Interestingly, this alternate conformation causes the last five residues to become disordered. Examination of the region from the product ternary complex

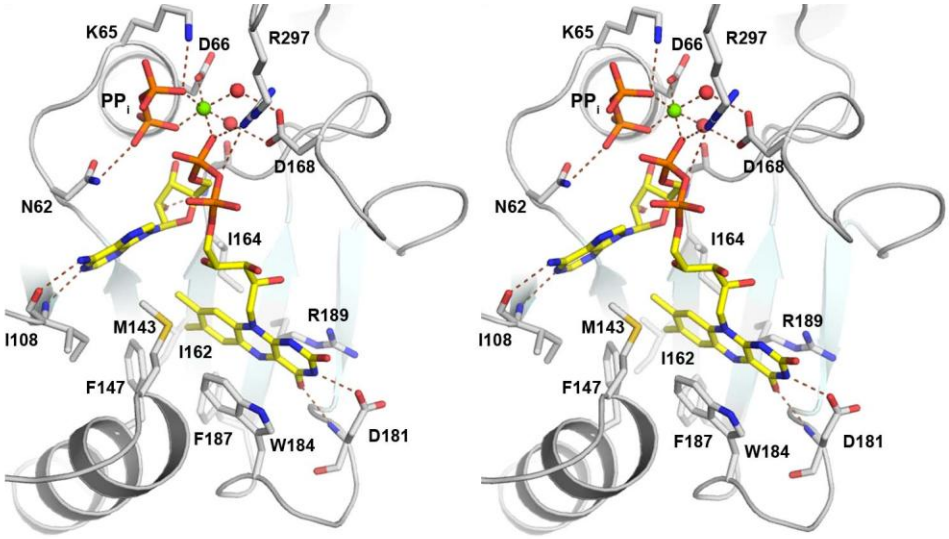

Figure 3.24 Stereo view of the FAD binding site. Protein residues interacting with bound ligands are shown as sticks. The Mg^{2+} ion is shown as a green sphere, and its two water ligands are shown as red spheres. Metal ligand and hydrogen bonds are shown as dashed lines.

indicates the diphosphate moiety of FAD interacts with Arg300 through a hydrogen bond and Arg297 is displaced and unable to interact with FAD (**Fig. 3.25**). Since, the alternate conformation is exhibited in the different ternary complexes Arg300 could also be involved in positioning the phosphate of FMN closer to ATP prior to catalysis.

Local conformational changes in different *Cg*FMNAT states

With four different structural states of *Cg*FMNAT providing snapshots of the subtle conformational changes before and after the catalytic process, we have gained first insights into the mechanics of substrate binding and product interaction. At the beginning, binding of ATP causes the nucleotide binding pocket to undergo subtle conformational changes, such that, the PP-loop Ser 60, Asn62 and Lys65 form hydrogen bonds with the nucleotide, and Asp66 and Cys67 reposition to avoid clashing with ATP (**Fig. 3.26a**). A notable feature of the PP-loop is Cys67 adopting double conformations, which causes Tyr61 to shift away with a rotation of the side chain to avoid clashes with the thiol of Cys67 (**Fig. 3.26a**). Other changes include Ile108 from the ADE motif to accommodate the adenine of ATP and Asp168 from the ARG1 motif that moves toward ATP. Ser222 from the γ-phosphate motif and Cys67 both adopt double conformations in the ATP binary complex, but not in the substrate ternary complex (**Table 3.2 and Fig. 3.26a**).

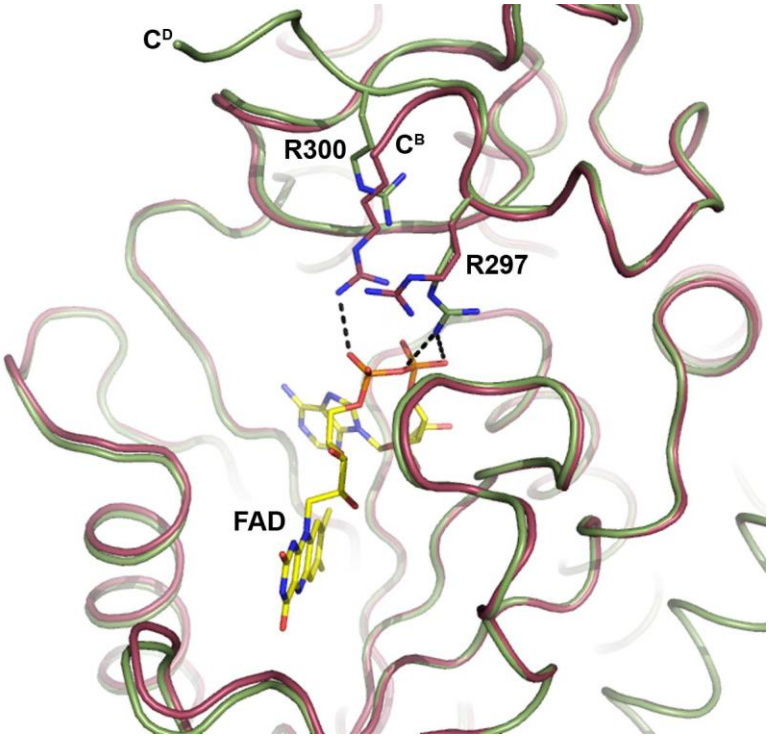

Figure 3.25 Alternate conformation of the C-terminal end. Superposition of product ternary complex monomer D (forest green) to monomer B (raspberry) illustrates the rearrangement of Arg297 and Arg300 interactions with product FAD, which is colored by atom type with carbon atoms colored yellow and hydrogen bonds are shown as dash lines.

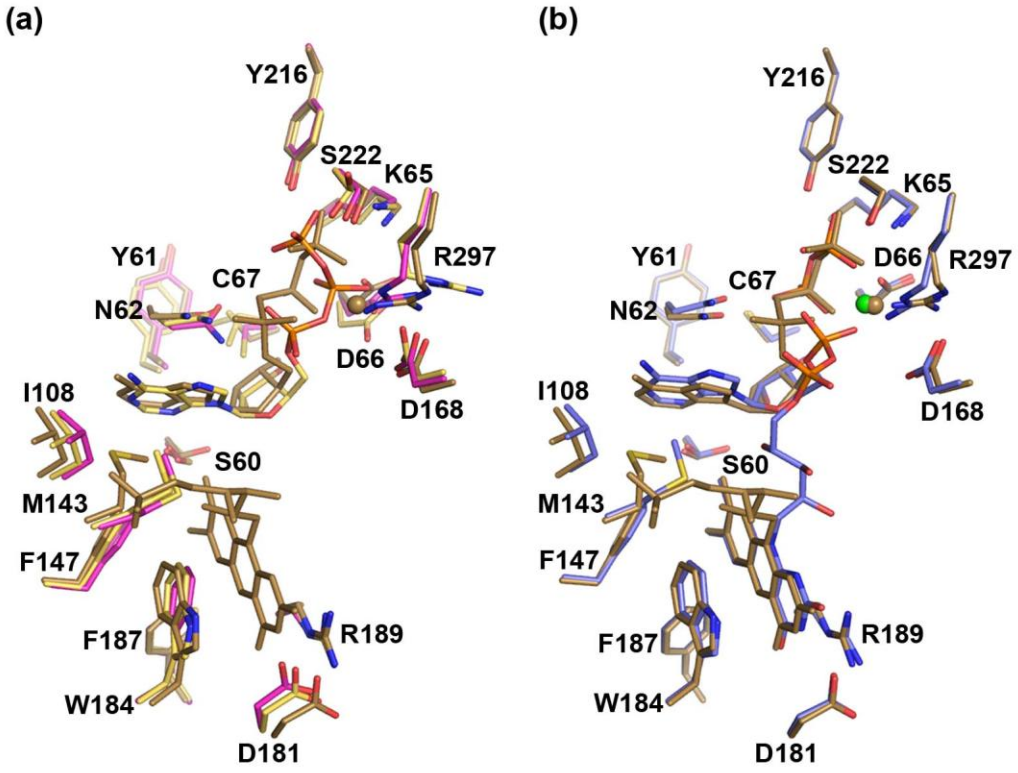

Figure 3.26 Binding site residue motion prior and after catalysis. The apo-form is magenta, ATP complex wheat, substrate ternary complex brown and product ternary complex light blue. a) Side chains conformational changes upon substrate binding. ATP, from the ATP binary complex, is shown as sticks and colored by atom types with carbon atoms colored tan. The AMPCPP, FMN and Mg^{2+} ion from the substrate ternary complex are colored brown, with substrates shown as sticks and Mg^{2+} ion as a sphere. (b) Superposition of the substrate and product ternary complex structures. The FAD and PP_i are shown as sticks and colored by atom types with carbon atoms in light blue. The Mg^{2+} ion is a green sphere.

When magnesium is present, there are limited but possibly pivotal changes as revealed from the substrate ternary complex. In the presence of magnesium, the ATP molecule is re-oriented and able to adopt the conformer I conformation for catalysis, which results in further conformational changes in Ser60, Asn62, Lys65, Asp66, Cys67 and Ile108 (**Fig. 3.26a**). Ser60 adopts double conformations, possibly to accommodate the movement of ATP in the binding site. Asp66 moves approximately to the same position as in the apo-protein, with the side chain carboxyl of Asp66 rotating to form an ionic interaction with the magnesium ion. The side chain thiol of Cys67 adopts a rotamer that faces away from ATP (**Fig. 3.26a**). The result of the different Cys67 conformation allows Tyr61 to have a similar position as in the apo-protein. Asp168 moves to a position that permits the coordination of two water molecules to ligand with the magnesium ion (**Fig. 3.18b and 3.26a**). Ser222 moves slightly and adopts a single conformation that coordinates a water molecule to interact with the γ-phosphate of ATP (**Fig. 3.18b and 3.26a**). Following catalysis, there are little conformational changes in the nucleotide binding site. Asn62 no longer forms a hydrogen bond with the adenylyl phosphate but now hydrogen bonds to the PP_i (**Fig. 3.26b**). As a result of the adenylyl transfer Arg297 in ARG2 motif adopts a rotamer that interacts with the diphosphate of FAD (**Fig. 3.26b**).

The movements of the flavin motif are similar to that of the motifs interacting with ATP, in which there are subtle conformational changes. One of the most prominent conformational changes is Met143, which rotates away from the binding cavity in the substrate ternary complex (**Fig. 3.26a and b**). For all *Cg*FMNAT structural states, this conformation is seen only in the substrate ternary complex. Phe147, Asp181, Trp184, Phe187 and Arg189 adjust to accommodate the isoalloxazine ring (**Fig. 3.26a and b**). All of the subtle changes are supported by the low B-factors for each structural state of *Cg*FMNAT.

Comparison of the active site with other adenine α hydrolase-like proteins

On the basis of structural alignment, the core of *Cg*FMNAT is similar to members of the PAPS reductase-like family where the 5^{th} β-strand of the central twisted six-stranded β-sheet is anti-parallel to the rest of the strands (**Fig. 3.27**). Compared to other PAPS reductase-like proteins, three of the five ATP binding motifs in *Cg*FMNAT, PP-loop, ADE and ARG1 motifs, are conserved (**Fig. 3.28**). Although the γ-phosphate motif is also present in members of the PAPS reductase-like family such as APS reductase and ATP sulfurylase, its role in substrate binding and catalysis in these enzymes is not clear. Unique to *Cg*FMNAT and APS reductase is the presence of the ARG2 motif.

Extending the comparison of the nucleotide binding site to included the N-type ATP pyrophosphatases and PP-loop ATPase families, which are in the same

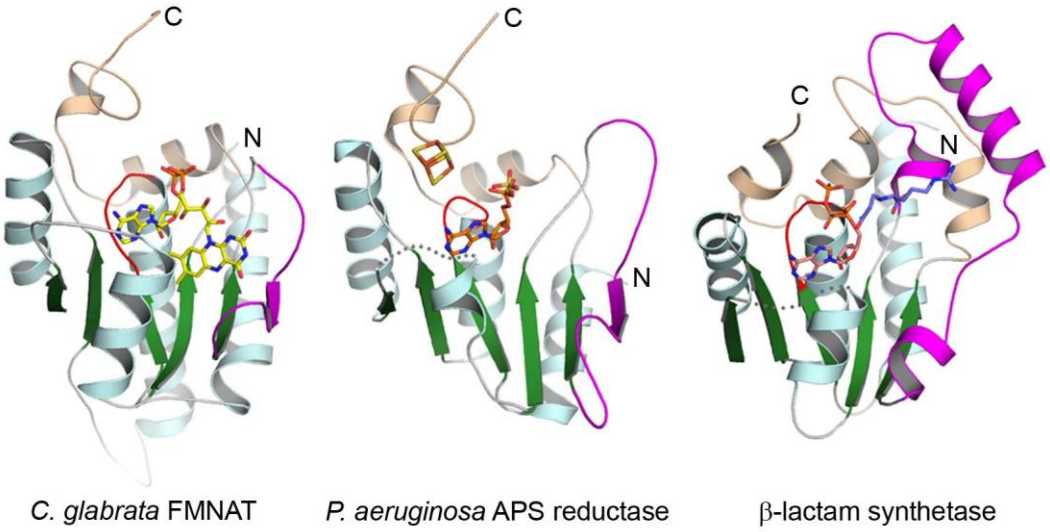

Figure 3.27 Comparison of the *Cg*FMNAT fold with representatives of "adenine nucleotide α hydrolase-like" proteins. Helix α1 and the last ~70 residues of *Cg*FMNAT are removed for clarity. Bound ligand FAD in *Cg*FMNAT, APS in APS reductase, and ATP and CEA (N^2-(carboxyethyl)-l-arginine) in β-lactam synthetase are shown as sticks colored by atom type with carbon atoms colored yellow, red-orange, pink and light blue, respectively. Equivalent structural motif PP-loop is colored red and C-terminal domain colored wheat. Regions in *Cg*FMNAT and APS reductase that deviate from the typical Rossmann-fold topology are shown in magenta. Corresponding regions in β-lactam synthetase are also shown in magenta for comparison.

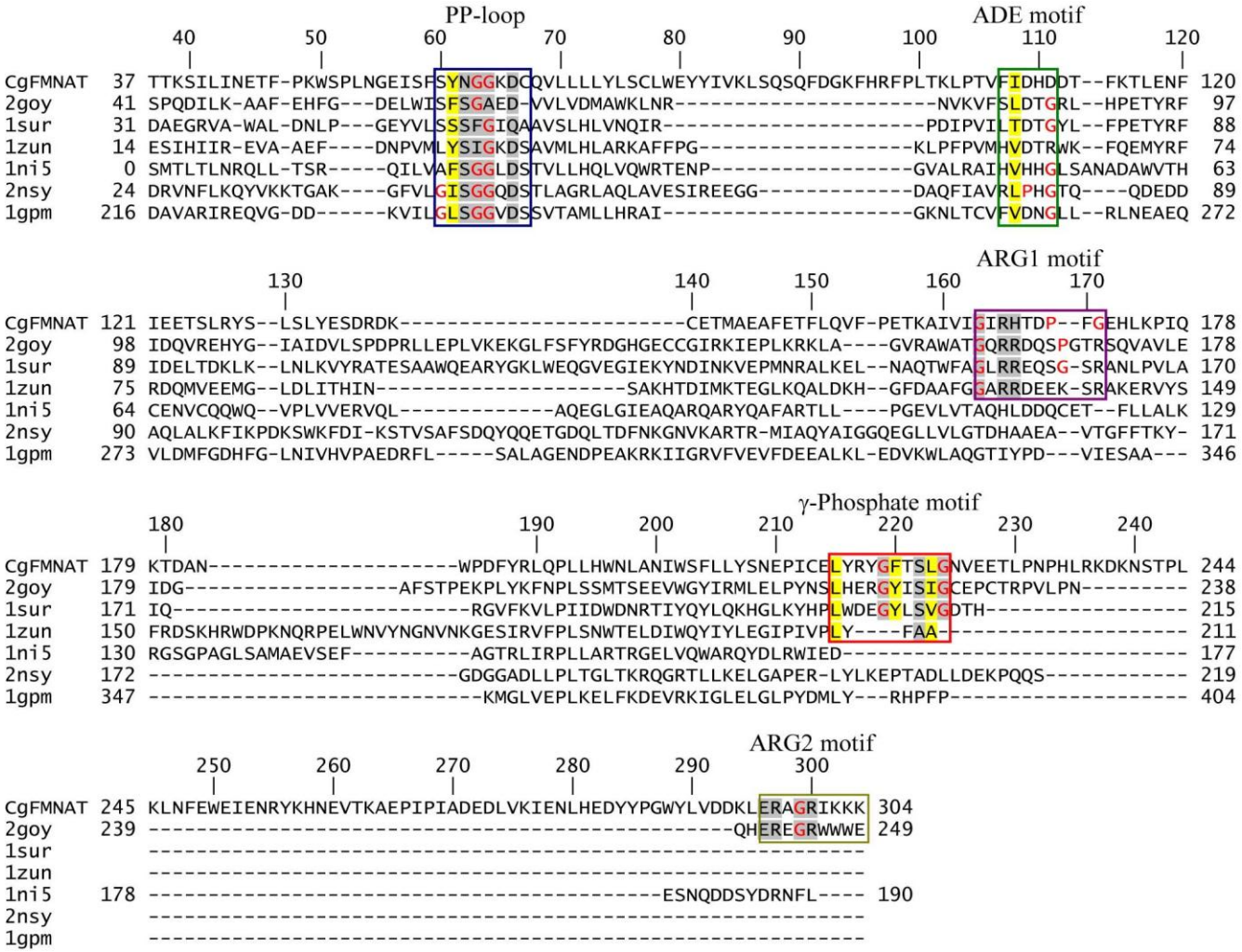
PP-loop
ADE motif
ARG1 motif
γ-Phosphate motif
ARG2 motif
CgFMNAT 37 TTKSILINETF-PKWSPLNGEISFSYNGGKDCQVLLLLYLSCLWEYYIVKLSQSQFDGKFHRFPLTKLPTVFIDHDDT--FKTLENF 120
2goy 41 SPQDILK-AAF-EHFG---DELWISFSGAED-VVLVDMAWKLNR----------NVKVFSLDTGRL--HPETYRF 97
1sur 31 DAEGRVA-WAL-DNLP---GEYVLSSSFGIQAAVSLHLVNQIR----------PDIPVILTDTGYL--FPETYRF 88
1zun 14 ESIHIIR-EVA-AEF----DNPVMLYSIGKDSAVMLHLARKAFFPG----------KLPFPVMHVDTRWK--FQEMYRF 74
1ni5 0 SMTLTLNRQLL-TSR-----QILVAFSGGLDSTVLLHQLVQWRTENP----------GVALRAIHVHHGLSANADAWVTH 63
2nsy 24 DRVNFLKQYVKKTGAK----GFVLGISGGQDSTLAGRLAQLAVESIREEGG----------DAQFIAVRLPHGTQ----QDEDD 89
1gpm 216 DAVARIREQVG-DD------KVILGLSGGVDSSVTAMLLHRAI----------GKNLTCVFVDNGLL--RLNEAEQ 272
CgFMNAT 121 IEETSLRYS--LSLYESDRDK----------CETMAEAFETFLQVF-PETKAIVIGIRHTDP--FGEHLKPIQ 178
2goy 98 IDQVREHYG--IAIDVLSPDPRLLEPLVKEKGLFSFYRDGHGECCGIRKIEPLKRKLA----GVRAWATGQRRDQSPGTRSQVAVLE 178
1sur 89 IDELTDKLK--LNLKVYRATESAAWQEARYGKLWEQGVEGIEKYNDINKVEPMNRALKEL--NAQTWFAGLRREQSG-SRANLPVLA 170
1zun 75 RDQMVEEMG--LDLITHIN----------SAKHTDIMKTEGLKQALDKH--GFDAAFGGARRDEEK-SRAKERVYS 149
1ni5 64 CENVCQQWQ--VPLVVERVQL----------AQEGLGIEAQARQARYQAFARTLL----PGEVLVTAQHLDDQCET--FLLALK 129
2nsy 90 AQLALKFIKPDKSWKFDI-KSTVSAFSDQYQQETGDQLTDFNKGNVKARTR-MIAQYAIGGQEGLLVLGTDHAAEA--VTGFFTKY- 171
1gpm 273 VLDMFGDHFG-LNIVHVPAEDRFL-----SALAGENDPEAKRKIIGRVFVEVFDEEALKL-EDVKWLAQGTIYPD---VIESAA--- 346
CgFMNAT 179 KTDAN----------WPDFYRLQPLLHWNLANIWSFLLYSNEPICELYRYGFTSLGNVEETLPNPHLRKDKNSTPL 244
2goy 179 IDG----------AFSTPEKPLYKFNPLSSMTSEEVWGYIRMLELPYNSLHERGYISIGCEPCTRPVLPN--------- 238
1sur 171 IQ----------RGVFKVLPIIDWDNRTIYQYLQKHGLKYHPLWDEGYLSVGDTH---------- 215
1zun 150 FRDSKHRWDPKNQRPELWNVYNGNVNKGESIRVFPLSNWTELDIWQYIYLEGIPIVPLY----FAA- 211
1ni5 130 RGSGPAGLSAMAEVSEF----------AGTRLIRPLLARTRGELVQWARQYDLRWIED---------- 177
2nsy 172 ----------GDGGADLLPLTGLTKRQGRTLLKELGAPER-LYLKEPTADLLDEKPQQS---------- 219
1gpm 347 ----------KMGLVEPLKELFKDEVRKIGLELGLPYDMLY---RHPFP---------- 404
CgFMNAT 245 KLNFEWEIENRYKHNEVTKAEPIPIADEDLVKIENLHEDYYPGWYLVDDKLERAGRIKKK 304
2goy 239 ----------QHEREGRWWWE 249
1sur ----------
1zun ----------
1ni5 178 ----------ESNQDDSYDRNFL---- 190
2nsy ----------
1gpm ----------

Figure 3.28 Structure-based multiple sequence alignment of protein representatives from "adenine nucleotide α hydrolase-like" superfamily. Each sequence is labeled by the PDB code, except *Cg*FMNAT. The residue numbers of *Cg*FMNAT are marked at the top of the alignment. The sequence numbers at the beginning and end of the alignment for each sequence are provided. Conserved structural motifs are boxed and conserved residues within the motifs highlighted. Glycine and proline residues are in red; conserved glycine and charged/polar residues are highlighted in gray and conserved hydrophobic/aromatic residues in yellow. Members of PAPS reductase-like family are 2goy (APS reductase), 1sur (PAPS reductase) and 1zun (ATP sulfurylase); member of PP-loop ATPase family is 1ni5 (tRNA-Ile-lysidine synthetase); and members of N-type ATP pyrophosphatases are 2nsy (NH^{3+}-dependent NAD synthetase) and 1gpm (GMP synthetase).

superfamily, underscored the similarities and differences between different the families. The conformation of the PP-loop between PAPS reductase-like, N-type ATP pyrophosphatases and PP-loop ATPase families is similar, however the generally conserved PP-loop sequence SGGxD(S/T) is altered in eukaryotic FMNAT (**Fig. 3.22 and 3.28**). In part, by the replacement of the first conserved Ser with *Cg*FMNAT Asn62. In addition, the determined *Cg*FMNAT PP-loop sequence motif ^{60}SYNGGKDC$_{67}$ is more similar to the canonical PP-loop sequence[142], due to the two conserved glycines, rather than to the PP-loop sequence of PAPS reductase-like family[140] (**Fig. 3.28**). The replacement of the first Ser of the canonical PP-loop sequence with Asn substitutes an electronegative Ser hydroxyl with a less electronegative amine, along with a longer side chain. The substitution may be responsible for the Asn amine of *Cg*FMNAT to hydrogen bond to the nucleotide α-phosphate, rather than the β-phosphate, as in ATP sulfurylase and NH^{3+}-dependent NAD synthetase (**Fig. 3.29c and d**). Aside from eukaryotic FMNAT, ATP sulfurylase is the only classified member of the superfamily with a Lys at the equivalent position to Lys65 of *Cg*FMNAT; however the ammonium group doesn't engage in hydrogen bonding, possibly due to the use of ATPγS[139] (**Fig. 3.29c**). A variant of the Lys interaction is observed in NH^{3+}-dependent NAD synthetase, where Lys186 from a

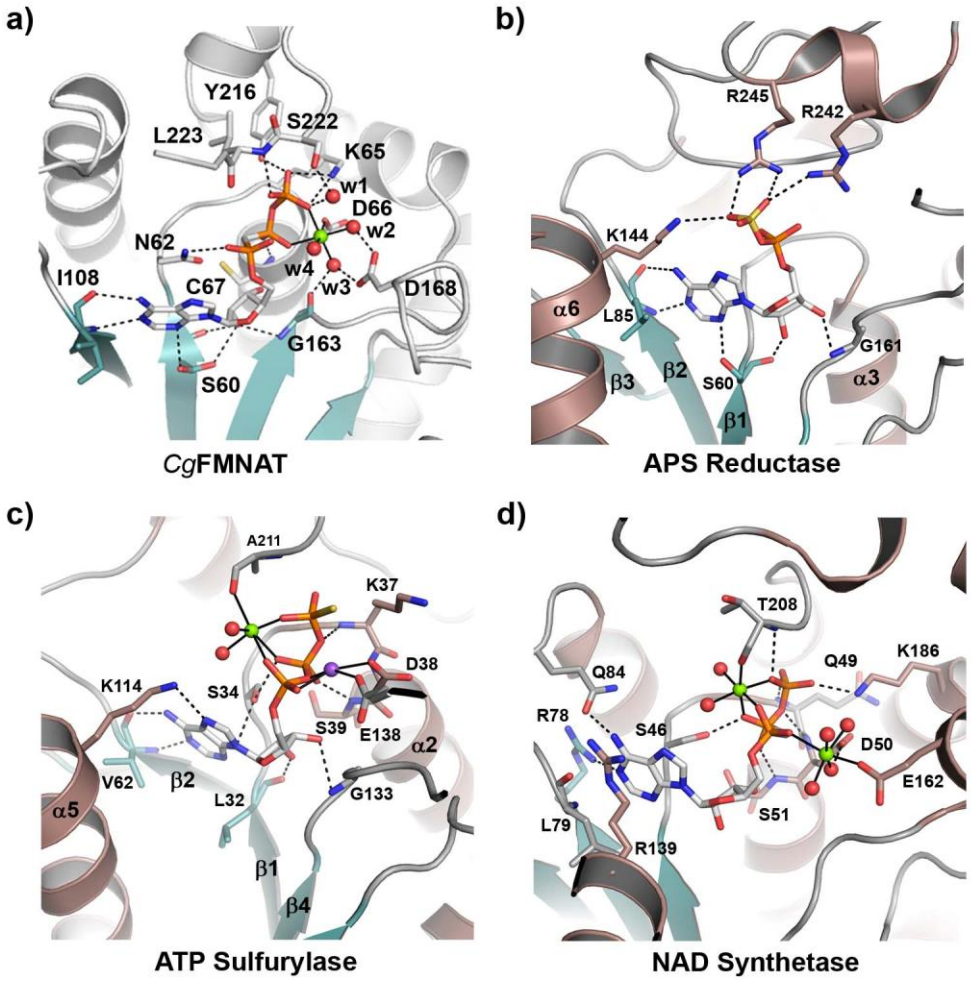

Figure 3.29 Comparison of nucleotide binding site in adenine nucleotide α hydrolase-like superfamily. a) Details of the ATP-binding site in *Cg*FMNAT. b) Details of the APS-binding site in APS reductase. c) Details of the ATP-binding site in ATP sulfurylase. d) Details of the ATP-binding site in NH^{3+}-dependent NAD synthetase. Nucleotides are colored by atom type with carbon atoms colored gray. The Mg^{2+} ions and Na^{+} ion are shown as a green and purple sphere, respectively, and water ligands are shown as red spheres. Metal ligand interactions are shown as solid lines and hydrogen bonds are shown as dashed lines.

nearby helix forms a hydrogen bond to the γ-phosphate (**Fig. 3.29d**). Residues at the equivalent position of *Cg*FMNAT Lys65 within the superfamily form a hydrogen bond to the γ-phosphate of ATP through the main chain amide (**Fig. 3.29c and d**). A similar interaction is not observed in *Cg*FMNAT (**Fig. 3.29a**). Asp66 is a highly conserved residue within the superfamily (**Fig. 3.28**) that is a direct ligand to a magnesium ion or a sodium ion, as is the case with ATP sulfurylase[139] (**Fig. 3.29a, c and d**). Cys67 of the *Cg*FMNAT PP-loop is replaced with a highly conserved Ser residue in the superfamily with both residues hydrogen bonding to the nucleotide β-phosphate (**Fig. 3.29a, c and d**).

As the PP-loop interacts with the phosphates and ribose of the nucleotide, the ADE motif of *Cg*FMNAT, which is conserved in the superfamily, is specific to adenine binding and contains a conserved hydrophobic residue. The adenine moiety of the nucleotide intimately forms hydrogen bonds to the hydrophobic residue main chain[143,200,210] (**Fig. 3.29a-c**). The interactions with the main chain explains the adenine specificity and why substitutions, such as guanine, prevent interaction at the adenine binding site[150]. Interestingly, the corresponding residue in NH^{3+}-dependent NAD synthetase does not engage in hydrogen bonding with the adenine moiety. Instead, the adenine moiety forms hydrogen bonds with the side chain of Arg78 and Gln84 from the same loop (**Fig. 3.29d**). There are additional interactions between the adenine moiety with NH^{3+}-dependent NAD

synthetase and ATP sulfurylase, which involve a stacking interaction with Arg139 (**Fig. 3.29d**) and a hydrogen bond to Lys114 (**Fig. 3.29c**), respectively.

In contrast to the PP-loop and ADE motifs, the ARG1 motif is present only in *Cg*FMNAT and the PAPS reductase-like family and is located on the loop connecting β5 to β6. For PAPS reductase-like family the motif has three conserved arginines[138,140], for which the first arginine occurring on the motif is invariant in eukaryotic FMNAT and the second arginine is highly conserved (**Fig. 3.22 and 3.28**). The conserved Gly of this motif, Gly163 in *Cg*FMNAT, Gly161 in APS reductase and Gly 133 in ATP sulfurylase interacts with the ribose of the nucleotide through a hydrogen bond from the main chain amide (**Fig. 3.29a-c**). Unlike Glu138 in ATP sulfurylase and Glu162 in NH^{3+}-dependent NAD synthetase that directly ligand to their respective cation species, *Cg*FMNAT Asp168 coordinates two waters to ligand to the metal ion.

For the last nucleotide binding motif, the γ-phosphate motif appears to be conserved only in PAPS reductase-like family[138,140]. In the structure of ATP sulfurylase, a portion of this motif is disordered in the crystal[139], but it is close to and could thus interact with ATP. Despite the structural and sequence similarity to *Cg*FMNAT γ-phosphate motif (**Fig. 3.28 and 3.29b and c**), few interactions occur in ATP sulfurylase and APS reductase[138,139]. Aside from the γ-phosphate motif, APS reductase Lys144, equivalent to Lys114 in ATP sulfurylase, hydrogen

bonds to the β-sulfate of the phosphosulfate group of APS. No similar interaction is observed for *Cg*FMNAT.

In APS reductase, Arg242 and Arg245 are near the protein C-terminus (corresponding to Arg297 and Arg300 of *Cg*FMNAT) and provide important interactions with the phosphosulfate group of APS (**Fig. 3.28 and 3.29b**). Our kinetic analysis of the R297A mutant shows that the apparent $K_{m,ATP}$ and $K_{m,FMN}$ of the mutant are increased 5 and 3 times, respectively, compared to the wild-type enzyme (discussed in Chapter 4), indicating that this Arg residue is indeed involved in substrate binding, presumably through interactions with the phosphoryl groups of the substrates.

The number of ions involved in nucleotide interaction is different for *Cg*FMNAT, N-type ATP pyrophosphatases and certain members of the PAPS reductase-like families. One Mg^{2+} was observed in the nucleotide binding site for *Cg*FMNAT, whereas the structure of ATP sulfurylase revealed two cation binding sites with one Mg^{2+} and Na^{+} ion. For N-type ATP pyrophosphatases family there are two Mg^{2+} binding sites as exemplified in GMP synthetase[143] and NH^{3+}-dependent NAD synthetase[201] (**Fig. 3.29d**). In each family, the second cation interaction occurs on the side of the PP-loop where the conserved Ser is replaced with Asn. In the absence of the second cation binding site in *Cg*FMNAT, there are seven hydrogen bonds, with five occurring to the γ-phosphate. For ATP

sulfurylase and NH^{3+}-dependent NAD synthetase, the phosphates of the nucleotide form three and six hydrogen bonds, with one and four occurring with the γ-phosphate, respectively.

Small molecule interaction sites on *Cg*FMNAT surface

Interactions with small molecules on the surface of *Cg*FMNAT were observed for the ATP complex and ternary complexes. With 5 mM (final concentration) magnesium sulfate added during cryoprotection of the substrate ternary complex, a sulfate molecule is located near the N-terminus of helix α9 between monomers D and its symmetry-related counter part (**Fig. 3.30a**). Since the sulfate lies close to the crystallographic 2-fold axis, the two symmetry-related sulfate molecules are modeled with 50% occupancy. Stabilization of the sulfate occurs through formation of hydrogen bonds with Asn119, Lys115 and a water molecule. A similar interaction is also observed in the product ternary complex where a sulfate concentration of 0.2 M is used in the crystallization condition (**Fig. 3.30b**). In this condition, the electron density is better defined for the two sulfate molecules. Another sulfate molecule is modeled with 50% occupancy binding to the product ternary complex monomer F, in which the sulfate doesn't lie close to a crystallographic 2-fold axis. Even with different packing symmetry around monomer F, the sulfate molecule maintains interaction with helix α9 and

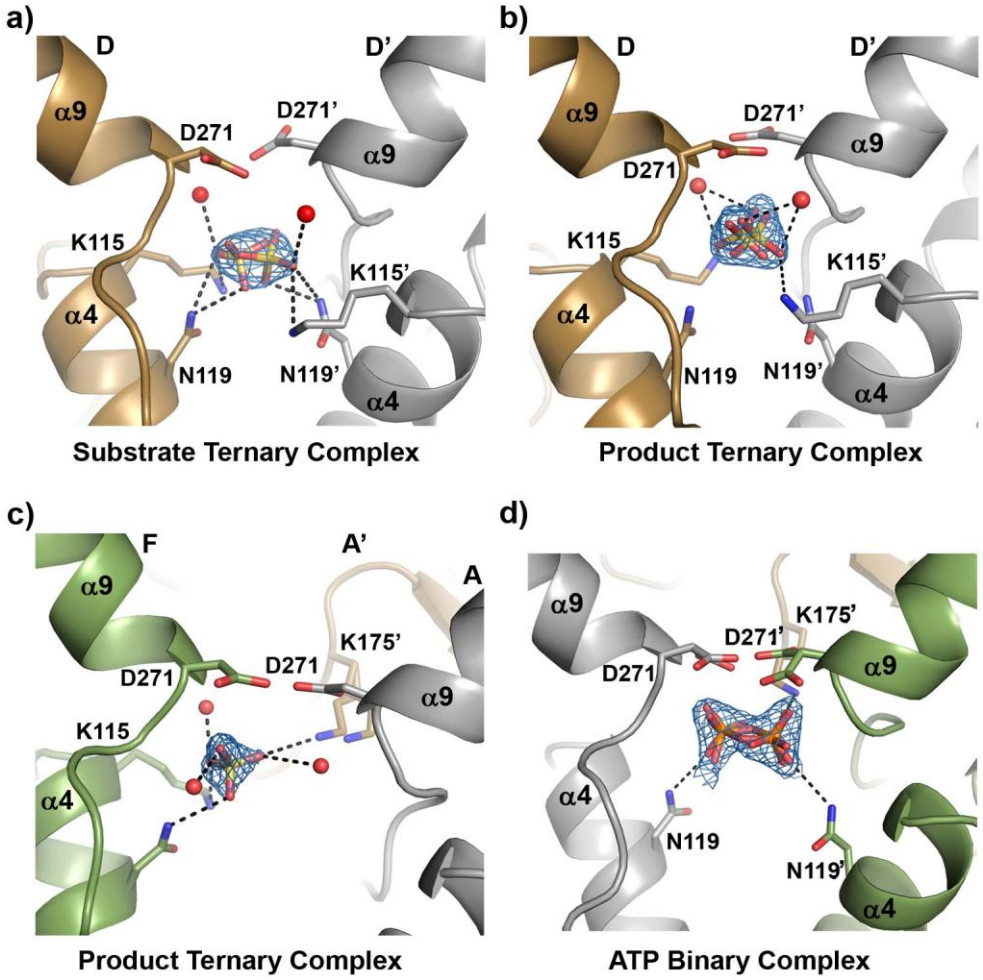

Figure 3.30 Small molecule interactions at the surface of ternary and binary complexes. Residues and small molecules are shown as sticks and are colored by atom type with carbon atoms colored by monomer. Waters are shown as red spheres. A $2F_o$-F_c electron density map (blue) contoured at 1.0σ is shown for the small molecules. For a) and b) a sulfate molecule is interacting with monomer D (brown) and a symmetry-related monomer D (gray). c) A sulfate molecule interacts with monomer F (forest green), adjacent to monomer A (gray), and with a symmetry-related monomer A (brown). d) A pyrophosphate is shown interacting with the monomer (gray) and two symmetry-related monomers (forest green and brown).

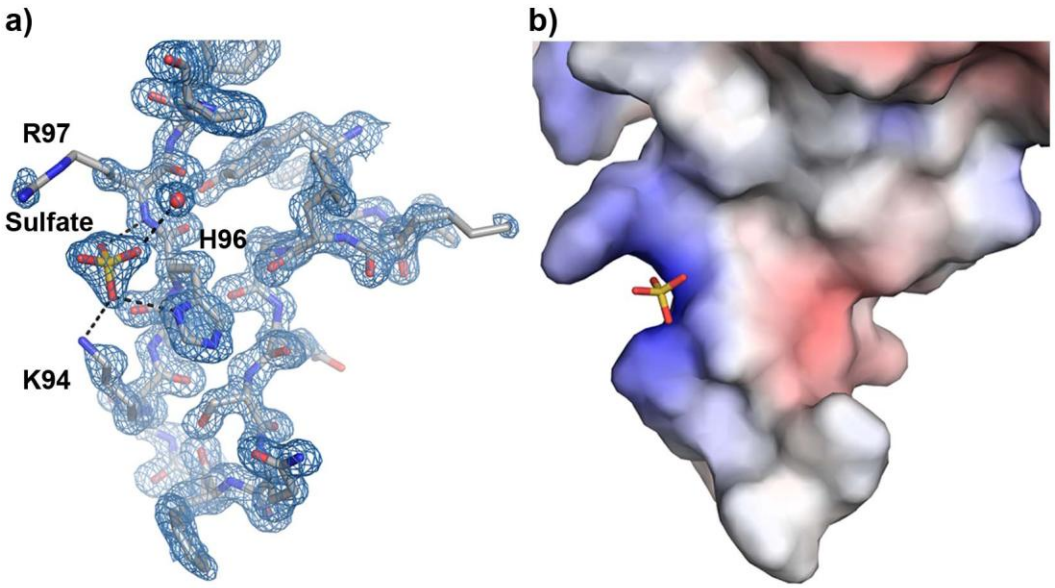

Figure 3.31 SQFD-loop interacting with a sulfate in the product ternary complex monomer B. a) Protein residues and the sulfate are shown as sticks with $2F_o$-F_c electron density maps (blue) contoured at 1.0σ. b.) An electrostatic potential mapped on the protein surface in the same orientation in a). Hydrogen bonds are shown as dash lines.

Asn119 (**Fig. 3.30c**). In the ATP complex, which crystallizes in a different space group from the ternary complexes, a pyrophosphate molecule is modeled and it engages in interactions with Asn119 and helix α9 of two symmetry-related monomers in a similar manner as that observed in the ternary complexes (**Fig. 3.30d**). The pyrophosphate, possibly derived from hydrolysis of ATP molecule, lies on a symmetry axis and is therefore modeled with two conformations at 50% occupancy. Depending on the pyrophosphate orientation the rotamer of Asp271 changes to avoid close contact.

In *Cg*FMNAT product ternary complex, a second sulfate molecule is found to interact with the ordered SQFD-loop. Hydrogen bond formations between the sulfate and monomer B (**Fig. 3.31a**) (or monomer D) SQFD-loop are essentially identical. Binding of a sulfate molecule could be aided by the electrostatic potential of the SQFD-loop, as the sulfate binds in a positively charge crevice (**Fig. 3.31b**). Both interaction sites for the two sulfate molecules, one near helix α9 and the other with the SQFD-loop (**Fig. 3.32a**) reside in a positively charge region (**Fig. 3.32b**)

In the product ternary complex a glucose molecule is modeled, as defined by the clear electron density, stacked between the protein monomer B in the asymmetric unit and a symmetry-related protein monomer B in a similar fashion as in Chapter 2 for apo-form (**Fig. 2.13a**). The glucose molecule interacts with

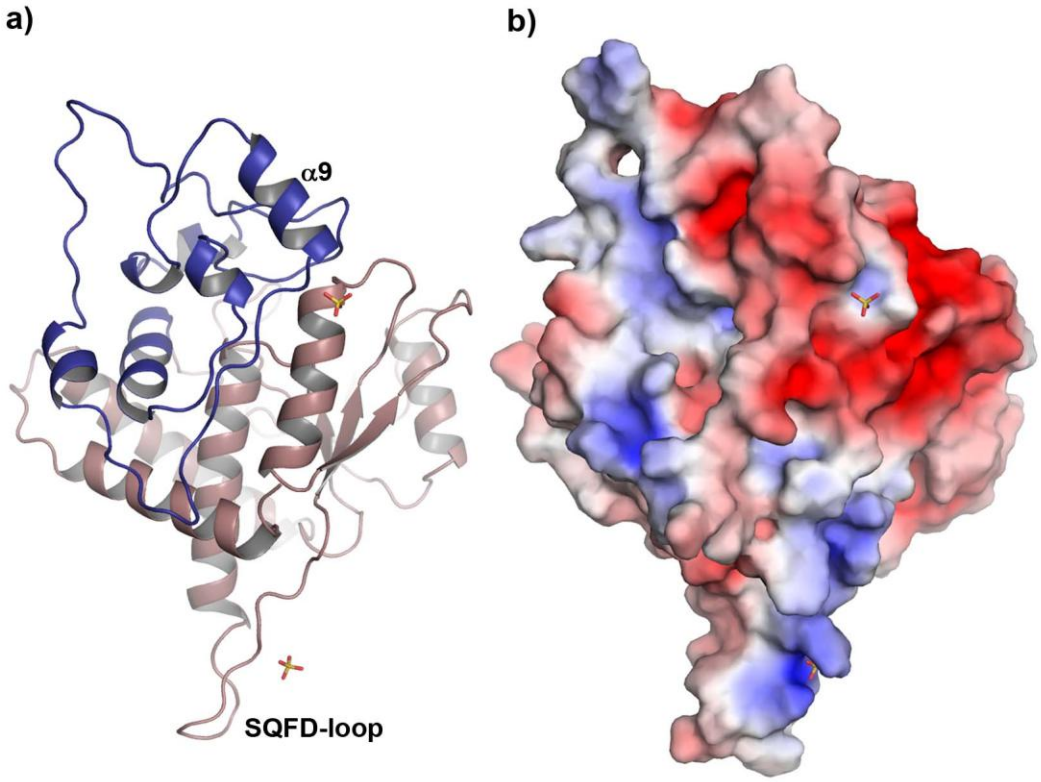

Figure 3.32 Overview of the sulfate interaction locations. Sulfates are shown as sticks and colored by atom type. a) A ribbon representation of monomer D product ternary complex colored raspberry for the N-terminal domain and dark blue for the C-terminal domain. b) An electrostatic surface potential of monomer D product ternary complex.

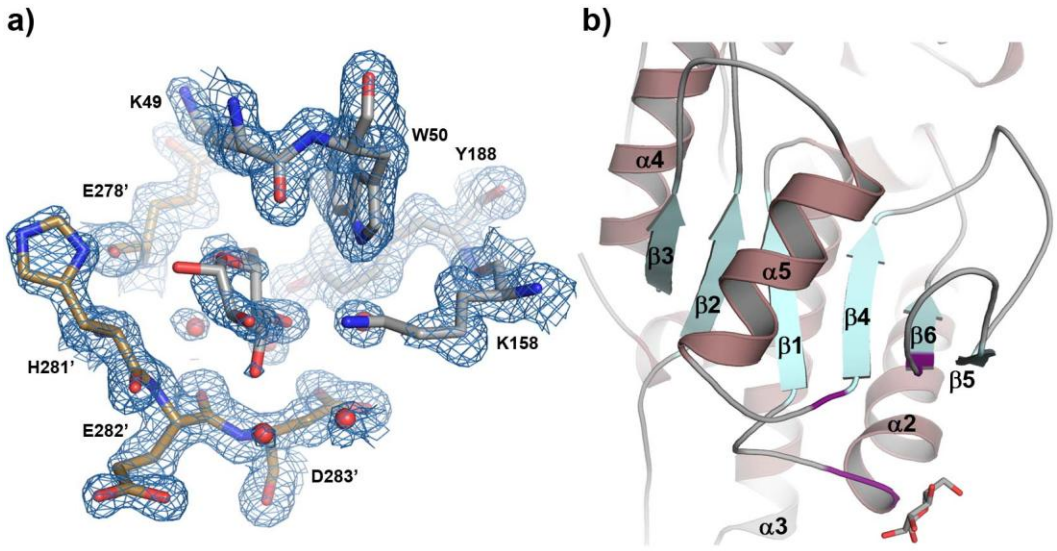

Figure 3.33 Glucose interaction site in a product ternary complex. a) A $2F_o$-F_c electron density map (blue) contoured at 1.0σ is shown around glucose interacting site. Atoms are colored by atom type with carbon atoms colored gray for monomer B and brown for the symmetry-related monomer B. b) Ribbon representation of monomer B with residue K49, W50, K158 and Y188 sites colored purple.

several residues from both monomers and well defined water molecules (**Fig. 3.33a**). The orientation of the symmetry-related protein is slightly different from that of apo-*Cg*FMNAT due to the different space groups, consequently leading to the different orientation of the glucose and weaker interactions as the glucose electron density is less well-defined (**Fig. 3.33a and b**).

DISCUSSION

Novel flavin binding site in *Cg*FMNAT

Our high-resolution structures of yeast FMNAT present the first characterization of a eukaryotic version of this essential enzyme. Although the overall structure of *Cg*FMNAT shares significant similarity with PAPS reductase-like family of proteins, as reflected in several shared ATP nucleotide binding motifs, it is the only member in the superfamily that binds to flavins. Unexpectedly, the mode of flavin binding by *Cg*FMNAT has not been observed before. In a 2001 survey by Dym and Eisenberg[209], all FAD-binding proteins with known 3D structures were categorized into four different groups, represented by glutathione reductase, ferredoxin reductase, *p*-cresol methylhydroxylase and pyruvate oxidase, respectively. *Cg*FMNAT is clearly distinct from any of these FAD-binding proteins in both the conserved sequence motifs and in flavin-binding mode. In Rossmann-fold FAD-binding proteins (e.g., glutathione

reductase and pyruvate oxidase groups) the isoalloxazine ring of FAD invariably binds on the side of the central β-sheet opposite from the adenine moiety and across the top of the sheet between β1 and β4 (**Fig. 3.34a and b**). It often interacts with residues from another domain. In contrast, in *Cg*FMNAT, the isoalloxazine ring binds to the face of the central β-sheet on the same side as the adenine, and the binding involves exclusively residues from the Rossmann-like N-terminal domain. The deviation from the typical Rossmann-fold topology, characterized by an anti-parallel strand β5 at the edge of the β-sheet, opens up the side of the β-sheet to form the flavin-binding pocket. In the *Cg*FMNAT product ternary complex structure, FAD adopts a bent conformation with adenosine moiety and isoalloxazine ring pack against each other. While the FAD cofactor in most flavoproteins adopts an extended conformation, bent FAD has been observed in flavodoxin reductase and DNA photolyase[209]. Yet, the conformations of these bent FADs are very different from that in *Cg*FMNAT (**Fig. 3.35**), further emphasizing the unique flavin-binding mode of eukaryotic FMNAT.

*Cg*FMNAT and its closely related members of the PAPS reductase-like family contain a unique ARG1-motif and an anti-parallel strand β5 at the edge of the β-sheet followed by a loop connecting β5 to β6. These structure elements form part of the flavin-binding pocket. Helices at the corresponding position in

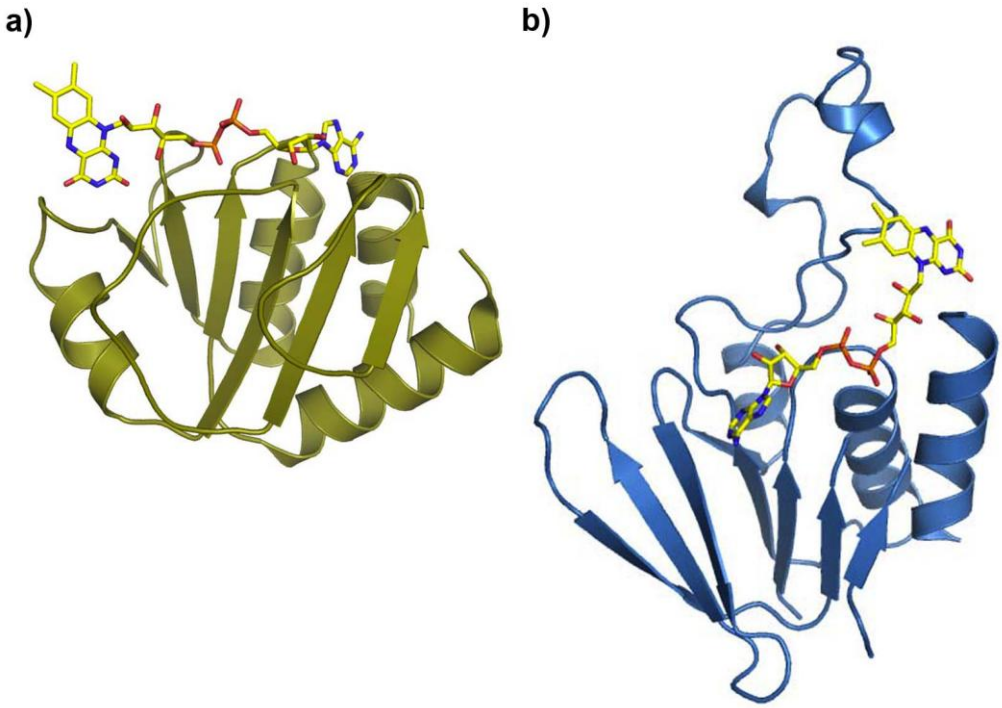

Figure 3.34 Ribbon representations of FAD binding proteins. a.) Rossmann-like fold present in pyruvate oxidase[211]. b.) Rossmann fold present in NADH peroxidase[212].

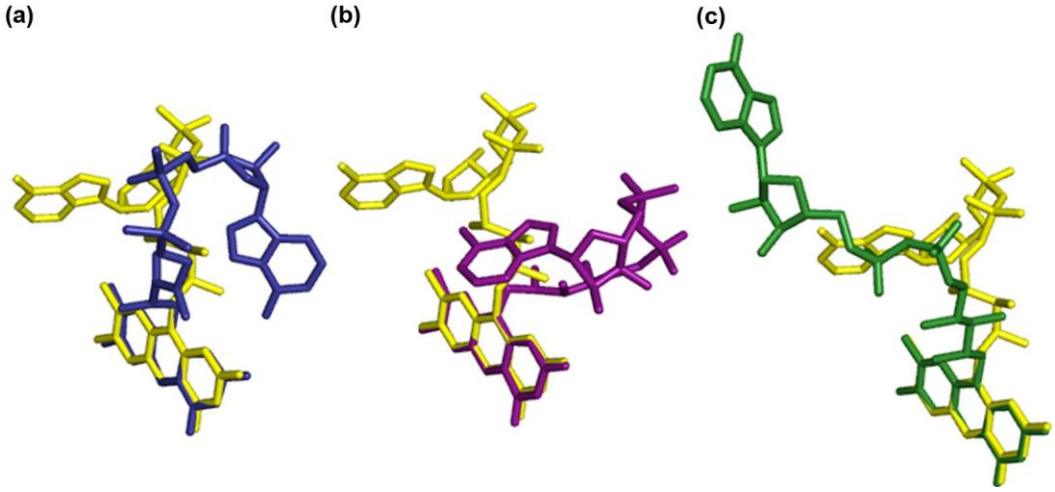

Figure 3.35 Comparison of protein-bound FAD conformations. Representative protein bound FAD molecules were superimposed over the isoalloxazine rings. FAD bound to CgFMNAT (yellow) is compared to FAD from a) flavodoxin reductase[213] (blue) (PDB code 1fdr); b) DNA photolyase[214] (magenta) (PDB code 1dnp); and c) glutathione reductase[215] (green) (PDB code 3grs).

other members of the superfamily (**Fig. 2.17 and 3.27**) would prevent such a binding pocket. Additionally, both APS reductase and *Cg*FMNAT also share an ARG2-motif at the C-terminus of the proteins. Whether the motif is present in PAPS reductase and ATP sulfurylase is unknown as the C-termini of the proteins are disordered in the models. Based on the sequence alignment, PAPS reductase and ATP sulfurylase appear to alter the conservation of the two arginines (**Fig. 2.1**). Conversely, structure variation exists in the PAPS reductase-like family, such as *Cg*FMNAT and ATP sulfurylase having an extended C-terminus. In the current model of ATP sulfurylase[139] 88 residues following the γ-phosphate motif are disordered, therefore are not modeled. Both proteins are the only members that have a conserved Lys (Lys65 and Lys37, respectively) and Asp (Asp66 and Asp38, respectively) in the PP-loop. Conservation of the Asp may explain that both *Cg*FMNAT and ATP sulfurylase have an ATP pyrophosphatase activity.

From a structure-based multiple sequence alignment, eukaryotic FMNAT shows evolutionary divergence from members of the PAPS reductase-like family. The Asn62 of the PP-loop, Tyr216 of the γ-phosphate motif and the flavin motif are unique to *Cg*FMNAT. The interaction with the α-phosphate of the nucleotide with the PP-loop is different from other members in PAPS reductase-like family, and could be a result of the substitution of Ser by Asn in eukaryotic FMNATs. The C-terminal domain provides additional interactions with the γ-phosphate from

Tyr216 and Ser222. The additional interactions with the phosphates of ATP may play a role in positioning the phosphates of ATP without the need of a second cation binding site.

Based on the superposition of different structural states of *Cg*FMNAT, the substrate binding and product formation occur in the absence of large conformational changes. However, subtle conformational changes are prevalent (**Fig. 3.10 and 3.11a and b**). Such as the alternate conformations of the ARG2 motif, with Arg297 and Arg300 exchanging interactions with the diphosphate moiety of product FAD (**Fig. 3.25**). Moreover, with Arg297 forming a hydrogen bond with the alternant FMN phosphoribityl tail (**Fig. 3.23**) suggests that the ARG2 motif may guide the FMN phosphoribityl tail toward the α-phosphate of ATP and stabilize the transition state during catalysis.

Bacterial and eukaryotic FMNATs – a case of convergent evolution

A comparison of the structures of *Cg*FMNAT, a prototypical eukaryotic FMNAT, and bacterial FMNAT as exemplified by *Tm*FADS[169] reveal remarkable differences in substrate binding modes and in the catalytic site configurations. *Tm*FADS belongs to the large nucleotidylyl transferase superfamily with the signature (H/T)xGH motif located between the end of the first β-strand and the first helix of the Rossmann-fold core. It has a different conformation from that of the corresponding PP-loop region of *Cg*FMNAT (**Fig. 3.36**). The second

conserved motif of the nucleotidylyl transferase superfamily, ISSTxxR, is located at the N-terminal end of an α-helix in a C-terminal subdomain and interacts with the β- and γ-phosphates of the ATP nucleotide. No equivalent structural motif corresponding to ISSTxxR exists in *Cg*FMNAT, though the γ-Phosphate motif appears to perform a similar role. Most strikingly, the bound adenine nucleotides in the two proteins are orientated in opposite directions with regard to the plane of the central β-sheet (**Fig. 3.36**), delineating two completely different nucleotide-binding modes in these two protein superfamilies. Currently, no flavin-bound bacterial FMNAT structure is available. Based on the structural similarity of *Tm*FADS to other members of nucleotidylyl transferases, such as nicotinamide mononucleotide adenylyltransferases (NMNAT) for which extensive structural information are available[134-136], the FMN substrate likely binds to a site corresponding to the NMN-binding site in NMNAT on the opposite side of the central β-sheet from ATP so that the product FAD adopts a largely extended conformation (**Fig. 3.36**). Again, this arrangement is very different from the flavin-binding mode observed in *Cg*FMNAT (**Fig. 3.36**). Thus, eukaryotic and bacterial FMNAT present a remarkable case of ancient Rossmann-fold proteins that, after first diverging into two distinct protein families with different nucleotide-binding modes, have developed the same enzymatic activity through different active site configurations.

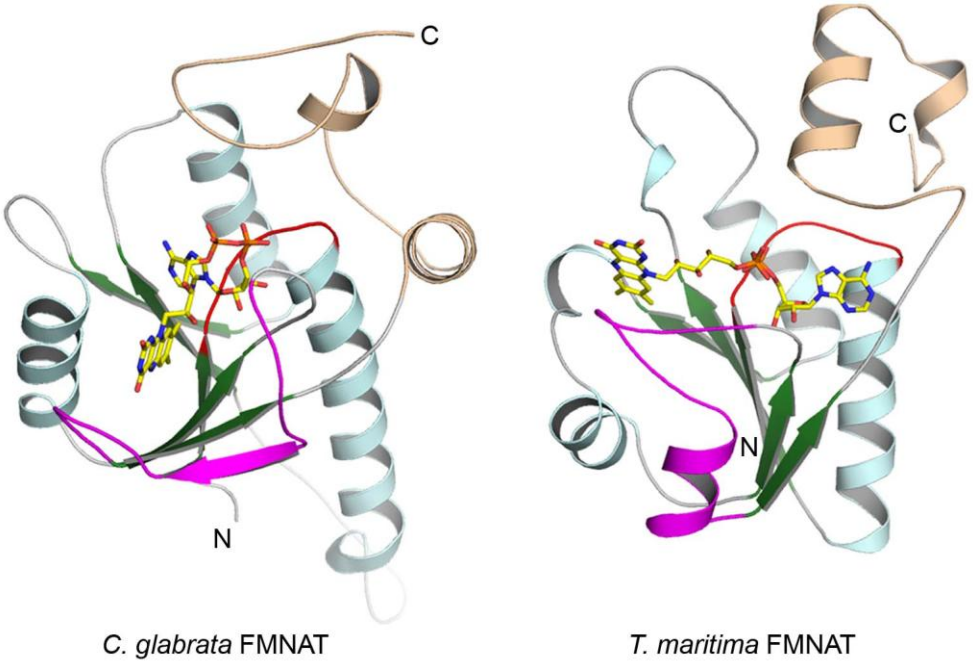

Figure 3.36 Comparison of eukaryotic and bacterial FMNAT structures. Ribbon diagrams of the Rossmann-like fold core of *Cg*FMNAT-FAD complex (*left*) and the FMNAT domain of *Tm*FADS (*right*) are shown in roughly the same orientation. An FAD molecule is modeled in the *Tm*FMNAT active site based on the *Tm*FADS-AMP complex structure (PDB identifier 1t6y)[169] and homologous NMNAT-NAD complex structures. Corresponding structural elements are colored identically in the two structures.

In summary, we present here high-resolution structures of a eukaryotic FMN adenylyltransferase in different complexed states, which reveal details about the active site configuration and a unique FAD-binding mode. Aside from the nucleotide interactions being contributed from the conserved nucleotide binding motifs shared in the PAPS reductase-like family, *Cg*FMNAT complexes revealed additional nucleotide binding motifs, namely the ARG1 and ARG2 motifs. The distinctly conserved Asn residue of the eukaryotic FMNAT PP-loop motif interacts with the ATP differently from that observed for the highly conserved Ser in other members of the family, as well as members of the superfamily, which leads to an alternate conformation of the ATP phosphates. Residues involved in flavin interactions are identified from the previously uncharacterized and unique flavin motif. These structures lay a foundation for future investigation of the functional roles of active-site residues and the kinetic mechanism of the enzyme.

CHAPTER 4

Steady-state kinetics and mutagenic analysis

(Parts of this chapter are adapted from Huerta *et al*., 2009)

INTRODUCTION

Endogenous mammalian FMNAT has been studied extensively by steady-state kinetics. These studies include determining flavin specificity using FMN analogs as substrates to synthesize FAD analogs, cation selectivity and product inhibition[145,146,150]. Mammalian FMNAT catalyze the formation of FAD through an ordered bi-bi mechanism with the substrate binding order being ATP binds first followed by FMN and the product release order of PP_i first followed by FAD[145]. Similar kinetic properties and the same substrate binding and product release order are determined for bacterial FMNAT[70]. Pronounced product feedback inhibition was observed for rat liver FMNAT, and it was suggested that such a property would enable FMNAT to play a role in regulating cellular FAD homeostasis as the K_i values of FAD against FMN (0.75 μM) and Mg^{2+}ATP (1.3 μM) are close to the concentration of free FAD (0.4 μM)[145]. Maintenance of FAD homeostasis is important, as several cellular processes, such as oxidative protein folding and homocysteine metabolism are sensitive to FAD levels[151,152]. Product inhibition seems to be specific for eukaryotic FMNATs. Although no such studies

are reported for bacterial FMNAT, the protein is not co-purified with any flavin product[168,169,216], suggesting a much less pronounced product inhibition.

From the thorough structural analysis of the four different structural states of *Cg*FMNAT, residues involved in substrate and product interactions, and potentially involved in catalysis were suggested. To investigate the role of these active site residues and to understand the catalytic mechanism of FAD synthesis by eukaryotic FMNAT, mutagenesis and steady-state kinetics were performed. The results allowed us to propose the substrate binding and product release order, which is similar to that reported for the mammalian enzyme in a previous study[145]. Site-directed mutagenesis identified, unexpectedly, several "supermutants", in which the turnover rates are much faster than the wild-type enzyme. Product inhibition analysis of the wild-type and a "supermutant" *Cg*FMNAT suggests that the enhanced activity is at least partially due to a relaxed product inhibition.

MATERIALS

Inorganic pyrophosphatase (PPase), purine nucleoside phosphorylase (PNP), FMN, ATP, FAD, sodium pyrophosphate, trisodium citrate dihydrate, ammonium molybdate tetrahydrate, malachite green oxalate salt and all other reagents were purchased from Sigma-Aldrich (St Louis, MO), unless stated

otherwise. 2-amino-6-mercapto-7-methylpurine riboside (MESG) was purchased from Berry & Associates (Ann Arbor, MI). EnzChek pyrophosphate assay kit was purchased from Molecular Probes (Eugene, OR). QuikChange site-directed mutagenesis kit was purchased from Stratagene (La Jolla, CA). Primers were ordered from Integrated DNA Technologies (Coralville, IA) and Sigma-Aldrich Corp. (The Woodlands, TX).

METHODS

Mutagenesis, protein expression and purification

Point mutations of *Cg*FMNAT were generated with primers containing the desired mutations using QuikChange site-directed mutagenesis PCR amplification procedure. The mutants generated were N62A, N62S, D66A, D168A, D181A, W184A, R297A and a deletion mutant was also generated where the last three lysines were removed (Δ3K). The forward and reverse primers for each mutant (with mutagenesis site underlined), along with the theoretical T_m and mutated nucleic acid bases are listed in **Table 4.1**. Incorporation of the desired mutants was confirmed by DNA sequencing from the McDermott Center at The University of Texas Southwestern Medical Center. Protein expression and purification were performed using the same procedure as that for apo-*Cg*FMNAT, except the last purification step. The phenyl-sepharose hydrophobic interaction

Table 4.1

Mutant[a]	Primer Sequence[b]	T_m[c]
N62A (AAT→GCT)	5'-GGTGAAATATCGTTTTCCTATGCTGGAGGCAAAGACTGCCAGGTG-3' 3'-CCACTTTATAGCAAAAGGATACGACCTCCGTTTCTGACGGTCCAC-5'	82.1ºC
N62S (AAT→TCA)	5'-GGTGAAATATCGTTTTCCTATTCAGGAGGCAAAGACTGCCAGGTG-3' 3'-CCACTTTATAGCAAAAGGATAAGTCCTCCGTTTCTGACGGTCCAC-5'	79.0ºC
D66A (GAC→GCT)	5'-CGTTTTCCTATAATGGAGGCAAAGCTTGCCAGGTGCTGTTATTACTATA-3' 3'-GCAAAAGGATATTACCTCCGTTTCGAACGGTCCACGACAATAATGATAT-5'	80.4ºC
D168A (GAT→GCT)	5'-GTCATCGGTATAAGACACACTGCTCCATTTGGCGAGCATTTAAAG-3' 3'-CAGTAGCCATATTCTGTGTGACGAGGTAAACCGCTCGTAAATTTC-5'	82.5ºC
D181A (GAT→GCT)	5'-AAGCCTATTCAAAAGACAGCTGCTAATTGGCCAGATTTC-3' 3'-TTCGGATAAGTTTTCTGTCGACGATTAACCGGTCTAAAG-5'	78.4ºC
W184A (TGG→GCT)	5'-CCTATTCAAAAGACAGATGCTAATGCTCCAGATTTCTATCGTCTACAACCT-3' 3'-GGATAAGTTTTCTGTCTACGATTACGAGGTCTAAAGATAGCAGATGTTGGA-5'	78.5ºC
R297A (AGA→GCT)	5'-GTACCTAGTCGATGACAAACTTGAAGCTGCAGGAAGAATTAAAAAGAAATGAG-3' 3'-CATGGATCAGCTACTGTTTGAACTTCGACGTCCTTCTTAATTTTTCTTTACTC-5'	78.6ºC
Δ3K (AAA→TAA)	5'-TGAAAGAGCAGGAAGAATTTAAAAGAAATGAGTCGACGAGC-3' 3'-ACTTTCTCGTCCTTCTTAAATTTCTTTACTCAGCTGCTCG-5'	78.6ºC

[a]Codons in parenthesis list the change from the native codon to the mutant codon.
[b]The forward and reverse primers for each mutant are listed with the mutagenesis site underlined.
[c]Theoretical T_m for primer set.

chromatography step was omitted for D181A and W184A mutants, as the protein samples were clear and contained no detectable flavin. The final step in purification was dialysis in 2 L gel filtration buffer. A UV/visible absorption spectrum for all mutants were performed to ensure no detectable flavin in the protein. Protein purity was monitored by SDS-PAGE and the protein concentration was determined by Bio-Rad protein assay. For native apo-*Cg*FMNAT kinetic studies, previously purified protein was utilized.

Steady-state kinetics analysis

A continuous spectrometric assay that couples the release of the product inorganic pyrophosphate (PP_i) to the generation of 2-amino-6-mercapto-7-methylpurine[217,218] was utilized to measure the steady-state kinetics of native and mutant *Cg*FMNATs (**Fig. 4.1a**). The rate of FAD formation by FMNAT is measured spectrometrically by the conversion of PP_i to inorganic phosphate (P_i) through PPase, which is then used to convert MESG to its products ribose-1-phosphate and 2-amino-6-mercapto-7-methylpurine by PNP. Conversion of MESG to 2-amino-6-mercapto-7-methylpurine results in an increase in absorption at 360 nm. To measure the initial rates of native *Cg*FMNAT, the reaction mixture (0.5 ml) contained 20 mM HEPES, pH 7.5, 2 mM magnesium chloride, 0.5 units PNP, 0.015 units PPase, 0.2 mM MESG, 21 nM (10.5 pmole or 378 ng) apo-*Cg*FMNAT, 2.5 to 20 μM FMN and 1 to 250 μM ATP. All enzyme reactions

a.)

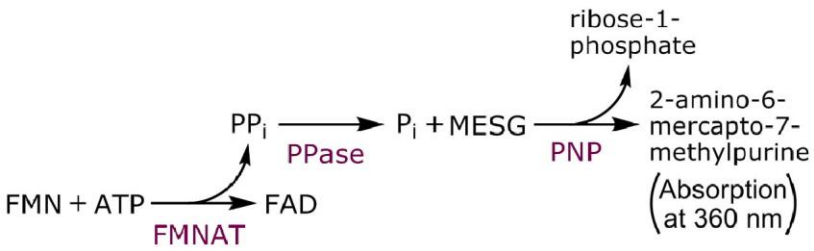

b.)

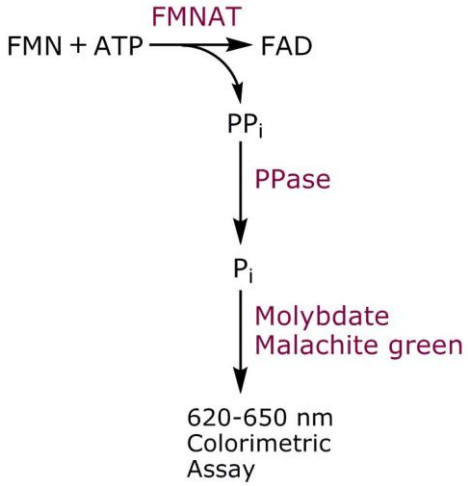

Figure 4.1 Scheme for coupled FMNAT assays. The rate of FAD formation by FMNAT is measured by the release of inorganic pyrophosphate (PP_i), which is converted to inorganic phosphate (P_i) through inorganic pyrophosphatase (PPase). a.) For the end-point assay, the P_i interacts with the malachite green reagent that cause an increase in absorption between 620-650 nm. b.) For the continuous coupled assay, MESG is converted to its products ribose-1-phosphate and 2-amino-6-mercapto-7-methylpurine by purine nucleoside phosphorylase (PNP) in the presence of P_i. Conversion of MESG to 2-amino-6-mercapto-7-methylpurine results in an increase in absorption at 360 nm.

were carried out in duplicates using a Quartz cuvette and performed at 25 °C. The reaction was initiated by the addition of 10 μl of enzyme, and progress was monitored by absorption at wavelength 360 nm for 5 minutes on a Beckman Coulter DU 640 spectrophotometer. As a blank, apo-*Cg*FMNAT was left out of the reaction mixture. Residual enzymatic activity was measured by saturating the reaction with 100 μM ATP and omitting FMN, or with 100 μM ATP and 20 μM FMN and omitting magnesium chloride. For each mutant, the protein concentration in the reaction mixture was ~21 nM for determining percent specific activity (nmole/min/mg protein), with ATP and FMN concentrations at 100 μM and 20 μM, respectively. For determination of steady-state kinetic parameters the protein concentrations used were: ~40 nM for N62A, ~80 nM for D168A, ~7 nM for D181A, ~300 nM for W184A and ~15.8 nM for R297A. A substrate concentration range of 5 to 500 μM FMN and 10 to 800 μM ATP was used for W184A mutant.

Steady-state kinetic parameters for native *Cg*FMNAT were determined by fitting the initial rates from multiple fixed FMN concentration while varying the ATP concentration (and vice versa) to the general equation (1) describing a bireactant ordered bi-bi system[219] (Eq. (1)).

$$\nu = \frac{V_{max}[\mathrm{ATP}][\mathrm{FMN}]}{\left(K_{iATP}K_{mFMN} + K_{mFMN}[\mathrm{ATP}] + K_{mATP}[\mathrm{FMN}] + [\mathrm{ATP}][\mathrm{FMN}]\right)} \qquad (1)$$

$K_{m,ATP}$ and $K_{m,FMN}$ are the Michaelis-Menten constants, and $K_{i,ATP}$ is the dissociation constant for an ATP-enzyme complex. For Eq. (1) a nonlinear least-squares method as implemented in the Sigma Plot Enzyme Kinetics module (Systat Software, http://www.sigmaplot.com/home.php) was used to global fit the data.

For native and mutant *Cg*FMNATs the apparent steady-state kinetic parameters were determined by fitting the initial rates to the general Michaelis-Menten equation (2) (Eq. (2)).

$$\nu = \frac{V_{max,app}[S]}{(K_{m,app} + [S])} \qquad (2)$$

$K_{m,app}$ is the apparent Michaelis-Menten constant, and [S] is the concentration of ATP when FMN is at saturated concentration (20 μM) or FMN when ATP is at saturated concentration (100 μM). A nonlinear least-squares method as implemented in Sigma Plot was used to fit the data.

Product inhibition analysis

A colorimetric end-point assay was utilized to measure product inhibition by FAD. The assay method measures the formation of PP_i by the hydrolysis to P_i through PPase using a modified malachite green end-point assay[220-222] (**Fig. 4.1b**). The malachite green end-point assay was used due its sensitivity to low phosphate concentrations and to avoid the potential interference from the flavin absorption

in the UV range. During the development of the product inhibition assay for *Cg*FMNAT, it is observed that the incubation time of FAD with *Cg*FMNAT affects the reaction rate. Therefore, the product inhibition assays were performed after incubation of FAD with the protein for 30 minutes. The reaction mixture (0.3 ml) contained 20 mM HEPES, pH 7.5, 2 mM magnesium chloride, 0.06 units PPase, 50 μM ATP, 10 μM FMN, 0.8 μM FAD and 5 nM (1.5 pmole or 53.9 ng) D181A mutant. The protein was preincubated with 0.8 μM FAD on ice for 0, 5, 30 and 50 minutes before initiating the reaction. All enzyme reactions were carried out in duplicates using polystyrene cuvettes and performed at 25 °C. The reaction was initiated by the addition of 10 μl of the enzyme and allowed to progress for 1 to 18 minutes, prior to stopping the reaction with 300 μL of the malachite green reagent. The color development was quenched after 2 minutes with 60 μL of quenching solution and incubated for 20 minutes at 25 °C before measuring the absorbance at wavelength 650 nm. Three different time points were collected within the linear range for determining the initial rates. As a blank, apo-*Cg*FMNAT was left out of the reaction mixture. The stock solutions for the assay were prepared as follow: reagent A, 41.9 mM ammonium molybdate in ddH_2O; reagent B, 3.1 M H_2SO_4; reagent C, 1.13 mM malachite green in ddH_2O; and reagent D, 0.660 % Poly (vinyl alcohol) in ddH_2O. The malachite green reagent was prepared by mixing the reagents to provide a final solution of 12.04 mM

ammonium molybdate, 0.9 M H_2SO_4, 0.24 mM malachite green, 0.14 % poly (vinyl alcohol). The malachite green reagent was filtered with a 0.2 μm syringe filter. A quenching solution was prepared with 40% (w/v) trisodium citrate dihydrate. All reagents were stored at 4ºC.

Product inhibition studies with native apo-*Cg*FMNAT and D181A mutant were conducted similarly to that as stated above using the malachite green end-point assay (**Fig. 4.1b**). The reaction mixture (0.3 ml) contained 20 mM HEPES, pH 7.5, 2 mM magnesium chloride, 0.06 units PPase, 21 nM (6.3 pmole or 277 ng) apo-*Cg*FMNAT or 5 nM (1.5 pmole or 53.9 ng) D181A mutant. In the reaction mixture, the concentration of the fixed substrate ATP or FMN was 6 μM and 4 μM for apo-*Cg*FMNAT, and 50 μM and 6 μM for D181A mutant, respectively. Inhibition by the product FAD was conducted at different concentrations of FAD (0, 0.1, 0.4, 0.8 μM) in the reaction mixture. For product inhibition with respect to ATP, the FMN concentration was held constant while varying the ATP concentration (2 to 100 μM for native FMNAT and 5 to 100 μM for D181A mutant). For product inhibition with respect to FMN, the ATP concentration was held constant while varying the FMN concentration (1 to 20 μM). The enzymes were preincubated with the appropriate concentration of FAD for 30 minutes on ice. The reaction was initiated by the addition of 10 μl of the

enzyme and allowed to progress for 1 to 18 minutes prior to stopping the reaction and allowing the color to develop before quenching.

The effect of product inhibition by FAD on the initial rates of native and D181A *Cg*FMNAT was investigated in order to provide support for the proposed substrate binding order and to evaluate the inhibitory effect brought upon by FAD. Initial rates were fitted to the general inhibition equation (3) (commonly referred to as mixed-type inhibition) for readily reversible inhibitors[219,223] (Eq. (3)).

$$v = \frac{V_{max}[S]}{\left(K_m(1+[I]/K_i)+[S](1+[I]/\alpha K_i)\right)} \qquad (3)$$

Where K_i is the inhibition constant, α is a quantitative parameter that provides a measure of the type of inhibition[219,223], and [I] is the concentration of the inhibitor (FAD). Deducing the type of inhibition is based on the value of α, where $\alpha = \infty$ indicates competitive inhibition; $\alpha = 1$ indicates noncompetitive inhibition; and $\alpha < 1$ or $\alpha > 1$ indicates mixed-type inhibition. For Eq. (3) a nonlinear least-squares method as implemented in the Sigma Plot Enzyme Kinetics module (Systat Software, http://www.sigmaplot.com/home.php) was used to global fit the data.

RESULTS

Steady-state kinetic analysis of *Cg*FMNAT

The steady-state kinetic parameters of *Cg*FMNAT were determined using the continuous coupled assay[217,218]. The Lineweaver-Burk reciprocal plots of 1/*v* vs. 1/[FMN] and 1/*v* vs. 1/[ATP] (**Fig. 4.2a and b**) are consistent with an ordered bi-bi mechanism[219], with the substrate binding order being ATP first followed by FMN. The same mechanism and substrate binding order were also proposed for rat liver and bacterial FMNATs in early studies[70,145]. The initial rates of the reaction were globally fitted to the general equation for an ordered steady-state bireactant model (insets of **Fig. 4.2a and b**). The steady-state kinetic parameters obtained for *Cg*FMNAT are: K_m for ATP 10.7 ± 2.3 μM, K_m for FMN 0.76 ± 0.15 μM, and k_{cat} 0.087 s^{-1}. The $K_{m,FMN}$ value for *Cg*FMNAT is similar to that obtained for human FMNAT isoform II in a recent study (apparent $K_{m,\mathrm{FMN}}$ 0.36 ± 0.06 μM), while the k_{cat} appears to be more than ten times higher than that of the human enzyme (0.0036 ± 0.0001 s^{-1})[112]. These values are somewhat different from those obtained for the endogenous rat-liver FMNAT, where the apparent K_m for ATP and FMN are 71 μM and 9.1 μM, respectively, with a V_{max} of 345 nmole FAD/min/mg of protein[145], corresponding to a k_{cat} of 0.15 s^{-1}.

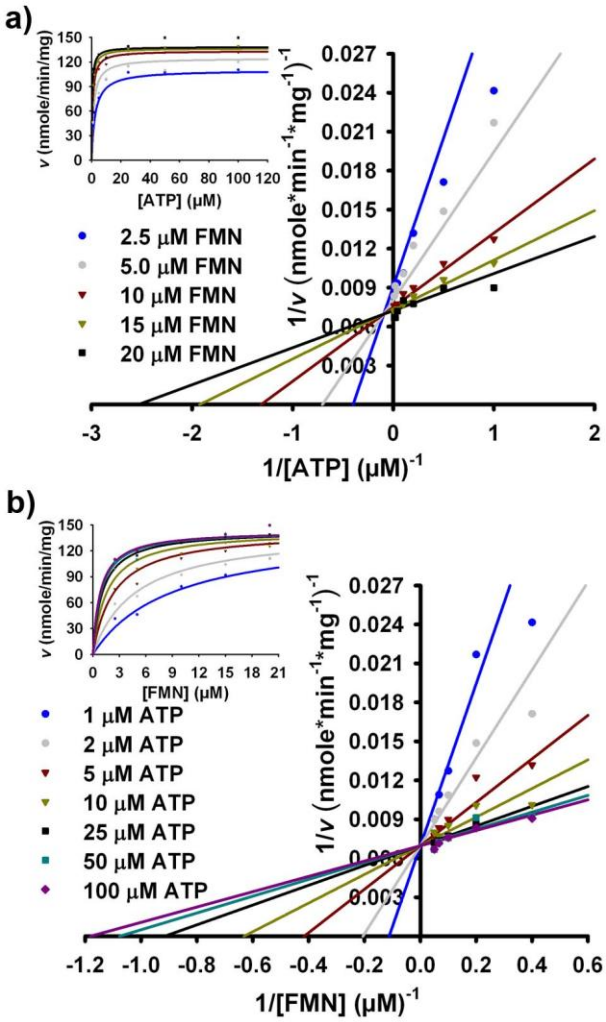

Figure 4.2 Adenylyl transfer mechanism for *Cg*FMNAT. a) Initial rates represented by the Lineweaver-Burk plots of 1/*v versus* 1/[ATP] at fixed FMN concentrations. Inset: The same data represented by a hyperbolic plot (inset) as a function of ATP concentration. b) Initial rates represented by the Lineweaver-Burk plot of 1/*v versus* 1/[FMN] at fixed ATP concentrations. Inset: The same data represented by a hyperbolic plot (inset) as a function of FMN concentration. The rates in a) and b) were global fitted to the velocity equation for an ordered bi-bi (Eq. (1)) reactant system.

Investigating roles of active site residues by mutagenesis

Based on sequence and structural analysis a set of active site residues was selected for mutagenesis studies to investigate their roles in substrate binding and/or catalysis (**Table 4.1**). Mutating the PP-loop motif residues (N62A, N62S and D66A) resulted in a drastic decrease in the enzyme specific activity. When mutating N62 to an Ala, the mutant retains about 58% of the specific activity compared to the native *Cg*FMNAT. However, mutating Asn62 to a Ser, an amino acid conserved in the superfamily, unexpectedly resulted in a practically inactive enzyme. Mutating the Mg^{2+} ion coordinating Asp66 to an Ala also resulted in a practically inactive enzyme, indicating the essential role of Asp66 to directly ligate to the catalytic Mg^{2+} ion. The ARG1 motif D168A mutant resulted in a moderate loss of ~60% specific activity. D168 coordinates two conserved water molecules that are the ligands of the catalytic Mg^{2+} ion. Therefore, D168 is indirectly involved in the catalysis. A similar loss of specific activity is seen with the flavin motif W184A mutant, which would lead to the loss of the stacking interaction with the isoalloxazine ring of FMN. Removing the last three positively charged lysines (Δ3K) of the ARG2 motif resulted in no appreciable difference in specific activity. Unexpectedly, specific activities of D181A of the flavin motif and R297A of the ARG2 motif increased significantly, nearly seven- and two-

times greater than native *Cg*FMNAT, respectively, and are thus referred to as "supermutants" (**Fig. 4.3**).

To assess the effect of the mutants on substrate interactions and turnover rate (k_{cat}), steady-state kinetic parameters were determined for *Cg*FMNAT mutants, except for N62S and N66A which have no measureable activity, and are listed in **Table 4.2**. As predicted, N62A and D168A mutants resulted in a decreased apparent k_{cat}. Interestingly, N62A mutant has a much lower apparent $K_{m,ATP}$ than native *Cg*FMNAT, which was not expected as the loss of the ATP interaction by Asn62 was predicted to increase the apparent $K_{m,ATP}$. D168A mutant gave a much higher apparent $K_{m,ATP}$, consistent with D168's role in ATP substrate and metal ion interactions. The "supermutant" D181A, which was designed to weaken the interaction with FMN, has an increased apparent k_{cat} about nine-times of native *Cg*FMNAT. Additionally, D181A has relatively no effect on the apparent $K_{m,FMN}$, but has an increased apparent $K_{m,ATP}$ of ~3 times that of the wild-type enzyme. In contrast to D181A, the loss of the stacking interactions with FMN by W184A mutant resulted in a considerable increased apparent $K_{m,FMN}$ of ~200 times that of the wild-type enzyme. W184A also resulted in an increased apparent $K_{m,ATP}$. Interestingly, the apparent k_{cat} increased ~2–3 times of the wild-type enzyme. Originally, mutating R297 to an Ala was expected to increase the apparent $K_{m,FMN}$. Consequently, the apparent $K_{m,ATP}$

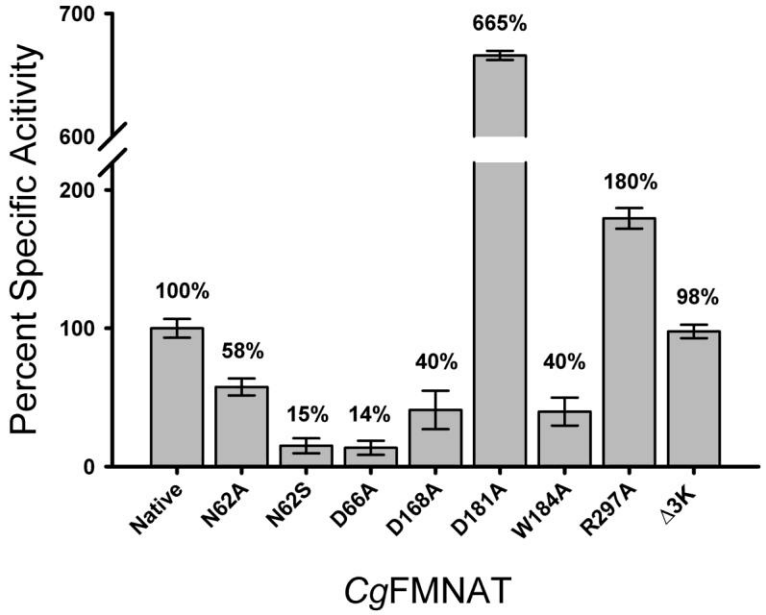

Figure 4.3 Percent specific activity (nmole/min/mg protein) of *Cg*FMNAT mutants.

Table 4.2

Apparent K_m and k_{cat} for native *Cg*FMNAT and mutants

*Cg*FMNAT	Motif	Functional role[1]	$K_{m,ATP}$ (μM)	k_{cat} (s^{-1})	$K_{m,FMN}$ (μM)	k_{cat} (s^{-1})
Native			2.0 ± 0.3	0.1	1.0 ± 0.4	0.09
N62A	PP-loop	ATP phosphate binding	0.5 ± 0.2	0.04	n.d.[2]	n.d.
D168A	ARG1	Indirect ligand to Mg^{2+}	24.9 ± 8.9	0.03	n.d.	n.d.
D181A	Flavin	Isoalloxazine ring binding	6.4 ± 0.4	0.8	1.5 ± 0.4	0.9
W184A[3]	Flavin	Isoalloxazine ring binding	23.6 ± 4.6	0.2	199.4 ± 27.9	0.3
R297A	ARG2	ATP and FMN phosphate binding	10.3 ± 1.6	0.2	3.0 ± 0.5	0.2

[1]Functional role based on crystal structures analysis
[2]n.d. means not determined.
[3]The K_m values were determined at non-saturating concentrations of FMN and ATP, respectively.

increased about ~5 times, in addition to the expected increase of the apparent $K_{m,FMN}$, which increased marginally (~3 times) (**Table 4.2**). Despite the increases in the apparent K_m, the "supermutant" R297A has an increased apparent k_{cat} of about two-times of native *Cg*FMNAT. These results indicate that R297 is involved in binding of both ATP and FMN, which is consistent with the observation in the product and substrate ternary complexes, where R297 is in position to interact with the adenylyl phosphate of FAD and the FMN phosphate, respectively (**Fig. 3.23 and 3.24**).

Product feedback inhibition analysis

It was observed that the incubation time of FAD with the D181A "supermutant" affects the reaction rates. When the reaction is initiated by mixing the reaction mixture containing FAD with D181A "supermutant", the initial rate is 614.7 nmole/min/mg of protein compared to that of 741.8 nmole/min/mg of protein in the absence of FAD (**Fig. 4.4**). However, when the enzyme is preincubated with FAD for 10 or 30 minutes the initial rate decreases by half (338.5 and 315.5 nmole/min/mg of protein, respectively), suggesting that free FAD binds slowly to the enzyme and eventually reaches equilibrium as there is practically no change in rates between the 10 and 30 minute incubation time. However, the rate after preincubation with FAD for 50 minutes is slightly higher (431.5 nmole/min/mg of protein) than after the 10 or 30 minute preincubation.

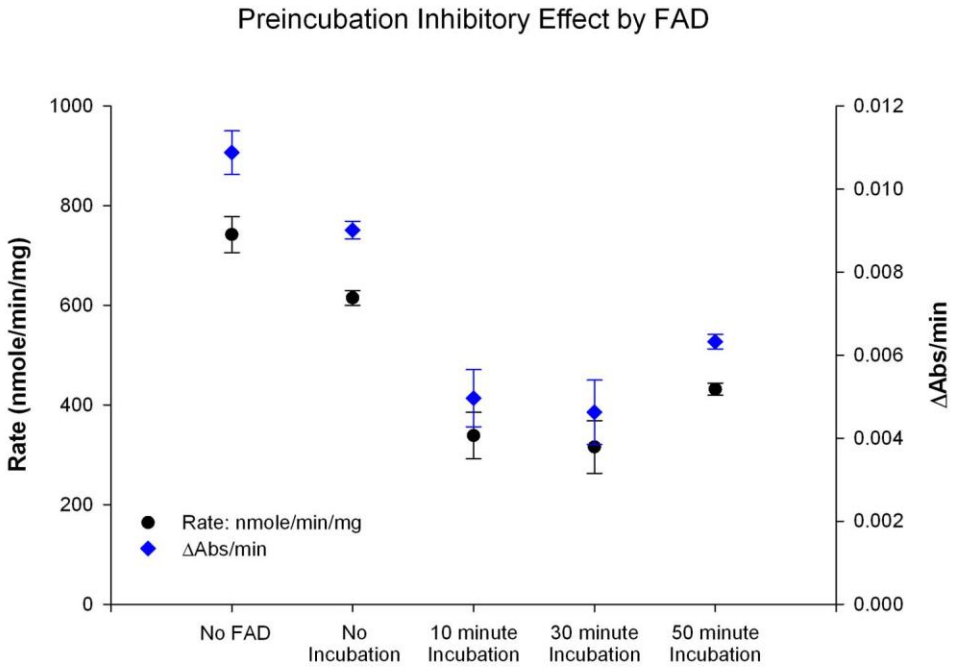

Figure 4.4 Initial rates after different preincubation times of protein with FAD. The left y-axis reports the initial rates in nmole/min/mg of protein (black circles) and the right y-axis reports initial rates in ΔAbsorption/min (ΔAbs/min; blue diamonds). Standard errors calculated from duplicate measurements.

The increase might be attributed to phosphate contamination.

The effect FAD product inhibition has on the initial rates was investigated to provide support of the proposed substrate binding order, as deduced from the global fitting of the initial rates in the absence of product inhibition, and to understand the observed kinetic parameters of the "supermutant" D181A. The inhibitory effect by FAD is strong as the K_i is 0.10 μM against ATP and 0.12 μM against FMN (**Fig. 4.5a and b**), which is considerably lower than that reported for the endogenous rat liver FMNAT, for which K_i of FAD against ATP and FMN are 1.3 μM and 0.75 μM, respectively. In the case of the "supermutant" D181A, the K_i value of FAD against ATP and FMN is 0.39 μM and 0.67 μM (**Fig. 4.6a and b**), respectively, which is higher than that of the native enzyme. The reciprocal plots of native *Cg*FMNAT (**Fig. 4.5a**) do not fit the profile of the proposed substrate binding order, as FAD does not show competitive inhibition with respect to ATP[219]. The value of $\alpha = 8.6$ suggests that FAD acts as a mixed-type inhibitor with respect to ATP. In light of the slow and tight binding of FAD to the D181A "supermutant", FAD seems to be a slow-tight binding inhibitor of *Cg*FMNAT, in which case the competitive inhibition profile will not be observed[224]. In the case of D181A, the reciprocal plot $1/v$ vs. 1/[ATP] is similar to that of native (**Fig. 4.6a**), with an $\alpha = 2.1$. However, the reciprocal plot of $1/v$ vs. 1/[FMN] for D181A is different from native *Cg*FMNAT, as the lines intersect slightly below

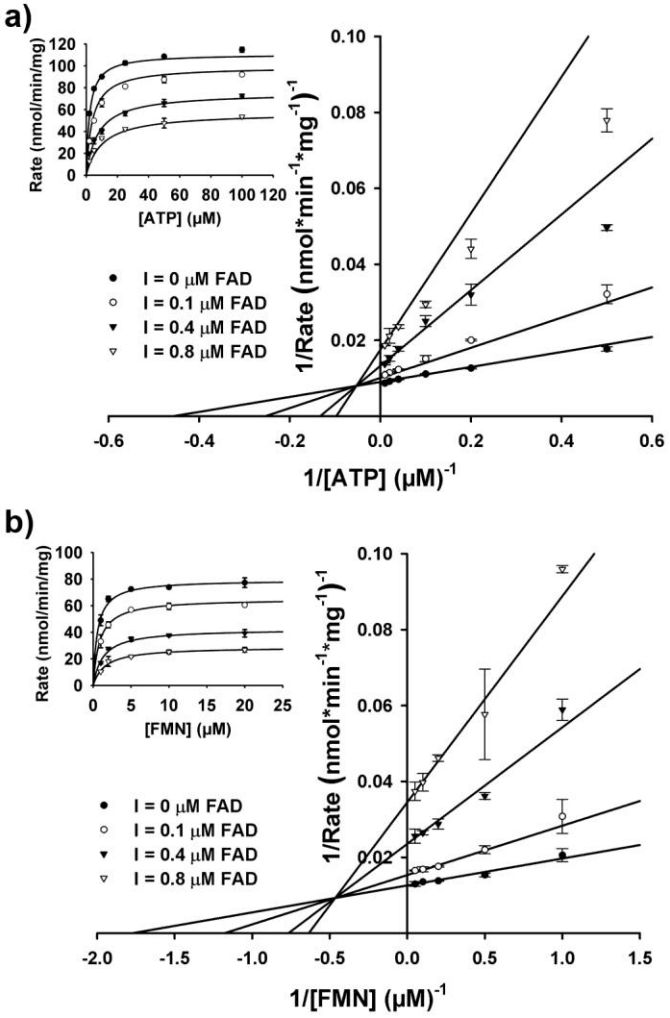

Figure 4.5 Product inhibition of *Cg*FMNAT by FAD. a) Initial rates represented by the Lineweaver-Burk plots of 1/*v versus* 1/[ATP] at fixed FMN concentrations. b) Initial rates represented by the Lineweaver-Burk plot of 1/*v versus* 1/[FMN] at fixed ATP concentrations. The rates in a) and b) were global fitted to the velocity equation for a general inhibition (Eq. (3)) reactant system.

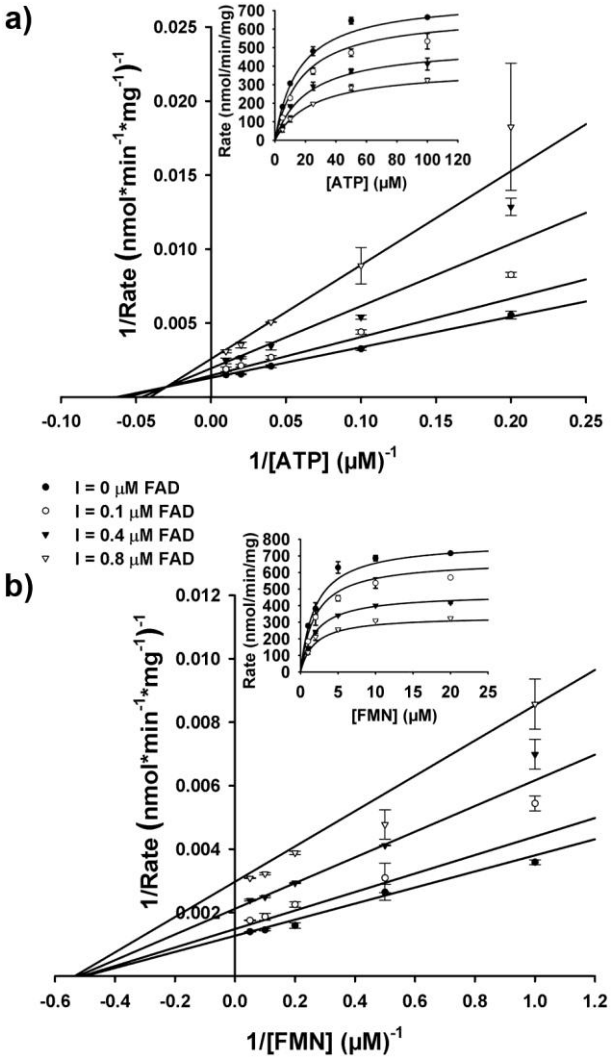

Figure 4.6 Product inhibition of *Cg*FMNAT D181A mutant by FAD. a) Initial rates represented by the Lineweaver-Burk plots of 1/*v versus* 1/[ATP] at fixed FMN concentrations. b) Initial rates represented by the Lineweaver-Burk plot of 1/*v versus* 1/[FMN] at fixed ATP concentrations. The rates in a) and b) were global fitted to the velocity equation for a general inhibition (Eq. (3)) reactant system.

the x-axis (**Fig. 4.5b and 4.6b**). The significance of the profile indicates that the affinity of FMN increase in the presence the inhibitor FAD.

Proposed catalytic mechanism for *Cg*FMNAT

The four high-resolution structures of *Cg*FMNAT (apo form, complexes with ATP, with substrate FMN+AMPCPP, and with products FAD+PP_i) alongwith the steady-state kinetic data allow us to envision the events in the enzyme active site during catalysis (**Fig. 4.7**). In this process, ATP binds preferably first to the enzyme as deduced from the global fitting of the steady-state kinetic data, and the fact that the binding pocket would be partially blocked by FMN, which binds at a site closer to the surface (**Fig. 3.22a and b**). Additionally, binding of ATP first may help properly position the FMN substrate as the C8M methyl group of the isoalloxazine ring is packed against the adenosine moiety of the bound ATP. The binding of ATP induces small adjustment (0.3-0.5 Å) of several surrounding residues, including Asn62, Lys65, Asp66, Ile108, and Asp168, presumably to optimize their interactions with Mg^{2+} and ATP. In the presence of Mg^{2+}, the phosphate tail of ATP can adopt either of the two discrete conformations I or II, in which the Mg^{2+} ion position remains the same (**Fig. 3.24**). Upon subsequent binding of FMN, side chains of several residues around the isoalloxazine ring, e.g., Met143, Phe147, Asp181 and Trp184, also make small adjustments to optimally interact with the substrate. Due to the lack of interaction between the

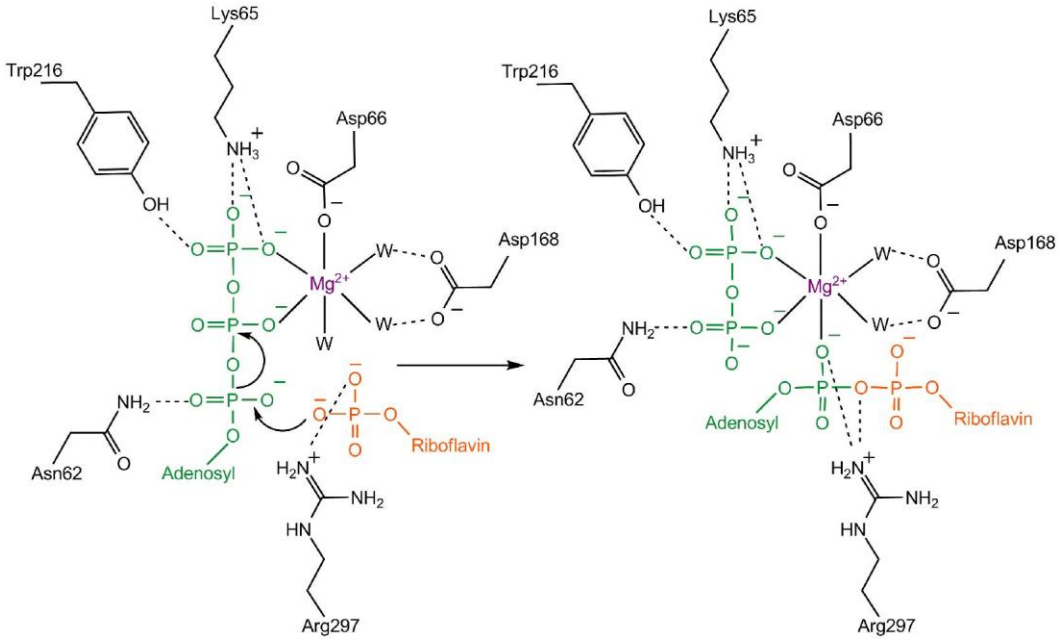

Figure 4.7 Proposed catalytic mechanism of *Cg*FMNAT.

enzyme and the phosphoribityl tail of FMN, this part of the FMN substrate is highly flexible and able to adopt multiple conformations. For the adenylation reaction to occur, the FMN phosphate would move close to the α-phosphate of ATP for the ensuing nucleophilic attack. The presence of Mg^{2+} ion and interaction with Arg297 (and potentially Arg300) of the ARG2 motif may help to overcomethe electrostatic repulsion between the phosphate groups of the two substrates, and position FMN phosphate for the attack on the α-phosphate of ATP. The cleavage of the αβ-phosphodiester bond is facilitated by the coordination of the Mg^{2+} ion, which is required for the reaction. The Mg^{2+}ATP in the Conformer I position appears to be the catalytically competent conformation which allows the FMN phosphate group to approach the α-phosphate from the direction opposite the β-phosphate for the direct in-line nucleophilic attack (**Fig. 4.8**). Minimal structural rearrangements are observed after product formation. The leaving diphosphate group is practically in the same position as the βγ-phosphates of the Conformer I of the nucleotide and interacts with the same set of protein residues and Mg^{2+} ion. The transferred α-phosphate moves about 2.5 Å away from its original position and is now directly liganded to the Mg^{2+} ion (**Fig. 3.24**).

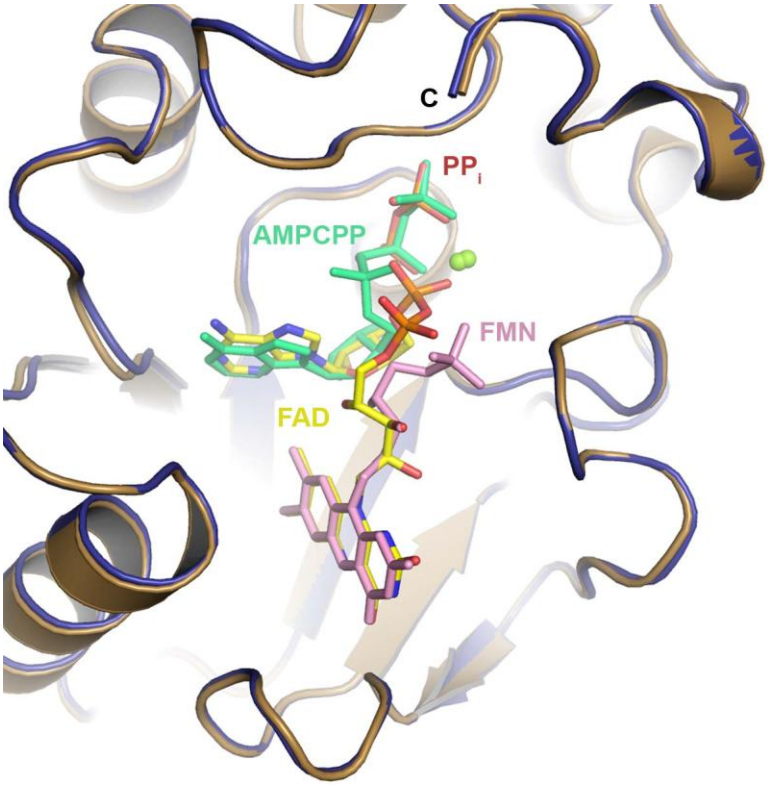

Figure 4.8 Superposition of substrate and product ternary complex monomer E. Substrates FMN (pink) and AMPCPP (teal), and products FAD and PP_i are shown as sticks. FAD and PP_i are colored by atom types with carbon atoms yellow and Mg^{2+} ions shown as a green sphere. Substrate and product ternary complex monomer E is colored brown and dark blue, respectively. The alternate FMN conformation allows the phosphoribityl tail of FMN to position closer to the α-phosphate of AMPCPP.

DISCUSSION

Roles of the catalytic residues

Since the PP-loop motif has sequence and structural similarity within the superfamily, a more in-depth understanding of their functional role in eukaryotic FMNAT may be gained for N62A, N62S and D66A mutants. Of these mutants, the most confounding is the N62A mutant that results in a decreased apparentin the absence of a branched residue, the backbone amide of the conserved Gly64 and Lys65 in the PP-loop may provide additional interactions to β- and γ-phosphate of ATP. Such an interaction is observed in the superfamily for residues equivalent to Lys65 (**Fig. 3.29**). Presumably, mutating Asn62 to a Ser should maintain the hydrogen bond to the α-phosphate of ATP and thus still permit the enzyme to synthesize FAD. Interestingly, the N62S mutant results in a practically dead enzyme. At the moment, there is no clear explanation for this observation. A potential explanation is that the orientation of the phosphates of ATP change upon mutating Asn62 to a Ser, which could be similar to that observed for the nucleotide in ATP sulfurylase[139] and NH^{3+}-dependent NAD synthetase[201] (**Fig. 3.29c and d**). The conformation of the nucleotide observed in ATP sulfurylase and NH^{3+}-dependent NAD synthetase may impede the nucleophilic attack by FMN on the α-phosphate of ATP in *Cg*FMNAT. The critical catalytic role of the

well conserved Asp66 of the PP-loop is confirmed as the D66A mutant produced a catalytic dead enzyme. Since an equivalent aspartate directly coordinates the catalytic Mg^{2+} ion for members of the superfamily, a catalytic dead enzyme should occur upon mutation.

The crystal structures of *Cg*FMNAT revealed for the first time the detailed interactions between the enzyme and the flavin substrate, which are different from that observed in all other flavoproteins. Unexpectedly, there is a lack of interaction between the enzyme and the phosphoribityl tail of FMN. In order for the adenylation reaction to proceed, the phosphoribityl tail of FMN is required to move closer to the α-phosphate of ATP for the ensuing nucleophilic attack. The crystal structures suggest that Arg297 of the ARG2 motif may interact with the FMN phosphate and position it for the ensuing nucleophilic attack on the α-phosphate of ATP (**Fig. 3.23 and 4.8**). Such an interaction is supported by the results from the R297A mutant, where an ~3 times increase in the apparent $K_{m,FMN}$ is observed. Interestingly, R297A also has an increased apparent $K_{m,ATP}$, suggesting Arg297 also has a direct interaction with ATP. Although not observed in the crystal structure (**Fig. 3.18b**), the proximity of the Arg297 side chain to both phosphates of the FAD product, which comes from the ATP α-phosphate and FMN phosphate, it is reasonable to speculate that Arg297 could be involved

in the interaction with the phosphate groups of both substrates, and help to position them for the nucleophilic attack and the adenylyltransfer reaction.

Interaction between ATP and FMN binding site

The most unexpected results are obtained with the "supermutant" D181A. The Asp181 is shown to form two hydrogen bonds with the hetero-atom groups at the hydrophilic edge of the isoalloxazine ring. However the "supermutant" D181A results in no appreciable change in the apparent $K_{m,FMN}$. Instead, the apparent $K_{m,ATP}$ increases ~3 times that of native *Cg*FMNAT. A potential explanation is the loop connecting β5 to β6 that is part of the flavin motif, which contains the mutant, becomes more flexible. For this explanation, the flexibility of the loop minimally perturbs the FMN interactions, but promotes instability in the binding of ATP. In any case, the D181A "supermutant" suggests that for the native *Cg*FMNAT, the substrate FMN plays a key role in maintaining the ATP inside the binding site. The W184A mutant also increases the apparent $K_{m,ATP}$. However, the effect is in conjunction with a substantial increase in the apparent $K_{m,FMN}$, which is opposite to that of the D181A "supermutant".

In light of the D181A "supermutant" affecting the apparent $K_{m,ATP}$ rather than the apparent $K_{m,FMN}$, an alternant role of Arg297 is postulated. The R297A "supermutant" results in an increased apparent $K_{m,FMN}$ greater than that for D181A, in which Asp181 is shown in the crystal structures to have more direct

interactions with the flavin substrate. Therefore, the increase in the apparent $K_{m,FMN}$ by R297A "supermutant" must be derived from another source of direct interaction. The ~3 times increased apparent $K_{m,FMN}$ by the R297A "supermutant" may be a direct result from the ~5 times increased apparent $K_{m,ATP}$. For such a case, the stability of ATP may have a direct affect on the binding of FMN in the substrate binding pocket. As shown in the crystal structures, the C8M methyl group of the isoalloxazine ring is packed against the adenosine moiety of the bound ATP (**Fig. 3.21**). Support for the proposal comes from Bowers-Komro, DM *et al*[150] studying the effect of FMN analogs on FAD biosynthesis. Replacing the C7M and C8M methyl groups with a strong electronegative 7,8-dichloro-FMN or less electronegative 7,8-dibromo-FMN analogue resulted in an increase and decrease of $K_{m,FMN}$, respectively, compared to FMN[150]. Suggesting the C8 position of the isoalloxazine ring forms a favorable interaction with the adenine of ATP. Thus, upon formation of the Mg^{2+}ATP binary complex an interaction site is formed for the C8 position of the isoalloxazine ring. Absent from the study is the effect of the FMN analogues on $K_{m,ATP}$. From our study and Bowers-Komro, DM *et al*[150], the interaction between ATP and FMN appear to be synergistic, whereby a properly positioned ATP affects FMN binding and a properly positioned FMN affects ATP binding, which provides more stability to each substrate.

Product inhibition of *Cg*FMNAT

The fact that D181A results in no appreciable change in the $K_{m,FMN}$ means Asp181 has an alternant role other than providing necessary stability for FMN in the binding site. Instead, the "supermutant" D181A has a much faster k_{cat}, ~9 times of the native enzyme. Since D181 is located far away from the catalytic sites and unlikely to affect the chemistry step of the adenylyl transfer, the only explanation is that it is primarily involved in regulating product release. Thus, product release is the rate limiting step of the reaction. The fact that Asp181 is involved in product release is also supported by FAD not co-purifying with D181A "supermutant", as it did with the native *Cg*FMNAT. A similar effect is also observed for Arg297. However, Arg297 may not contribute much to regulating product release, as the turnover rate (k_{cat}) is ~4 times less than D181A, and the fact that FAD partially co-purifies with the R297A "supermutant". These "supermutants" provide support for earlier kinetic studies of rat liver FMNAT that revealed the enzyme is markedly inhibited by the product FAD and suggested that the biosynthesis of FAD is most likely regulated by product FAD at the last FMNAT step of the pathway[145].

To corroborate *Cg*FMNAT has the same substrate binding order of ATP first followed by FMN, as described for rat liver FMNAT[145], product inhibition by FAD was performed. Yamada Y. *et al*[145] was able to propose a substrate binding

order based on FAD displaying competitive inhibition with respect to ATP. However, we could not obtain the same results with *Cg*FMNAT probably because FAD has a slow-tight binding mode. Consequently, the inhibition kinetics has a mixed-type characteristic, which is in-line with slow-tight binding inhibitors[224].

Instead, support for our proposed substrate binding order that ATP binds first followed by FMN comes from the "supermutants" D181A and R297A. Since, the lines intersect on the 1/*v*-axis for the Lineweaver-Burk plot of 1/*v* vs. 1/[FMN], an ordered bi-bi substrate binding mechanism was proposed[219] (**Fig. 4.2b**). A potential explanation of the behavior is the effect ATP has on the binding of FMN, as shown with the "supermutant" R297A. The "supermutant" results in an increased apparent $K_{m,FMN}$, indicating that binding of ATP increases the stability of FMN. However, overcoming the dependence of ATP is shown with the "supermutant" D181A. Therefore, increasing the concentration of FMN at low ATP concentration, the same V_{max} can be obtained as in the saturating condition[219]. A product release order is supported by the fact that during the crystallization of native *Cg*FMNAT, which co-purifies with FAD, the addition of PP_i is needed in order to form single crystals, indicating PP_i releases first before FAD.

A structure guided steady-state kinetic and mutagenesis study elaborated on the residues defining the substrate binding site and highlighted the inter-

dependency of the two substrates. The study also provided the first detailed description about the catalytic process and characterization of important catalytic residues. Our study identified two “supermutants”, D181A of the flavin motif and R297A of the ARG2 motif, which affect substrate binding but have faster turnover rates probably due to an alleviated product inhibition. As such, the residues may be referred to as “gate-keepers” of the product FAD. The kinetic studies provided additional information that the product release may be the rate limiting step of the *Cg*FMNAT catalyzed reaction.

CHAPTER 5

Conclusions and future directions

Characterization of eukaryotic FMNAT began in 1949 with the partial purification of the enzyme from brewer's yeast (*S. cerevisiae*)[225]. Since then many studies of this essential enzyme have been carried out in a number of eukaryotic species[72,73,111-113,226]. Extensive biochemical studies have been performed for rat liver FMNAT that span from product inhibition, specificity for flavin analogues, alternative nucleotide triphosphate substrate and cation requirement[145,146,150]. However, the three dimensional structure and detailed active site architecture of the enzyme remained unknown.

Over a half century later the first structure of a eukaryotic FMNAT from yeast *Candida glabrata*, an opportunistic yeast pathogen, is presented in four different complex states through the use of X-ray crystallography, with resolutions ranging from 1.20-1.95 Å. These high resolution structures (apo-form, and complexes with ATP, AMPCPPMg^{2+}+FMN and PP_iMg^{2+}+FAD) of this essential enzyme revealed the overall structure of *Cg*FMNAT and the architectures of the substrate binding and catalytic sites, which provided insight into the structural basis of the kinetic properties of the enzymes[145]. In addition to

maintaining the well conserved PP-loop and ADE motifs in the adenine nucleotide α hydrolase-like superfamily, eukaryotic FMNATs also has the nucleotide binding motifs ARG1[138] and ARG2 (**Fig. 2.17 and Fig. 3.28**), as well as the γ-phosphate motif. Furthermore, eukaryotic FMNAT has a different PP-loop consensus sequence of "SYNGGKDC," which contains an Asn, Lys, and Cys residues (**Fig. 3.22 and 3.28**). The additional SQFD-loop and the elaborate organization of the C-terminal domain are also unique structural elements in *Cg*FMNAT, which are shared with the *S. cerevisiae* enzyme (**Fig. 3.22**).

Aside from the shared nucleotide binding motifs, the evolutionary relationship of eukaryotic FMNAT to the PAPS reductase-like family proteins seems to reside in the core fold that permits a FMN binding site (**Fig. 3.27**). As a result, based on the substrate and product ternary complexes, the flavin binding site (termed flavin motif) has no sequence and structural similarity to other known flavoproteins. Additionally, the flavin binding mode in the substrate binding site and the conformation of the bent FAD in *Cg*FMNAT is also unique. It is different from all other FAD-binding proteins with known 3D structures based on the 2001 survey by Dym and Eisenberg[209]. The uniqueness of the flavin binding mode may pose as an opportunity to selectively target yeast pathogens, such as the pathogenic *Candida* species that cause invasive candidiasis and candidemia[164-167], without affecting other FAD binding proteins in humans and potentially human

FMNAT. To accomplish such a task, more information is required from human FMNAT that includes variations within the substrate binding site, which our research may help foster.

The structure guided site-directed mutagenesis allowed the discovery of two "supermutants", D181A and R297A. D181 of the flavin motif is implicated in regulating product release as the turnover rate for the D181A mutant increases ~9 times with minimal change in the apparent $K_{m,FMN}$ when compared to native *Cg*FMNAT. This result suggests that product release is likely the rate limiting step of the reaction. As for R297 of the ARG2 motif, the involvement in product release is also implicated, though to a lesser extent, as the R297A mutant increases the turnover rate only ~2 times. With the identification of the two "supermutants", the term "gate-keeper" is given to these two residues (D181 and R297) based on the kinetic parameters. Furthermore, FAD doesn't co-purify with D181A mutant and co-purifies to a smaller degree with the R297A mutant (data not shown).

Structural analysis of *Cg*FMNAT complex states and data from the site-directed mutagenesis suggests further research to understand the catalytic process, product inhibition, product FAD release, and potential cellular cues that may regulate FAD synthesis and release. One of the first studies to undertake is defining the role of the Asn residue in the PP-loop. The N62S mutant generates a

dead enzyme for reasons we can only speculate. Structure determination of the mutant in an ATP binary or substrate ternary complex state is the key to understanding the mechanism for such an outcome. As the D181A mutant resulted in a ~4–7 times decrease in the K_i value of FAD when compared to native *Cg*FMNAT, the K_i value is still in the nano-Molar range. However, FAD doesn't co-purify with the "supermutant", suggesting that the affinity of the FAD to the "supermutant" enzyme is much lower than the wild-type *Cg*FMNAT. Determining the binding affinity (K_d) and the off rate (k_{off}) for FAD will aide in understanding whether FAD release is the rate limiting step. A glucose molecule was observed to interact with *Cg*FMNAT in the apo-form and product ternary complex. Whether the site of interaction is a crystallographic artifact or possesses an actual protein-protein or protein-ligand interaction site, can be partially investigated by the effect different glucose concentrations have on the initial rates in steady-state kinetics. To this end, a larger question can be asked that pertains to eukaryotic FMNAT associating with other proteins that may regulate catalysis and FAD release.

One of the first observations that may suggest *Cg*FMNAT participates in protein-protein interaction comes from the C-terminal domain of *Cg*FMNAT composed of a roughly flat surface. From an electrostatic surface potential view, a negatively charged pocket exists on this face of the molecule, flanked by a

positively charged patch on the left and a negatively charged patch on the right (**Fig. 2.10a and 2.10b**). In the ternary complexes, the negatively charge pocket changes shape and size, that leads to changes of the electrostatic surface potential. Due to the nature of the surface shape and electrostatic potential, the region of the C-terminal domain can be proposed as a potential protein-protein interaction site. A possible candidate would be the MoCo-binding protein-like domain that is in the gene encoding FMNAT in higher eukaryotes (**Fig. 1.9**). A protein with 27% sequence identity to the MoCo-binding protein-like domain exists in *C. glabrata* (gi:50286295) and can be purified. Spectroscopic analysis can be performed to determine if a metabolite co-purifies with the "MoCo" protein. Determining if the "MoCo" protein interacts with *Cg*FMNAT can be investigated by mixing the proteins together and measuring FMNAT activity in the presence of the "MoCo" protein. Further investigations into the potential protein-protein interaction can be done with isothermal calorimetry and X-ray crystallography to determine the site of interaction, as well as with site-directed mutagenesis.

Secondly, *Cg*FMNAT is homologous in sequence and structure to members of the PAPS reductase-like family, for which their respective catalysis is modulated through protein-protein interactions[138,139]. As shown in Chapter 2, *Cg*FMNAT fits into the equivalent position as ATP sulfurylase in a complex with a regulatory G protein (CysN), with minimal structure clashes (**Fig. 2.19a**). In a

study by Davierwala AP *et al*, *Sc*FMNAT was shown to interact with Cdc42, a Rho-like small GTPase, in a yeast-two-hybrid screen[227]. Lastly, in bacterial FADS the FMNAT domain is associated with RFK domain[71,109]. Whether eukaryotic FMNAT associates with RFK is not known.

In closing, our high-resolution structures of yeast FMNAT presents the first characterization of a eukaryotic version of this essential enzyme. The structures and kinetic studies provided many new insights into the architecture and function of the enzyme. The structural comparison between eukaryotic and bacterial FMNATs delineated the structural differences in the substrate binding sites. With the essentiality of bacterial FMNAT already established experimentally, the significant differences between eukaryotic and bacterial FMNATs may promote the development of selective anti-infectious drugs towards pathogenic bacteria. Moreover, two "supermutants" were discovered that increased the turnover rates and allowed identification of two residues functioning as "gate-keepers" of FAD. To determine whether their biological significance is in the maintenance of FAD homeostasis, which is important in eukaryotic cellular processes, will require *in vivo* studies. As such, the outcome of the current studies may facilitate the development of novel anti-infectious drugs and lead to profound changes in our understanding of the way RFK and FMNAT function in the cell.

REFERENCES

1. Massey, V. (2000). The chemical and biological versatility of riboflavin. *Biochem Soc Trans* **28**, 283-96.

2. Joosten, V. & van Berkel, W. J. (2007). Flavoenzymes. *Curr Opin Chem Biol* **11**, 195-202.

3. Merrill, A. H., Jr., Lambeth, J. D., Edmondson, D. E. & McCormick, D. B. (1981). Formation and mode of action of flavoproteins. *Annu Rev Nutr* **1**, 281-317.

4. (1991). *Chemistry and Biochemistry of Flavoenzymes* (Müller, F., Ed.), I, CRC Press, Boca Raton, FL.

5. Powers, H. J. (2003). Riboflavin (vitamin B-2) and health. *Am J Clin Nutr* **77**, 1352-60.

6. De Colibus, L. & Mattevi, A. (2006). New frontiers in structural flavoenzymology. *Curr Opin Struct Biol* **16**, 722-8.

7. Mansoorabadi, S. O., Thibodeaux, C. J. & Liu, H. W. (2007). The diverse roles of flavin coenzymes--nature's most versatile thespians. *J Org Chem* **72**, 6329-42.

8. Salomon, M., Christie, J. M., Knieb, E., Lempert, U. & Briggs, W. R. (2000). Photochemical and mutational analysis of the FMN-binding domains of the plant blue light receptor, phototropin. *Biochemistry* **39**, 9401-10.

9. Crosson, S. & Moffat, K. (2002). Photoexcited structure of a plant photoreceptor domain reveals a light-driven molecular switch. *Plant Cell* **14**, 1067-75.

10. Mewies, M., McIntire, W. S. & Scrutton, N. S. (1998). Covalent attachment of flavin adenine dinucleotide (FAD) and flavin mononucleotide (FMN) to enzymes: the current state of affairs. *Protein Sci* **7**, 7-20.

11. Huang, C. H., Lai, W. L., Lee, M. H., Chen, C. J., Vasella, A., Tsai, Y. C. & Liaw, S. H. (2005). Crystal structure of glucooligosaccharide oxidase

from Acremonium strictum: a novel flavinylation of 6-S-cysteinyl, 8alpha-N1-histidyl FAD. *J Biol Chem* **280**, 38831-8.

12. Massey, V. (1994). Activation of molecular oxygen by flavins and flavoproteins. *J Biol Chem* **269**, 22459-62.

13. Mattevi, A., Vanoni, M. A., Todone, F., Rizzi, M., Teplyakov, A., Coda, A., Bolognesi, M. & Curti, B. (1996). Crystal structure of D-amino acid oxidase: a case of active site mirror-image convergent evolution with flavocytochrome b2. *Proc Natl Acad Sci U S A* **93**, 7496-501.

14. van Berkel, W. J. H. (2008). Chemistry of Flavoenzymes. In *Wiley Encyclopedia of Chemical Biology* August 15, 2008 edit. John Wiley & Sons, Inc.

15. Shi, Y., Lan, F., Matson, C., Mulligan, P., Whetstine, J. R., Cole, P. A., Casero, R. A. & Shi, Y. (2004). Histone demethylation mediated by the nuclear amine oxidase homolog LSD1. *Cell* **119**, 941-53.

16. Forneris, F., Binda, C., Dall'Aglio, A., Fraaije, M. W., Battaglioli, E. & Mattevi, A. (2006). A highly specific mechanism of histone H3-K4 recognition by histone demethylase LSD1. *J Biol Chem* **281**, 35289-95.

17. Ballas, N., Grunseich, C., Lu, D. D., Speh, J. C. & Mandel, G. (2005). REST and its corepressors mediate plasticity of neuronal gene chromatin throughout neurogenesis. *Cell* **121**, 645-57.

18. Saleque, S., Kim, J., Rooke, H. M. & Orkin, S. H. (2007). Epigenetic regulation of hematopoietic differentiation by Gfi-1 and Gfi-1b is mediated by the cofactors CoREST and LSD1. *Mol Cell* **27**, 562-72.

19. Metzger, E., Wissmann, M., Yin, N., Muller, J. M., Schneider, R., Peters, A. H., Gunther, T., Buettner, R. & Schule, R. (2005). LSD1 demethylates repressive histone marks to promote androgen-receptor-dependent transcription. *Nature* **437**, 436-9.

20. Kahl, P., Gullotti, L., Heukamp, L. C., Wolf, S., Friedrichs, N., Vorreuther, R., Solleder, G., Bastian, P. J., Ellinger, J., Metzger, E., Schule, R. & Buettner, R. (2006). Androgen receptor coactivators lysine-

specific histone demethylase 1 and four and a half LIM domain protein 2 predict risk of prostate cancer recurrence. *Cancer Res* **66**, 11341-7.

21. Culhane, J. C. & Cole, P. A. (2007). LSD1 and the chemistry of histone demethylation. *Curr Opin Chem Biol* **11**, 561-8.

22. Shi, Y. (2007). Histone lysine demethylases: emerging roles in development, physiology and disease. *Nat Rev Genet* **8**, 829-33.

23. Ye, H., Cande, C., Stephanou, N. C., Jiang, S., Gurbuxani, S., Larochette, N., Daugas, E., Garrido, C., Kroemer, G. & Wu, H. (2002). DNA binding is required for the apoptogenic action of apoptosis inducing factor. *Nat Struct Biol* **9**, 680-4.

24. Mate, M. J., Ortiz-Lombardia, M., Boitel, B., Haouz, A., Tello, D., Susin, S. A., Penninger, J., Kroemer, G. & Alzari, P. M. (2002). The crystal structure of the mouse apoptosis-inducing factor AIF. *Nat Struct Biol* **9**, 442-6.

25. Susin, S. A., Lorenzo, H. K., Zamzami, N., Marzo, I., Snow, B. E., Brothers, G. M., Mangion, J., Jacotot, E., Costantini, P., Loeffler, M., Larochette, N., Goodlett, D. R., Aebersold, R., Siderovski, D. P., Penninger, J. M. & Kroemer, G. (1999). Molecular characterization of mitochondrial apoptosis-inducing factor. *Nature* **397**, 441-6.

26. Yu, S. W., Wang, H., Poitras, M. F., Coombs, C., Bowers, W. J., Federoff, H. J., Poirier, G. G., Dawson, T. M. & Dawson, V. L. (2002). Mediation of poly(ADP-ribose) polymerase-1-dependent cell death by apoptosis-inducing factor. *Science* **297**, 259-63.

27. Miramar, M. D., Costantini, P., Ravagnan, L., Saraiva, L. M., Haouzi, D., Brothers, G., Penninger, J. M., Peleato, M. L., Kroemer, G. & Susin, S. A. (2001). NADH oxidase activity of mitochondrial apoptosis-inducing factor. *J Biol Chem* **276**, 16391-8.

28. Vahsen, N., Cande, C., Briere, J. J., Benit, P., Joza, N., Larochette, N., Mastroberardino, P. G., Pequignot, M. O., Casares, N., Lazar, V., Feraud, O., Debili, N., Wissing, S., Engelhardt, S., Madeo, F., Piacentini, M., Penninger, J. M., Schagger, H., Rustin, P. & Kroemer, G. (2004). AIF deficiency compromises oxidative phosphorylation. *Embo J* **23**, 4679-89.

29. Joza, N., Oudit, G. Y., Brown, D., Benit, P., Kassiri, Z., Vahsen, N., Benoit, L., Patel, M. M., Nowikovsky, K., Vassault, A., Backx, P. H., Wada, T., Kroemer, G., Rustin, P. & Penninger, J. M. (2005). Muscle-specific loss of apoptosis-inducing factor leads to mitochondrial dysfunction, skeletal muscle atrophy, and dilated cardiomyopathy. *Mol Cell Biol* **25**, 10261-72.

30. Klein, J. A., Longo-Guess, C. M., Rossmann, M. P., Seburn, K. L., Hurd, R. E., Frankel, W. N., Bronson, R. T. & Ackerman, S. L. (2002). The harlequin mouse mutation downregulates apoptosis-inducing factor. *Nature* **419**, 367-74.

31. Terman, J. R., Mao, T., Pasterkamp, R. J., Yu, H. H. & Kolodkin, A. L. (2002). MICALs, a family of conserved flavoprotein oxidoreductases, function in plexin-mediated axonal repulsion. *Cell* **109**, 887-900.

32. Nadella, M., Bianchet, M. A., Gabelli, S. B., Barrila, J. & Amzel, L. M. (2005). Structure and activity of the axon guidance protein MICAL. *Proc Natl Acad Sci U S A* **102**, 16830-5.

33. Siebold, C., Berrow, N., Walter, T. S., Harlos, K., Owens, R. J., Stuart, D. I., Terman, J. R., Kolodkin, A. L., Pasterkamp, R. J. & Jones, E. Y. (2005). High-resolution structure of the catalytic region of MICAL (molecule interacting with CasL), a multidomain flavoenzyme-signaling molecule. *Proc Natl Acad Sci U S A* **102**, 16836-41.

34. Pasterkamp, R. J., Dai, H. N., Terman, J. R., Wahlin, K. J., Kim, B., Bregman, B. S., Popovich, P. G. & Kolodkin, A. L. (2006). MICAL flavoprotein monooxygenases: expression during neural development and following spinal cord injuries in the rat. *Mol Cell Neurosci* **31**, 52-69.

35. Pollegioni, L., Piubelli, L., Sacchi, S., Pilone, M. S. & Molla, G. (2007). Physiological functions of D-amino acid oxidases: from yeast to humans. *Cell Mol Life Sci* **64**, 1373-94.

36. Kleckner, N. W. & Dingledine, R. (1988). Requirement for glycine in activation of NMDA-receptors expressed in Xenopus oocytes. *Science* **241**, 835-7.

37. Baranano, D. E., Ferris, C. D. & Snyder, S. H. (2001). Atypical neural messengers. *Trends Neurosci* **24**, 99-106.

38. Harrison, P. J. & Owen, M. J. (2003). Genes for schizophrenia? Recent findings and their pathophysiological implications. *Lancet* **361**, 417-9.

39. Katsuki, H., Nonaka, M., Shirakawa, H., Kume, T. & Akaike, A. (2004). Endogenous D-serine is involved in induction of neuronal death by N-methyl-D-aspartate and simulated ischemia in rat cerebrocortical slices. *J Pharmacol Exp Ther* **311**, 836-44.

40. Sasamura, T., Matsuda, A. & Kokuba, Y. (2002). Determination of D-amino acid oxidase activity in tumour cells. *Ann Clin Biochem* **39**, 595-8.

41. Stegman, L. D., Zheng, H., Neal, E. R., Ben-Yoseph, O., Pollegioni, L., Pilone, M. S. & Ross, B. D. (1998). Induction of cytotoxic oxidative stress by D-alanine in brain tumor cells expressing Rhodotorula gracilis D-amino acid oxidase: a cancer gene therapy strategy. *Hum Gene Ther* **9**, 185-93.

42. Shih, J. C., Chen, K. & Ridd, M. J. (1999). Monoamine oxidase: from genes to behavior. *Annu Rev Neurosci* **22**, 197-217.

43. Krishnan, K. R. (2007). Revisiting monoamine oxidase inhibitors. *J Clin Psychiatry* **68 Suppl 8**, 35-41.

44. Fischer, M. & Bacher, A. (2005). Biosynthesis of flavocoenzymes. *Nat Prod Rep* **22**, 324-50.

45. Bacher, A., Eberhardt, S., Fischer, M., Kis, K. & Richter, G. (2000). Biosynthesis of vitamin b2 (riboflavin). *Annu Rev Nutr* **20**, 153-67.

46. Ritz, H., Schramek, N., Bracher, A., Herz, S., Eisenreich, W., Richter, G. & Bacher, A. (2001). Biosynthesis of riboflavin: studies on the mechanism of GTP cyclohydrolase II. *J Biol Chem* **276**, 22273-7.

47. Baugh, C. M. & Krumdieck, C. L. (1969). Biosynthesis of riboflavine in Corynebacterium species: the purine precursor. *J Bacteriol* **98**, 1114-9.

48. Mailander, B. & Bacher, A. (1976). Biosynthesis of riboflavin. Structure of the purine precursor and origin of the ribityl side chain. *J Biol Chem* **251**, 3623-8.

49. Foor, F. & Brown, G. M. (1975). Purification and properties of guanosine triphosphate cyclohydrolase II from Escherichia coli. *J Biol Chem* **250**, 3545-51.

50. Graham, D. E., Xu, H. & White, R. H. (2002). A member of a new class of GTP cyclohydrolases produces formylaminopyrimidine nucleotide monophosphates. *Biochemistry* **41**, 15074-84.

51. Burrows, R. B. & Brown, G. M. (1978). Presence of Escherichia coli of a deaminase and a reductase involved in biosynthesis of riboflavin. *J Bacteriol* **136**, 657-67.

52. Fischer, M., Romisch, W., Saller, S., Illarionov, B., Richter, G., Rohdich, F., Eisenreich, W. & Bacher, A. (2004). Evolution of vitamin B2 biosynthesis: structural and functional similarity between pyrimidine deaminases of eubacterial and plant origin. *J Biol Chem* **279**, 36299-308.

53. Richter, G., Fischer, M., Krieger, C., Eberhardt, S., Luttgen, H., Gerstenschlager, I. & Bacher, A. (1997). Biosynthesis of riboflavin: characterization of the bifunctional deaminase-reductase of Escherichia coli and Bacillus subtilis. *J Bacteriol* **179**, 2022-8.

54. Chen, S. C., Chang, Y. C., Lin, C. H., Lin, C. H. & Liaw, S. H. (2006). Crystal structure of a bifunctional deaminase and reductase from Bacillus subtilis involved in riboflavin biosynthesis. *J Biol Chem* **281**, 7605-13.

55. Stenmark, P., Moche, M., Gurmu, D. & Nordlund, P. (2007). The crystal structure of the bifunctional deaminase/reductase RibD of the riboflavin biosynthetic pathway in Escherichia coli: implications for the reductive mechanism. *J Mol Biol* **373**, 48-64.

56. Chatwell, L., Krojer, T., Fidler, A., Romisch, W., Eisenreich, W., Bacher, A., Huber, R. & Fischer, M. (2006). Biosynthesis of riboflavin: structure and properties of 2,5-diamino-6-ribosylamino-4(3H)-pyrimidinone 5'-phosphate reductase of Methanocaldococcus jannaschii. *J Mol Biol* **359**, 1334-51.

57. Graupner, M., Xu, H. & White, R. H. (2002). The pyrimidine nucleotide reductase step in riboflavin and F(420) biosynthesis in archaea proceeds by the eukaryotic route to riboflavin. *J Bacteriol* **184**, 1952-7.

58. Bacher, A. & Lingens, F. (1970). Biosynthesis of riboflavin. Formation of 2,5-diamino-6-hydroxy-4-(1'-D-ribitylamino)pyrimidine in a riboflavin auxotroph. *J Biol Chem* **245**, 4647-52.

59. Keller, P. J., Le Van, Q., Kim, S. U., Bown, D. H., Chen, H. C., Kohnle, A., Bacher, A. & Floss, H. G. (1988). Biosynthesis of riboflavin: mechanism of formation of the ribitylamino linkage. *Biochemistry* **27**, 1117-20.

60. Sadique, J., Shanmugasundaram, R. & Shanmugasundaram, E. R. (1966). Isolation of 5-amino-4-ribitylaminouracil from a riboflavineless mutant of Aspergillus nidulans. *Biochem J* **101**, 2C-3C.

61. Harzer, G., Rokos, H., Otto, M. K., Bacher, A. & Ghisla, S. (1978). Biosynthesis of riboflavin. 6,7-Dimethyl-8-ribityllumazine 5'-phosphate is not a substrate for riboflavin synthase. *Biochim Biophys Acta* **540**, 48-54.

62. Neuberger, G. & Bacher, A. (1986). Biosynthesis of riboflavin. Enzymatic formation of 6,7-dimethyl-8-ribityllumazine by heavy riboflavin synthase from Bacillus subtilis. *Biochem Biophys Res Commun* **139**, 1111-6.

63. Kis, K., Volk, R. & Bacher, A. (1995). Biosynthesis of riboflavin. Studies on the reaction mechanism of 6,7-dimethyl-8-ribityllumazine synthase. *Biochemistry* **34**, 2883-92.

64. Volk, R. & Bacher, A. (1990). Studies on the 4-carbon precursor in the biosynthesis of riboflavin. Purification and properties of L-3,4-dihydroxy-2-butanone-4-phosphate synthase. *J Biol Chem* **265**, 19479-85.

65. Volk, R. & Bacher, A. (1991). Biosynthesis of riboflavin. Studies on the mechanism of L-3,4-dihydroxy-2-butanone 4-phosphate synthase. *J Biol Chem* **266**, 20610-8.

66. Harvey, R. A. & Plaut, G. W. (1966). Riboflavin synthetase from yeast. Properties of complexes of the enzyme with lumazine derivatives and riboflavin. *J Biol Chem* **241**, 2120-36.

67. Plaut, G. W. (1963). Studies on the nature of the enzymic conversion of 6,7-dimethyl-8-ribityllumazine to riboflavin. *J Biol Chem* **238**, 2225-43.

68. Plaut, G. W., Beach, R. L. & Aogaichi, T. (1970). Studies on the mechanism of elimination of protons from the methyl groups of 6,7-dimethyl-8-ribityllumazine by riboflavin synthetase. *Biochemistry* **9**, 771-85.

69. Wacker, H., Harvey, R. A., Winestock, C. H. & Plaut, G. W. (1964). 4-(1'-D-Ribitylamino)-5-Amino-2,6-Dihydroxypyrimidine, the Second Product of the Riboflavin Synthetase Reaction. *J Biol Chem* **239**, 3493-7.

70. Efimov, I., Kuusk, V., Zhang, X. & McIntire, W. S. (1998). Proposed steady-state kinetic mechanism for Corynebacterium ammoniagenes FAD synthetase produced by Escherichia coli. *Biochemistry* **37**, 9716-23.

71. Manstein, D. J. & Pai, E. F. (1986). Purification and characterization of FAD synthetase from *Brevibacterium ammoniagenes*. *J. Biol. Chem.* **261**, 16169-16173.

72. Santos, M. A., Jimenez, A. & Revuelta, J. L. (2000). Molecular characterization of FMN1, the structural gene for the monofunctional flavokinase of *Saccharomyces cerevisiae*. *J. Biol. Chem.* **275**, 28618-28624.

73. Wu, M., Repetto, B., Glerum, D. M. & Tzagoloff, A. (1995). Cloning and characterization of FAD1, the structural gene for flavin adenine dinucleotide synthetase of Saccharomyces cerevisiae. *Mol Cell Biol* **15**, 264-71.

74. Mashhadi, Z., Zhang, H., Xu, H. & White, R. H. (2008). Identification and characterization of an archaeon-specific riboflavin kinase. *J Bacteriol* **190**, 2615-8.

75. Ammelburg, M., Hartmann, M. D., Djuranovic, S., Alva, V., Koretke, K. K., Martin, J., Sauer, G., Truffault, V., Zeth, K., Lupas, A. N. & Coles, M. (2007). A CTP-dependent archaeal riboflavin kinase forms a bridge in the evolution of cradle-loop barrels. *Structure* **15**, 1577-90.

76. Bereswill, S., Hinkelmann, S., Kist, M. & Sander, A. (1999). Molecular analysis of riboflavin synthesis genes in Bartonella henselae and use of the ribC gene for differentiation of Bartonella species by PCR. *J Clin Microbiol* **37**, 3159-66.

77. Fuller, T. E. & Mulks, M. H. (1995). Characterization of Actinobacillus pleuropneumoniae riboflavin biosynthesis genes. *J Bacteriol* **177**, 7265-70.

78. Lee, C. Y., O'Kane, D. J. & Meighen, E. A. (1994). Riboflavin synthesis genes are linked with the lux operon of Photobacterium phosphoreum. *J Bacteriol* **176**, 2100-4.

79. Fassbinder, F., Kist, M. & Bereswill, S. (2000). Structural and functional analysis of the riboflavin synthesis genes encoding GTP cyclohydrolase II (ribA), DHBP synthase (ribBA), riboflavin synthase (ribC), and riboflavin deaminase/reductase (ribD) from Helicobacter pylori strain P1. *FEMS Microbiol Lett* **191**, 191-7.

80. Lin, J. W., Chao, Y. F. & Weng, S. F. (2001). Riboflavin synthesis genes ribE, ribB, ribH, ribA reside in the lux operon of Photobacterium leiognathi. *Biochem Biophys Res Commun* **284**, 587-95.

81. Grill, S., Yamaguchi, H., Wagner, H., Zwahlen, L., Kusch, U. & Mack, M. (2007). Identification and characterization of two Streptomyces davawensis riboflavin biosynthesis gene clusters. *Arch Microbiol* **188**, 377-87.

82. Oltmanns, O., Bacher, A., Lingens, F. & Zimmermann, F. K. (1969). Biochemical and genetic classification of riboflavine deficient mutants of Saccharomyces cerevisiae. *Mol Gen Genet* **105**, 306-13.

83. Oltmanns, O. & Bacher, A. (1972). Biosynthesis of riboflavine in Saccharomyces cerevisiae: the role of genes rib 1 and rib 7. *J Bacteriol* **110**, 818-22.

84. Santos, M. A., Garcia-Ramirez, J. J. & Revuelta, J. L. (1995). Riboflavin biosynthesis in Saccharomyces cerevisiae. Cloning, characterization, and expression of the RIB5 gene encoding riboflavin synthase. *J Biol Chem* **270**, 437-44.

85. Garcia-Ramirez, J. J., Santos, M. A. & Revuelta, J. L. (1995). The Saccharomyces cerevisiae RIB4 gene codes for 6,7-dimethyl-8-ribityllumazine synthase involved in riboflavin biosynthesis. Molecular characterization of the gene and purification of the encoded protein. *J Biol Chem* **270**, 23801-7.

86. Kanehisa, M. & Goto, S. (2000). KEGG: kyoto encyclopedia of genes and genomes. *Nucleic Acids Res* **28**, 27-30.

87. Herz, S., Eberhardt, S. & Bacher, A. (2000). Biosynthesis of riboflavin in plants. The ribA gene of Arabidopsis thaliana specifies a bifunctional GTP cyclohydrolase II/3,4-dihydroxy-2-butanone 4-phosphate synthase. *Phytochemistry* **53**, 723-31.

88. Jordan, D. B., Bacot, K. O., Carlson, T. J., Kessel, M. & Viitanen, P. V. (1999). Plant riboflavin biosynthesis. Cloning, chloroplast localization, expression, purification, and partial characterization of spinach lumazine synthase. *J Biol Chem* **274**, 22114-21.

89. Koch, M., Breithaupt, C., GerhardtHaase, S., Weber, S., Cushman, M., Huber, R., Bacher, A. & Fischer, M. (2004). Structural basis of charge transfer complex formation by riboflavin bound to 6,7-dimethyl-8-ribityllumazine synthase. *Eur J Biochem* **271**, 3208-14.

90. Gerhardt, S., Haase, I., Steinbacher, S., Kaiser, J. T., Cushman, M., Bacher, A., Huber, R. & Fischer, M. (2002). The structural basis of riboflavin binding to Schizosaccharomyces pombe 6,7-dimethyl-8-ribityllumazine synthase. *J Mol Biol* **318**, 1317-29.

91. Meining, W., Mortl, S., Fischer, M., Cushman, M., Bacher, A. & Ladenstein, R. (2000). The atomic structure of pentameric lumazine synthase from Saccharomyces cerevisiae at 1.85 A resolution reveals the binding mode of a phosphonate intermediate analogue. *J Mol Biol* **299**, 181-97.

92. Braden, B. C., Velikovsky, C. A., Cauerhff, A. A., Polikarpov, I. & Goldbaum, F. A. (2000). Divergence in macromolecular assembly: X-ray crystallographic structure analysis of lumazine synthase from Brucella abortus. *J Mol Biol* **297**, 1031-6.

93. Persson, K., Schneider, G., Jordan, D. B., Viitanen, P. V. & Sandalova, T. (1999). Crystal structure analysis of a pentameric fungal and an icosahedral plant lumazine synthase reveals the structural basis for differences in assembly. *Protein Sci* **8**, 2355-65.

94. Zhang, X., Meining, W., Fischer, M., Bacher, A. & Ladenstein, R. (2001). X-ray structure analysis and crystallographic refinement of lumazine synthase from the hyperthermophile Aquifex aeolicus at 1.6 A resolution: determinants of thermostability revealed from structural comparisons. *J Mol Biol* **306**, 1099-114.

95. Mortl, S., Fischer, M., Richter, G., Tack, J., Weinkauf, S. & Bacher, A. (1996). Biosynthesis of riboflavin. Lumazine synthase of Escherichia coli. *J Biol Chem* **271**, 33201-7.

96. Haase, I., Mortl, S., Kohler, P., Bacher, A. & Fischer, M. (2003). Biosynthesis of riboflavin in archaea. 6,7-dimethyl-8-ribityllumazine synthase of Methanococcus jannaschii. *Eur J Biochem* **270**, 1025-32.

97. Zhang, X., Meining, W., Cushman, M., Haase, I., Fischer, M., Bacher, A. & Ladenstein, R. (2003). A structure-based model of the reaction catalyzed by lumazine synthase from Aquifex aeolicus. *J Mol Biol* **328**, 167-82.

98. Ritsert, K., Huber, R., Turk, D., Ladenstein, R., Schmidt-Base, K. & Bacher, A. (1995). Studies on the lumazine synthase/riboflavin synthase complex of Bacillus subtilis: crystal structure analysis of reconstituted, icosahedral beta-subunit capsids with bound substrate analogue inhibitor at 2.4 A resolution. *J Mol Biol* **253**, 151-67.

99. Ladenstein, R., Ritsert, K., Huber, R., Richter, G. & Bacher, A. (1994). The lumazine synthase/riboflavin synthase complex of Bacillus subtilis. X-ray structure analysis of hollow reconstituted beta-subunit capsids. *Eur J Biochem* **223**, 1007-17.

100. Ladenstein, R., Schneider, M., Huber, R., Bartunik, H. D., Wilson, K., Schott, K. & Bacher, A. (1988). Heavy riboflavin synthase from Bacillus subtilis. Crystal structure analysis of the icosahedral beta 60 capsid at 3.3 A resolution. *J Mol Biol* **203**, 1045-70.

101. Eberhardt, S., Korn, S., Lottspeich, F. & Bacher, A. (1997). Biosynthesis of riboflavin: an unusual riboflavin synthase of Methanobacterium thermoautotrophicum. *J Bacteriol* **179**, 2938-43.

102. Fischer, M., Schott, A. K., Romisch, W., Ramsperger, A., Augustin, M., Fidler, A., Bacher, A., Richter, G., Huber, R. & Eisenreich, W. (2004). Evolution of vitamin B2 biosynthesis. A novel class of riboflavin synthase in Archaea. *J Mol Biol* **343**, 267-78.

103. Ramsperger, A., Augustin, M., Schott, A. K., Gerhardt, S., Krojer, T., Eisenreich, W., Illarionov, B., Cushman, M., Bacher, A., Huber, R. & Fischer, M. (2006). Crystal structure of an archaeal pentameric riboflavin synthase in complex with a substrate analog inhibitor: stereochemical implications. *J Biol Chem* **281**, 1224-32.

104. Fischer, M., Romisch, W., Illarionov, B., Eisenreich, W. & Bacher, A. (2005). Structures and reaction mechanisms of riboflavin synthases of eubacterial and archaeal origin. *Biochem Soc Trans* **33**, 780-4.

105. Liao, D. I., Wawrzak, Z., Calabrese, J. C., Viitanen, P. V. & Jordan, D. B. (2001). Crystal structure of riboflavin synthase. *Structure* **9**, 399-408.

106. Vitreschak, A. G., Rodionov, D. A., Mironov, A. A. & Gelfand, M. S. (2002). Regulation of riboflavin biosynthesis and transport genes in bacteria by transcriptional and translational attenuation. *Nucleic Acids Res* **30**, 3141-51.

107. Burgess, C. M., Slotboom, D. J., Geertsma, E. R., Duurkens, R. H., Poolman, B. & van Sinderen, D. (2006). The riboflavin transporter RibU in Lactococcus lactis: molecular characterization of gene expression and the transport mechanism. *J Bacteriol* **188**, 2752-60.

108. Fischer, M. & Bacher, A. (2008). Biosynthesis of vitamin B2: Structure and mechanism of riboflavin synthase. *Arch Biochem Biophys* **474**, 252-65.

109. Coquard, D., Huecas, M., Ott, M., van Dijl, J. M., van Loon, A. P. & Hohmann, H. P. (1997). Molecular cloning and characterisation of the ribC gene from Bacillus subtilis: a point mutation in ribC results in riboflavin overproduction. *Mol Gen Genet* **254**, 81-4.

110. Sandoval, F. J. & Roje, S. (2005). An FMN hydrolase is fused to a riboflavin kinase homolog in plants. *J Biol Chem* **280**, 38337-45.

111. Sandoval, F. J., Zhang, Y. & Roje, S. (2008). Flavin nucleotide metabolism in plants: monofunctional enzymes synthesize fad in plastids. *J Biol Chem* **283**, 30890-900.

112. Galluccio, M., Brizio, C., Torchetti, E. M., Ferranti, P., Gianazza, E., Indiveri, C. & Barile, M. (2007). Over-expression in Escherichia coli, purification and characterization of isoform 2 of human FAD synthetase. *Protein Expr Purif* **52**, 175-81.

113. Brizio, C., Galluccio, M., Wait, R., Torchetti, E. M., Bafunno, V., Accardi, R., Gianazza, E., Indiveri, C. & Barile, M. (2006). Over-expression in Escherichia coli and characterization of two recombinant isoforms of human FAD synthetase. *Biochem Biophys Res Commun* **344**, 1008-16.

114. Liu, M. T., Wuebbens, M. M., Rajagopalan, K. V. & Schindelin, H. (2000). Crystal structure of the gephyrin-related molybdenum cofactor biosynthesis protein MogA from Escherichia coli. *J Biol Chem* **275**, 1814-22.

115. Schrag, J. D., Huang, W., Sivaraman, J., Smith, C., Plamondon, J., Larocque, R., Matte, A. & Cygler, M. (2001). The crystal structure of Escherichia coli MoeA, a protein from the molybdopterin synthesis pathway. *J Mol Biol* **310**, 419-31.

116. Solovieva, I. M., Kreneva, R. A., Leak, D. J. & Perumov, D. A. (1999). The ribR gene encodes a monofunctional riboflavin kinase which is involved in regulation of the Bacillus subtilis riboflavin operon. *Microbiology* **145**, 67-73.

117. Kearney, E. B., Goldenberg, J., Lipsick, J. & Perl, M. (1979). Flavokinase and FAD synthetase from Bacillus subtilis specific for reduced flavins. *J Biol Chem* **254**, 9551-7.

118. Clarebout, G., Villers, C. & Leclercq, R. (2001). Macrolide resistance gene mreA of Streptococcus agalactiae encodes a flavokinase. *Antimicrob Agents Chemother* **45**, 2280-6.

119. Cheek, S., Zhang, H. & Grishin, N. V. (2002). Sequence and structure classification of kinases. *J. Mol. Biol.* **320**, 855-881.

120. Camporeale, G. & Zempleni, J. (2003). Oxidative folding of interleukin-2 is impaired in flavin-deficient jurkat cells, causing intracellular accumulation of interleukin-2 and increased expression of stress response genes. *J Nutr* **133**, 668-72.

121. Manthey, K. C., Rodriguez-Melendez, R., Hoi, J. T. & Zempleni, J. (2006). Riboflavin deficiency causes protein and DNA damage in HepG2 cells, triggering arrest in G1 phase of the cell cycle. *J Nutr Biochem* **17**, 250-6.

122. Werner, R., Manthey, K. C., Griffin, J. B. & Zempleni, J. (2005). HepG2 cells develop signs of riboflavin deficiency within 4 days of culture in riboflavin-deficient medium. *J Nutr Biochem* **16**, 617-24.

123. Foraker, A. B., Khantwal, C. M. & Swaan, P. W. (2003). Current perspectives on the cellular uptake and trafficking of riboflavin. *Adv Drug Deliv Rev* **55**, 1467-83.

124. Forster, C., Revuelta, J. L. & Kramer, R. (2001). Carrier-mediated transport of riboflavin in Ashbya gossypii. *Appl Microbiol Biotechnol* **55**, 85-9.

125. Perl, M., Kearney, E. B. & Singer, T. P. (1976). Transport of riboflavin into yeast cells. *J Biol Chem* **251**, 3221-8.

126. Cecchini, G., Perl, M., Lipsick, J., Singer, T. P. & Kearney, E. B. (1979). Transport and binding of riboflavin by Bacillus subtilis. *J Biol Chem* **254**, 7295-301.

127. Reihl, P. & Stolz, J. (2005). The monocarboxylate transporter homolog Mch5p catalyzes riboflavin (vitamin B2) uptake in Saccharomyces cerevisiae. *J Biol Chem* **280**, 39809-17.

128. Vogl, C., Grill, S., Schilling, O., Stulke, J., Mack, M. & Stolz, J. (2007). Characterization of riboflavin (vitamin B2) transport proteins from Bacillus subtilis and Corynebacterium glutamicum. *J Bacteriol* **189**, 7367-75.

129. Karthikeyan, S., Zhou, Q., Mseeh, F., Grishin, N. V., Osterman, A. L. & Zhang, H. (2003). Crystal structure of human riboflavin kinase reveals a Beta barrel fold and a novel active site arch. *Structure (Camb)* **11**, 265-273.

130. Murzin, A. G., Brenner, S. E., Hubbard, T. & Chothia, C. (1995). SCOP: a structural classification of proteins database for the investigation of sequences and structures. *J. Mol. Biol.* **247**, 536-540.

131. Finn, R. D., Tate, J., Mistry, J., Coggill, P. C., Sammut, S. J., Hotz, H. R., Ceric, G., Forslund, K., Eddy, S. R., Sonnhammer, E. L. & Bateman, A. (2008). The Pfam protein families database. *Nucleic Acids Res* **36**, D281-8.

132. Bork, P., Holm, L., Koonin, E. V. & Sander, C. (1995). The cytidylyltransferase superfamily: identification of the nucleotide-binding site and fold prediction. *Proteins* **22**, 259-66.

133. Izard, T. & Geerlof, A. (1999). The crystal structure of a novel bacterial adenylyltransferase reveals half of sites reactivity. *Embo J* **18**, 2021-30.

134. Saridakis, V., Christendat, D., Kimber, M. S., Dharamsi, A., Edwards, A. M. & Pai, E. F. (2001). Insights into ligand binding and catalysis of a central step in NAD+ synthesis: structures of Methanobacterium thermoautotrophicum NMN adenylyltransferase complexes. *J Biol Chem* **276**, 7225-32.

135. Zhang, H., Zhou, T., Kurnasov, O., Cheek, S., Grishin, N. V. & Osterman, A. (2002). Crystal structures of E. coli nicotinate mononucleotide adenylyltransferase and its complex with deamido-NAD. *Structure (Camb)* **10**, 69-79.

136. Zhou, T., Kurnasov, O., Tomchick, D. R., Binns, D. D., Grishin, N. V., Marquez, V. E., Osterman, A. L. & Zhang, H. (2002). Structure of human nicotinamide/nicotinic acid mononucleotide adenylyltransferase. Basis for the dual substrate specificity and activation of the oncolytic agent tiazofurin. *J Biol Chem* **277**, 13148-54.

137. Weber, C. H., Park, Y. S., Sanker, S., Kent, C. & Ludwig, M. L. (1999). A prototypical cytidylyltransferase: CTP:glycerol-3-phosphate cytidylyltransferase from bacillus subtilis. *Structure* **7**, 1113-24.

138. Chartron, J., Carroll, K. S., Shiau, C., Gao, H., Leary, J. A., Bertozzi, C. R. & Stout, C. D. (2006). Substrate recognition, protein dynamics, and iron-sulfur cluster in Pseudomonas aeruginosa adenosine 5'-phosphosulfate reductase. *J Mol Biol* **364**, 152-69.

139. Mougous, J. D., Lee, D. H., Hubbard, S. C., Schelle, M. W., Vocadlo, D. J., Berger, J. M. & Bertozzi, C. R. (2006). Molecular basis for G protein control of the prokaryotic ATP sulfurylase. *Mol Cell* **21**, 109-22.

140. Savage, H., Montoya, G., Svensson, C., Schwenn, J. D. & Sinning, I. (1997). Crystal structure of phosphoadenylyl sulphate (PAPS) reductase: a new family of adenine nucleotide alpha hydrolases. *Structure* **5**, 895-906.

141. Aravind, L., Anantharaman, V. & Koonin, E. V. (2002). Monophyly of class I aminoacyl tRNA synthetase, USPA, ETFP, photolyase, and PP-ATPase nucleotide-binding domains: implications for protein evolution in the RNA. *Proteins* **48**, 1-14.

142. Bork, P. & Koonin, E. V. (1994). A P-loop-like motif in a widespread ATP pyrophosphatase domain: implications for the evolution of sequence motifs and enzyme activity. *Proteins* **20**, 347-55.

143. Tesmer, J. J., Klem, T. J., Deras, M. L., Davisson, V. J. & Smith, J. L. (1996). The crystal structure of GMP synthetase reveals a novel catalytic triad and is a structural paradigm for two enzyme families. *Nat Struct Biol* **3**, 74-86.

144. Rossmann, M. G., Moras, D. & Olsen, K. W. (1974). Chemical and biological evolution of nucleotide-binding protein. *Nature* **250**, 194-9.

145. Yamada, Y., Merrill, A. H., Jr. & McCormick, D. B. (1990). Probable reaction mechanisms of flavokinase and FAD synthetase from rat liver. *Arch Biochem Biophys* **278**, 125-30.

146. Oka, M. & McCormick, D. B. (1987). Complete purification and general characterization of FAD synthetase from rat liver. *J Biol Chem* **262**, 7418-22.

147. Walsh, C., Fisher, J., Spencer, R., Graham, D. W., Ashton, W. T., Brown, J. E., Brown, R. D. & Rogers, E. F. (1978). Chemical and enzymatic properties of riboflavin analogues. *Biochemistry* **17**, 1942-51.

148. Light, D. R., Walsh, C. & Marletta, M. A. (1980). Analytical and preparative high-performance liquid chromatography separation of flavin and flavin analog coenzymes. *Anal Biochem* **109**, 87-93.

149. Hausinger, R. P., Honek, J. F. & Walsh, C. (1986). Separation of flavins and flavin analogs by high-performance liquid chromatography. *Methods Enzymol* **122**, 199-209.

150. Bowers-Komro, D. M., Yamada, Y. & McCormick, D. B. (1989). Substrate specificity and variables affecting efficiency of mammalian flavin adenine dinucleotide synthetase. *Biochemistry* **28**, 8439-46.

151. Hustad, S., Ueland, P. M., Vollset, S. E., Zhang, Y., Bjorke-Monsen, A. L. & Schneede, J. (2000). Riboflavin as a determinant of plasma total homocysteine: effect modification by the methylenetetrahydrofolate reductase C677T polymorphism. *Clin Chem* **46**, 1065-71.

152. Tu, B. P. & Weissman, J. S. (2002). The FAD- and O(2)-dependent reaction cycle of Ero1-mediated oxidative protein folding in the endoplasmic reticulum. *Mol Cell* **10**, 983-94.

153. Brewer, J. W. & Diehl, J. A. (2000). PERK mediates cell-cycle exit during the mammalian unfolded protein response. *Proc Natl Acad Sci U S A* **97**, 12625-30.

154. Pahl, H. L. (1999). Signal transduction from the endoplasmic reticulum to the cell nucleus. *Physiol Rev* **79**, 683-701.

155. Gelfand, M. S., Mironov, A. A., Jomantas, J., Kozlov, Y. I. & Perumov, D. A. (1999). A conserved RNA structure element involved in the regulation of bacterial riboflavin synthesis genes. *Trends Genet* **15**, 439-42.

156. Kil, Y. V., Mironov, V. N., Gorishin, I., Kreneva, R. A. & Perumov, D. A. (1992). Riboflavin operon of Bacillus subtilis: unusual symmetric arrangement of the regulatory region. *Mol Gen Genet* **233**, 483-6.

157. Mack, M., van Loon, A. P. & Hohmann, H. P. (1998). Regulation of riboflavin biosynthesis in *Bacillus subtilis* is affected by the activity of the flavokinase/flavin adenine dinucleotide synthetase encoded by ribC. *J. Bacteriol.* **180**, 950-955.

158. Solovieva, I. M., Kreneva, R. A., Leak, D. J. & Perumov, D. A. (1999). The ribR gene encodes a monofunctional riboflavin kinase which is involved in regulation of the Bacillus subtilis riboflavin operon. *Microbiology* **145 (Pt 1)**, 67-73.

159. Winkler, W. C., Cohen-Chalamish, S. & Breaker, R. R. (2002). An mRNA structure that controls gene expression by binding FMN. *Proc Natl Acad Sci U S A* **99**, 15908-13.

160. Mironov, A. S., Gusarov, I., Rafikov, R., Lopez, L. E., Shatalin, K., Kreneva, R. A., Perumov, D. A. & Nudler, E. (2002). Sensing small molecules by nascent RNA: a mechanism to control transcription in bacteria. *Cell* **111**, 747-56.

161. Gerdes, S. Y., Scholle, M. D., D'Souza, M., Bernal, A., Baev, M. V., Farrell, M., Kurnasov, O. V., Daugherty, M. D., Mseeh, F., Polanuyer, B. M., Campbell, J. W., Anantha, S., Shatalin, K. Y., Chowdhury, S. A., Fonstein, M. Y. & Osterman, A. L. (2002). From genetic footprinting to antimicrobial drug targets: examples in cofactor biosynthetic pathways. *J. Bacteriol.* **184**, 4555-4572.

162. Becker, D., Selbach, M., Rollenhagen, C., Ballmaier, M., Meyer, T. F., Mann, M. & Bumann, D. (2006). Robust Salmonella metabolism limits possibilities for new antimicrobials. *Nature* **440**, 303-7.

163. Rollenhagen, C. & Bumann, D. (2006). Salmonella enterica highly expressed genes are disease specific. *Infect Immun* **74**, 1649-60.

164. Krcmery, V. & Barnes, A. J. (2002). Non-albicans Candida spp. causing fungaemia: pathogenicity and antifungal resistance. *J Hosp Infect* **50**, 243-60.

165. Ostrosky-Zeichner, L., Rex, J. H., Pappas, P. G., Hamill, R. J., Larsen, R. A., Horowitz, H. W., Powderly, W. G., Hyslop, N., Kauffman, C. A., Cleary, J., Mangino, J. E. & Lee, J. (2003). Antifungal susceptibility survey of 2,000 bloodstream Candida isolates in the United States. *Antimicrob Agents Chemother* **47**, 3149-54.

166. Fidel, P. L., Jr., Vazquez, J. A. & Sobel, J. D. (1999). Candida glabrata: review of epidemiology, pathogenesis, and clinical disease with comparison to C. albicans. *Clin Microbiol Rev* **12**, 80-96.

167. Li, L., Redding, S. & Dongari-Bagtzoglou, A. (2007). Candida glabrata: an emerging oral opportunistic pathogen. *J Dent Res* **86**, 204-15.

168. Wang, W., Kim, R., Jancarik, J., Yokota, H. & Kim, S.-H. (2003). Crystal Structure of a Flavin-Binding Protein from *Thermotoga maritima*. *Proteins* **52**, 633-635.

169. Wang, W., Kim, R., Yokota, H. & Kim, S. H. (2005). Crystal structure of flavin binding to FAD synthetase of Thermotoga maritima. *Proteins* **58**, 246-8.

170. Komarnisky, L. A., Christopherson, R. J. & Basu, T. K. (2003). Sulfur: its clinical and toxicologic aspects. *Nutrition* **19**, 54-61.

171. Marzluf, G. A. (1997). Molecular genetics of sulfur assimilation in filamentous fungi and yeast. *Annu Rev Microbiol* **51**, 73-96.

172. Saito, K. (2004). Sulfur assimilatory metabolism. The long and smelling road. *Plant Physiol* **136**, 2443-50.

173. Townsend, D. M., Tew, K. D. & Tapiero, H. (2004). Sulfur containing amino acids and human disease. *Biomed Pharmacother* **58**, 47-55.

174. Moore, K. L. (2003). The biology and enzymology of protein tyrosine O-sulfation. *J Biol Chem* **278**, 24243-6.

175. Hemmerich, S. & Rosen, S. D. (2000). Carbohydrate sulfotransferases in lymphocyte homing. *Glycobiology* **10**, 849-56.

176. Hemmerich, S., Verdugo, D. & Rath, V. L. (2004). Strategies for drug discovery by targeting sulfation pathways. *Drug Discov Today* **9**, 967-75.

177. Pei, J. & Grishin, N. V. (2007). PROMALS: towards accurate multiple sequence alignments of distantly related proteins. *Bioinformatics* **23**, 802-8.

178. Sheffield, P., Garrard, S. & Derewenda, Z. (1999). Overcoming expression and purification problems of RhoGDI using a family of "parallel" expression vectors. *Protein Expr Purif* **15**, 34-9.

179. Doublie, S. (1997). Preparation of selenomethionyl proteins for phase determination. *Methods Enzymol.* **276**, 523-530.

180. Minor, W., Cymborowski, M., Otwinowski, Z. & Chruszcz, M. (2006). HKL-3000: the integration of data reduction and structure solution--from diffraction images to an initial model in minutes. *Acta Crystallogr D Biol Crystallogr* **62**, 859-66.

181. Potterton, E., Briggs, P., Turkenburg, M. & Dodson, E. (2003). A graphical user interface to the CCP4 program suite. *Acta Crystallogr D Biol Crystallogr* **59**, 1131-7.

182. Hendrickson, W. A., Horton, J. R. & LeMaster, D. M. (1990). Selenomethionyl proteins produced for analysis by multiwavelength anomalous diffraction (MAD): a vehicle for direct determination of three-dimensional structure. *Embo J* **9**, 1665-72.

183. Gonzalez, A. (2003). Optimizing data collection for structure determination. *Acta Crystallogr D Biol Crystallogr* **59**, 1935-42.

184. Dodson, E. (2003). Is it jolly SAD? *Acta Crystallogr D Biol Crystallogr* **59**, 1958-65.

185. Otwinowski, Z. (1991). Maximum likelihood refinement of heavy atom parameters. In *Isomorphous Replacement and Anomalous Scattering* (Wolf, W., Evans, P. R. & Leslie, A. G. W., eds.), pp. 80-86. Daresbury Laboratory, Warrington, UK.

186. Cowtan, K. (1994). 'DM': an automated procedure for phase improvement by density modification. *Joint CCP4 and ESF-EACBM Newsletter on Protein Crystallography* **31**, 34-38.

187. Terwilliger, T. C. (2003). SOLVE and RESOLVE: automated structure solution and density modification. *Methods Enzymol* **374**, 22-37.

188. Morris, R. J., Perrakis, A. & Lamzin, V. S. (2003). ARP/wARP and automatic interpretation of protein electron density maps. *Methods Enzymol* **374**, 229-44.

189. Murshudov, G. N., Vagin, A. A. & Dodson, E. J. (1997). Refinement of macromolecular structures by the maximum-likelihood method. *Acta Crystallogr D Biol Crystallogr* **53**, 240-55.

190. Emsley, P. & Cowtan, K. (2004). Coot: model-building tools for molecular graphics. *Acta Crystallogr D Biol Crystallogr* **60**, 2126-32.

191. Merritt, E. A. (1999). Expanding the model: anisotropic displacement parameters in protein structure refinement. *Acta Crystallogr D Biol Crystallogr* **55**, 1109-17.

192. Lovell, S. C., Davis, I. W., Arendall, W. B., 3rd, de Bakker, P. I., Word, J. M., Prisant, M. G., Richardson, J. S. & Richardson, D. C. (2003). Structure validation by Calpha geometry: phi,psi and Cbeta deviation. *Proteins* **50**, 437-50.

193. Dolinsky, T. J., Nielsen, J. E., McCammon, J. A. & Baker, N. A. (2004). PDB2PQR: an automated pipeline for the setup of Poisson-Boltzmann electrostatics calculations. *Nucleic Acids Res* **32**, W665-7.

194. Sitkoff, D., Sharp, K. A. & Honig, B. (1994). Accurate Calculation of Hydration Free Energies Using Macroscopic Solvent Models. *The Journal of Physical Chemistry* **98**, 1978-1988.

195. Baker, N. A., Sept, D., Joseph, S., Holst, M. J. & McCammon, J. A. (2001). Electrostatics of nanosystems: application to microtubules and the ribosome. *Proc Natl Acad Sci U S A* **98**, 10037-41.

196. Krissinel, E. & Henrick, K. (2004). Secondary-structure matching (SSM), a new tool for fast protein structure alignment in three dimensions. *Acta Crystallogr D Biol Crystallogr* **60**, 2256-68.

197. Krissinel, E. & Henrick, K. (2007). Inference of macromolecular assemblies from crystalline state. *J Mol Biol* **372**, 774-97.

198. Holm, L. & Sander, C. (1995). Dali: a network tool for protein structure comparison. *Trends Biochem. Sci.* **20**, 478-480.

199. Miller, M. T., Bachmann, B. O., Townsend, C. A. & Rosenzweig, A. C. (2001). Structure of beta-lactam synthetase reveals how to synthesize antibiotics instead of asparagine. *Nat Struct Biol* **8**, 684-9.

200. Nakanishi, K., Fukai, S., Ikeuchi, Y., Soma, A., Sekine, Y., Suzuki, T. & Nureki, O. (2005). Structural basis for lysidine formation by ATP pyrophosphatase accompanied by a lysine-specific loop and a tRNA-recognition domain. *Proc Natl Acad Sci U S A* **102**, 7487-92.

201. Devedjiev, Y., Symersky, J., Singh, R., Jedrzejas, M., Brouillette, C., Brouillette, W., Muccio, D., Chattopadhyay, D. & DeLucas, L. (2001). Stabilization of active-site loops in NH3-dependent NAD+ synthetase from Bacillus subtilis. *Acta Crystallogr D Biol Crystallogr* **57**, 806-12.

202. Chayen, N. E., Shaw Steward, P.D., Maeder, D.L., and Blow D.M. (1990). An automated system for micro-batch protein crystallization and screening. *Journal of Applied Crystallography* **23**, 297-302.

203. Otwinowski, Z. & Minor, W. (1997). Processing of X-ray diffraction data collected in oscillation mode. *Methods Enzymol.* **276**, 307-326.

204. Teplyakov, A. V. a. A. (1997). MOLREP: an Automated Program for Molecular Replacement. *Journal of Applied Crystallography* **30**, 4.

205. Adams, P. D., Grosse-Kunstleve, R. W., Hung, L. W., Ioerger, T. R., McCoy, A. J., Moriarty, N. W., Read, R. J., Sacchettini, J. C., Sauter, N. K. & Terwilliger, T. C. (2002). PHENIX: building new software for automated crystallographic structure determination. *Acta Crystallogr D Biol Crystallogr* **58**, 1948-54.

206. Davis, I. W., Leaver-Fay, A., Chen, V. B., Block, J. N., Kapral, G. J., Wang, X., Murray, L. W., Arendall, W. B., 3rd, Snoeyink, J., Richardson, J. S. & Richardson, D. C. (2007). MolProbity: all-atom contacts and

structure validation for proteins and nucleic acids. *Nucleic Acids Res* **35**, W375-83.

207. Sayers, E. W., Barrett, T., Benson, D. A., Bryant, S. H., Canese, K., Chetvernin, V., Church, D. M., DiCuccio, M., Edgar, R., Federhen, S., Feolo, M., Geer, L. Y., Helmberg, W., Kapustin, Y., Landsman, D., Lipman, D. J., Madden, T. L., Maglott, D. R., Miller, V., Mizrachi, I., Ostell, J., Pruitt, K. D., Schuler, G. D., Sequeira, E., Sherry, S. T., Shumway, M., Sirotkin, K., Souvorov, A., Starchenko, G., Tatusova, T. A., Wagner, L., Yaschenko, E. & Ye, J. (2009). Database resources of the National Center for Biotechnology Information. *Nucleic Acids Res* **37**, D5-15.

208. Benson, D. A., Karsch-Mizrachi, I., Lipman, D. J., Ostell, J. & Sayers, E. W. (2009). GenBank. *Nucleic Acids Res* **37**, D26-31.

209. Dym, O. & Eisenberg, D. (2001). Sequence-structure analysis of FAD-containing proteins. *Protein Sci* **10**, 1712-28.

210. Larsen, T. M., Boehlein, S. K., Schuster, S. M., Richards, N. G., Thoden, J. B., Holden, H. M. & Rayment, I. (1999). Three-dimensional structure of Escherichia coli asparagine synthetase B: a short journey from substrate to product. *Biochemistry* **38**, 16146-57.

211. Muller, Y. A., Schumacher, G., Rudolph, R. & Schulz, G. E. (1994). The refined structures of a stabilized mutant and of wild-type pyruvate oxidase from Lactobacillus plantarum. *J Mol Biol* **237**, 315-35.

212. Yeh, J. I., Claiborne, A. & Hol, W. G. (1996). Structure of the native cysteine-sulfenic acid redox center of enterococcal NADH peroxidase refined at 2.8 A resolution. *Biochemistry* **35**, 9951-7.

213. Ingelman, M., Bianchi, V. & Eklund, H. (1997). The three-dimensional structure of flavodoxin reductase from Escherichia coli at 1.7 A resolution. *J Mol Biol* **268**, 147-57.

214. Park, H. W., Kim, S. T., Sancar, A. & Deisenhofer, J. (1995). Crystal structure of DNA photolyase from Escherichia coli. *Science* **268**, 1866-72.

215. Karplus, P. A. & Schulz, G. E. (1987). Refined structure of glutathione reductase at 1.54 A resolution. *J Mol Biol* **195**, 701-29.

216. Grill, S., Busenbender, S., Pfeiffer, M., Kohler, U. & Mack, M. (2008). The bifunctional flavokinase/flavin adenine dinucleotide synthetase from Streptomyces davawensis produces inactive flavin cofactors and is not involved in resistance to the antibiotic roseoflavin. *J Bacteriol* **190**, 1546-53.

217. Webb, M. R. (1992). A continuous spectrophotometric assay for inorganic phosphate and for measuring phosphate release kinetics in biological systems. *Proc Natl Acad Sci U S A* **89**, 4884-7.

218. Upson, R. H., Haugland, R. P., Malekzadeh, M. N. & Haugland, R. P. (1996). A spectrophotometric method to measure enzymatic activity in reactions that generate inorganic pyrophosphate. *Anal Biochem* **243**, 41-5.

219. Segel, I. H. (1993). *Enzyme Kinetics: Behavior and Analysis of Rapid Equilibrium and Steady-State Enzyme Systems*, Wiley-Interscience, New York.

220. Newton, G. L., Ta, P., Sareen, D. & Fahey, R. C. (2006). A coupled spectrophotometric assay for l-cysteine:1-D-myo-inosityl 2-amino-2-deoxy-alpha-D-glucopyranoside ligase and its application for inhibitor screening. *Anal Biochem* **353**, 167-73.

221. Cogan, E. B., Birrell, G. B. & Griffith, O. H. (1999). A robotics-based automated assay for inorganic and organic phosphates. *Anal Biochem* **271**, 29-35.

222. Rumsfeld, J., Ziegelbauer, K. & Spaltmann, F. (2000). High-throughput assay for inorganic pyrophosphatases using the cytosolic enzymes of Saccharomyces cerevisiae and human as an example. *Protein Expr Purif* **18**, 303-9.

223. Kolobe, D., Sayed, Y. & Dirr, H. W. (2004). Characterization of bromosulphophthalein binding to human glutathione S-transferase A1-1: thermodynamics and inhibition kinetics. *Biochem J* **382**, 703-9.

224. Williams, J. W. & Morrison, J. F. (1979). The Kinetics of Reversible Tight-Binding Inhibition. In *Methods in Enzymology* (Purich, D. L., ed.), Vol. 63, pp. 437-467. Elsevier Academic Press, Boston.

225. Schrecker, A. W. & Kornberg, A. (1950). Reversible Enzymatic Synthesis of Flavin-Adenine Dinucleotide. *J Biol Chem* **182**, 795-803.

226. Giri, K. V., Rao, N. A., Cama, H. R. & Kumar, S. A. (1960). Studies on flavinadenine dinucleotide-synthesizing enzyme in plants. *Biochem J* **75**, 381-6.

227. Davierwala, A. P., Haynes, J., Li, Z., Brost, R. L., Robinson, M. D., Yu, L., Mnaimneh, S., Ding, H., Zhu, H., Chen, Y., Cheng, X., Brown, G. W., Boone, C., Andrews, B. J. & Hughes, T. R. (2005). The synthetic genetic interaction spectrum of essential genes. *Nat Genet* **37**, 1147-52.